Influence of rare-earth element substitution on the structural and physical properties of trigonal iron sulphide at the nano scale

by

Shubhra Jyotsna
10PP15J26031

A thesis submitted to the
Academy of Scientific & Innovative
Research for the award of the degree of
DOCTOR OF PHILOSOPHY
In
SCIENCE

Under the supervision of
Dr. Pankaj Poddar

CSIR-National Chemical Laboratory, Pune

Academy of Scientific and Innovative Research
AcSIR Headquarters, CSIR-HRDC campus
Sector 19, Kamla Nehru Nagar,
Ghaziabad, U.P. 201 002, India

January, 2023

Certificate

This is to certify that the work incorporated in this Ph.D. thesis entitled “*Influence of rare-earth element substitution on the structural and physical properties of trigonal iron sulphide at the nano scale*”, submitted by *Shubhra Jyotsna* to the Academy of Scientific and Innovative Research (AcSIR), in partial fulfillment of the requirements for the award of the Degree of *Doctor of Philosophy in Science*, embodies original research work carried-out by the student. We further certify that this work has not been submitted to any other University or Institution in part or full for the award of any degree or diploma. Research material(s) obtained from other source(s) and used in this research work has/have been duly acknowledged in the thesis. Image(s), illustration(s), figure(s), table(s) etc., used in the thesis from other source(s), have also been duly cited and acknowledged.

Shubhrajyotsna

(Signature of Student)
Shubhra Jyotsna
04.01.2023

(Signature of Supervisor)
Dr. Pankaj Poddar
04.01.2023

STATEMENTS OF ACADEMIC INTEGRITY

I, Shubhra Jyotsna, a Ph.D. student of the Academy of Scientific and Innovative Research (AcSIR) with Registration No. 10PP15J26031 hereby undertake that the thesis entitled "Influence of rare-earth element substitution on the structural and physical properties of trigonal iron sulphide at the nano scale" has been prepared by me and that the document reports original work carried out by me and is free of any plagiarism in compliance with the UGC Regulations on *"Promotion of Academic Integrity and Prevention of Plagiarism in Higher Educational Institutions (2018)"* and the CSIR Guidelines for "*Ethics in Research and in Governance (2020)".*

Shubhrajyotsna

Signature of the Student
Date: 04.01.2023
Place: Pune

It is hereby certified that the work done by the student, under my/our supervision, is plagiarism-free in accordance with the UGC Regulations on *"Promotion of Academic Integrity and Prevention of Plagiarism in Higher Educational Institutions (2018)"* and the CSIR Guidelines for "*Ethics in Research and in Governance (2020)".*

Signature of the Supervisor
Name: Dr. Pankaj Poddar
Date: 04.01.2023
Place: Pune

Dedicated to

My Nana Ji, Nani,
Nannan, my parents on
both sides and all my
teachers

ACKNOWLEDGEMENTS

There has been support, blessing, encouragement, learning, and inspiration from many people which made this work possible. For me, this thesis is such an important destiny, and I am indeed indebted to many people for their wishes and blessings in completing this journey. I take this opportunity to acknowledge and extend my sincere gratitude to all these people who have been involved, directly or indirectly, in making the research work described in this thesis possible.

First and foremost, I would like to express my sincere gratitude to my thesis advisor, Dr. Pankaj Poddar for introducing me to exciting interdisciplinary science and for his continuous advice, inspiration, encouragement, and unconditional support throughout my Ph.D. journey. His enthusiasm and integral view on research have made a deep impression on me. During my interactions with him, I have learned extensively from him, including how to raise new possibilities, regard an old question from a new perspective, approach a problem by systematic thinking, data-driven decision-making, and exploiting serendipity, which even extended deep to health science, and spirituality. I have learned from him why should we always go down to the basics, as the answers to all the questions lie there. I am grateful to him for having me shown this way to inculcate the habit of critical thinking and for teaching about dos and don'ts in every aspect of life, including science. I take this opportunity to admire his way of teaching, where he starts from a basic level and move towards an advanced level to make any topic crystal clear and simpler. His deep knowledge of a multitude of topics and subjects has motivated me to be a constant learner. I feel fortunate and privileged to be associated with him and be a part of his research group.

I would also like to thank my doctoral advisory committee members, Dr. Suresh Bhatt, Dr. Sreekumar Kurungot, Dr. Kirandeep Singh, and Dr. Guruswamy Kumaraswamy for their time, constructive suggestions, guidance, and support. I wish to thank my external expert Dr. Avinash Khare, University of Pune, for evaluating my work in my up-gradation meeting. I warmly thank him for his precious time, advice, and discussion of my work.

I wish to extend my sincere thanks to the present Director of CSIR-NCL, Dr. Ashish Lele, Dr. Ashwini Kumar Nangia (former Director), and Dr. Sourav Pal (former Director) for giving me an opportunity to work in this prestigious institute and making the facilities available to carry out the research. I am also grateful to the present Head of the Physical and Materials Chemistry Division, Dr. T. Ajithkumar, Dr. P. A. Joy (former HoD), Dr. B. L. V. Prasad (former HoD), and Dr. Anil Kumar (former HoD) for their kind help during my Ph.D. Many thanks to the staff members of our division, who have helped me with the routine official work. I wish to thank all the administrative and non-teaching staff of CSIR-NCL for their kind support and assistance over the years on various occasions.

My sincere thanks to Mr. S. S. Deo, Mr. R. S. Gholap, Venkatesh, Sheetal, Pankaj, and Harsha in the Center for Materials Characterization Division, NCL, for their timely help in XPS, TEM, and SEM measurements.

My special thanks to Dr. Rajesh Gonnade for his teachings on crystallography and XRD in the coursework. I admire his outstanding knowledge and enthusiasm during the entire course of his teachings. Many thanks for explaining the space groups in detail. I want to express my deepest gratitude to Dr. Guruswamy Kumaraswamy, IIT Bombay for his teaching on SAXS in the course work, which helped in my research on GQDs in the initial days of my Ph.D.

I wish to thank my collaborator— Dr. Raju Mondal (IACS, Kolkata) for introducing me and giving me an opportunity to work on a metal oxide framework.

I am grateful to the Department of Science and Technology, New Delhi, India, for providing me with DST-INSPIRE funding and a fellowship to pursue research at NCL.

I take this opportunity to thank my seniors from the lab, Dr. Puneet Khandelwal, Dr. Mousumi Sen, Dr. Preeti Padhye, Dr. Preeti Gupta, and Dr. Chandrashekhar for their help. I also thank the Postdoctoral fellows, Dr. Geeta Sharma (special thanks to you Di, for all the discussions and suggestions), Dr. Chiti Tank, Dr. Manorama Lakhe, Dr. Subodh Gautam and Dr. Bhavana Joshi (special thanks to you, Di, for your kind and loving gesture), for the interesting discussions. I would also like to thank my fellow lab mate, Dr. Monika Malik for her support and love. I especially acknowledge my fellow juniors, Supriya (special thanks for your lovely and kind gestures all the time), Monika (special thanks for keeping the lab cheerful), Dinesh, and Manisha for your loving company. I will never forget the experiences we've shared.

I would like to acknowledge my friends in NCL— Vrushali, Ruchi, Ashish, Amit, Sayantan, Tubai, Ravi, Ragini Di, Reshma, Anup, Roby, Divya, Ayesha, Pravin, and Shahebaz for the memorable times we've shared.

I would like to take this opportunity to express my deepest gratitude to all my teachers right from primary school who loved me and encouraged me to do better.

My heartfelt gratitude to Dr. Goutam Sheet (IISER Mohali) for giving me an opportunity to work with him. I cannot be thankful enough to you for your lifelong teachings, which I still implement in my research and day-to-day activities.

I extend my gratitude to my fellow lab mates and friends from IISER Mohali— Abhishek, and Leena, for the useful discussions and beautiful times spent together.

A special thanks to Brajesh Bhaiya, Sarita Di, and lovely Pragya and Pratyush in Pune for the time-to-time stay at their home and their constant love, care, and support. I extend my gratitude to Waghmare Nana Ji in Pune for his immense love towards me.

I would like to thank my friends in Pune— Kanak and Ashutosh, for all the care and every little celebration. Your presence has touched me deeply.

Special thanks to my school-time friend— Palak, for believing in me, and for your constant love and support.

I would like to extend my gratitude to Dadi Ji, Chacha Ji, Bua Ji, and Fufa Ji for being so affectionate and believing in me. My deep gratitude to Bade Mama Ji for always being caring and loving to me.

Nana Ji and Nani, we all miss you. I can't thank you enough for the endless love, and care, for always believing in me and guiding me through the hard times. Nannan, with you I have learned a lot in multiple directions since my childhood. My expression of gratitude towards you can never be enough. I can't thank you enough for believing in me, for all the love care, and support in every way, and for always proving me with the direction to move ahead. I cannot thank my parents enough for what they have done for me. I am deeply grateful for their patience, endless love, and time-to-time moral support, even during my tough times. I am deeply grateful to my parents after my wedding (my mother- and father-in-law) for providing me with endless love and unmatched support. This thesis is dedicated to all of you.

I would like to extend my deep gratitude to Bhaiya and Krutika for their constant love and guidance. I would like to acknowledge Amita Aunty Ji, Deepika, and Siddhesh for their lovely presence in my life. I wish to deeply thank Bittu Bhaiya, Bhumi Di, Nitu Bhaiya, and Bhawana Di for encouraging and supporting me to achieve my dreams. My deepest affection to my nephews, and nieces— Harsh, Moksh, Alviya, and Alvina for their endless love.

Umesh, I thank you for your understanding, patience, and loving support during my thesis work. Thank you for making this journey easier for me with your kind and loving presence.

…. Shubhra Jyotsna

Table of Contents

Chapter 1: Introduction

Chapter 2: Synthesis and structural study of 3C Fe_7S_8 and Gd-substituted 3C Fe_7S_8 nanoparticles

Chapter 3: Study of magnetism in 3C Fe_7S_8 and Gd-substituted 3C Fe_7S_8 nanoparticles

Chapter 4: Dielectric properties of 3C Fe_7S_8 and Gd-substituted 3C Fe_7S_8 nanoparticles

Chapter 5: Summary and future outlook

Abstract

List of publications

List of abbreviations

1.	Nanoparticles	NPs
2.	Wide-angle X-ray scattering	WAXS
3.	Transmission electron microscopy	TEM
4.	X-ray diffraction	XRD
5.	Space group	SG
6.	Periodic Bond Chain	PBC
7.	Inter-planar spacing	d_{hkl}
8.	Rate of growth	R_{hkl}
9.	Morphological importance	MI
10.	Transition metal chalcogenides	TMCs
11.	Metal chalcogenides (MC)	MC
12.	Transition metal dichalcogenides	TMDs
13.	Transition metal sulfides	TMSs
14.	Hydrogen evolution reaction	HER
15.	Oxygen evolution reaction	OER
16.	Iron-selenide	Fe-S
17.	Iron-selenium	Fe-Se
18.	Room temperature	RT
19.	Curie temperature	T_C
20.	Nanometres	nm
21.	Magnetic nanoparticles	MNPs
22.	Saturation magnetization	M_S
23.	Coercivity	H_C
24.	Remnant magnetization	M_R
25.	Average blocking temperature	T_B
26.	Anisotropy constant	K_u
27.	Surface energy	SE
28.	Oleylamine	OLA
29.	X-ray photoemission spectroscopy	XPS
30.	Round-bottom	RB
31.	Binding energies	BE
32.	Physical Property Measurement System	PPMS
33.	Vibrating sample magnetometer	VSM
34.	Magnetization versus temperature	M−T
35.	Zero-field-cooled	ZFC
36.	Field-cooled	FC
37.	Magnetization versus field	M H
38.	Crystal field splitting	CFS
39.	Rare-earth	RE
40.	Maximum energy product	$(BH)_{max}$
41.	Effective magnetic anisotropy constant	K_{eff}
42.	Full width at half maxima	FWHM

43.	Superconducting quantum interference device	SQUID
44.	Relative intensities	RI
45.	Anisotropy field	H_a
46.	Magnetic susceptibility	χ

Chapter1

Introduction

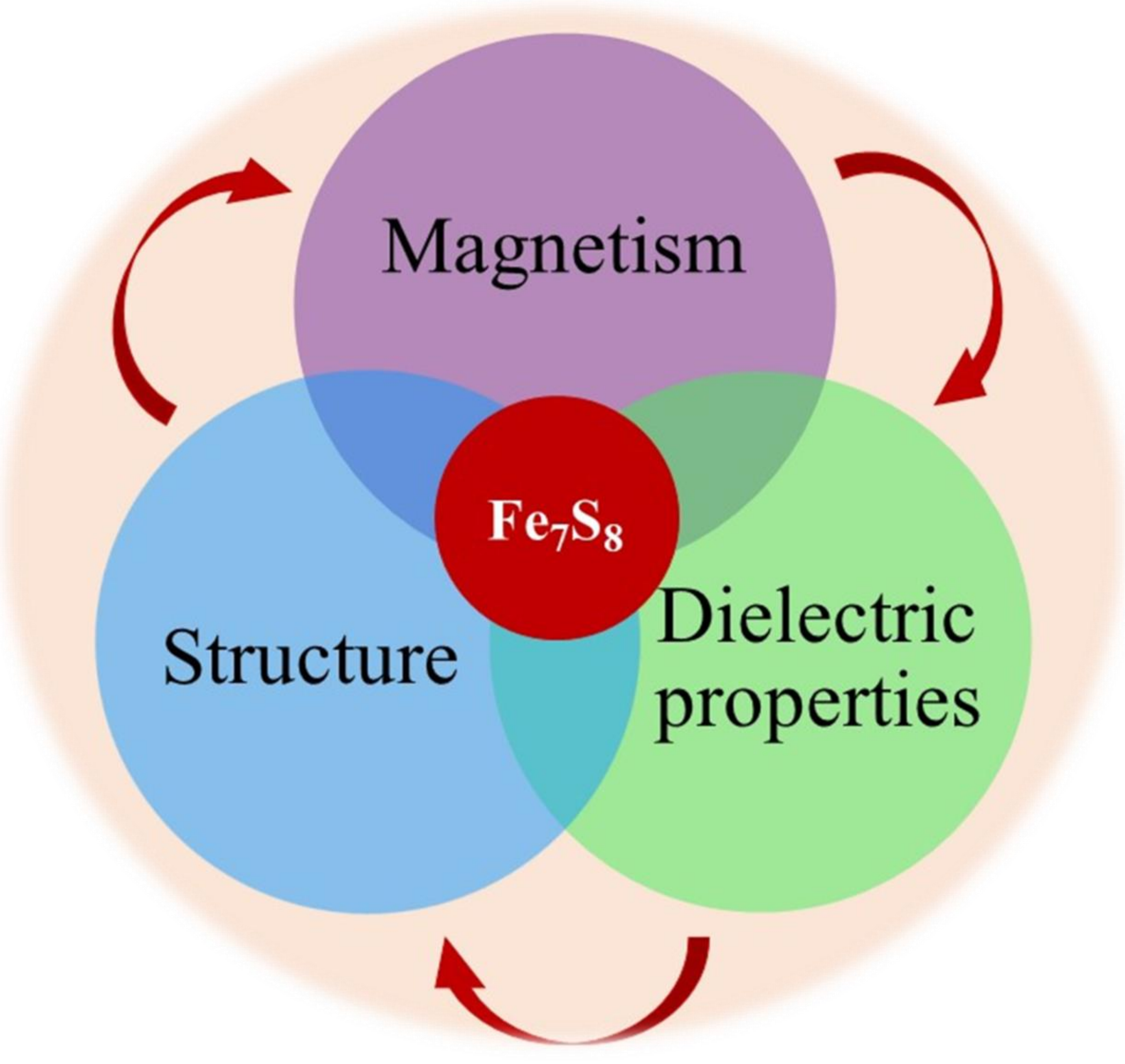

Highlights

The chapter starts with a discussion on the properties and importance of transition metal chalcogenides in a number of areas of science.

The iron-sulphur (Fe-S) system, as the most important earth mineral, shares some unique properties, mainly due to their complex crystal structures. The binary phases of Fe-S system are discussed in detail with the help of phase diagram.

Emphasis on the pyrrhotite group has been given, as they have important contribution as the earth mineral and to the several industrial applications. The structure and the interesting magnetic properties of some important pyrrhotites are highlighted.

The uniqueness of pyrrhotite with trigonal phase of Fe_7S_8 is highlighted and brief history of the material is presented. A literature review is explored to discuss the crystal structure, synthesis pathways, and the magnetic properties of the trigonal Fe_7S_8 pyrrhotite.

The scope of this thesis is mentioned at the end of this chapter.

Keywords: Transition metal chacogenides, Iron-sulphide group, pyrrhotite, magnetism, phase diagram, crystal structure

1.1. Transition metal chalcogenides

The sulphides, selenides, and tellurides of the elements[1] are commonly referred to as "chalcogenides" of transition metals. The accessible *d* orbitals of the chalcogens take part in bonding with transition metals, strengthening the metal-to-chalcogen bonds[1]. These bonds contribute in deciding the properties of the TMCs, making them very attractive candidate for applications in devices including magnetic materials, thermoelectric devices[2], batteries[3], supercapacitors[4], fuel-cells[5], sensors, etc. For this reason, transition metal chalcogenides, especially the late transition metal (Fe, Co and Ni) chalcogenides have recently gained interest in last few decades. The two-dimensional transition metal dichalcogenides (TMD's) materials are of fundamental and technological[5–8] importance. A large gap between two inequivalent valleys in the *k*-space leads to the formation of band gap in TMDs. Such an arrangement of the valleys give rise to many applications in the field of valley-coupled spintronics[9–11]. The spacing between the layers in TMD's introduces of many species, which makes the materials a potential candidate for energy storage[6,12,13] applications in Li-ion batteries, supercapacitors etc. Bismuth selenide (Bi_2Se_3) is a well-studied topological insulator[14] (TI), possessing robust surface states. These surface states in Tis are protected by time-reversal symmetry. The career transport in a TIs has a purely quantum topological origin, making them a potential candidate for application in spintronics and dissipation-less electronics[15]. Some compounds belonging to the family M_2X_3 (M refers to Pb, Sb, Bi and X refers to S, Se, Te) possess thermoelectric (TE) properties with low bandgap[16–18]. A material with low electrical resistivity and high Seebeck coefficient is a potential TE material. Following the criteria, the materials with M_2Te_3 composition are theoretically considered to be the best thermoelectric materials. However, the toxicity of tellurium led to the development of alternate materials. It has been shown that the highly crystalline and oriented nanostructures[19–21] of these materials (such as Bi_2S_3) enhance the thermoelectric properties.

In Bi_2S_3, the *c*-axis[16] is the direction of highly anisotropic and covalent chemical bonds, while the directions associated with *a* and *b*-axes are bonded by weak ionic and van Der Waal's interactions. Because of effective mass anisotropy, the *c*-axis direction possesses higher career mobility than *a*-axis, making the oriented nanostructures preferable for enhancing the TE properties. The TE materials are used in the various power generation applications. Decades of discoveries and studies have shown that some of the metal sulphides are cost-effective and ample due to their occurrences as minerals in the earth's crust. For example—Pyrite (FeS_2) has a band gap of ~0.9 eV, find diverse applications in photovoltaic cells, glass colorants, etc[22],[23]. Metal chalcogenide semiconductor—galena (PbS) has a bandgap of ~0.37 eV and hence is found suitable as infrared detectors and photo optic devices[24]. Sphalerite (β-ZnS), hawleyite (CdS), and wurtzite (α-ZnS) have gained popularity because of their effortless conversion to quantum dots[24–26] and their application in LEDs of narrow wavelength for display. Materials such as cobalt sulphide (Co_3S_4), and $FeNi_2S_4$ (violarite) have gained attention as anode material[27]. Owing to the ferrimagnetic ordering in Fe_3S_4 (greigite), the material has various vital functions in both the bio-geochemical cycle and novel technological applications[28,29]. The iron-suphur (Fe-S) system is an exceptional illustration of the diversity in structure and properties ranging from semiconductor to metallic behaviour and diamagnetic to magnet-like properties, and so forth.

In recent years, the nanoparticles of MCs have been discovered to have extensive biomedical applications[30,31]. The iron sulphide nanoparticles have been intensively used in photothermal therapy and performing imaging[32]. The superparamagnetic iron nanoparticles have also been suitably used for magnetic resonance imaging, when combined with high near infra-red absorbance. The bismuth selenide nanoparticles have shown applications in both real-time monitoring of tumor, as well as in therapeutic functions[30]. Figure 1.1 represent the summary of vast and diverse fields of applications associated with transition metal chalcogenides.

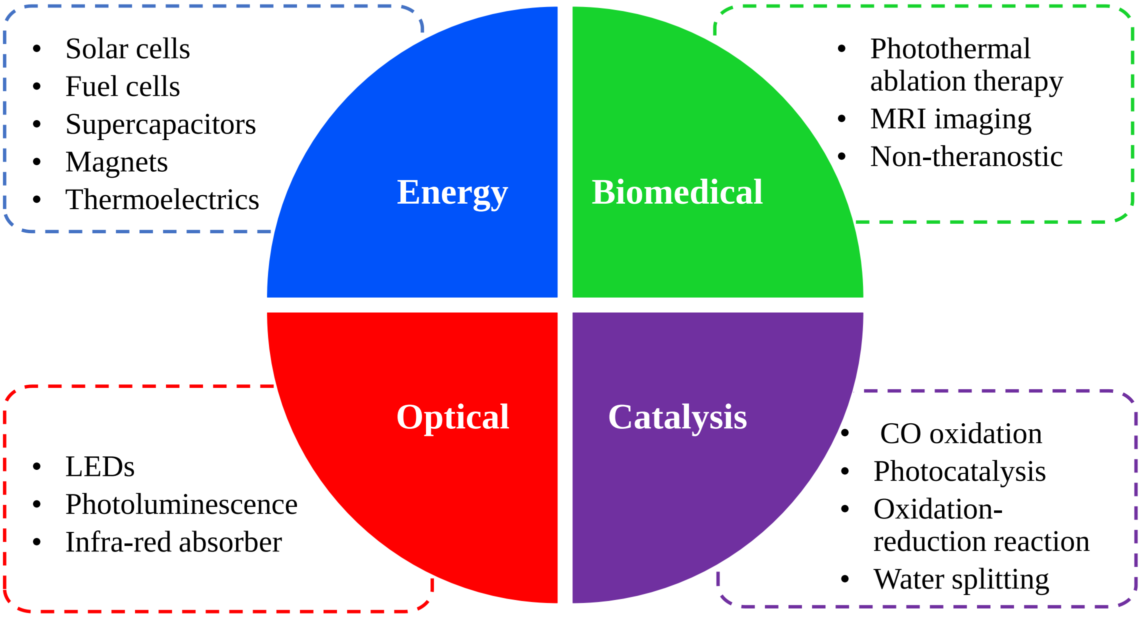

Figure 1.1: Schematic to show the diversity in applications of transition metal chalcogenides. Some of the areas are indicated under each class where TMCs are used.

1.2. What makes chalcogenides different from oxides?

Considerable differences have been observed between the chalcogenides and their oxide counterparts. Dr. Jellinek in 1988 used qualitative arguments in one his review articles[1] to illustrated the differences in composition, structure, and physical properties between chalcogenides and the oxides. Primarily, the origin of these differences lies in difference between the atoms of oxygen and chalcogen. Compared to the oxygen atom, the chalcogen atoms exhibit relatively lesser electronegativity, are relatively larger and heavier down the group in the periodic table. These atomic differences cause the differences in the bond between transition metal and chalcogen, and bond between the transition metal and oxygen. As the consequence of less electronegativity of chalcogen atoms, the bonds between metal and chalcogen become relatively more covalent than bonds between metal and oxygen. Usually, oxygen possesses the oxidation state of -2 in transition metal oxides, however, the smaller size and lesser electronegativity of chalcogen atoms allow them to have additional oxidation states (for instance -1). The chalcogen atoms have *d*-orbitals of accessible energy (3*d* for S, 4*d* for Se, 5*d* for Te) in contrast to oxygen atom, which contribute in making metal-chalcogen bonds. These differences are also highlighted in figure 1.2. The metal-chalcogen bonds are primarily covalent due to the comparatively less electronegativity of chalcogen atoms, which is caused by a substantial mixing of the valence s and p orbitals of the chalcogen. Chalcogenides consequently have a wide valence band and a wide conduction band. Chalcogenides therefore possess a smaller energy-gap than oxides between the top of the valence band and the bottom of the conduction band. In contrast, the valence band of oxides likes to dwell at a substantially lower energy than that of chalcogenides because oxygen has a much higher electronegativity than chalcogen elements, however, the conduction band is mostly unaffected. The energy gap in sulphides is typically 1-3 eV, however it can be less in selenides and even zero in tellurides. Chalcogenides have a variety of electrical and optical properties as a result of their narrow bandgap.

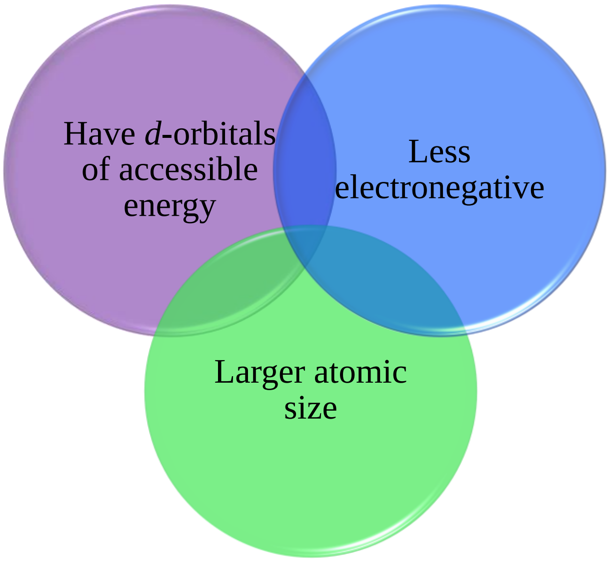

Figure 1.2: Scheme to highlight the atomic properties of chalcogen atom as compared to the oxygen atom.

1.3. The binary iron-sulphur (Fe-S) system:

The experimental data obtained by thermo-analytical method was used to deducet the phase relationship of Fe-S system. Charma and Chang (0-100%) and Schiirmann and Henke (0-50 at. % S) [33] performed the thermodynamic measurements to establish the phase relationships (temperature concentration) up to a 1 bar S_2 pressure in the Fe-S system. The empirically determined phase relationships between the various phases of the Fe-S system are shown in Figure 1.3.

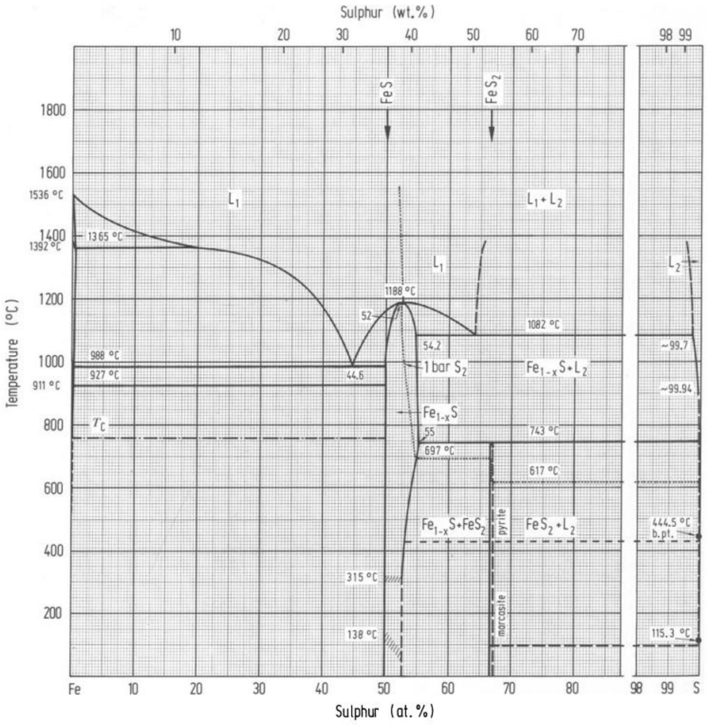

Figure 1.3: Experimentally established phase relationships between the phases of the Fe-S system[34].

The three important regions (Fe-FeS, $Fe_{1-x}S$ and FeS_2, and FeS-S) have been identified. The data of Hansen, Nagamori *et. al.*[35], Burgmann *et. al.*[36] and Rau[37] were used to construct the part diagram Fe-FeS region, and the part diagram FeS-S region was constructed from the data of Arnold, Hansen[33], Elliott[33] and Shunk and Rau[33]. The system consists of a monotectic between FeS and S (1082°C, ~ 64.5 at. % S), a eutectic between Fe and FeS (988°C, 44.6 at. % S) and a melting phase (l188 °C, 52 at.% S), $Fe_{l-x}S$. These regions are discussed here.

1.3.1 Fe-FeS region

Using experimental data that was published by Nagamori *et. al.*, Hansen and Shunk, the phase relationship in the Fe-S system was established. The curve of S_2 (vapour, 1 bar) saturates between 1200-1600 °C, as taken from discovery made by Henke and Schiirmann. Suphur is observed to be soluble with Fe in solid form, which is shown in Figure 1.4. The maximum solubility in α-Fe, δ-Fe, γ-Fe and corresponds to concentrations of 0.033, 0.24, 0.09 at.% S, respectively, at 927 °C, according to data from Hansen, Margot *et. al.*, Grabke, and. and Barloga *et. al.*

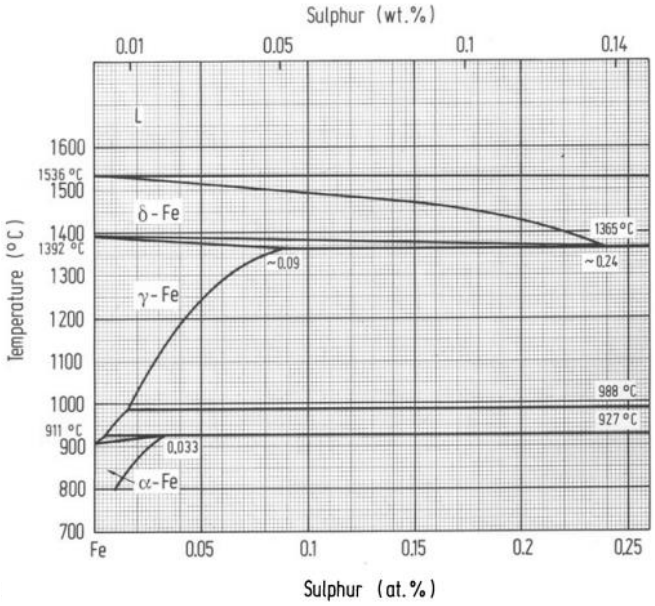

Figure 1.4: Part of Fe-S phase diagram which represents the solid solubility of S in Fe[34].

1.3.2. $Fe_{1-x}S$ and FeS_2

The NiAs-like structure of $Fe_{1-x}S$ crystallizes with two low-temperature modifications. It also exhibits a broad homogeneity range with congruent melting point at 1188 °C. Figure 1.3 shows the transformation temperature (shown as hatched lines) of $Fe_{1-x}S$ at 315 °C and 138 °C, obtained from the specific heat measurements by Hirone[38]. Recent studies by Rau (547-1100 °C, 100 bar) and Burgmann (700-1300 °C) have established the phase boundaries in the range 500-1188 °C. All these except the FeS are superstructures of the NiAs structure[39]. The two structural types of iron disulphide (FeS2) that are found are cubic pyrite and orthorhombic marcasite. It melts incongruently[34] at (742 ± 1) °C and decomposes[34] at 697 °C. The transformation temperature, obtained from specific heat measurements, is ~425 °C[40].

1.3.3. FeS-S region

Following specific heat experiments by Arnold[33], Figure 1.3 shows that FeS-S (L_1 and L_2) can cohabit in equilibrium with crystalline $Fe_{1-x}S$ and vapour at temperatures of 1092 °C or 1082 °C. The phase diagram demonstrates that the monotectic type of phase relationships exist at this temperature, with the monotectic point located at ~64.5 at.% S. Pyrrhotite ($Fe_{1-x}S$) may coexist in equilibrium with L_2 and vapour between the ranges of 742 and 1082 °C, and between 425 and 742 °C with pyrite and vapour.

1.4. Iron sulphides in Earth and Mineral Sciences

The iron sulphides (pyrites and pyrrhotites) are by far the most common sulphide biogeochemical minerals[41]. The properties of these minerals are of at par importance in many applications including mineral processing, metallurgical extraction, geophysical response, detection of submarine bacteria movement, prevention of corrosion in sulphide atmosphere, coal beneficiation, rock magnetism and so forth[41].

1.5. The NiAs structure—basic building block of pyrrhotite structures:

The phases in the Fe-S system are characterised by the general formula $Fe_{1-x}S$[42], are derivatives of based on the hexagonal NiAs structure. There are three basic compositions with $Fe_{1-x}S$ formula—hexagonal troilite (FeS, stoichiometric end member of $Fe_{1-x}S$ group), hexagonal smythite (Fe_9S_{11}, metastable phase related to $Fe_{1-x}S$ group), and monoclinic and trigonal pyrrhotite ($Fe_{1-x}S$, non-stoichiometric stable group)[42]. The crystal structure of NiAs ($a = 3.438$, $c = 5.880$)[43] provides the basis for the structure of many pyrrhotite superstructures. In the composition Fe_7S_8, the hexagonal NiAs structure is found. The metal atoms (Ni) are arranged in a hexagonal lattice within the basic structure of NiAs, whereas the

As atoms are arranged in a hexagonal close-packed lattice[44]. The relatively more electronegative As atoms form an octahedral coordination with the Ni atoms while being in trigonal prismatic coordination (figure 1.5). With such a structure, metal atoms can be omitted along specific crystallographic orientations, which leads to the non-stoichiometry within the derivatives of NiAs-type structures.

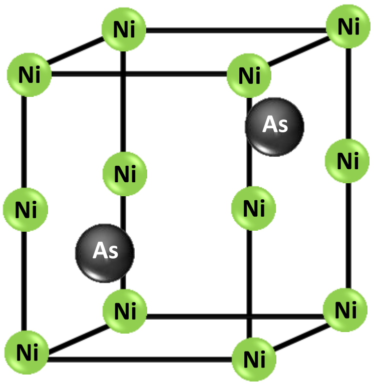

Figure 1.5: Illustration of the simple NiAs fundamental structure of pyrrhotite.

1.6. The pyrrhotite group:

One of the most prevalent metal sulphide minerals, pyrrhotites, is found in several ore deposits around the globe. The pyrrhotite mineral group has the general formula— $Fe_{1-x}S$, where $0 \leq x < 0.125$. Owing to the ordered vacancies within the structure of the pyrrhotites, they tend to occur in several superstructures[45,46]. Extension of the unit cell dimension in the direction of perpendicular to *ab*-plane results in the formation of the $Fe_{1-x}S$ family of superstructures[45]. Because of variations in composition (Fe_7S_8 to $Fe_{11}S_{12}$), the crystal system, and the physical qualities, these pyrrhotite superstructures possess non-stoichiometry within the structure. Such variations arise due to metal cation vacancies in the pyrrhotite structure (which is confined to every alternate layer)[45,47,48], the associated stacking sequence of these vacancies, and repetition of the Fe vacancy layers along a particular direction within the superstructure. Thus, the magnetic ordering in these superstructures is the consequence of the ordered Fe vacancies within the structure[47,49,50].

A number of pyrrhotite superstructures have been identified in the literature, however, the naturally occurring pyrrhotites exist in only three phases— stoichiometric troilite (FeS)[36,45], magnetic 4C pyrrhotite (4C Fe_7S_8), and non-magnetic NC pyrrhotite[36]. Owing to the iron site vacancies, the high temperature disordered forms of pyrrhotite structures tend to develop ordered states upon cooling, leading to the development of a variety of pyrrhotite superstructures[46,48,51], which are shown in table 1.1.

Table 1.1: Summary of the different pyrrhotite varieties with some of their key physical attributes. Adapted from Posfai *et al.*[46] (2000) and Fleet[51] (2006).

Type	Composition	Structure	Magnetic properties	Other names	Stability	Occurrence
1C	FeS	Hexagonal	Paramagnetic	-	High temperature phase	Synthetic
2C	FeS	Hexagonal	Antiferromagnetic	Troilite	<147 °C	Natural and lunar
3C	Fe_7S_8	Trigonal	Antiferromagnetic	2A, 3C	<262 °C	Synthetic
4C	Fe_7S_8	Monoclinic	Ferrimagnetic	Magnetic Pyrrhotite	<254 °C	Natural
NC	Fe_9S_{10}, $Fe_{11}S_{12}$	Orthorhombic, Monoclinic	Antiferromagnetic	5C, 6C pyrrhotite	<209 °C	Natural
-	$Fe_{7+x}S_8$	Monoclinic	Antiferromagnetic	Anomalous Pyrrhotite	-	Natural

In 1963, Wuench established a nomenclature system[52] based on the structural dimensions of the NiAs lattice to identify and describe these superstructures. The unit cell dimension of

NiAs being repeated either along the *c*-axis or *a*-axis is used to characterise the dimensions of superlattice. For instance, pyrrhotite is named as a 1C pyrrhotite if it has the structure and cell dimension of NiAs. Similar to this, the 2C (troilite), 3C (trigonal pyrrhotite), and 4C (monoclinic pyrrhotite) are used to refer to pyrrhotites with unit cell parameters of *c* that are, respectively, two, three, and four times as large as that of *c* in the NiAs unit cell, and so forth. Following this nomenclature system, numerous pyrrhotites varieties were identified, and the distinct physical attributes of these pyrrhotite superstructures are summarized in table 1.1. The unit cell parameters and symmetry of each superstructure are given in table 1.2.

Table 1.2: Summary of pyrrhotite superstructures and unit cell dimensions found in the literature. * Indicates no structure solution presented in the given references.

Type	**Composition**	**Structure**	**Symmetry**	**a (Å)**	**b (Å)**	**c (Å)**	**β (°)**	**Reference**
1C	FeS	Hexagonal	$P\bar{6}3mc$	3.602	-	5.009	-	53,54
2C	FeS	Hexagonal	$P\bar{6}2c$	5.962	-	11.750	-	39,51
3C	Fe_7S_8	Trigonal	$P31$	6.867	-	17.062	-	54–57
3C	Fe_7S_8	Trigonal	$P3121$	6.866	-	17.088		56
4C	Fe_7S_8	Monoclinic	F2/*d*	11.902	6.859	22.787	90.26	47,58
4C	Fe_7S_8	Monoclinic	C2/c or F2/*d*	11.926	6.882	12.925	118.00	39,47
5C*	Fe_9S_{10}	Orthorhombic	C*ca	6.885	11.94	28.676	-	39,54
6C	$Fe_{11}S_{12}$	Monoclinic	F*d*	*6.895*	11.95	34.518	90.00	39,51

1.6.1. Crystal structure

A) Metastable 1C pyrrhotite

One of the high temperature forms of pyrrhotites, 1C pyrrhotite, consists of disordered distribution of iron vacancies[53,54] within the structure (figure 1.3). Pyrrhotite with single derivative of the unit cell dimension of NiAs in the direction of *c*-axis[53] is called a NiAs-type structure (figure 1.6a). The 1C pyrrhotite possesses paramagnetic ordering[53,54].

B) 2C Troilite

Stoichiometric troilite (FeS) possesses hexagonal structure with space group $P62c$[39], and structural parameters as a =1.7A, and c = 2C, where A and C correspond to the NiAs unit cell dimensions (figure 1.6b). The FeS has ordered structure with completely filled metal cation sites and no vacancies. In general, triolite forms in environments with stable ferrous iron. Because of the favourable reducing conditions found in extraterrestrial locations, troilite is widely known for its existence in lunar samples[39]. However, at times it has also been found in some nickel deposits. Troilite possesses antiferromagnetic ordering[39] below than 140 °C. However, the compound has a tendency to experience a shift ~315 °C (T_C). The troilite structure then takes the form of 1C structure of the NiAs at this temperature. However, the structural transformation with the α-magnetic phase transition is still a matter of debate.

C) 3C pyrrhotite structure

Fleet (1971) was able to identify and determine the structure of 3C Fe_7S_8 (space group $P3_1$)[48], which is metastable at room temperature and is formed either by shock or quenching of crystals with compositions in the vicinity of ~Fe_7S_8. A single crystal of 3C Fe_7S_8 was taken to determine its crystal structure by considering the contribution of the twinning of crystals. Based on the $P3_1$ space group, another structural study was carried out by Nishiguchi (1977)[59] on a synthesized single crystal of 3C Fe_7S_8. However, Fleet and Nishiguchi did not examine the possibility of a $P3_121$ space group in the structure. Later in 1979, the structure of

3C Fe_7S_8 was refined by Nakano *et. al*. with space group $P3_121$[56] based on Fe-vacanies and unit cell parameters a = 6.8652±0.0006 Å, c = 17.047±0.002 Å, confirming the trigonal symmetry. The structure is essentially the same as that of 3C Fe_7Se_8, as reported by Okazaki & Hirakawa (1956), which has the $P3_121$ symmetry[49]. The structure is better considered as $P3_121$, as Fleet (1971) in his study suggested general positions of Fe-vacancies in $P3_1$ symmetry, whereas in $P3_121$, the arrangement of Fe-vacancies is suggested to be on one set of Wyckoff 3*a* sites[56]. Figure 1.6c illustrates a layered 3C Fe_7S_8 structure with vacant and filled iron layers stacked normal to the *c*-axis in an order expressed as AFBFCF, where A, B, and C identify the layers containing Fe-vacancies, and F denotes the layer without Fe-vacancy. The arrangement of vacancy-containing alternate layers is same for both 4C and 3C superstructures. The arrangement of vacancies and the type of Fe-clustering in the alternate layers of Fe and S in the lattice[53], however, differ between the 4C and 3C structures of Fe_7S_8, according to Nakazawa *et. al*.

D) 4C pyrrhotite structure

Bertaut (1953) first proposed the structure of 4C pyrrhotite, where unit cell parameters of a = 3.46A, b=2A, c = 4C, where A and C stand for the dimensions of the NiAs unit cell. This structure is known to be a monoclinic structure with the F2/d space group[47]. Fe-vacany layers ordered along the *c*-axis define the 4C pyrrhotite superstructure. Due to the presence of iron vacancies, iron occupies the octahedral coordination, and sulphur is in a combination of the five-fold and six-fold coordination. The Fe layers with and without vacancy are alternately sequenced as AFBFCFDF, where A, B, C, and D denote layers containing Fe-vacanies (marked by blue circles), and F is an iron layer without vacancy, as shown in figure 1.6d. Because the structure lacks one-fourth of the iron atoms, according to Bertuat[47] (1953) and Tokonami *et. al.*[56] (1972), the presence of ferric iron preserves the charge balance and to explain the non-stoichiometry in the pyrrhotite structure, and the formula Fe_7S_8 can be described as $Fe_2^{3+}Fe_5^{2+}S_8$. The description of the stalking of layers with and without vacancies for the 4C structure was subsequently used to develop the vacancy arrangement for the 3C pyrrhotite[48,56] and 6C pyrrhotite[39] structures. However, Powell[58] in 2004 refined the 4C pyrrhotite structure as *C*2/c space group[58] using a synthetic pyrrhotite sample by means of powder neutron diffraction.

The 4C pyrrhotite is a well-documented form of pyrrhotite found in abundance in natural terrestrial occurrences as well as different geographical regions around the world (Carpenter and Desborough (1964), Arnold (1967))[60,61]. However, Arnold (1967) demonstrated that naturally occurring 4C pyrrhotites may co-exist with NC pyrrhotites (figure 1.3), which has been verified by many subsequent studies of pyrrhotite done by Naldrett and Kullerud, Lianxing and Vokes, Posfai[62–64].

Further, Clark (1966) has identified an anomalous pyrrhotite with $Fe_{7+x}S_8$ composition[65], which is recognized with having a monoclinic structure and antiferromagnetic ordering unlike normal monoclinic pyrrhotite that is ferrimagnetic.

E) NC pyrrhotite structures (5C and 6C)

Nakazawa and Morimoto in 1971 grouped together a certain type of pyrrhotites for simplicity during phase relationship studies[53]. This group of pyrrhotites is classified as NC pyrrhotite (intermediate or *non-magnetic* pyrrhotite). The value of N, which ranges from 5 to 11 and may be either integral or non-integral, represents the repetition of a unit cell dimension in the direction of *c*-axis of the NiAs unit cell. According to Morimoto *et al.* (1970), the NC superstructures (N is integral) of pyrrhotite can be represented as: $Fe_{n-1}S_n$ (n>8)[39]. The structure will either be n/2C for an even number of n (for example, 5C pyrrhotite with composition Fe_9S_{10} or 6C pyrrhotite with composition $Fe_{11}S_{12}$) or nC for an odd value of n (for example, 11C pyrrhotite with composition $Fe_{10}S_{11}$). Due to the complexity in the ordering of vacancies in NC structure, there aren't any comprehensive crystal structure solutions in the literature. Theoretically, Vaughan[66], Nakazawa and Morimoto[53] in 1971, Posfai and Dodony[46] in 1990 gave the number of vacancies for integral NC pyrrhotites based on the 4C monoclinic structure. By indtroducing more filled Fe layers to the 4C structure, it is possible to estimate the distribution of vacancies in these pyrrhotites. Furthermore, in 1964, Carpenter and Desborough[67] quantitatively deduced the iron content for NC pyrrhotites, which varies between 47.0 and 48.0 atomic % iron. For 5C pyrrhotites, Vaughan[66] suggested a structure in 1971 by alternating the vacancies between filled layers as shown in figure 1.6e. Based on the earlier model given by Morimoto[39] in 1975, De Villiers[68] in 2009 reported a *C*mca structure of 5C pyrrhotite, which was later studied by Elliot[69] in 2010 and reported a *P*21/c structure, and finally refined in 2012 by Liles and De Villiers[70] to a *P*21 structure.

The structure of 6C pyrrhotite was first determined by Koto *et. al.*[39] (1975) using a single crystal with $Fe_{11}S_{12}$ stoichiometry. Two possible space groups (*F*d and *F*2/d) were proposed in the study. However, Koto[39] in 1975 carried out the study using the space group *F*d, which gave occupancies as a subset of a a Wyckoff set, where 12 independent Fe positions were possible. Further, in 1971, Nakazawa and Morimoto[53] observed that every third layer of the 6C superstructure has a Fe-vacancy layer. However, according to Koto *et al.* (1975), the vacancy distribution in 6C superstructure consisted of partially-occupied Fe sites with fully occupied Fe sites in the alternate layer.

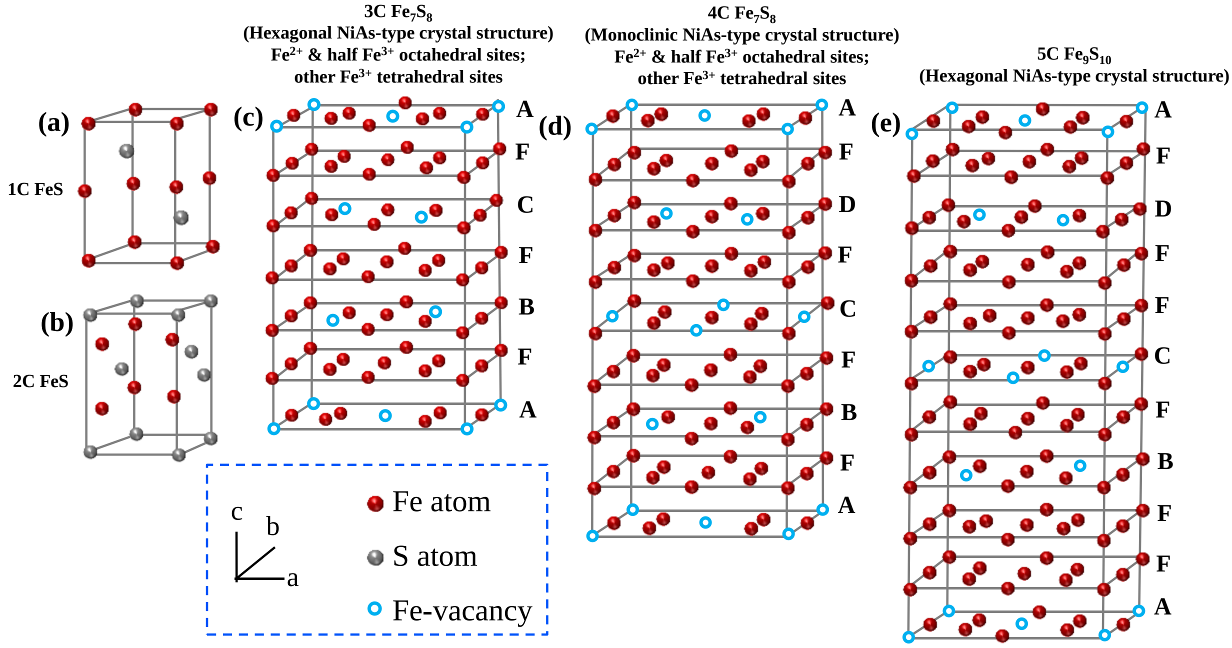

Figure 1.6: Schematic shows essential phases from the binary Fe-S phase diagram with a different crystalline structure.

1.6.2. Magnetic structure

An initial study of the magnetic structures of the $Fe_{1-x}S$ solid solution, extracted from the naturally obtained samples, was carried out by Haraldsen[71] (1941). Much later in 1956 and 1961, Schwarz work on both synthetic[66] (e.g., LOTGERING, 1956) and natural pyrrhotites (SCHWARZ, 1968) render a much more detailed examination desirable. Furthermore, standards yielding a correlation between composition and intrinsic magnetic properties are required for the calibration of a thermomagnetic method of analysis of coexisting natural pyrrhotites (SCHWARZ, 1968). The literature on the structural and magnetic characteristics of some pyrrhotites has been reviewed in detail by WARD (1970)[72]. One of the most recently published diagrams is that of TAYLOR[73] (1970), as shown in figure 1.7.

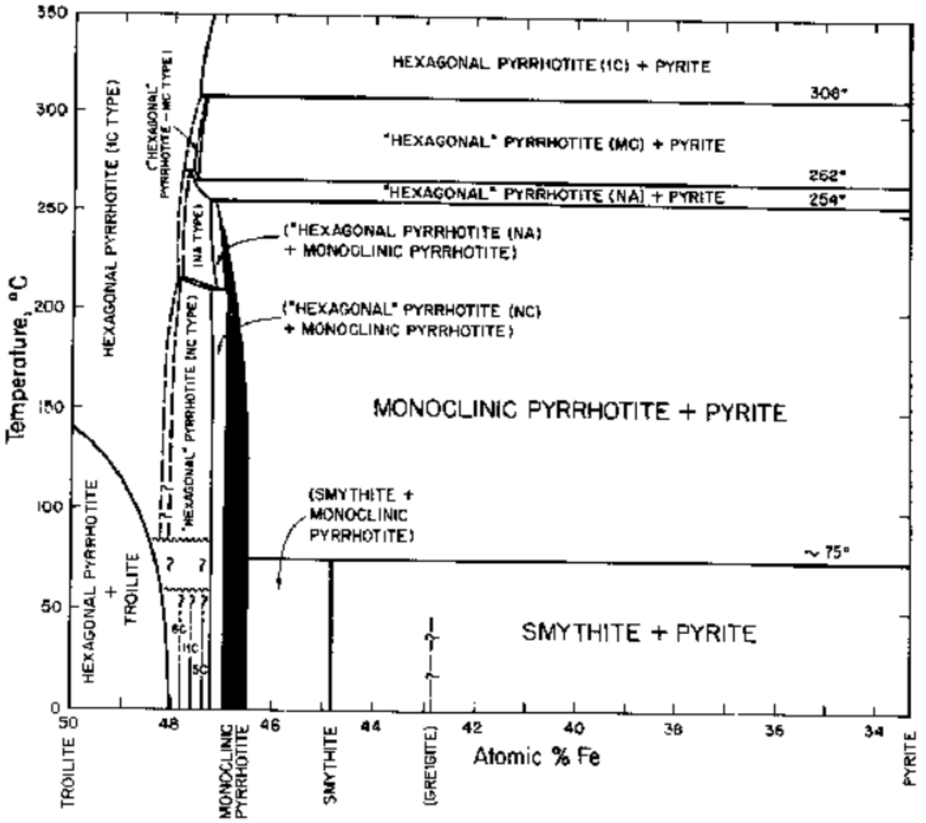

Figure 1.7: Relations among condensed phases in the central portion of the Fe-S system below 350°C[66].

The magnetic properties in the pyrrhotite are determined by the distribution of Fe vacancies in the alternate layers of the structures. The disordered vacancies in 1C pyrrhotite leads to the paramagnetism in the structure. In the absence of vacancies in the stoichiometric 2C FeS, the even and the odd Fe-layers are fully occupied and possess equal and opposite magnetic moments, causing antiferromagnetic ordering.

A) 3C pyrrhotite structure

In 2004, Powell *et al.* showed from the neutron diffraction data of 4C pyrrhotite that the crystallographic cell and magnetic unit cell of 4C pyrrhotite[58] are identical. The Fe atoms within each *c*-plane in the structure are ferromagnetically aligned, while they are antiferromagnetically aligned in the adjacent plane, giving rise to the overall ferrimagnetic ordering in the structure. When vacancies preferentially arrange onto just one of the sets of layers, ferrimagnetism results[48,58]. The structure of 3C structure pyrrhotite with $P3_121$ is similar to that of the 4C structure[47,48,56], as in both structures ordered vacancies are present in alternate Fe-layers. However, there is a little information available in the literature about the magnetic structure of the 3C Fe_7S_8. However, in the equivalent phase, 3C Fe_7Se_8[49,50], the magnetic moment of Fe ions are aligned parallelly to one another (ferromagnetic ordering of moments) in the same *c*-plane, whereas the moments in neighboring *c*-plane are antiparallel (antiferromagnetic ordering of moments). Thus, 3C Fe_7Se_8 possesses ferrimagnetic ordering owing to a net spontaneous moment caused by the deficiency of Fe ions in the alternate layers[50]. Based on the structural similarity between 3C Fe_7Se_8 and 3C Fe_7S_8, the 3C pyrrhotites are known to exhibit ferrimagnetism.

B) 4C pyrrhotite structure

The ferrimagnetism in 4C Fe_7S_8 pyrrhotite was first explained by Neel[74] in 1953 based on the crystal structure proposed by Bertaut (1953). The magnetic moments of Fe atoms are aligned parallelly within each Fe-layer, whereas the moments are antiparallelly aligned in the alternate Fe-layer. Such an interlayer arrangement of moments causes ferrimagnetic ordering in the lattice.

C) NC structures (5C and 6C)

Perhaps less clear than those of the well-understood 3C and 4C structures are the crystallographic space groups of the pyrrhotite structures with the 5C and 6C superstructures. The 5C structure (*P*21 space group), and the 6C structure (Cc space group), are reported to have partially ordered Fe/vacancy sites and monoclinic symmetry. When it comes to their magnetic characteristics, an antiferromagnetic pattern (or ferrimagnetic pattern, depending on the distribution of vacancies) is anticipated, with moments at high temperatures in the *ab*-plane and at low temperatures perpendicular to the *ab*-plane.

1.7. What makes 3C Fe_7S_8 unique to study?

The superstructure 3C Fe_7S_8 is based on the NiAs-type structure, which is revealed in the diffraction spots obtained from X-ray diffraction patterns[48,56] for the single crystals of 3C Fe_7S_8. Due to the Fe-vacancies[48,56] in the layered structure of 3C Fe_7S_8, the superstructures were identified as the weak spots in the diffraction pattern, which correspond to the NiAs-type structure. Along the a-, b-, and c-axes, the lattice parameters of the superstructure are twice as those of the fundamental NiAs structure. The 3C Fe_7S_8 is known to be a metastable form of 4C Fe_7S_8[75,76], which is formed as a consequence of shock, or quenching. The 3C trigonal phase also possesses NiAs-type structure and exhibits ferrimagnetic properties[47,48,50]. The structural studies of 3C Fe_7S_8, done by Fleet[48] (1971) with $P3_1$ symmetry and Nakano[56] (1979) with $P3_121$ symmetry, reported the ferrimagnetic ordering[74] in the compound as a result of ordered Fe vacancies within the layered structure. The 3C ($P3_121$ symmetry) and 4C pyrrhotite structures are known to be similar as the Fe vacancies in both the structures lie in the alternate layers. The information about the magnetic structure of the 3C pyrrhotite appears to be little known. However, the equivalent phase, 3C Fe_7Se_8[49,77] is well documented and a known ferrimagnetic, as studied by Kawaminami and Okazaki in 1970. The discovery of 3C Fe_7S_8 is recent in a sense that the compound is the metastable form of 4C Fe_7S_8, and after many decades the compound started to gain little attention when a small group of researchers collected the sample from various submarine sediments around the world to study the mineral. In bulk phase, the compound showed ferrimagnetic ordering[75–77] and some other promising magnetic properties. These properties are discussed in detail in the upcoming sections.

1.8. Magnetic properties of 3C Fe_7S_8

Before discussing the magnetism in 3C Fe_7S_8, we will first discuss below some basic phenomenon in the magnetism.

1.8.1. Ferrimagnetism:

The term ferrimagnetism was coined by Neel (1948)[74] while giving theoretical understanding of ferrites. Metal ions in two different crystallographic sites (A-site and B-site) combine to form a ferrite crystal. According to the assumption made by Neel, the ions at A-site and B-site interact *via* a negative exchange interaction, making the two sublattices (A and B) magnetized spontaneously in opposite directions (figure 1.8a). The magnetic moments possess unequal magnitude in both sublattices in ferrimagnets. As a result, there is a net spontaneous magnetization in the crystal[50] since the moments do not totally cancel one another, as shown for 3C Fe_7S_8 (figure 1.8b). A ferrimagnet[78],[79] consist of magnetic domains and exhibits features of a ferromagnet, such as— Curie temperature, hysteresis, remanence, and so forth.

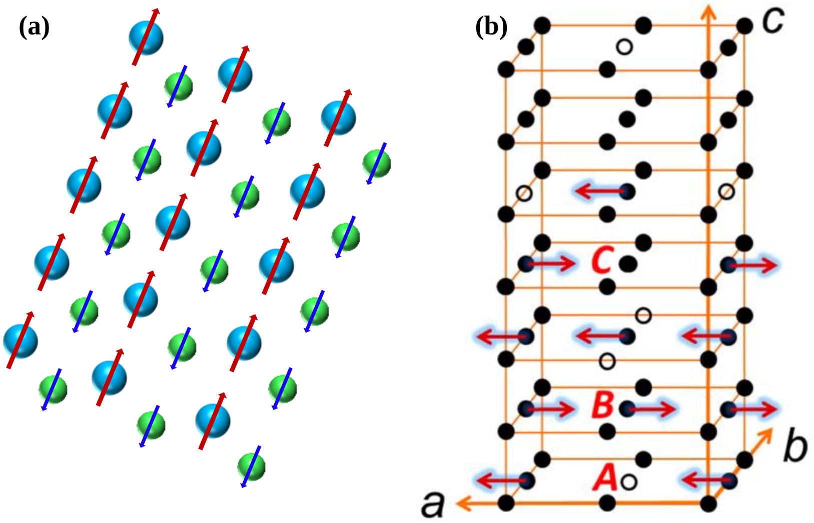

Figure 1.8: (a) In ferrimagnets, the magnetic structure is composed of two magnetic sublattices (blue and green). The magnetic moments (symbolized by length of the arrow here) of two sublattices are not equal and result in a net magnetic moment, (b) unit cell for a 3C Fe_7Se_8 superstructure, where black circles represent Fe atoms, open circles represent Fe vacancies, and Se atoms are omitted for clarity. A, B, and C represent the three nonequivalent Fe sites (atoms to the right of the label) as proven by Mössbauer spectroscopy[49].

1.8.2. Magnetocrystalline anisotropy

Magnetocrystalline anisotropy[78,80] is an inherent characteristic of a crystal, which means that, the magnetic moments of the crystal have taken some amount of energy to get magnetized along one particular direction. Therefore, the amount of energy required to magnetize the moments in one specific direction is known as anisotropy energy[78,80] (E_a). For materials exhibiting uniaxial anisotropy, E_a can be expressed as following equation by neglecting the higher order terms.

$$E_a = K_u Sin^2\theta \qquad (1.1)$$

Where, K_u is the anisotropy constant and the angle between the easy-axis and the magnetization vector is denoted by θ, as shown in figure 1.9.

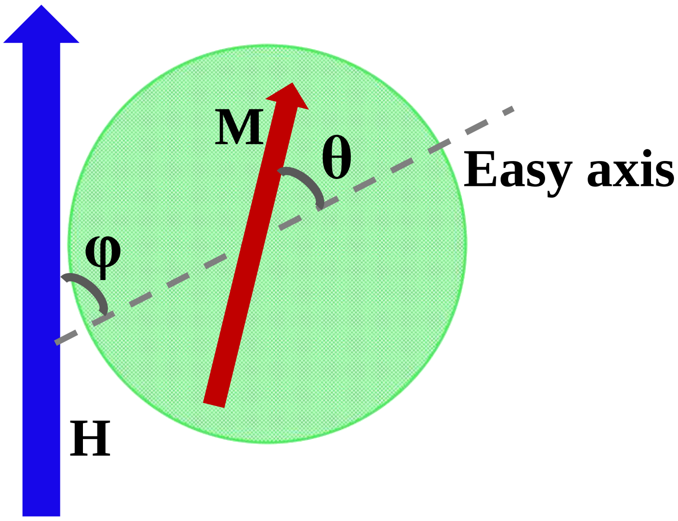

Figure 1.9: Directions of easy-axis, magnetization and external field in case of single domain particle (Stoner-Wohlfarth particle) with uniaxial anisotropy are shown for representative purpose.

The anisotropy constant (K_u) for a polycrystalline sample, aligned in an external magnetic field, can be estimated by extrapolating the M-H hysteresis curves in both the hard and easy axes[80] (figure 1.10).

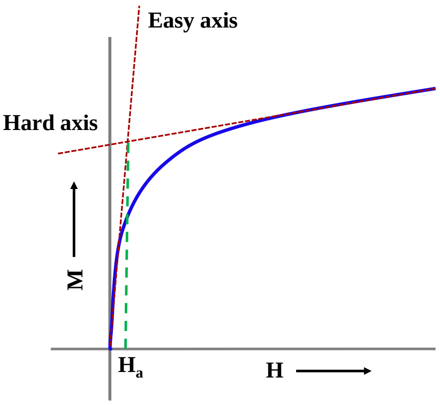

Figure 1.10: Schematic illustrating the calculation of K_u by extrapolating the hysteresis curves in hard and easy directions in a M-H hysteresis curve.

The magnitude of the anisotropy constant determines the strength of the magnetocrystalline anisotropy in a material. The two local energy minima are separated by an energy barrier[81], E_B, and occur at $\theta = 0$ and π, according to equation 1.1.

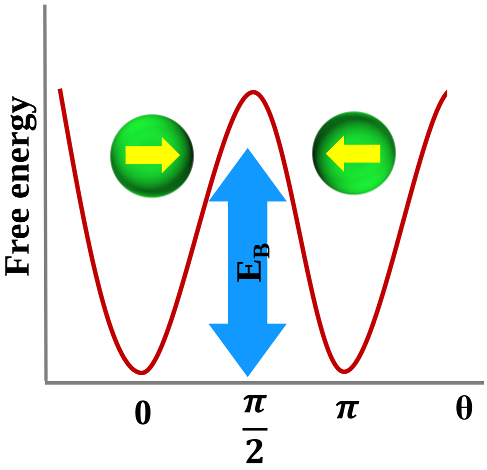

Figure 1.11: Schematic of the free energy of a single-domain particle with uniaxial anisotropy as a function of magnetization direction.

Spin-orbit coupling of electrons induces the magnetocrystalline anisotropy in a crystal[80]. When an external field is applied, the spin of an electron tends to reorient under the influence of applied field, which in-turn induces the reorientation of the orbit of that electron, as the spin and orbital motion of the electron is coupled. However, the orbit resists the spin orientation as it is strongly coupled to the lattice.

1.8.3. Stoner-Wohlfarth model (SW model)

The simplest analytical model to explain the hysteresis in ferromagnets[82] was developed in 1948 by Edmund Clifton Stoner and Erich Peter Wohlfarth. Based on coherent reversal in single-domain particles, it is an exactly soluble coercivity model. As a result of free energy minimization, formation of domain structure in ferromagnets and ferrimagnets takes place. In the model, a system of non-interacting uniaxial randomly oriented single domain particles[80] (Stoner–Wohlfarth particle in figure 1.9) was considered. As depicted from figure 1.9, φ represents the angle between the direction of the applied magnetic field (H) and the easy-axis. The shape of the hysteresis loops was estimated for different values of φ. The free energy density of the system is defined as[81]:

$$E_{tot} = K_u Sin^2\theta - \mu_0 MHCos(\alpha - \theta) \qquad (1.2)$$

Minimizing E_{tot} with respect to θ will give rise to one of the energy minima (figure 1.12). In the range of magnetic field, hysteresis occurs where there are two minima[80].

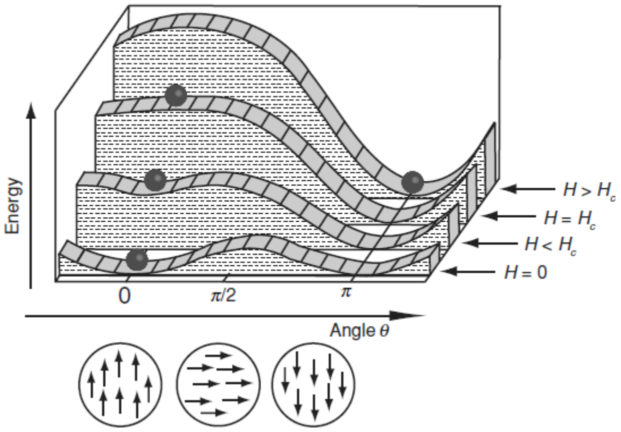

Figure 1.12: An energy landscape with metastable minima gives rise to remanence and coercivity[83].

According to the above equation, when α= 0, the hysteresis loop is exactly square, and the coercivity then equals the anisotropy field, as given below:

$$H_C = \frac{2K_u}{\mu_0 M_S} \tag{1.3}$$

where M_s represents the saturation magnetization of a particle. The SW model was developed for a single-domain, uniaxial, randomly oriented, non-interacting particle system. The fact that the anisotropy constant, K_u, is proportional to the cube of saturation magnetization, M_S, suggests that the material exhibits uniaxial magnetocrystalline anisotropy[80].

1.8.4. Maximum energy product

After a permanent magnet is manufactured, its usefulness is decided by the amount of energy that can be stored in it[80]. The maximum energy product (BH_{max}) is the figure of merit for assessing the quality of a permanent magnet. It is a measurement of the magnetic energy of a material. Figure 1.13 shows the path followed by induction B when a magnet is subjected to and then removal of an external magnetic field H. The point P designates the operational point of the magnet, which is established by the point where the line OC and the second quadrant of the hysteresis loop converge. The demagnetization curve of the material is located in this quadrant.

The rectangle drawn through the point P under the B-H curve in the second quadrant of hysteresis loop shows largest area, and gives the BH_{max} of the material[80].

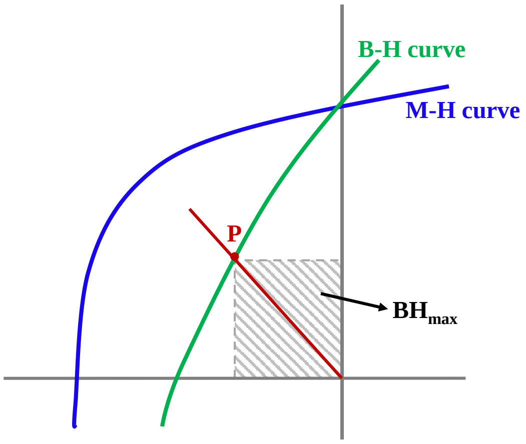

Figure 1.13: Calculation of maximum energy product is done on the second quadrant of the B-H hysteresis loop. The area of the shaded region gives the maximum energy product value for the material. Point P is the operating point.

1.8.5. Besnus transition

A discontinuous change in magnetic properties at a temperature ~30-34 K is denoted as Besnus transition[84]. This transition is known for the key diagnostic feature to identify the 4C pyrrhotite. The Besnus transition can be explained as the spin rotation that correlates with the structural changes at an atomic level, caused by the highly ordered vacancy arrangement in 4C pyrrhotite[75,77]. Fe^{2+} spin rotation affects the spin-orbit coupling with no crystallography change, as a result magnetocrystalline anisotropy changes[77]. Besnus transition represents a close link between the structural and magnetic properties in Earth mineral. Such a transition has been observed for merely 4C pyrrhotite in bulk and nano phases so far[75–77]. However, a deeper investigation about Besnus transition in variety of compounds is required to build the understanding of the magnetic phenomenon that occurs at low-temperature.

1.9. Synthesis pathways of 3C Fe_7S_8

There have been limited synthetic pathways reported in the literature for 3C pyrrhotite. In 1968, Fleet[48] made a single crystal of 3C Fe_7S_8 using a solid-state route, wherein Fe sponge and S crystals were used with composition 45.48 atomic per cent Fe. The mixture was kept in an evacuated SiO_2 tube at 900 °C for 2 days, 500 °C for 3 days, and then was quenched in water. Two years later in 1970, the synthesized single crystal was used to study its crystal structure ($P3_1$ symmetry) for the first time. After a decade, in 1978, dry method was used by Nakano *et. al.* to form single crystals of 3C Fe_7S_8, which was further used to refine its crystal structure with $P3_121$ symmetry[56]. Very recently in two subsequent years (2017 and 2018), Horng and Roberts identified occurrence of 3C pyrrhotite (as a metastable phase of 4C pyrrhotite) in various marine sediment cores around the world[76,85]. Extracts were obtained by crushing the rock into powder and extracting pyrrhotite with a rare-earth magnet. These powder samples were used to investigate the magnetic properties.

Table 1.13: List of the synthesis routes for the preparation of 3C Fe_7S_8 pyrrhotites.

S. No.	Year	Phase	Method	Temperature
1.	1968	Single crystal	Solid-state	900 °C → Quenched
2.	1978	Single crystal	Solid-state	900 °C → Quenched
3.	1980	Single crystal	Solid-state	923 K
4.	2017	Bulk powder sample	Solid-state	Laboratory temperature
5.	2018	Bulk powder sample	Solid-state	Laboratory temperature

The aforementioned methods are solid-state procedures that require complex pathways (including high-temperature furnaces with a particular environment), high purity elements as precursors, which can worsen the energy-economy scale and so on. Contrarily, solid-state methods have quite a few important advantages over chemical methods when it comes to cost, extensive manufacturing, and so forth. In comparison to solid-state approaches, chemical procedures are significantly more effective, efficient, affordable, and give greater phase purity. Additionally, these techniques offer simpler control over size, shape, and structure and often need significantly lower temperatures for phase formation. Several reports have dealt with the synthesis of many phases of $Fe_{1-x}S$ system, both in bulk and nano phases.

However, there is no report in the literature upon the synthesis of trigonal phase of pyrrhotite using the chemical route. Therefore, it is important to adopt a straightforward and cost-effective reaction pathway, as well as one with clearly defined tunability and high crystallinity of the system.

it is necessary to adapt a simple and economical reaction pathway (low temperature, quick reaction time, and cost-effective).

1.10. Significance of nano dimension in magnetism

Materials with at least one dimension between 1 and 100 nanometers (nm) are known as nanoparticles. The reduction in the size of a particle is reduced induces an increased surface area to volume ratio[86]. The surface area to volume ratio increases dramatically in nanoparticles, bringing a high proportion of atoms to the particle's surface. The change in size of the particle brings change in its structure, which leads to the change in its properties and mechanism from its bulk counterpart[86] (figure 1.14).

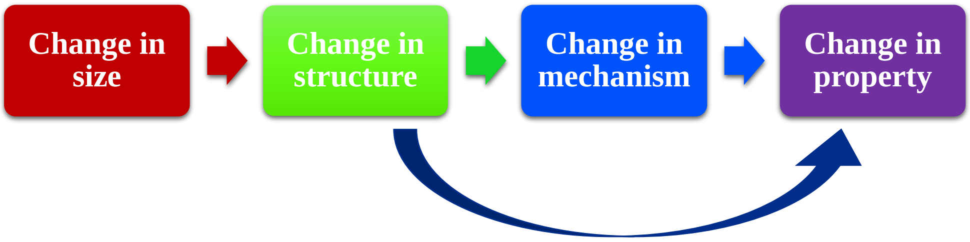

Figure 1.14: Representation of effects of size reduction on the structure and properties of a material from bulk to nano dimension.

When we go from bulk to nano dimension, only the structure sensitive magnetic properties—coercivity, blocking temperature, Neel or Curie temperature, and others, are expected to change significantly. Analysis of geometric data, such as—composition, size, shape, and crystal structure and magnetic data (magnetization values, coercivity (H_C), transition temperature values) provide information about the characteristics of a magnetic nanoparticle.

Some of the possibilities when we go from bulk to nano are: (a) Ferromagnetic particles becoming single domain

(b) Superparamagnetism in small ferromagnetic particles (i.e., particles which are ferromagnetic in bulk)

(c) Antiferromagnetic particles (in bulk) behaving like ferromagnets, and so forth.

The characteristics of a nanoparticles are governed by two fundamental aspects:

(a) Effects of finite-size (quantum confinement of electron and single/multi-domain structures)

(b) Surface symmetry breaking at the surface of particle, dangling bonds, oxidation, surface strain, surfactants, or even different physical and chemical structures of the inside (core) and surface (shell) components the nanoparticles[86] can all lead to surface effects.

As we reduce the dimension of the system, there is an increase in magnetic moment. This demonstrates the basic differences in magnetic behaviour between bulk materials and nanostructures. Since surface spins typically do not follow the same ordering as spins inside the material, this effect is more notable. Thus, nanocrystals with more surface will have lower μ_B/atom values than bulk materials (table 1.4)[86].

Table 1.4: Example of the systems, indicating an increase in magnetic moment/atom as size of nanoparticles is reduced.

	Magnetic Moment (μ_B/atom)			
	0D	1D	2D	Bulk
Ni	2.0	1.1	0.68	0.56
Fe	4.0	3.3	2.96	2.27

Increasing magnetic moment/atom

←

When the surface to bulk atoms ratio is high (due to the decreased dimensions of the particle), the role of surface in magnetism becomes significant. In contrast to the core of the particle, the surface atoms are exposed to different surroundings, which causes certain types of surface defects, such as— dangling bonds, lattice disorder, vacancies, and so forth. Thus, these surface imperfections give rise to uncompensated disordered spins at the surface of the nanoparticles, resulting in surface magnetization.

The surface effects can cause alteration (up or down) in the value of magnetization and enhancement in effective magnetic anisotropy of a nanoparticle. There has been a reported decrease in the magnetization of certain oxide nanoparticles, which has been connected to the surface of nanoparticles having a magnetic dead layer, the surface spins behaving like spin glasses, or the canted spins. In contrary, certain metallic nanoparticles were observed to exhibit an increased value of magnetization. The overall magnetization of a nanoparticle can be thought as a result of spins on the surface and the contribution from the core of the particle[86]. Investigating the pyrrhotite's magnetic properties of the pyrrhotites at the nano scale will therefore be interesting and intriguing. In this thesis, some of the most significant properties of magnetic nanoparticles are addressed and discussed.

1.11. Influence of Gd-substitution

Substitution is well known to be one of the effective routes to modulate various physical properties of nanoparticles, such as—optical, electrical, magnetic properties. Co, Ni, Mn, and Pt are recognised to be efficient dopants[87–93] of magnetic nanoparticles with the potential to enhance their magnetic properties. However, a rare-earth element has a significantly greater potential for displaying strong magnetic characteristics than a transition metal because of the substantial unquenched orbital angular momentum assigned to the *f*-electrons, which exhibit higher spin-orbit coupling[94,95]. The orbital component of the magnetic moment is significantly larger for the rare-earth ions than the transition metal ions because crystal-field effects are less and spin-orbit coupling is stronger for *f*-electrons of transition metal ions than for *d*-electrons. Additionally, materials formed from these elements have the potential to display highly advantageous magnetic properties due to the special *f*-electronic structure of metals in the rare earth series. Rare earth elements comprise of 15 kinds of lanthanide elements ranging from lanthanum to lutetium in the periodic table. In recent decades, the development of lanthanides-based nanomaterials with novel optical, electrical and magnetic properties has been an emerging research field[96,97]. Substitution with rare-earth ions in the parent structure induces many interesting optical, electrical and magnetic properties due to their partially occupied 4*f* electronic state, thereby modulating the structural disorder and lattice strain in the structure. In particular, the gadolinium (Gd) ion is of importance because of its large magnetic moment[94], which comes from the partially occupied 4*f* electronic state (figure 1.15), resulting in excellent magnetic properties.

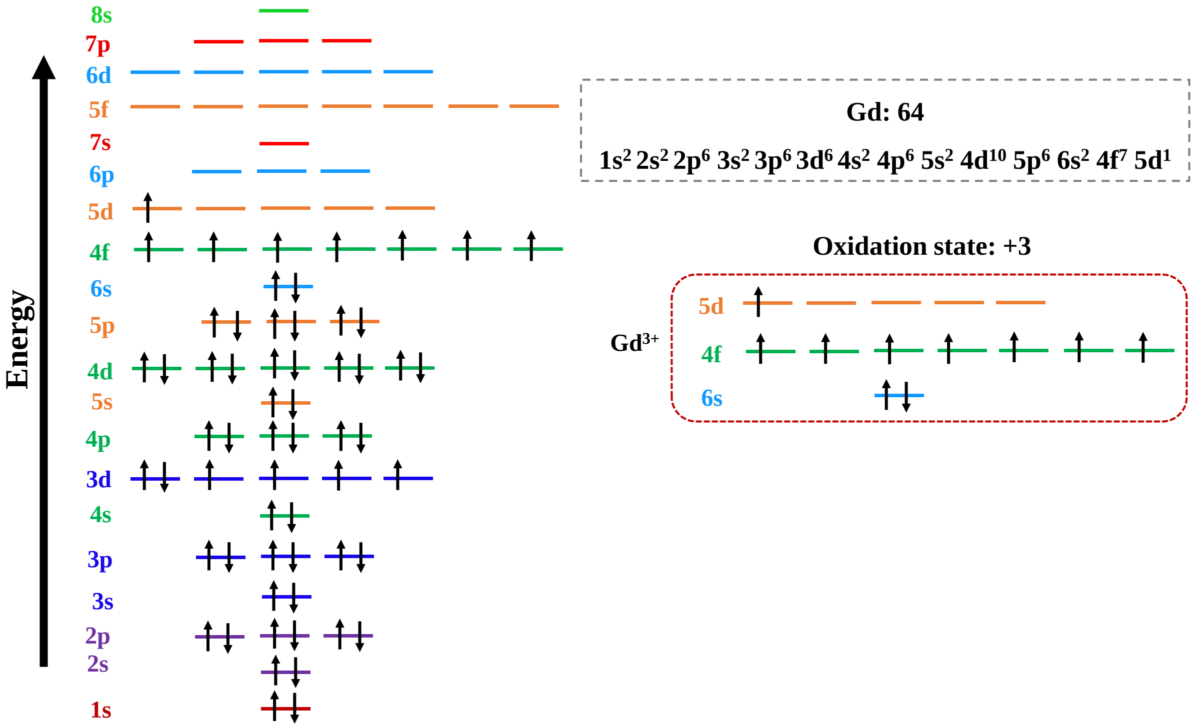

Figure 1.15: Schematic illustration of the electronic configuration of gadolinium with +3 oxidation state.

There has been no report on the modulation of trigonal iron sulphide nanoparticles upon the addition of Gd ion. In this study, we substitute Gd ions using the thermal decomposition method to synthesize Gd-substituted trigonal phase of iron sulphide nanoparticles and investigate the influence of Gd-substitution on the various structural characteristics and physical properties of the fundamental compound.

1.12. Objective of the thesis

As discussed in the previous section, the research is focused primarily on understanding the physical characteristics of the compound at nanoscale. The trigonal Fe_7S_8 may hold copious potential for many industrial and technical applications. In order to use this material in real life applications, it is very important to understand the structure and the physical properties of this material. The literature holds narrow information about the phases and properties of the compound. for e.g., magnetic properties and dielectric properties. In this thesis, efforts are dedicated to understand the physical properties— magnetic and dielectric characteristics of the compound, and how are they important for fundamental understanding and technical applications. Further, in order to modify the existing properties of trigonal iron sulphide, the structure of the compound was modified by substituting a rare-earth element.

1.13. Thesis Outline:

Chapter 1

In the first chapter, the transition metal chalcogenides are introduced and their applications in various fields are discussed. A review about Fe-S system is presented, which was narrowed down to the pyrrhotites. It is highlighted in the chapter as why the trigonal Fe_7S_8 is of fundamental and technological importance. Brief literature review of the trigonal Fe_7S_8 is given, highlighting the structural and magnetic characteristics of the compound. In the end, objective of the thesis is discussed.

Chapter 2

The second chapter discusses the structural aspects of trigonal phase of Fe_7S_8 at nanoscale. In order to modify the characteristics, the compound was substituted with a rare-earth element—Gd. The chapter further discusses and compares the different structural parameters of all the samples.

Chapter 3

The third chapter discusses the magnetic characteristic of trigonal phase of Fe_7S_8 at nanoscale with the aim of understanding the magnetism in the compound and finally to calculate the energy product. The magnetic characteristics of the compound were modified by the substitution of Gd of varying at%. The chapter further discusses and compares the different magnetic parameters of all the samples.

Chapter 4

The fourth chapter discusses the dielectric properties of trigonal phase of Fe_7S_8 at nanoscale The dielectric characteristics of the compound were modified by the substitution of Gd of varying at%. The chapter further discusses and compares the different dielectric parameters of all the samples.

Chapter 5

The conclusion of this thesis and scope of future works are discussed in fifth chapter.

References

1 F. Jellinek, Transition metal chalcogenides. relationship between chemical composition, crystal structure and physical properties, *React. Solids*, , DOI:10.1016/0168-7336(88)80031-7.

2 M.-R. Gao, Y.-F. Xu, J. Jiang and S.-H. Yu, Nanostructured metal chalcogenides: synthesis, modification, and applications in energy conversion and storage devices, *Chem. Soc. Rev.*, 2013, **42**, 2986–3017.

3 C.-H. Lai, K.-W. Huang, J.-H. Cheng, C.-Y. Lee, B.-J. Hwang and L.-J. Chen, Direct growth of high-rate capability and high capacity copper sulfide nanowire array cathodes for lithium-ion batteries, *J. Mater. Chem.*, 2010, **20**, 6638–6645.

4 G. Giuffredi, T. Asset, Y. Liu, P. Atanassov and F. Di Fonzo, Transition Metal Chalcogenides as a Versatile and Tunable Platform for Catalytic CO2 and N2 Electroreduction, *ACS Mater. Au*, 2021, **1**, 6–36.

5 M.-R. Gao, J. Jiang and S.-H. Yu, Solution-Based Synthesis and Design of Late Transition Metal Chalcogenide Materials for Oxygen Reduction Reaction (ORR), *Small*, 2012, **8**, 13–27.

6 M. Chhowalla, H. S. Shin, G. Eda, L.-J. Li, K. P. Loh and H. Zhang, The chemistry of two-dimensional layered transition metal dichalcogenide nanosheets, *Nat. Chem.*, 2013, **5**, 263–275.

7 T. Heine, Transition Metal Chalcogenides: Ultrathin Inorganic Materials with Tunable Electronic Properties, *Acc. Chem. Res.*, 2015, **48**, 65–72.

8 E. M. Vogel and J. A. Robinson, Two-dimensional layered transition-metal dichalcogenides for versatile properties and applications, *MRS Bull.*, 2015, **40**, 558–563.

9 H. Yuan, Z. Liu, G. Xu, B. Zhou, S. Wu, D. Dumcenco, K. Yan, Y. Zhang, S.-K. Mo, P. Dudin, V. Kandyba, M. Yablonskikh, A. Barinov, Z. Shen, S. Zhang, Y. Huang, X. Xu, Z. Hussain, H. Y. Hwang, Y. Cui and Y. Chen, Evolution of the Valley Position in Bulk Transition-Metal Chalcogenides and Their Monolayer Limit, *Nano Lett.*, 2016, **16**, 4738–4745.

10 P.-C. Yeh, W. Jin, N. Zaki, D. Zhang, J. T. Liou, J. T. Sadowski, A. Al-Mahboob, J. I. Dadap, I. P. Herman, P. Sutter and R. M. Osgood, Layer-dependent electronic structure of an atomically heavy two-dimensional dichalcogenide, *Phys. Rev. B*, 2015,

91, 41407.

11 J. S. Ross, S. Wu, H. Yu, N. J. Ghimire, A. M. Jones, G. Aivazian, J. Yan, D. G. Mandrus, D. Xiao, W. Yao and X. Xu, Electrical control of neutral and charged excitons in a monolayer semiconductor, *Nat. Commun.*, 2013, **4**, 1474.

12 J. Feng, X. Sun, C. Wu, L. Peng, C. Lin, S. Hu, J. Yang and Y. Xie, Metallic Few-Layered VS2 Ultrathin Nanosheets: High Two-Dimensional Conductivity for In-Plane Supercapacitors, *J. Am. Chem. Soc.*, 2011, **133**, 17832–17838.

13 K. Chang and W. Chen, In situ synthesis of MoS2/graphene nanosheet composites with extraordinarily high electrochemical performance for lithium ion batteries, *Chem. Commun.*, 2011, **47**, 4252–4254.

14 J. Li, F. Jiang, B. Yang, X.-R. Song, Y. Liu, H.-H. Yang, D.-R. Cao, W.-R. Shi and G.-N. Chen, Topological insulator bismuth selenide as a theranostic platform for simultaneous cancer imaging and therapy, *Sci. Rep.*, 2013, **3**, 1998.

15 J. E. Moore, The birth of topological insulators, *Nature*, 2010, **464**, 194–198.

16 S.-C. Liufu, L.-D. Chen, Q. Yao and C.-F. Wang, Assembly of one-dimensional nanorods into Bi2S3 films with enhanced thermoelectric transport properties, *Appl. Phys. Lett.*, 2007, **90**, 112106.

17 K. Kadel, L. Kumari, W. Z. Li, J. Y. Huang and P. P. Provencio, Synthesis and Thermoelectric Properties of Bi2Se3 Nanostructures, *Nanoscale Res Lett*, 2010, **6**, 57.

18 R. J. Mehta, C. Karthik, W. Jiang, B. Singh, Y. Shi, R. W. Siegel, T. Borca-Tasciuc and G. Ramanath, High Electrical Conductivity Antimony Selenide Nanocrystals and Assemblies, *Nano Lett.*, 2010, **10**, 4417–4422.

19 R. Malakooti, L. Cademartiri, A. Migliori and G. A. Ozin, Ultrathin Sb2S3nanowires and nanoplatelets, *J. Mater. Chem.*, 2008, **18**, 66–69.

20 M. S. Dresselhaus, G. Chen, M. Y. Tang, R. G. Yang, H. Lee, D. Z. Wang, Z. F. Ren,

J.-P. Fleurial and P. Gogna, New Directions for Low-Dimensional Thermoelectric Materials, *Adv. Mater.*, 2007, **19**, 1043–1053.

21 A. J. Minnich, M. S. Dresselhaus, Z. F. Ren and G. Chen, Bulk nanostructured thermoelectric materials: current research and future prospects, *Energy Environ. Sci.*, 2009, **2**, 466–479.

22 J. Puthussery, S. Seefeld, N. Berry, M. Gibbs and M. Law, Colloidal Iron Pyrite (FeS2) Nanocrystal Inks for Thin-Film Photovoltaics, *J. Am. Chem. Soc.*, 2011, **133**, 716–719.

23 L. Zhu, B. Richardson, J. Tanumihardja and Q. Yu, Controlling morphology and phase of pyrite FeS2 hierarchical particles via the combination of structure-direction and chelating agents, *CrystEngComm*, 2012, **14**, 4188–4195.

24 I. U. Arachchige and S. L. Brock, Sol-gel methods for the assembly of metal chalcogenide quantum dots., *Acc. Chem. Res.*, 2007, **40**, 801–809.

25 Y. Shirasaki, G. J. Supran, M. G. Bawendi and V. Bulović, Emergence of colloidal quantum-dot light-emitting technologies, *Nat. Photonics*, 2013, **7**, 13–23.

26 S. V Kershaw, A. S. Susha and A. L. Rogach, Narrow bandgap colloidal metal chalcogenide quantum dots: synthetic methods, heterostructures, assemblies, electronic and infrared optical properties., *Chem. Soc. Rev.*, 2013, **42**, 3033–3087.

27 C.-H. Lai, K.-W. Huang, J.-H. Cheng, C.-Y. Lee, W.-F. Lee, C.-T. Huang, B.-J. Hwang and L.-J. Chen, Oriented growth of large-scale nickel sulfide nanowire arrays via a general solution route for lithium-ion battery cathode applications, *J. Mater. Chem.*, 2009, **19**, 7277–7283.

28 M.-R. Gao, Q. Gao, J. Jiang, C.-H. Cui, W.-T. Yao and S.-H. Yu, A Methanol-Tolerant Pt/CoSe2 Nanobelt Cathode Catalyst for Direct Methanol Fuel Cells, *Angew. Chemie Int. Ed.*, 2011, **50**, 4905–4908.

29 M.-R. Gao, S. Liu, J. Jiang, C.-H. Cui, W.-T. Yao and S.-H. Yu, In situ controllable synthesis of magnetite nanocrystals/CoSe2 hybrid nanobelts and their enhanced catalytic performance, *J. Mater. Chem.*, 2010, **20**, 9355–9361.

30 Z. Li, Y. Hu, K. A. Howard, T. Jiang, X. Fan, Z. Miao, Y. Sun, F. Besenbacher and M. Yu, Multifunctional Bismuth Selenide Nanocomposites for Antitumor Thermo-Chemotherapy and Imaging., *ACS Nano*, 2016, **10**, 984–997.

31 K. Yang, G. Yang, L. Chen, L. Cheng, L. Wang, C. Ge and Z. Liu, FeS nanoplates as a multifunctional nano-theranostic for magnetic resonance imaging guided photothermal therapy, *Biomaterials*, 2015, **38**, 1–9.

32 X.-R. Song, X. Wang, S.-X. Yu, J. Cao, S.-H. Li, J. Li, G. Liu, H.-H. Yang and X. Chen, Co_9 Se_8 nanoplates as a new theranostic platform for photoacoustic/magnetic resonance dual-modal-imaging-guided chemo-photothermal combination therapy., *Adv. Mater.*, 2015, **27**, 3285–3291.

33 M. Hansen, K. Anderko and H. W. Salzberg, Constitution of Binary Alloys, *J. Electrochem. Soc.*, 1958, **105**, 260C.

34 G. Kullerud, Sulfide Phase Relations, *Miner. Soc. Amer. Spec. Pap*, 1970, **3**, 199–210.

35 M. Nagamori, Metal loss to slag: Part I. Sulfidic and oxidic dissolution of copper in fayalite slag from low grade matte, *Metall. Trans.*, 1974, **5**, 531–538.

36 P. H. Ribbe, Ed., De Gruyter, pp. 245–276.

37 H. Rau, Range of homogeneity and defect energetics in Co1−x S, *J. Phys. Chem. Solids*, 1976, **37**, 931–934.

38 T. Hirone, S. Maeda, S. Chiba and N. Tsuya, Thermal Analysis of Iron Sulfides at the Temperature Range of β-transformation, *J. Phys. Soc. Japan*, 1954, **9**, 500–502.

39 K. Koto, N. Morimoto and A. Gyobu, The superstructure of the intermediate pyrrhotite. I. Partially disordered distribution of metal vacancy in the 6{\it C} type,

Fe${\sb 11}$S${\sb 12}$, *Acta Crystallogr. Sect. B*, 1975, **31**, 2759–2764.

40 F. Grønvold and E. F. Westrum, Heat capacities of iron disulfides Thermodynamics of marcasite from 5 to 700 K, pyrite from 300 to 780 K, and the transformation of marcasite to pyrite, *J. Chem. Thermodyn.*, 1976, **8**, 1039–1048.

41 D. Rickard and G. W. Luther, *Chem. Rev.*, 2007.

42 H. Wang and I. Salveson, A review on the mineral chemistry of the non-stoichiometric iron sulphide, Fe1− x S ($0 \leq x \leq 0.125$): polymorphs, phase relations and transitions, electronic and magnetic structures, *Phase Transitions*, 2005, **78**, 547–567.

43 J. Zemann, Crystal structures, 2nd edition. Vol. 1 by R. W. G. Wyckoff, *Acta Crystallogr.*, 1965, **18**, 139.

44 T. Chen, J. C. Mikkelsen and G. B. Charlan, Crystal growth and crystal chemistry of NiAs-type compounds: MnSb, CoSb, and NiSb, *J. Cryst. Growth*, 1978, **43**, 5–12.

45 F. Tweefon-, Pyrrhotites: Composition, **168**, 8–10.

46 M. PÓSFAI, K. CZINER, E. MÁRTON, P. MÁRTON, P. R. BUSECK, R. B. FRANKEL and D. A. BAZYLINSKI, Crystal-size distributions and possible biogenic origin of Fe sulfides, *Eur. J. Mineral.*, 2001, **13**, 691–703.

47 E. F. Bertaut, Contribution à l'étude des structures lacunaires: la pyrrhotine, *Acta Crystallogr.*, 1953, **6**, 557–561.

48 M. E. Fleet, The crystal structure of a pyrrhotite (Fe7S8), *Acta Crystallogr. Sect. B Struct. Crystallogr. Cryst. Chem.*, 1971, **27**, 1864–1867.

49 A. Okazaki and K. Hirakawa, Structural Study of Iron Selenides FeSex. I Ordered Arrangement of Defects of Fe Atoms, *J. Phys. Soc. Japan*, 1956, **11**, 930–936.

50 M. Kawaminami and A. Okazaki, Neutron Diffraction Study of Fe7Se8. II, *J. Phys. Soc. Japan*, 1970, **29**, 649–655.

51 M. E. Fleet, Phase equiliabria at high temperatures, *Rev. Mineral. Geochemistry*, 2006,

61, 365–419.

52 J. WuenschBernhardt, On the superstructure and twinning of pyrrhotite, *Spec. Pap. - Mineral. Soc. Am.*, 1963, **1**, 157–163.

53 H. Nakazawa and N. Morimoto, Phase relations and superstructures of pyrrhotite, Fe1−xS, *Mat. Res. Bull*, 1971, **6**, 345–358.

54 R. J. Ellis and P. W. Scott, Evaluation of hyperspectral remote sensing as a means of environmental monitoring in the St. Austell China clay (kaolin) region, Cornwall, UK, *Remote Sens. Environ.*, , DOI:10.1016/j.rse.2004.07.004.

55 C. A. Francis and J. R. Craig, Pyrrhotite: the nA (or 2A, 3C) superstructure reviewed, *Am. Mineral.*, 1976, **61**, 21–25.

56 A. Nakano, M. Tokonami and N. Morimoto, Refinement of 3C Pyrrhotite, Fe7S8, *Acta Cryst.*, 1979, **35**, 724–725.

57 F. Keller-Besrest, G. Collin and R. Comès, Structure and planar faults in the defective NiAs-type compound 3c Fe7S8, *Acta Crystallogr. Sect. B*, 1983, **39**, 296–303.

58 A. V Powell, P. Vaqueiro, K. S. Knight, L. C. Chapon and R. D. Sánchez, Structure and magnetism in synthetic pyrrhotite ${\text{Fe}}_{7}{\mathrm{S}}_{8}$: A powder neutron-diffraction study, *Phys. Rev. B*, 2004, **70**, 14415.

59 M Nishiguchi, Osaka University, 1977.

60 R. T. B. T.-D. in E. G. SHUEY, Ed., in *Semiconducting Ore Minerals*, Elsevier, 1975, vol. 4, pp. 290–303.

61 R. G. Arnold, RANGE IN COMPOSITION AND STRUCTURE OF 82 NATURAT TERRESTRIAI PYRRHOTITES.

62 A. J. Naldrett, J. R. Craig and G. Kullerud, The central portion of the Fe-Ni-S system and its bearing on pentlandite exsolution in iron-nickel sulfide ores, *Econ. Geol.*, 1967, **62**, 826–847.

63 G. Lianxing and F. M. Vor, Intergrowths of hexagonal and monoclinic pyrrhotites in some sulphide ores from Norway, 1996, **60**, 303–316.

64

65 A. H. CLARK, Iron-deficient Low-temperature Pyrrhotite, *Nature*, 1965, **205**, 792–793.

66 E.J. SCHWARZ and D.J. VAUGHAN, Magnetic Phase Relations of Pyrrhotite, *J. Geomag. Geoelectr*, 1972, **139**, 66–89.

67 *Elements*, 2020, 16, 128–129.

68 J. P. R. de Villiers, D. C. Liles and M. Becker, The crystal structure of a naturally occurring 5C pyrrhotite from Sudbury, its chemistry, and vacancy distribution, 2009, **94**, 1405–1410.

69 A. D. Elliot, Structure of pyrrhotite 5C (Fe9S10), *Acta Crystallogr. Sect. B*, 2010, **66**, 271–279.

70 D. C. Liles and P. R. de Villiers, Redetermination of the structure of 5C pyrrhotite at low temperature and at room temperature, 2012, **97**, 257–261.

71

72 A. Živković, H. E. King, M. Wolthers and N. H. De Leeuw, Magnetic structure and exchange interactions in pyrrhotite end member minerals: Hexagonal FeS and monoclinic Fe7S8, *J. Phys. Condens. Matter*, , DOI:10.1088/1361-648X/ac1cb2.

73

74 L. Néel, Some New Results on Antiferromagnetism and Ferromagnetism, *Rev. Mod. Phys.*, 1953, **25**, 58–63.

75 D. Koulialias, B. Lesniak, M. Schwotzer, P. G. Weidler, J. F. Löffler and A. U. Gehring, *Geochemistry, Geophys. Geosystems*, 2019, 20, 5216–5224.

76 C. S. Horng and A. P. Roberts, The Low-Temperature Besnus Magnetic Transition:

Signals Due to Monoclinic and Hexagonal Pyrrhotite, *Geochemistry, Geophys. Geosystems*, 2018, **19**, 3364–3375.

77 C. R. S. Haines, C. J. Howard, R. J. Harrison and M. A. Carpenter, Group-theoretical analysis of structural instability, vacancy ordering and magnetic transitions in the system troilite (FeS){--}pyrrhotite (Fe${\sb 1{$-$}{\it x}}$S), *Acta Crystallogr. Sect. B*, 2019, **75**, 1208–1224.

78 J. M. D. Coey, *Magnetism and magnetic materials*, 2010.

79 S. Chikazumi, Physics of Ferromagnetism.

80 B. D. Cullity and C. D. Graham, *Introduction to Magnetic Materials*, 2008.

81 S. Bedanta and W. Kleemann, Supermagnetism, *J. Phys. D. Appl. Phys.*, 2009, **42**, 13001.

82 E. C. Stoner and E. P. Wohlfarth, A Mechanism of Magnetic Hysteresis in Heterogeneous Alloys, *Philos. Trans. R. Soc. A Math. Phys. Eng. Sci.*, , DOI:10.1098/rsta.1948.0007.

83 B. D. Cullity, *Introduction to Magnetic Materials*, Addision Wesley Publicating Company, Reading, MA, 1972.

84 D. Koulialias, R. Schäublin, G. Kurtuldu, P. G. Weidler, J. F. Löffler and A. U. Gehring, On the Magnetism Behind the Besnus Transition in Monoclinic Pyrrhotite, *J. Geophys. Res. Solid Earth*, 2018, **123**, 6236–6246.

85 D. Koulialias, B. Lesniak, M. Schwotzer, P. G. Weidler, J. F. Löffler and A. U. Gehring, The Besnus Transition in Single-Domain 4C Pyrrhotite, *Geochemistry, Geophys. Geosystems*, 2019, **20**, 5216–5224.

86 Y. A. Koksharov, in *Magnetic Nanoparticles*, 2009, pp. 197–254.

87 R. Nongjai, S. Khan, K. Asokan, H. Ahmed and I. Khan, Magnetic and electrical properties of In doped cobalt ferrite nanoparticles, *J. Appl. Phys.*, 2012, **112**, 84321.

88 R. Jabbar, S. H. Sabeeh and A. M. Hameed, Structural, dielectric and magnetic properties of Mn+2 doped cobalt ferrite nanoparticles, *J. Magn. Magn. Mater.*, 2020, **494**, 165726.

89 K. Maaz, S. Karim, A. Mashiatullah, J. Liu, M. D. Hou, Y. M. Sun, J. L. Duan, H. J. Yao, D. Mo and Y. F. Chen, Structural analysis of nickel doped cobalt ferrite nanoparticles prepared by coprecipitation route, *Phys. B Condens. Matter*, 2009, **404**, 3947–3951.

90 D. D. Andhare, S. R. Patade, J. S. Kounsalye and K. M. Jadhav, Effect of Zn doping on structural, magnetic and optical properties of cobalt ferrite nanoparticles synthesized via. Co-precipitation method, *Phys. B Condens. Matter*, 2020, **583**, 412051.

91 S. Chakrabarty, A. Dutta and M. Pal, Enhanced magnetic properties of doped cobalt ferrite nanoparticles by virtue of cation distribution, *J. Alloys Compd.*, 2015, **625**, 216–223.

92 Y. Köseoğlu, F. Alan, M. Tan, R. Yilgin and M. Öztürk, Low temperature hydrothermal synthesis and characterization of Mn doped cobalt ferrite nanoparticles, *Ceram. Int.*, 2012, **38**, 3625–3634.

93 S. Kavitha and M. Kurian, Effect of zirconium doping in the microstructure, magnetic and dielectric properties of cobalt ferrite nanoparticles, *J. Alloys Compd.*, 2019, **799**, 147–159.

94 J. H. L. Voncken, *Handbook on the Physics and Chemistry of Rare Earths*, Springer, 2016.

95 A. R. Jha, *Rare Earth Materials: Properties and Applications*, CRC Press, Boca Raton, 2016.

96 Y. Zhang, W. Wei, G. K. Das and T. T. Yang Tan, Engineering lanthanide-based

materials for nanomedicine, *J. Photochem. Photobiol. C Photochem. Rev.*, 2014, **20**, 71–96.

97 G. Wang, Q. Peng and Y. Li, Lanthanide-Doped Nanocrystals: Synthesis, Optical-Magnetic Properties, and Applications, *Acc. Chem. Res.*, 2011, **44**, 322–332.

Chapter 2

Synthesis and structural study of 3C Fe$_7$S$_8$ and Gd-substituted 3C Fe$_7$S$_8$ nanoparticles

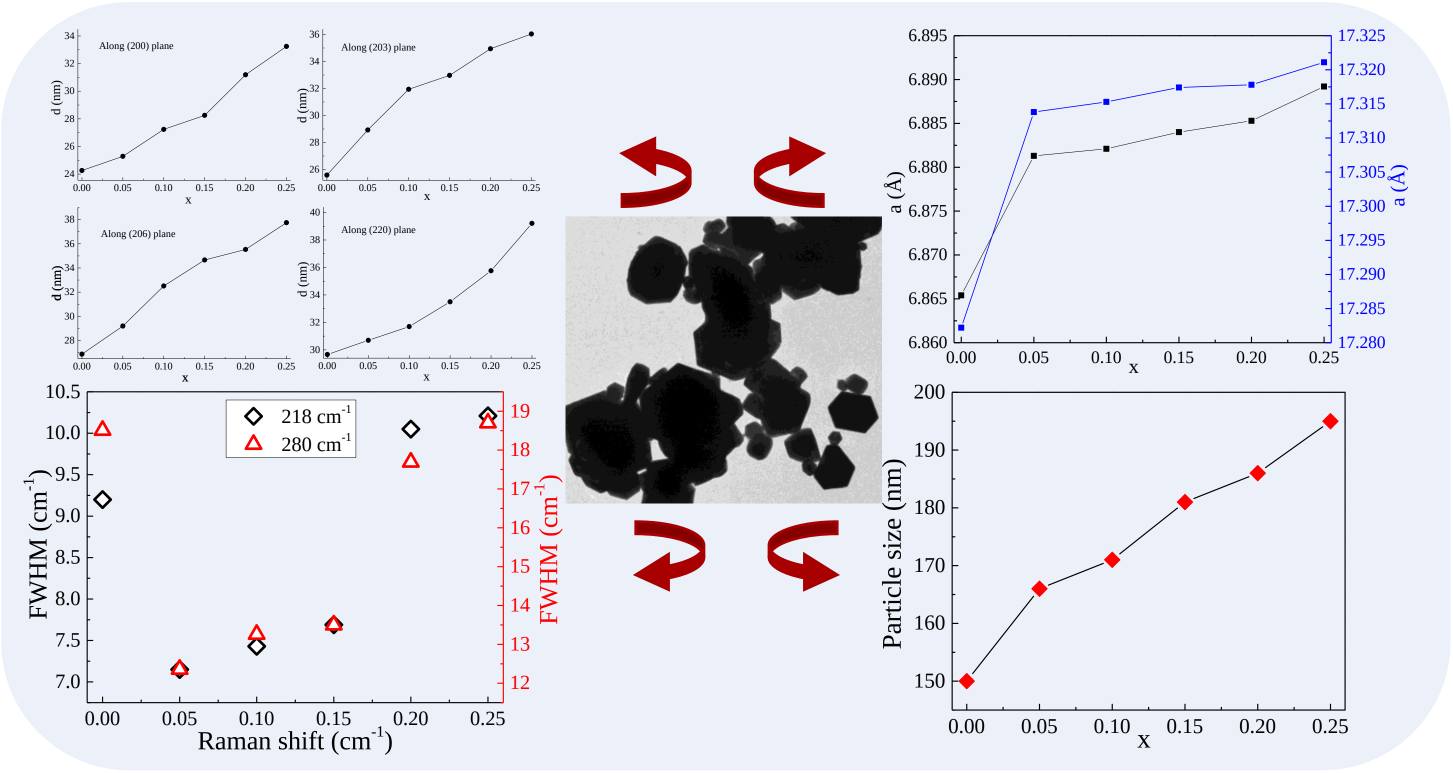

Highlights

Below are some of the findings that we would like to highlight.

- The trigonal 3C Fe_7S_8 and the Gd-substituted iron sulphide samples were synthesized using the thermal decomposition method at the nanoscale.
- The trigonal phase was obtained after quenching the sample from a high temperature to the wet ice.
- The Gd-substituted samples were substituted in 5%, 10%, 15%, 20% and 20% concentration in the trigonal 3C Fe_7S_8 lattice are represented as x=0.05, 0.1, 0.15, 0.2, 0.20.
- The crystallite size of the nanoparticles increases as the concentration of Gd is increased in the trigonal 3C Fe_7S_8 lattice.
- The lattice parameters, obtained after the refinement, increase with the increase in the concentration of Gd-substitution in the lattice.
- The as-synthesized samples exhibit distorted hexagonal shaped morphology of variable size. However, the average particle size of the nanoparticles increases with the increase in the concentration Gd in the lattice.
- The presence of Fe^{2+}, Fe^{3+} and Gd^{3+} ions in all the as-synthesized samples were confirmed by the means of XPS analysis. Raman spectra indicate towards the lattice strain in the samples.

Keywords: x-ray diffraction, Rietveld refinement, transmission electron microscopy, Raman spectroscopy, x-ray photospectroscopy, crystal structure

2.1. Introduction

2.1.1. Powder X-ray diffraction (PXRD)

The classical phenomena of wave interference, whereby monochromatic electromagnetic waves superimpose to generate a resultant wave, serves as the basis for X-ray diffractive diffraction[1]. The path difference between the two interfering waves determines the amplitude of the resulting wave. The amplitude of the wave increases as a result of constructive interference when the path difference between the interfering waves is an integral (N) multiple of the incident wavelength[1]. Conversely, if the path difference is N/2 of the incident wavelength, the amplitude decreases and the monochromatic waves get destructively interfered with[1]. Diffraction happens when the waves resulted from constructive interference get scattered by an object. Theoretically, the atoms in an infinite crystal are periodically arranged. The incident X-ray beam is diffracted by the atoms of the crystal, and a reflection pattern is created in the reciprocal space. Bragg's law governs the positions and magnitudes of intensities according to the following equation[1].

$$2d_{hkl}Sin\theta_{hkl} = n\lambda \qquad (2.1)$$

Where, θ_{hkl} is the diffraction angle (Bragg angle), λ is the wavelength of the incident X-ray beam, n represents the diffraction order, {hkl} are the Miller indices, representing the reflection in the reciprocal space, and d_{hkl} is the d-spacing between planes of the lattice.

Each diffracted wave has a unique phase and intensity when it is diffracted by a crystal lattice at Bragg angles. As a result, the information about the crystal structure is contained in the intensity, direction, and phase of the diffracted waves. However, the only data received directly from the XRD experiments is electron density[1–5]. The electron density is used to calculate the intensity of the wave. Atoms are arranged in regular, orderly patterns in crystalline materials. A crystal may diffract wave because its atoms are arranged in a periodic pattern of coherent scatterers. When the atoms of a periodic array scatter light coherently, it is called diffraction. A diffraction pattern is created as a result of diffraction from several atomic planes and contains details on the atomic configuration within the crystal. The incident X-rays diffract as lines and resolve as "spots" of Bragg intensities on the detector plane for a single crystal (figure 2.1). The incident X-rays for a polycrystalline powder sample diffract as cones and resolve as Debye rings[1,6] (figure 2.1).

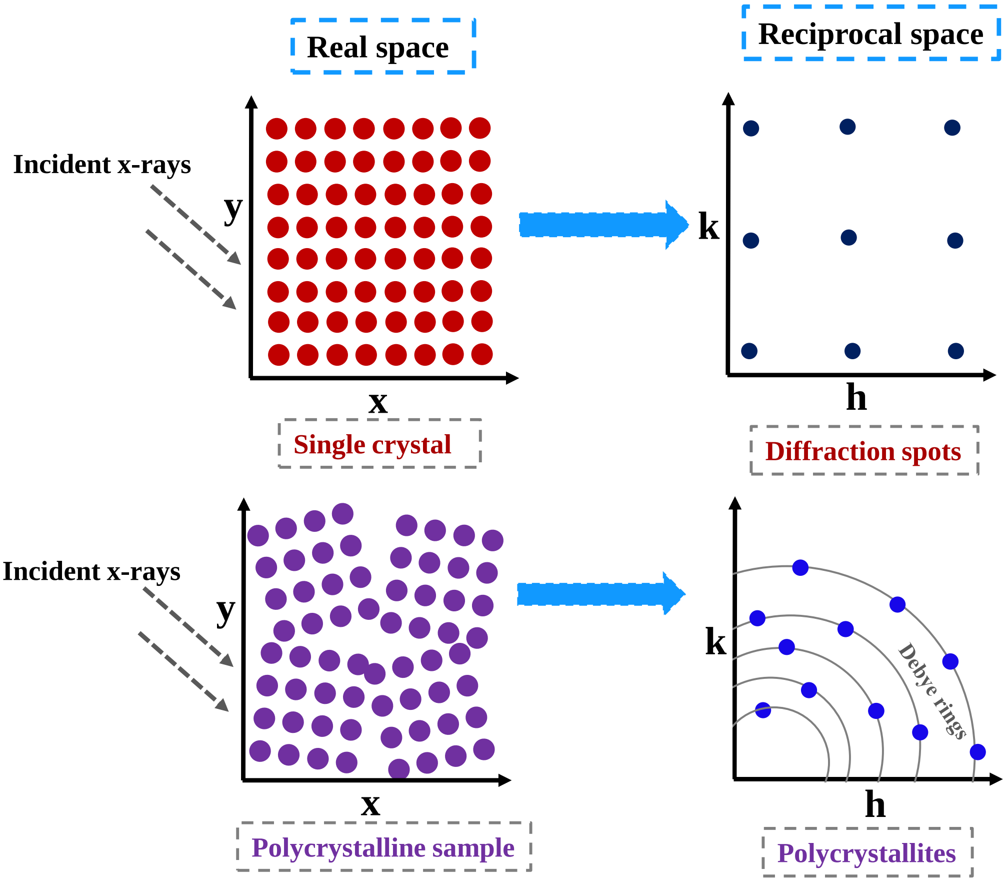

Figure 2.1: The intensities observed (schematic) from XRD experiments performed using a single crystal and powder sample are projected in the 2D reciprocal space. Intensity ‘spots’ are formed if the diffracting material is in the form of a single crystal. (Debye) ‘Rings’ are formed[6] if the diffracting material is an ideal powder.

2.1.2. Rietveld method

A list of experimental Bragg intensities (I_{hkl}) diffracted at different angles (hkl) is required in order to reconstruct structural information about a crystalline material from the X-ray diffraction data[7],[8]. Due to systematic and accidental factors, the measured diffractogram (or observed powder patterns) in powder diffraction frequently consists of several overlapped Bragg peaks. Thus, it becomes crucial to refine the structure and index the Bragg peaks., The Rietveld method[9] is intended to refine the crystal structure from the integrated intensities derived from the experimental XRD data using the parameters in the models of the structure. By minimizing the difference between a (theoretical) powder pattern generated from a model and the experimentally observed powder pattern in a least squares sense, the observed intensities obtained from the diffraction data are often refined. The lattice parameters, space group details, profile parameters, and background parameters are used to calculate the theoretical powder pattern. The feedback[9] between improving the structural knowledge and allocating observed intensity to partially overlapping individual Bragg reflections is a vital component.

2.1.3. Core mathematics and procedures in the Rietveld method

The fact that no effort is made to assign the measured intensity to a specific Bragg reflection or to resolve the overlapped reflections is a key component of a Rietveld method[9]. As a result, a reasonably good starting theoretical model is required[10]. A known approximation of structural model of the specimen[11,12] is used to calculate the starting values for the structure factors in the Rietveld method. At each of the several thousand equal steps *(i)* in the diffraction pattern, a numerical intensity value (y_i) is recorded[9,10]. At any arbitrary position in the pattern, many Bragg reflections contribute to the intensity. By adding the calculated contributions from the neighboring Bragg reflections and the background, the computed intensities (y_{ci}) are derived from $|F_K|^2$ values, according to the following equation[9,11].

$$y_{ci} = s \sum_{K} L_K \, |F_K|^{\,2} \, \varphi(2\theta_i - 2\theta_K) P_K A + y_{bi} \qquad (2.2)$$

Where, s represents the scale factor, K stands for the Miller indices, h, k, l, represents Bragg reflection, L_K represents the Lorentz factor, φ represents profile function of each reflection, P_K stands for function of preferred orientation, A stands for the absorption factor, F_K represents the structure factor, and y_{bi} stands for the background intensity.

2.1.4. Chemical structure of trigonal 3C Fe_7S_8

The first ever determination of the crystal structure of trigonal 3C Fe_7S_8 was done by Fleet[13] (1971) using a single crystal of 3C Fe_7S_8 (space group $P3_1$), which was formed as a consequence of quenching. The crystal structure was solved by considering the contribution of the crystal twinning. Based on the $P3_1$ space group, another structural study was carried out by Nishiguchi[14] (1977) on a synthesized single crystal of 3C Fe_7S_8. However, Fleet and Nishiguchi did not examine the possibility of a $P3_121$ space group in the structure. Later in 1979, the structure of 3C Fe_7S_8 was refined by Nakano[15], with space group $P3_121$ based on Fe-vacanies and unit cell parameters a = 6.8652±0.0006 Å, c = 17.047±0.002 Å, confirming the trigonal symmetry. The structure is essentially the same as that of 3C Fe_7Se_8, as reported by Okazaki & Hirakawa[16,17] (1956), which has the $P3_121$ symmetry. Figure 2.2 illustrates a layered 3C Fe_7S_8 structure with vacant and filled iron layers stacked normal to the *c*-axis in a sequence described as AFBFCF, where A, B, and C denote the layers containing Fe-vacancies, and F represents the layer without Fe-vacancy. The arrangement of vacancy-containing alternate layers is same for both 4C and 3C superstructures[13,15,18]. However, the arrangement of vacancies and the type of Fe-clustering in the alternate layers of Fe and S in the lattice are different[19] in the 4C and 3C structures of Fe_7S_8, as suggested by Nakazawa *et.*

al. Based on Bertuat (1953) model for 4C Fe_7S_8, the Fe ions position as Fe^{2+} and Fe^{3+} in the vacancy layers to account for the non-stoichiometry in the structure.

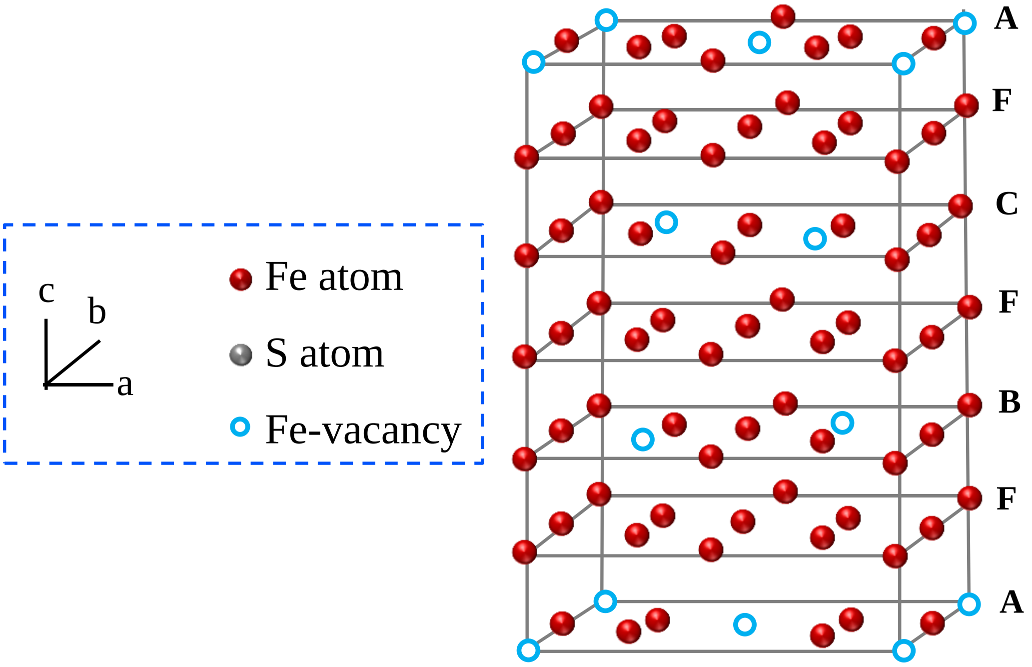

Figure 2.2: Crystal structure of trigonal 3C Fe_7S_8 with $P3_121$ space group, according to Nakano *et. al*[15].

However, being a metastable state[20,21] of 4C Fe_7S_8, the compound is usually synthesized in the laboratories. Probably, for this particular reason, there has been a little information about the various physical and chemical properties the compound. However, a few marine sediment cores around the world have been recently identified[20–22] as the source of trigonal 3C Fe_7S_8. As a consequence of either shock or quenching effect, the compound is known to occur as the metastable (at room temperature) form of 4C Fe_7S_8. A few scientific groups[20–22] have extracted the powder sample from such natural resources and confirmed its trigonal symmetry. The study was done using the bulk sample. Significant shift in the properties is known when the size is reduced to nano-dimensions, owing to the large surface to volume ratio[23–25]. However, to the best of our literature survey, we have not encountered the synthesis of the trigonal phase of Fe_7S_8 in nano-dimension, may be because the compound is lesser known. Synthesis of iron sulphide production is highly sophisticated as even slight stoichiometry variations have big impact on the structural and physical properties of the material. The solid-state synthesis approaches, however, are not adaptable enough to produce the necessary phase. In contrast, thermal decomposition method[26–30] appears to be a promising wet synthesis pathway for fabricating the trigonal phase of iron sulphide among the other chemical pathways, especially, when control over size of the particles is of importance. Therefore, it will be intriguing and interesting to understand the various behavior of the compound at nanoscale. This chapter discusses the synthesis of 3C Fe_7S_8 nanoparticles and the structural analysis. We have further investigated the changes in the structural properties, when substituted with a rare earth element—Gd. Substitution with Gd has been taken as a case study.

2.2. Experiment details

2.2.1. Materials

Thiourea (NH_2CSNH_2, 99.9 %), iron (II) chloride ($FeCl_2.4H_2O$, 99.9 %), gadolinium (III) nitrate ($Gd(NO_3)_3.6H_2O$, 99.99 %) and olaylamine (OLA, 99.9 %) were purchased from Sigma-Aldrich chemicals. All chemicals were used without any further purification.

2.2.2. Characterization techniques

Technical description of the instruments used for characterization

The phase purity and crystallinity of the as-synthesized samples were characterized by powder X-ray diffraction (PXRD) using a PANalytical X’PERT PRO instrument, and the iron-filtered Cu-Kα radiation (λ = 1.54 Å) in the 2θ range of 10°−80° covered in a step size of 0.08° with a count time of 2s. The operating voltage and current for the PXRD instrument were kept at 30 kV and 40 mA, respectively. A highly sensitive surface technique—X-ray Photoelectron Spectroscopy data were recorded for Fe and S on Thermo Fisher Scientific X-ray Photoelectron Spectrometer (XPS) K-Alpha+. The monochromatic Al Kα (h_ν = 1486.6

eV) as the X-ray source was operated with a beam current of 6 mA and voltage of 12 kV coupled with a Physical Electronics 04–548 dual Mg/Al anode and in an ultra-high vacuum system with a base pressure of $\leq 5 \times 10^{-9}$ Torr. The spot size of 400 μm was used during the XPS measurement. The recorded XPS data were deconvoluted using XPS PEAK 41. All measurements mentioned above were performed at a laboratory temperature (23 °C ± 2 °C). Raman spectroscopy measurements were recorded at laboratory temperature (23 °C ± 2 °C) on an HR 800 Raman spectrophotometer (Jobin Yvon, HORIBA, France) equipped with an achromatic Czerny−Turner type monochromator (800 mm focal-length) with silver-treated mirrors. Monochromatic radiation emitted by a 632 nm laser, operating at 20 mW, was used. The specific structural details and morphology were obtained using an FEI Tecnai T20 transmission electron microscope (TEM) equipped with a super-twin (s-twin) lens operated at 200 keV accelerating voltage. The powders obtained were dispersed in n-hexane and then drop-casted on a carbon-coated copper TEM grid with 200 mesh and loaded in a single-tilt sample holder.

Calculation of crystallite size

Following the method given by Paul Scherrer[31] in 1918, the crystallite size of as-synthesized 3C Fe_7S_8 is calculated considering the effect of limited particle size on XRD patterns. Paul Scherrer approximated an expression to relate peak-broadening and crystallite size. The formula to estimate the crystallite size along the hkl plane from the measured width of their diffraction curves is given as equation 2.3:

$$D = \frac{K\lambda}{\beta cos\theta} \qquad (2.3)$$

here, the width β of the diffraction curve at an intensity equal to half the maximum intensity, known as the full width at half maxima (FWHM), is usually measured in radians. The wavelength, λ of the incident X-rays for Cu K_α is λ ~0.154 nm, θ is the Bragg angle, corresponding to the hkl plane (hkl are the Miller indices of the planes being analyzed), and K is the numerical constant typically referred to as the crystallite-shape factor, however, in the absence of details of shape information, K = 0.94 is a good approximation. Instead of directly considering the β values from peak broadening, the diffraction pattern from the line broadening of a standard material[1], high crystalline silicon powder was measured to determine the instrumental profile, it is corrected from standard data using equation 2.4.

$$\beta = \beta_M^2 - \beta_S^2 \qquad (2.4)$$

Where β_M and β_S are the measured widths of the diffraction peaks of Fe_7S_8 and the standard sample. This results in subtracting the instrumental errors from the peak broadening.

2.2.3. Synthesis pathway of 3C Fe_7S_8 nanoparticles

Polycrystalline 3C Fe_7S_8 was synthesized by a thermal decomposition method, according to the steps reported by Lin *et al.*[32] for the synthesis of hexagonal $Fe_{1-x}S$ pyrrhotite with a slight modification at the end of the procedure. A mixture of iron–oleylamine (Fe–OLA) and sulphur–oleylamine (S–OLA) complexes were prepared separately in a three-neck flask equipped with an inlet of nitrogen gas, condenser, magnetic stirrer, thermocouple, and heating mantle. The S–OLA complex was obtained from the reaction of NH_2CSNH_2 (4 mmol) dissolved in OLA (10 mL) at 180 °C under nitrogen gas and then cooled down to laboratory temperature (27 °C ± 3 °C). The Fe–OLA complex was prepared separately by dissolving $FeCl_2.4H_2O$ (2 mmol) at 150 °C in OLA. Further, the S–OLA complex was injected into the Fe–OLA complex. The mixture was initially heated at 180 °C for 2 h, followed by reflux (260 °C) for another 2 h, and was quenched from a relatively high temperature (260 °C) to wet ice (0 °C ± 3 °C). As the temperature of the suspension reached the laboratory temperature (27 °C ± 3 °C), *n*-hexane was added to it. Black precipitates were obtained, further separated via centrifugation, and then vacuum-dried to obtain the 3C Fe_7S_8 nanoparticles. The schematic for the synthesis of trigonal 3C Fe_7S_8 nanoparticles is shown in figure 2.3.

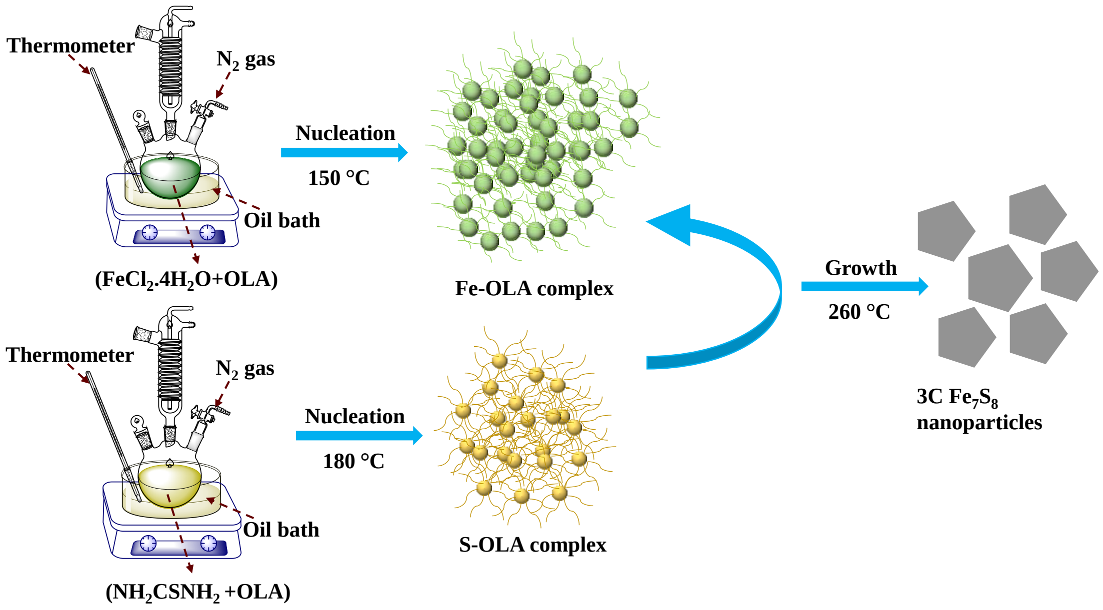

Figure 2.3: Synthesis pathway of 3C Fe_7S_8 nanoparticles using a thermal decomposition method.

2.2.4. Synthesis pathway of Gd-substituted 3C Fe_7S_8 nanoparticles

Polycrystalline 3C Fe_7S_8 substituted with gadolinium (Gd) was synthesized by a thermal decomposition method[32] with a slight modification at the end of the procedure. A mixture of iron with gadolinium–oleylamine (FeGd–OLA) and sulphur–oleylamine (S–OLA) complexes were prepared separately in a three-neck flask equipped with an inlet of nitrogen gas, condenser, magnetic stirrer, thermocouple, and heating mantle. The S–OLA complex was obtained from the reaction of NH_2CSNH_2 (4 mmol) dissolved in OLA (10 mL) at 180 °C under nitrogen gas and then cooled down to laboratory temperature (27 °C ± 3 °C). The FeGd–OLA complex was prepared separately by dissolving 2(1-x) mmol of $FeCl_2.4H_2O$ and 2x mmol of $Gd(NO_3)_3.6H_2O$ at 150 °C in OLA, where x denotes the atomic weight percent of Gd-substitition as x= 0.05, 0.1, 0.15, 0.2, 0.25, corresponding to the Gd substitution percentage as 0, 5%, 10%, 15%, 20% and 25%, respectively. Further, the S–OLA complex was injected into the Fe–OLA complex. followed by reflux (260 °C) for another 2 h, and was quenched from a relatively high temperature (260 °C) to wet ice (0 °C ± 3 °C). As the temperature of the suspension reached the laboratory temperature (27 °C ± 3 °C), *n*-hexane was added to it. Black precipitates were obtained, further separated via centrifugation, and then vacuum-dried to obtain the. The schematic for the synthesis of Gd-substituted iron sulphide nanoparticles is shown in figure 2.4.

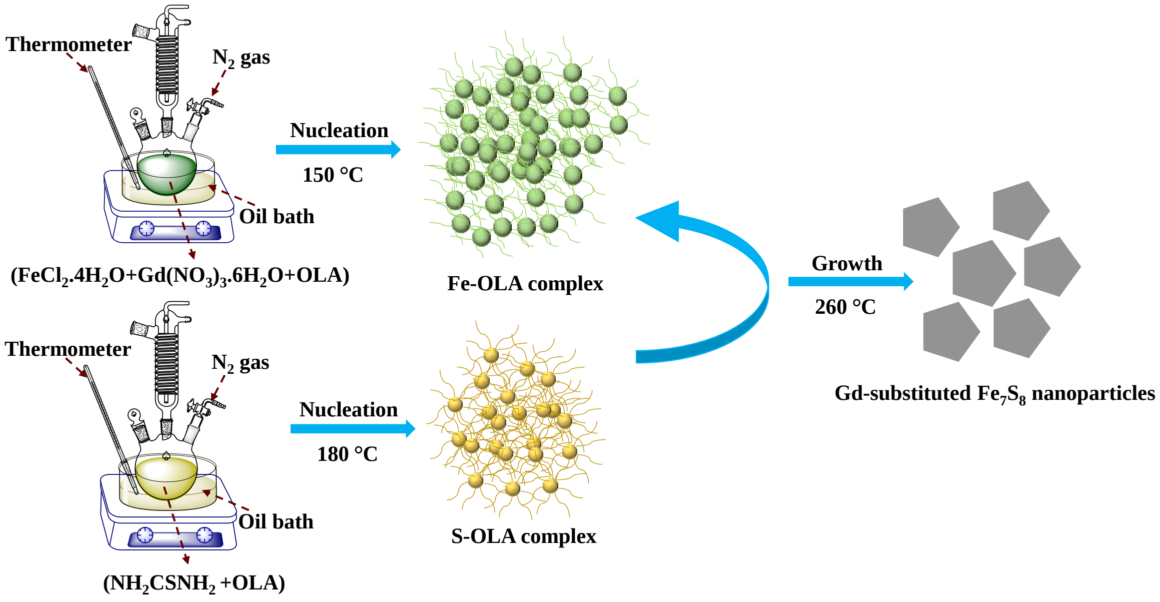

Figure 2.4: Synthesis pathway of Gd-substituted Fe_7S_8 nanoparticles using a thermal decomposition method.

2.3. Results and discussions

2.3.1. Crystallinity and phase formation of the as-synthesized samples

The PXRD is used to confirm the composition, crystallinity, and phase purity of 3C Fe_7S_8 and Gd-substituted 3C Fe_7S_8 nanoparticles, as shown in Figure 2.5a. The experimentally obtained diffraction peaks (relative intensities containing the *c*-axis and peak positions (table 2.1)) for the as-synthesized unsubstituted 3C Fe_7S_8 are in good agreement with standard JCPDS data[33] (JCPDS no. 710591), ensuring the hexagonal phase with the trigonal crystal structure ($P3_121$ space group) of the as-synthesized product with no additional peak within the detection limit of the instrument. The most intense diffraction peak centered at 2θ ~44°

corresponds to the plane (206). The peaks around 10°, 30°, 32°, 34°, 53°, 57°, 63°, 72°, and 73° correspond to planes (100), (200), (006), (203), (220), (029), (400), (316), (046), and (0310), respectively.

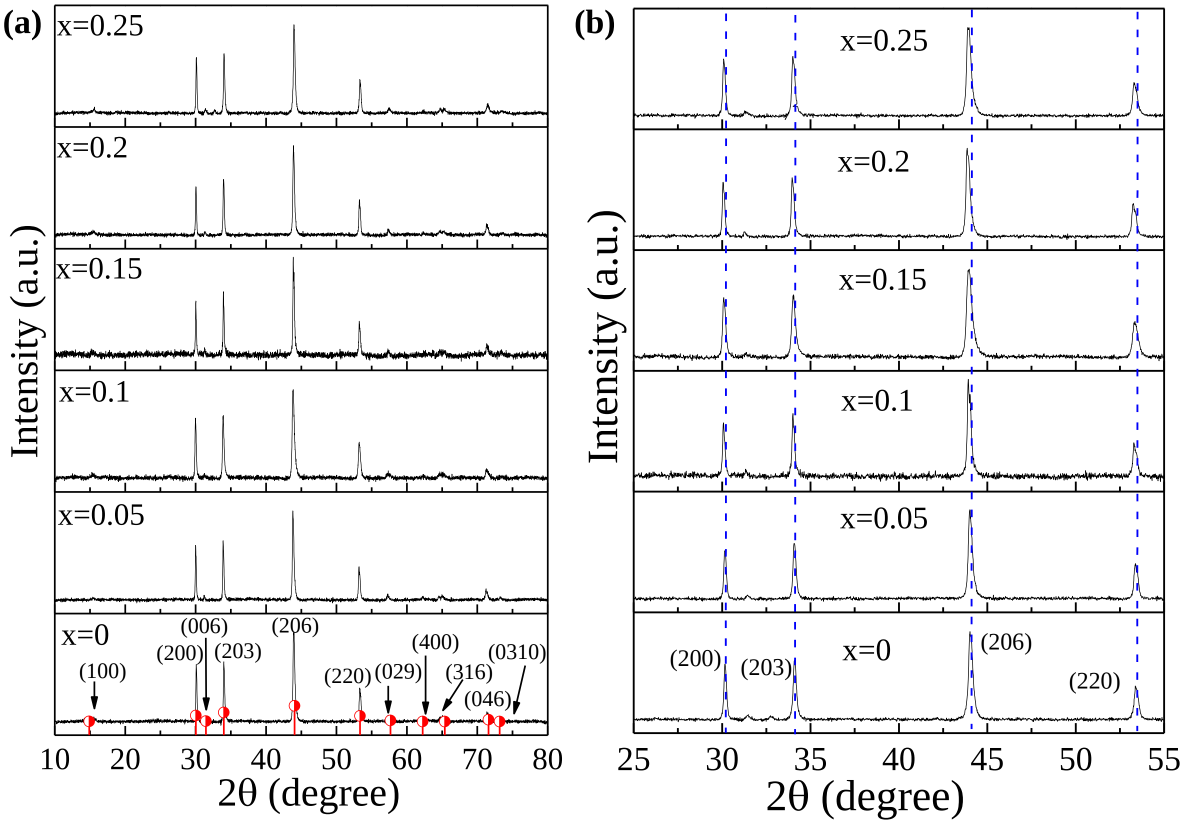

Figure 2.5: (a) Experimentally obtained XRD data for as-synthesized unsubstituted and Gd-substituted (x=0, 0.05, 0.1, 0.15, 0.2, 0.25) trigonal Fe_7S_8 nanoparticles. The reflection peaks are indexed according to the JCPDS no: 710591, (b) representation of shift in peak position as the percentage of Gd increases from x=0 to x=0.25. The samples are labeled as x=0, 0.05, 0.1, 0.15, 0.2, and 0.25, corresponding to the Gd substitution percentage as 0, 5%, 10%, 15%, 20% and 25%, respectively.

Table 2.1: Comparison of the relative intensities reported in JCPDS no: 710591 with that of the obtained experimental PXRD data for 3C Fe_7S_8 and Gd-substituted iron sulphide samples. The samples are labeled as x=0, 0.05, 0.1, 0.15, 0.2, and 0.25, corresponding to the Gd substitution percentage as 0, 5%, 10%, 15%, 20% and 25%, respectively. The relative intensities are compared only for the planes containing *c*-axis.

Plane containing *c*-axis	**(006)**		**(203)**		**(206)**		**(029)**		**(316)**		**(046)**	
	2θ (°)	Relative intensity	2θ (°)	Relative intensity	2θ (°)	Relative intensity	2θ (°)	Relative intensity	2θ (°)	Relative intensity	2θ (°)	Relative intensity
JCPDS # 710591	31.463	0.033	34.01	0.58	44.053	1	57.66	0.075	65.382	0.003	71.558	0.119
x=0	31.373	0.034	34.06	0.59	44.007	1	57.44	0.076	65.004	0.0035	71.186	0.107
x=0.05	31.428	0.035	34.26	0.62	44.119	1	57.58	0.074	65.281	0.0036	71.329	0.134
x=0.1	31.667	0.032	34.52	0.65	44.341	1	57.72	0.077	65.455	0.0038	71.562	0.168
x=0.15	31.734	0.036	34.78	0.61	44.547	1	57.76	0.078	65.624	0.0041	71.622	0.171
x=0.2	31.786	0.039	34.83	0.62	44.621	1	57.84	0.072	65.877	0.0037	71.864	0.179
x=0.25	31.942	0.031	32.97	0.64	44.843	1	58.03	0.077	65.992	0.0039	71.972	0.18

However, for Gd-substituted nanoparticles, the peak positions (figure 2.5b, 2.6) slightly shift towards lower angle side upon increasing the substitution percentage of Gd from x=0 to x=0.25. The lattice expansion[34,35] caused by the inclusion of Gd^{3+} ions in the iron sulphide nanoparticles is responsible for the shifting of the peaks toward the lower angle side. It might as well be due to the relatively higher ionic radius of Gd^{3+} (0.94 Å) ions than Fe^{3+} (0.63 Å) and Fe^{2+} (0.77 Å) ions, structural modification, formation of gases and internal compressive stress. Moreover, no impurity peaks were observed upon Gd^{3+} substitution within the detection limit of the XRD instrument.

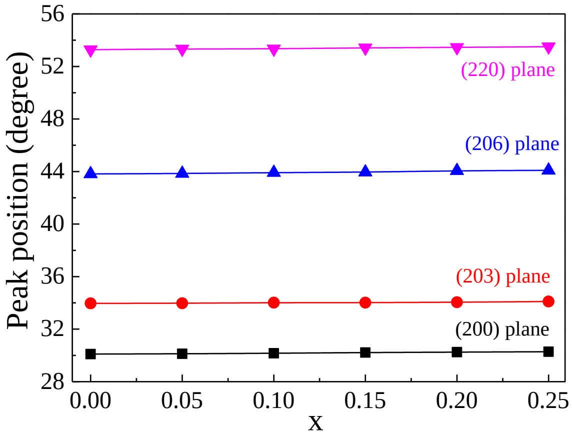

Figure 2.6: Shift in peak positions of various reflection planes as the Gd content is increased. The samples are labeled as x=0, 0.05, 0.1, 0.15, 0.2, and 0.25, corresponding to the Gd substitution percentage as 0, 5%, 10%, 15%, 20% and 25%, respectively.

Additionally, as seen in Figure 2.5b, the diffraction peaks become broader after Gd-substitution, demonstrating that the substitution of Gd^{3+} ions in the lattice has an impact on the crystal size and crystallinity of the samples. The crystallite size for all the samples along different planes has been estimated according to the equation 2.3. For as-synthesized 3C Fe_7S_8 nanoparticles, the crystallite size corresponding to the highest intensity peak along the (206) plane is ~27 nm for 3C Fe_7S_8 nanoparticles, which keeps on increasing upon increasing the Gd-content in the lattice. The variation of crystallite size along different planes— (200), (203), (206), and (220), for all the samples are shown in figure 2.7 and tabulated in table 2.2.

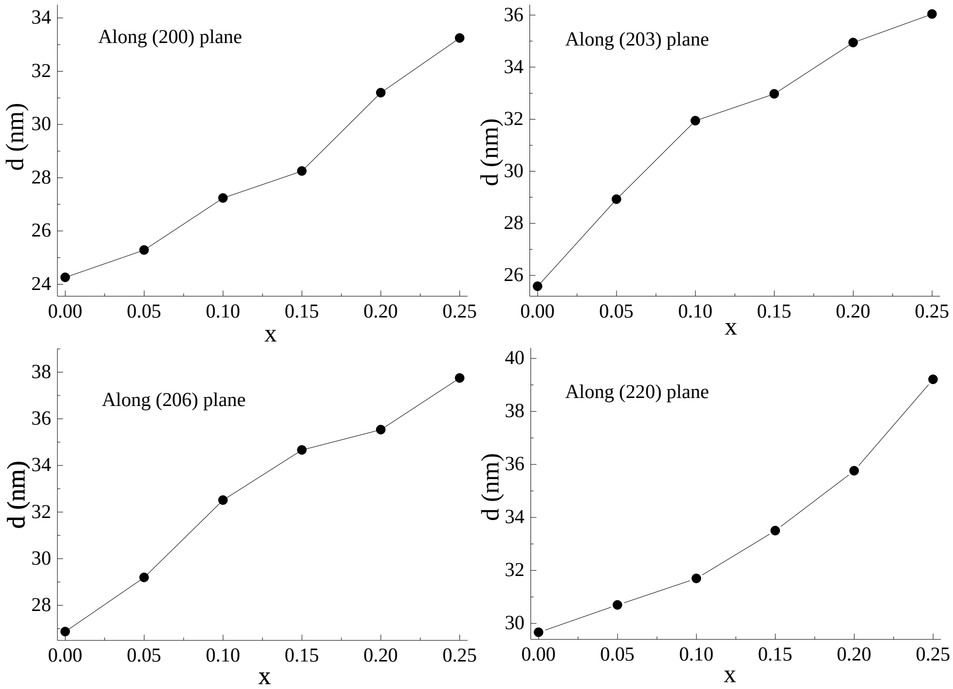

Figure 2.7: Variation of crystallite size of the as-synthesized samples along various reflection planes— (200), (203), (206), and (220). The samples are labeled as x=0, 0.05, 0.1, 0.15, 0.2, and 0.25, corresponding to the Gd substitution percentage as 0, 5%, 10%, 15%, 20% and 25%, respectively.

Table 2.2: Crystallite size of as-synthesized samples along different reflection planes. The samples are labeled as x=0, 0.05, 0.1, 0.15, 0.2, and 0.25, corresponding to the Gd substitution percentage as 0, 5%, 10%, 15%, 20% and 25%, respectively.

x	Crystallite size (nm)			
	Along (200) plane	Along (203) plane	Along (206) plane	Along (220) plane
0	24	26	27	30
0.05	25	29	29	31
0.1	27	32	33	32
0.15	28	33	35	34
0.2	31	35	36	36
0.25	33	36	38	39

Furthermore, to establish the phase purity of the as-synthesized 3C Fe_7S_8 and the series of Gd-substituted samples, the comprehensive analysis of crystal structure for all the samples was carried out by the Rietveld refinement technique[9] in the trigonal phase with space group $P3_121$ using the FullProf Suite program to determine structural parameters like the fractional lattice parameters, atomic coordinates, lattice parameters, and occupancy. The refinement is performed with the Fe_7S_8 model[33] (ICSD collection code no. 2106932), and the corresponding profile for all the samples is shown in Figure 2.8. The twelve-coefficient polynomial has been used to model the background intensity. The Pseudo-Voigt profile functions were applied to refine the shape and FWHM parameters of the XRD peak profiles for all the samples. The refinement shows that the diffraction peaks corresponding to all the samples may be indexed in the hexagonal system with the $P3_121$ space group. The goodness of fit parameter (χ^2) was used to evaluated the quality of the refinement. The experimental diffraction pattern in Figure 2.8 is displayed as black circles, and the calculated diffraction pattern is shown as a red line. The vertical green lines indicate the Bragg-allowed peak positions. The bottom blue curve indicates the difference profile between the calculated and observed XRD pattern. As no extra diffraction peaks associated with impurity phases of Gd are seen in the Gd-substituted iron sulphide samples within the detection limit of the instrument, the XRD patterns show that substitution of Gd in the 3C Fe_7S_8 lattice has no effect on the trigonal structure of the 3C Fe_7S_8. The data obtained reveals the refined 3C Fe_7S_8 crystal structure with trigonal crystal geometry and the $P3_121$ space group for all the samples.

The values of refined cell parameters (a, b, c, α, β, and γ), the cell volume (V), the R-factors— profile factor (R_p), weighted profile factor (wR_p) along with χ^2 for the as-synthesized samples are summarized in table 2.3. The low values[36] of various R-factors and χ^2, obtained after the refinement, justify that the experimental data and the model used to refine the XRD data match well. The samples are labeled as x=0, 0.05, 0.1, 0.15, 0.2, and 0.25, corresponding to the Gd substitution percentage as 0, 5%, 10%, 15%, 20% and 25%, respectively.

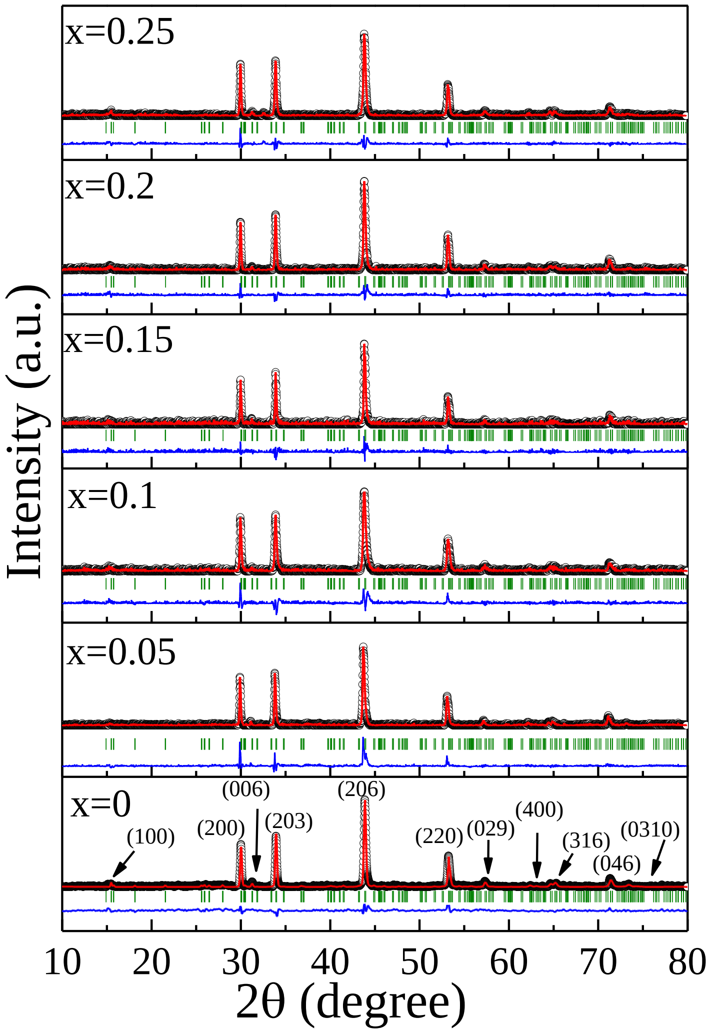

Figure 2.8: Comparison between the observed XRD patterns of 3C Fe_7S_8 and Gd-substituted 3C Fe_7S_8 nanoparticles (black circles), calculated XRD curve after crystal structure refinement by Rietveld method (red line), the difference ($I_{obs}-I_{cal}$) between observed intensity (I_{obs}) and calculated intensity (I_{cal}) (blue line), and Bragg positions (green vertical line) for various samples labeled as x=0, 0.05, 0.1, 0.15, 0.2, and 0.25, corresponding to the Gd substitution percentage as 0, 5%, 10%, 15%, 20% and 25%, respectively.

Table 2.3: The structural parameters obtained after Rietveld refinement of XRD data of as-synthesized 3C Fe_7S_8 and Gd-substituted nanoparticles, using the Fullprof Suite program. The samples are labeled as x=0, 0.05, 0.1, 0.15, 0.2, and 0.25, corresponding to the Gd substitution percentage as 0, 5%, 10%, 15%, 20% and 25%, respectively. The values $\chi 2$ and wR_P (%) represent the chi-square and weighted profile R-value, respectively. Unit cell parameters are denoted by a, b, c, and γ.

Sample	**Lattice parameters**					**Reliability factors**		**Goodness factor**
	a=b (Å)	**c (Å)**	**$\alpha = \beta$ (°)**	**γ (°)**	**V (Å^3)**	**wR_p (%)**	**R_p (%)**	**χ^2**
x=0	6.865	17.224	90	120	702	6.2	5.1	3.6
x=0.05	6.881	17.302	90	120	703	6.1	5.3	3.8
x=0.1	6.882	17.315	90	120	704	6.4	5.3	3.7
x=0.15	6.885	17.317	90	120	704	6.1	4.9	3.6
x=0.2	6.885	17.318	90	120	705	6.2	5.1	3.3
x=0.25	6.889	17.321	90	120	708	6.1	5.1	3.1

The lattice parameters obtained after the refinement show an increment in both *a* and *c* lattice constants (figure 2.9). The increase of the lattice parameters and no secondary peaks in the diffraction patterns indicated that the Gd ions have substituted the Fe^{3+} and Fe^{2+} sites and the resulting structures are isostructural with the 3C Fe_7S_8 crystal. The ionic radii of the Gd^{3+} ion can be used to directly relate the variation in lattice parameter values. The Fe^{2+} and Fe^{3+} ions with relatively smaller ionic radii are replaced by the Gd^{3+} ions having larger ionic radius.

The ionic radii of the Gd^{3+} ion can be used to directly correlated to the fluctuation in lattice parameter values. The larger ionic radii Gd^{3+} ions are substituted for the smaller ionic radii Fe^{2+} and Fe^{3+} ions[37,38].

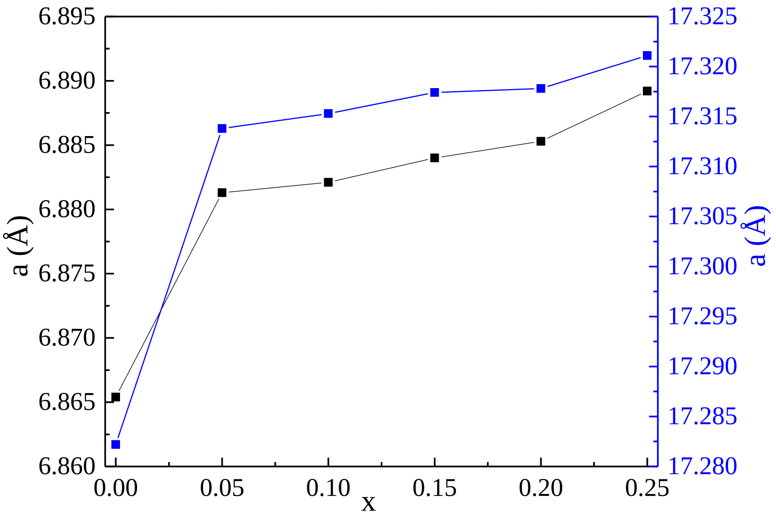

Figure 2.9: Variation in the lattice parameters, *a* and *c*, of the as-synthesized samples with increasing Gd-substitution. The samples are labeled as x=0, 0.05, 0.1, 0.15, 0.2, and 0.25, corresponding to the Gd substitution percentage as 0, 5%, 10%, 15%, 20% and 25%, respectively.

2.3.2. Transmission electron microscopy (TEM)

The shape, size, and existence of any secondary phases in a specimen can be revealed using TEM measurement. TEM measurement is used to reveal the information about the shape, size, and the presence of any secondary phase in a specimen. The bright-field TEM images (Figure 2.9a-f) show the morphology of the 3C Fe_7S_8 and Gd-substituted iron sulphide nanoparticles. Since the nanostructures are ferrimagnetic at room temperature, they are highly aggregated as seen in the figure. Additionally, the strong Lorentz interaction between the electrons and the orientated spins inside the particles has an impact on the image quality for magnetic particles[39]. The nanoparticles are oriented in different directions with respect to electron beams. This interaction between the particles and the electron beam changes the elastic scattering diffraction, which appears as different contrast in the TEM image. The nanoparticles were grown in hexagonal-shaped particles. However, some nanoparticles in all the samples were observed to be disordered in shape, which can be related to the preferential growth of the low-interfacial energy surface planes. The hexagonal morphology observed in TEM can be related to the diffracted planes, which confirms that the dominant growth of direction is <0001>. This indicates that the growth of a low-energy facet occurs along its *c*-axis[40]. The HCP packing and tendency of the nanoparticles to have energy stability through energy minimization are thought to facilitate the formation of hexagonal-shaped nanoparticles. Figure 2.9-2.11 show the morphology of all the samples at three different scales— 0.5 μm, 200 nm and 50 nm. After Gd substitution, the morphology of the samples has not changed noticeably.

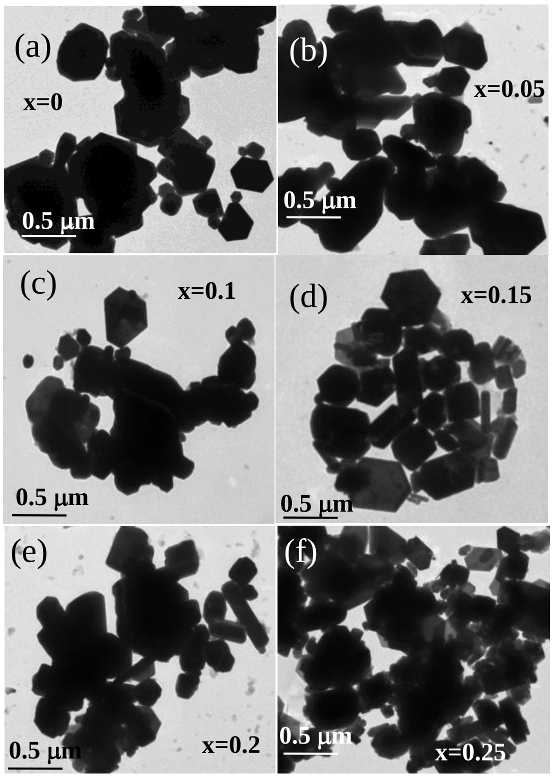

Figure 2.9: High-resolution transmission electron microscope images (a) for 3C Fe_7S_8 and (b-f) for Gd-substituted iron sulphide samples as x = 0.01, 0.02, 0.03, 0.04, 0.05, 0.07, and 0.1, at 0.5 μm scale. The samples are labeled as x=0, 0.05, 0.1, 0.15, 0.2, and 0.25, corresponding to the Gd substitution percentage as 0, 5%, 10%, 15%, 20% and 25%, respectively.

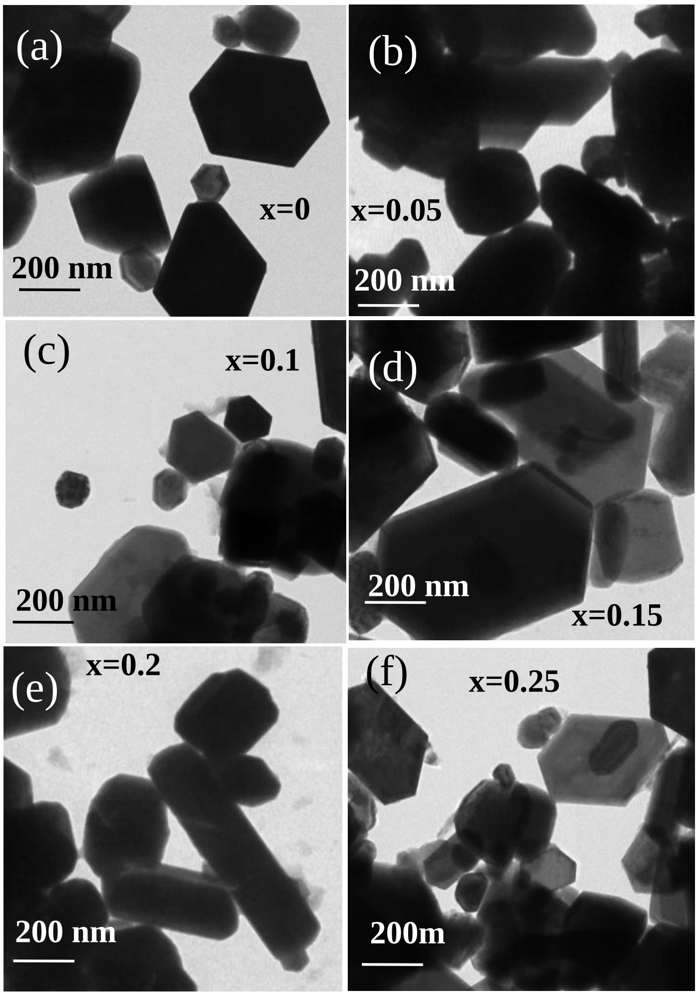

Figure 2.10: High-resolution transmission electron microscope images (a) for 3C Fe_7S_8 and (b-f) for Gd-substituted iron sulphide samples as x = 0.01, 0.02, 0.03, 0.04, 0.05, 0.07, and 0.1, at 200 nm scale. The samples are labeled as x=0, 0.05, 0.1, 0.15, 0.2, and 0.25, corresponding to the Gd substitution percentage as 0, 5%, 10%, 15%, 20% and 25%, respectively.

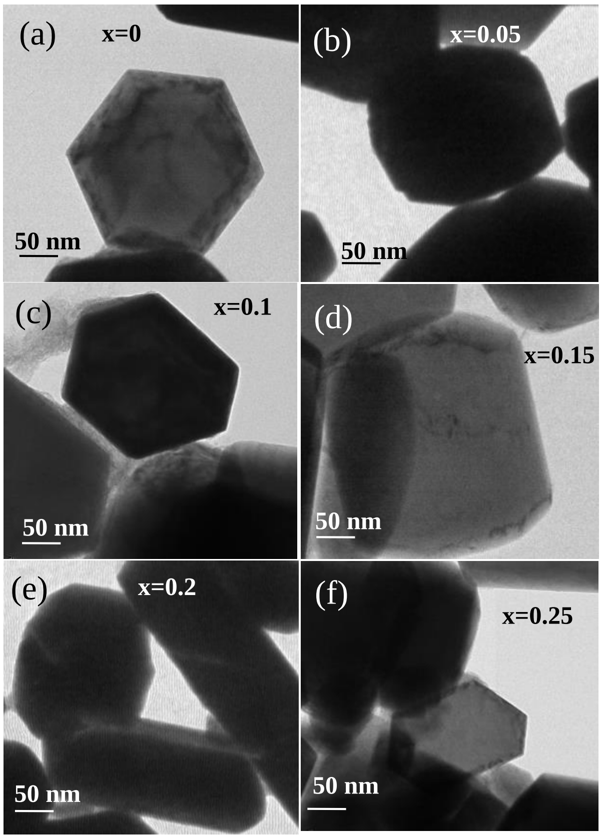

Figure 2.11: High-resolution transmission electron microscope images (a) for 3C Fe_7S_8 and (b-f) for Gd-substituted iron sulphide samples as x = 0.01, 0.02, 0.03, 0.04, 0.05, 0.07, and 0.1, at 200 nm scale. The samples are labeled as x=0, 0.05, 0.1, 0.15, 0.2, and 0.25, corresponding to the Gd substitution percentage as 0, 5%, 10%, 15%, 20% and 25%, respectively.

From high resolution images (figure 2.12), the region (marked as the black circle) gives the interplanar spacing of ~0.59 nm, which corresponds to the (200) plane of the 3C Fe_7S_8 lattice.

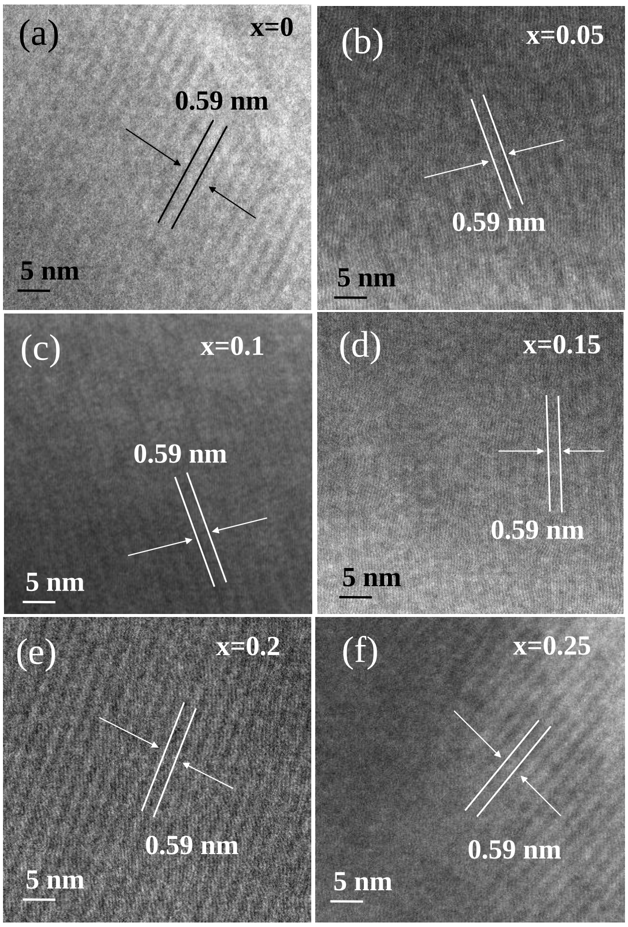

Figure 2.12: High-resolution transmission electron microscope images (a) for 3C Fe_7S_8 and (b-f) for Gd-substituted iron sulphide samples as x = 0.01, 0.02, 0.03, 0.04, 0.05, 0.07, and 0.1. The samples are labeled as x=0, 0.05, 0.1, 0.15, 0.2, and 0.25, corresponding to the Gd substitution percentage as 0, 5%, 10%, 15%, 20% and 25%, respectively.

In the SAED pattern (Figure 2.13a-f), the reflection planes (200), (203), (006), and (206) are indexed for all the samples, revealing the crystalline nature of 3C Fe_7S_8 nanoparticles. The analysis is consistent with the findings of XRD data. The prepared nanoparticles are composed of many nanocrystals. The growth direction of these nanocrystallites, along <0001> direction, reveals the most stable (minimum energy) facet. This particular growth of the nanoparticles may strongly be favored by OLA used as the surfactant[41] in the synthesis.

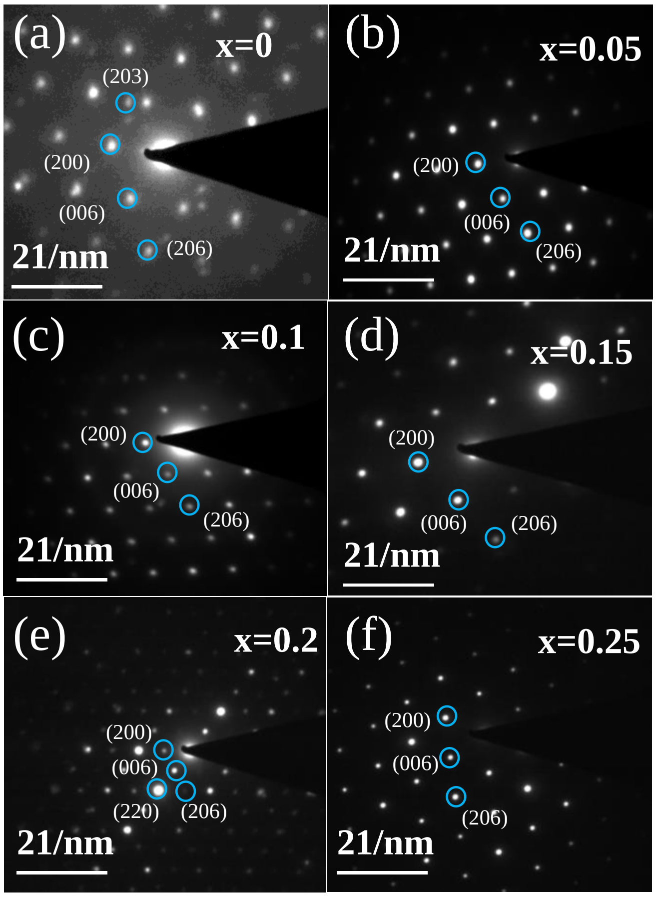

Figure 2.13: Selected area electron diffraction pattern (a) for 3C Fe_7S_8 and (b-f) for Gd-substituted iron sulphide samples as x = 0.01, 0.02, 0.03, 0.04, 0.05, 0.07, and 0.1. The samples are labeled as x=0, 0.05, 0.1, 0.15, 0.2, and 0.25, corresponding to the Gd substitution percentage as 0, 5%, 10%, 15%, 20% and 25%, respectively.

Figure 2.14(a–f) displays the particle-size distribution histogram for each sample. It appears that when the concentration of Gd increases, the average particle size increases as well (figure 2.15). The agglomeration of the particles reveals that the particles are nanocrystalline, which may be related to the Oswald ripening process[42], in which the synthesis temperature significantly affects the growth rate of nanoparticles. When the reaction temperature is high, the dissolution rate of small nanoparticles in a supersaturated solution increase, resulting in the formation of large nanoparticles.

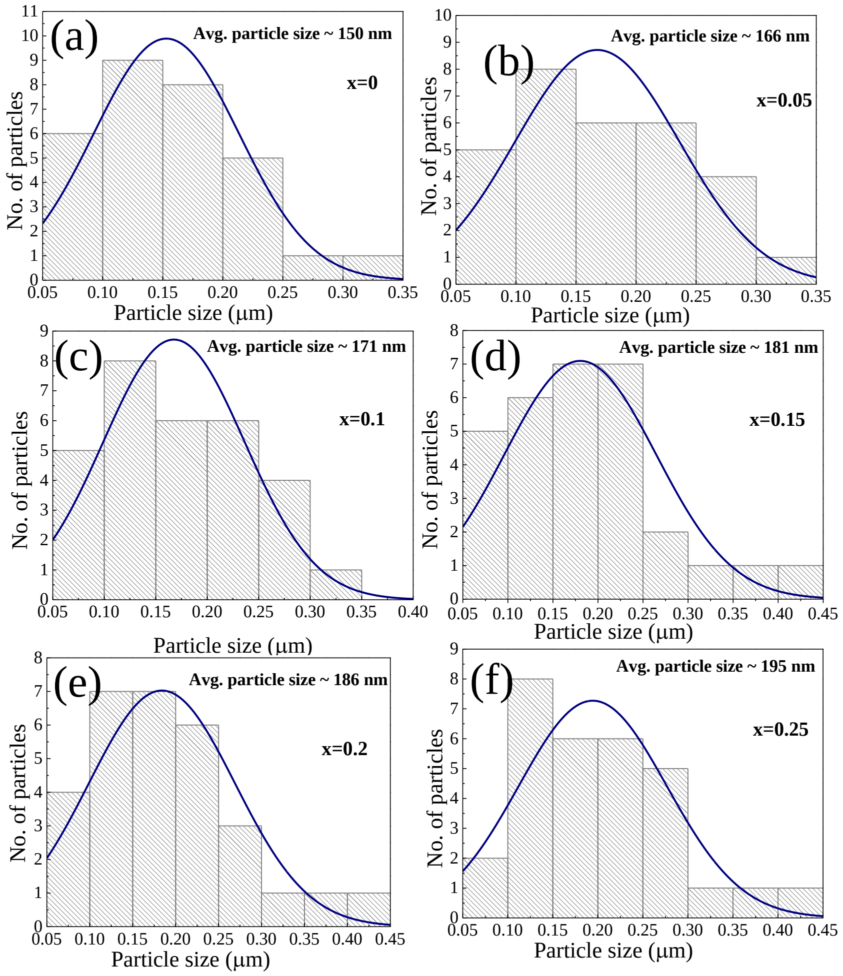

Figure 2.14: Particle size distribution (a) for 3C Fe$_7$S$_8$ and (b-f) for Gd-substituted iron sulphide samples as x = 0.01, 0.02, 0.03, 0.04, 0.05, 0.07, and 0.1. The samples are labeled as x=0, 0.05, 0.1, 0.15, 0.2, and 0.25, corresponding to the Gd substitution percentage as 0, 5%, 10%, 15%, 20% and 25%, respectively.

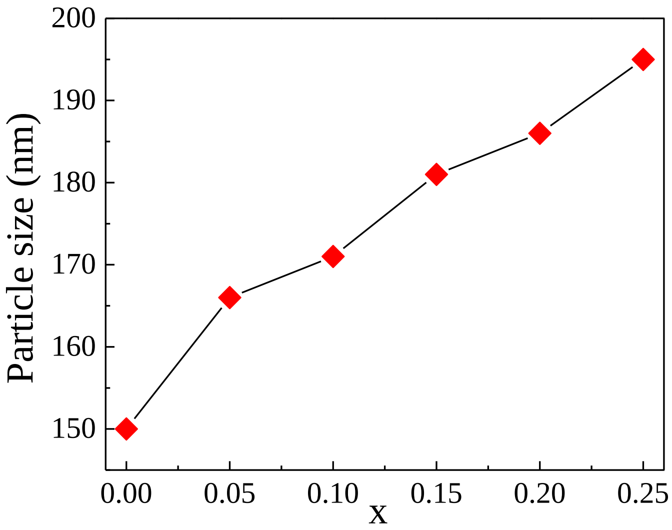

Figure 2.15: Variation of average particle size distribution for the samples with increasing Gd content.

2.3.3. X-ray photoelectron spectroscopy (XPS) measurements

The XPS technique was used to investigate the surface composition and the oxidation state in 3C Fe_7S_8 and Gd-substituted iron sulphide samples of the Fe, S, and Gd. For all samples, the core-level binding energy (BE) was aligned with the carbon[43] BE (~284 eV). The survey scan spectrum confirmed the existence of Fe and S in the material, as seen in figure 2.16a. The survey spectra depicted in figure 2.16(b–f) provide evidence of Gd, Fe, and S. The presence of C 1*s* and N 1*s* in the survey spectra may be due to the capping of oleylamine on the surface of the nanoparticles[41]. The survey spectra for all the samples show the presence of O 1*s* due to the surface oxidation of the compound by the local ambiance.

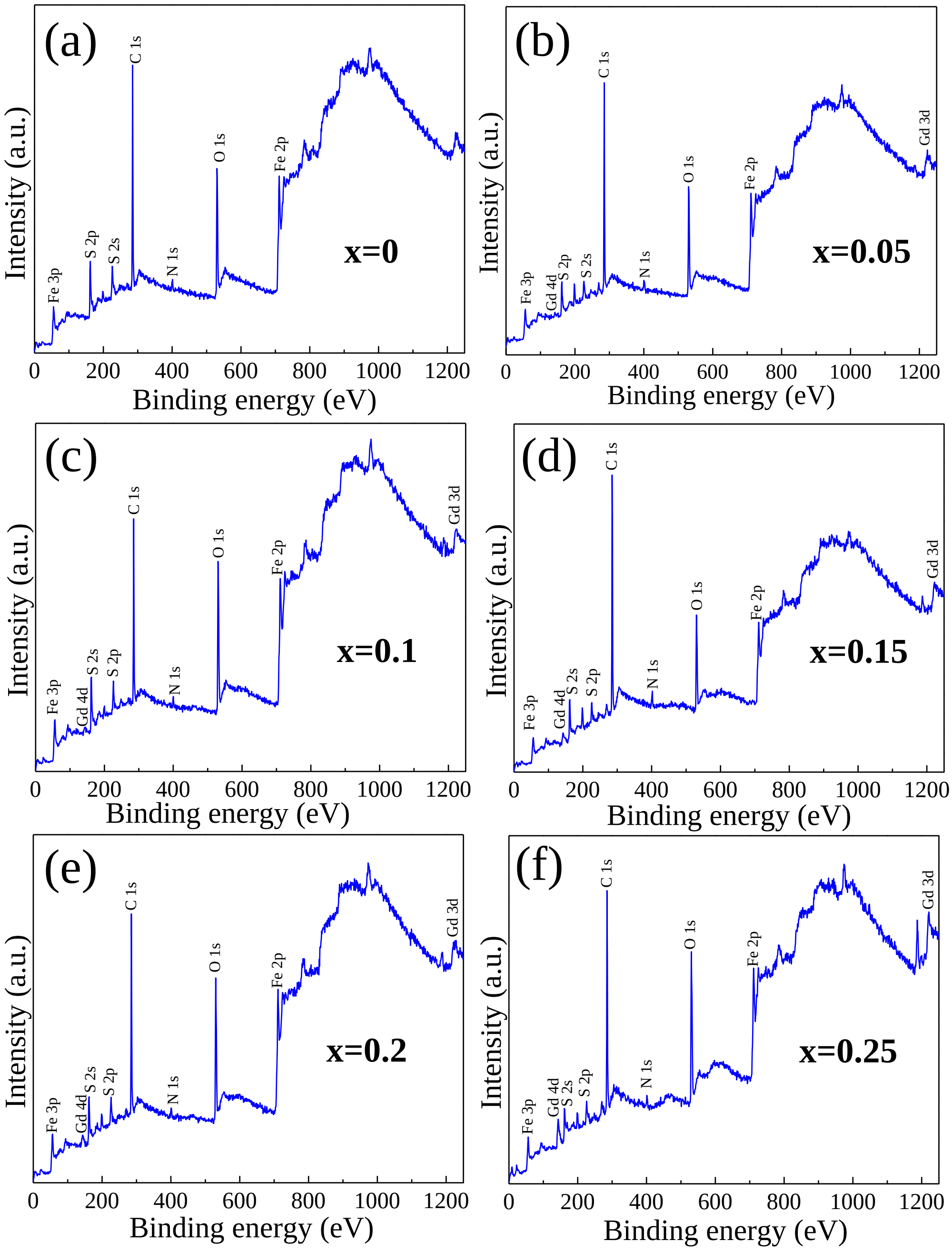

Figure 2.16: XPS survey spectra (a) for 3C Fe_7S_8 and (b-f) for Gd-substituted iron sulphide samples as x = 0, 0.05, 0.1, 0.15, 0.2, and 0.25. The spectra confirmed the presence of Fe, and S in 3C Fe_7S_8 nanoparticles and Fe, S, and Gd in Gd-substituted samples. The samples are labeled as x=0, 0.05, 0.1, 0.15, 0.2, and 0.25, corresponding to the Gd substitution percentage as 0, 5%, 10%, 15%, 20% and 25%, respectively.

The Fe 2*p* XPS spectra

Figure 2.17a shows the XPS spectra of Fe 2*p* core level BE of 3C Fe_7S_8 containing two characteristic peaks at ~711 and ~724 eV corresponding to Fe $2p_{3/2}$ and Fe $2p_{1/2}$, respectively[44], with the spin-orbit splitting energy of 13 eV. The peak Fe $2p_{1/2}$ (~724 eV) further divides into two peaks at ~723 eV and ~725 eV. In the Fe 2*p* core-level spectrum, the presence of the Fe^{2+} state in the compound[44] is implied by the peaks at 707 and 720 eV. The deconvoluted peaks of Fe^{3+} $2p_{3/2}$ and Fe^{3+} $2p_{1/2}$ states of iron at ∼711 eV and ~724 eV, respectively, correspond to the presence of Fe^{3+} in the compound[44]. The deconvoluted peaks at BE ~711 eV and ~723 eV are due to the Fe-S bond. The peak at ~725 eV is due to $2p_{1/2}$ of Fe^{2+} in the compound, attributed to the Fe-O bond may be due to the surface oxidation[45]. Peaks at ~714 eV in figure 2.19(b-f) correspond to the +3 oxidation state of Fe. Hence, Fe exists in two oxidation states─Fe^{2+} and Fe^{3+}, to account for the electron neutrality in the compound. In figure 2.17b-f, the core level Fe 2p spectra are shown for Gd-substituted iron sulphide sample.

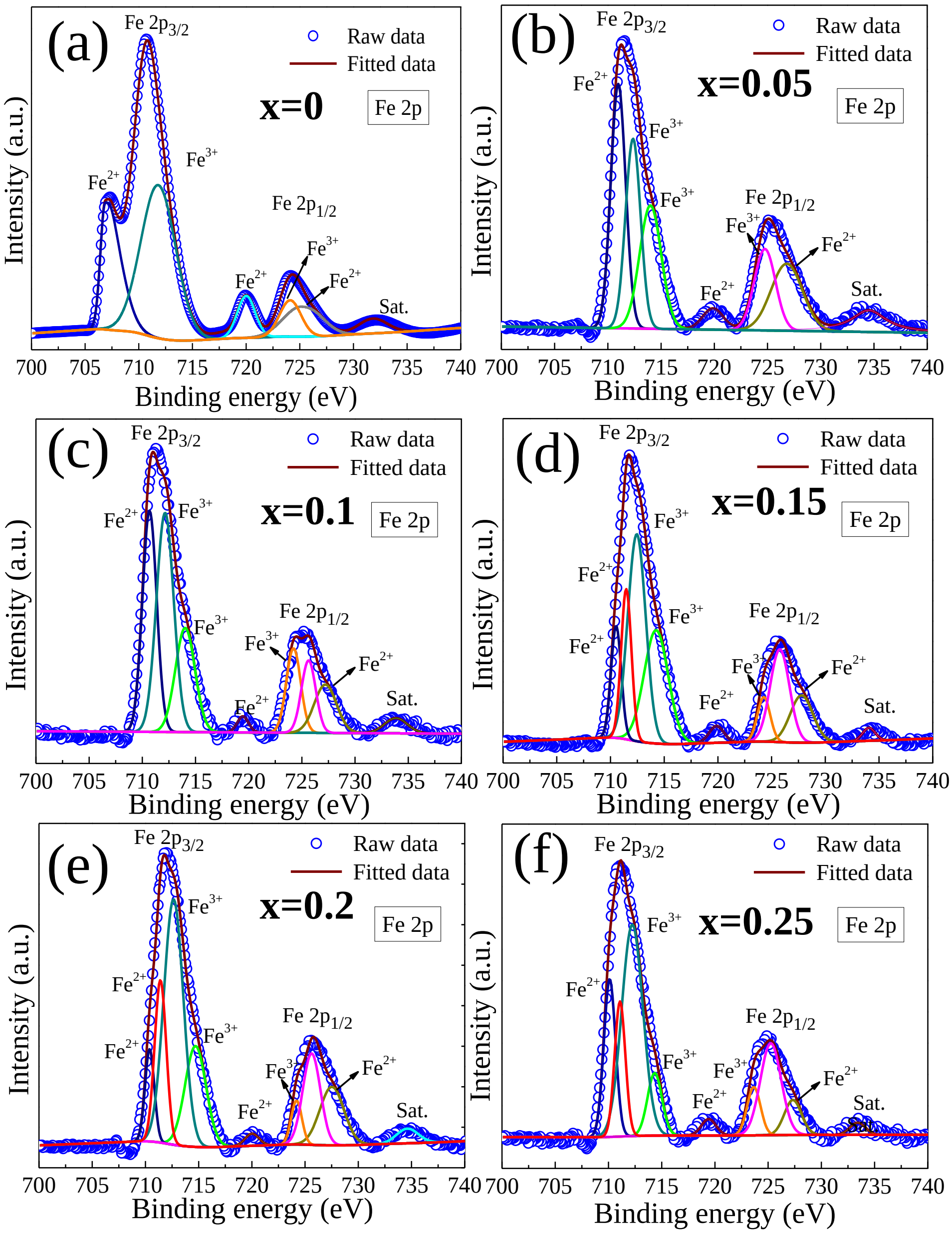

Figure 2.17: High-resolution spectra of Fe 2*p* (a) for 3C Fe_7S_8 and (b-f) for Gd-substituted iron sulphide samples as x = 0, 0.05, 0.1, 0.15, 0.2, and 0.25. The samples are labeled as x=0, 0.05, 0.1, 0.15, 0.2, and 0.25, corresponding to the Gd substitution percentage as 0, 5%, 10%, 15%, 20% and 25%, respectively.

The S 2*p* XPS spectra

Figure 2.18a-f shows the XPS spectrum of S 2*p* in 3C Fe_7S_8 and Gd-substituted iron sulphide samples. In figure 2.20a, the spin-orbit doublets at ~161 and ~164 eV correspond to the characteristic peaks of S $2p_{3/2}$ and S $2p_{1/2}$ of Fe-S species[46], respectively. After deconvolution, two subpeaks were obtained for a distinct peak at ~162 eV, whose binding energies are nearly the same, signifying the presence of C-S-C and C=S bonds[46], respectively. In addition, the deconvolution also depicts that the core S $2p$ contains S-O bond, corresponding to the peaks ~165 and ~168 eV, indicating the surface oxidation[45,46]. Upon Gd-substitution, similar binding energies can be seen in the S $2p$ spectra of all Gd-substituted samples, with the S $2p_{3/2}$ and S $2p_{1/2}$ peaks located at ~161 and ~164 eV, respectively. For Gd-substituted materials, the peak at higher binding energy of ~169 eV is attributed to the S-O associated sulphate species[46], indicating that the surface of the samples are susceptible to oxidation upon air exposure.

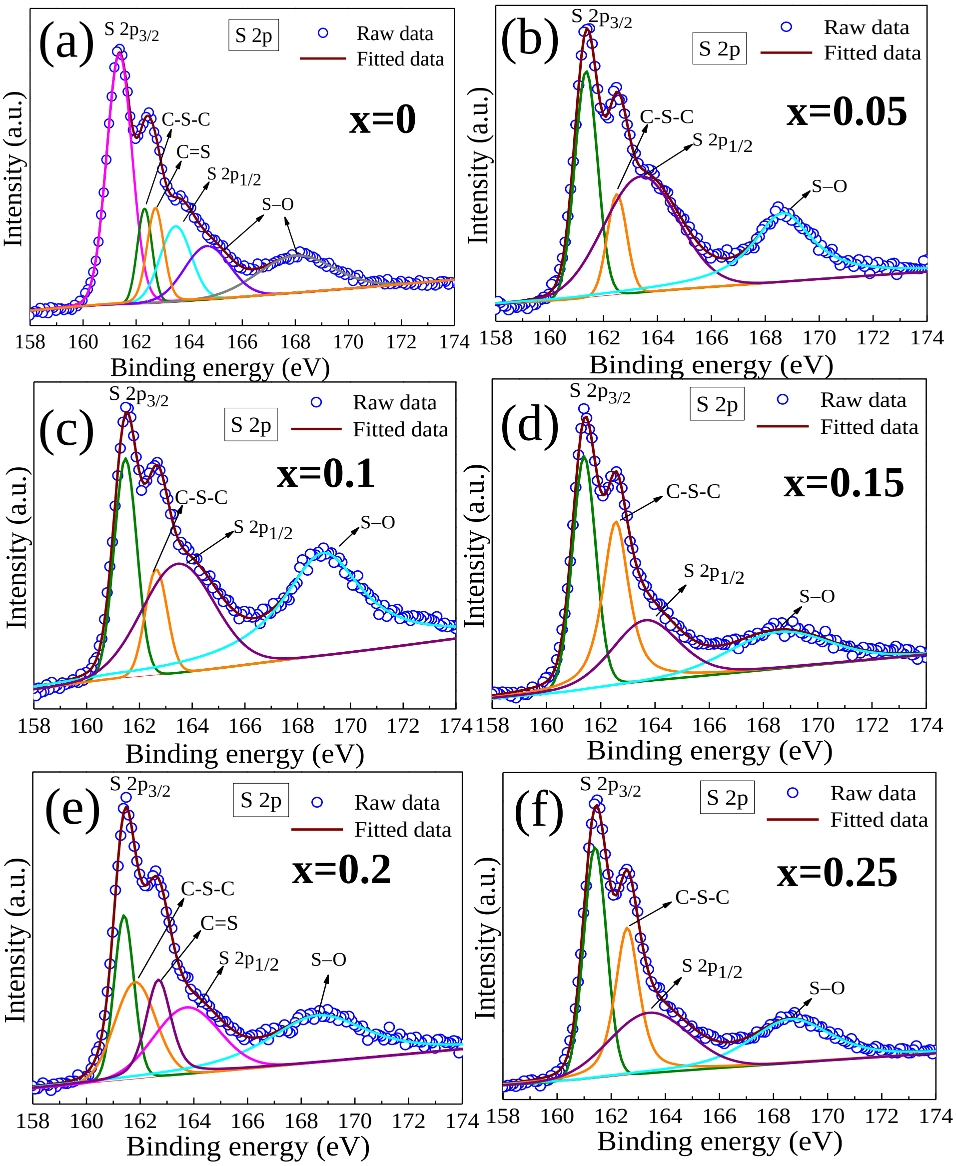

Figure 2.18: High-resolution spectra of S 2*p* (a) for 3C Fe_7S_8 and (b-f) for Gd-substituted iron sulphide samples as x = 0, 0.05, 0.1, 0.15, 0.2, and 0.25. The samples are labeled as x=0, 0.05, 0.1, 0.15, 0.2, and 0.25, corresponding to the Gd substitution percentage as 0, 5%, 10%, 15%, 20% and 25%, respectively.

The Gd 3*d* XPS spectra

In figure 2.19, Gd 3*d* peaks of Gd-substituted samples verify the presence of Gd in the samples. The spectra exhibit a similar shape and equivalent peak position for x=0.05, 0.1 and 0.15. However, the shape of spectra changes for x=0.2 and 0.25, and the peak positions remain equivalent. Additionally, Gd 3$d_{3/2}$ and Gd 3$d_{5/2}$ levels are observed in all samples at binding energies of ~1220 and ~1187 eV, respectively. The position of Gd 3*d* level for all the samples suggests that Gd ions are in the Gd^{3+} oxidation state.

Additionally, Gd 3$d_{3/2}$ and Gd 3$d_{5/2}$ levels are seen in all samples ~1220 and ~1187 eV, respectively. According to the position of Gd 3*d* level, +3 oxidation state of Gd is present in all samples.

Also, Gd 3$d_{3/2}$ and Gd 3$d_{5/2}$ levels are observed at binding energy ~1220 and ~1187 eV, respectively for all the samples. The positions of Gd 3*d* levels suggest that the oxidation state of Gd ion is Gd^{3+} in all the samples. The multiplet splitting at binding energy ~1190 eV and ~1225 eV in Gd 3*d* spectra indicate the presence of Gd-O bond due to the surface oxidation[47].

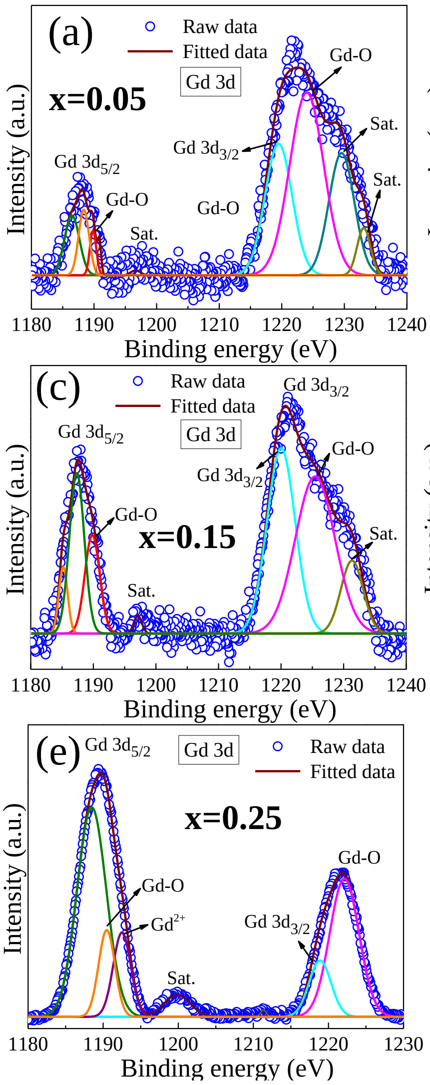

Figure 2.19: (a-e) High-resolution spectra of Gd 3*d* for Gd-substituted iron sulphide samples as x = 0, 0.05, 0.1, 0.15, 0.2, and 0.25. The samples are labeled as x=0, 0.05, 0.1, 0.15, 0.2, and 0.25, corresponding to the Gd substitution percentage as 0, 5%, 10%, 15%, 20% and 25%, respectively.

The Gd 4*d* XPS spectra

As shown in figure 2.20, the two prominent peaks at ~141 eV and ~149 eV in the deconvoluted Gd 4*d* core level XPS spectra can be attributed to the Gd $4d_{5/2}$ and Gd $4d_{3/2}$ states, respectively. These two peaks, which are indicative of the existence of Gd^{3+} ions in as-synthesised samples, are the result of spin-orbit coupling[47] for Gd-substituted iron sulphide materials. Moreover, the intensity of signals shows little change, including the Gd 4*d* peak. This indicates that Gd ions were within the bulk of the magnetite crystals and not just on the surface. Due to interactions between the 4*d* and 4*f* valence band electrons, which result in the formation of the final ionic states at ~148 and ~149 eV, the Gd 4*d* peak exhibits multiplet splitting. The literature states[47] that the position of Gd 4*d* binding energy for pure metal is between 140.4 eV and 141.6 eV. Our measured profiles reveal a profile that is similar to those that have been documented in the literature. However, in this instance, the lines show FWHM for the peaks at ~141 eV of 2.2 eV (x=0.05), 2.3 eV (x=0.1), 2.2 eV (x=0.15), 2.4 eV (x=0.2 eV), and 2.3 (x=0.25). Additionally, the fact that the peak position in all samples at a lower binding energy suggests that there is a mixture of metal and oxide phases present[47], with binding energies ranging from 141 eV (rare-earth metal) to 143 eV. (oxide).

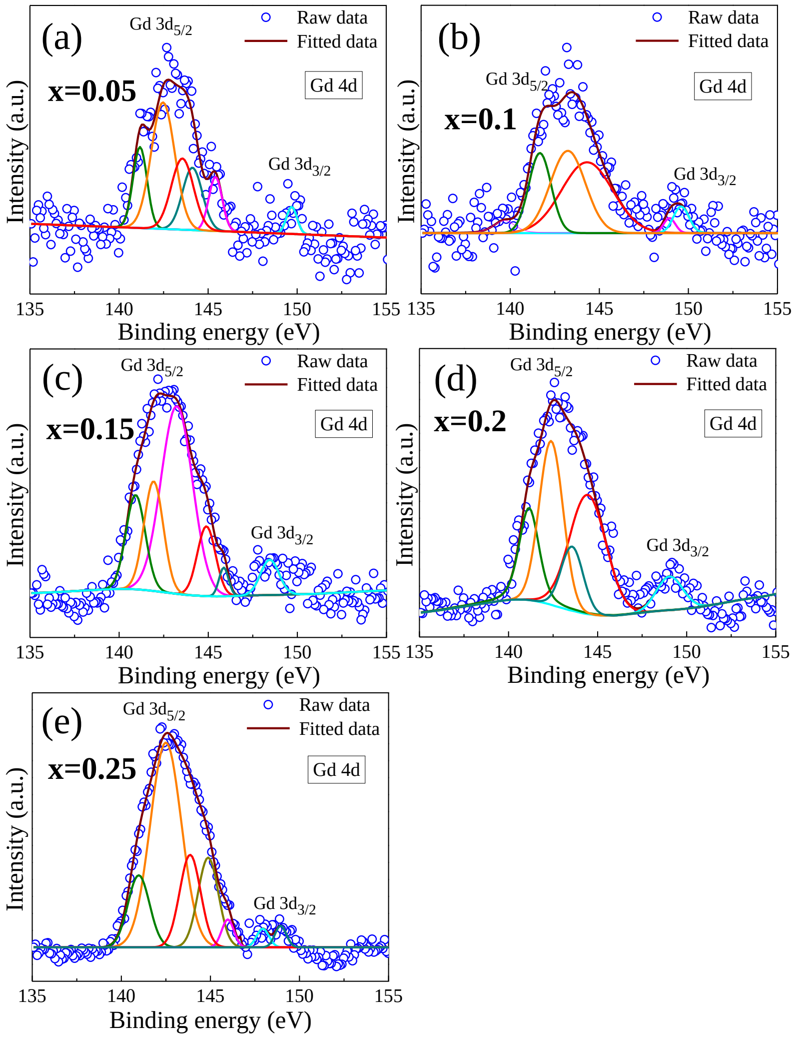

Figure 2.20: (a-e) High-resolution spectra of Gd 4*d* for Gd-substituted iron sulphide samples as x = 0, 0.05, 0.1, 0.15, 0.2, and 0.25. The samples are labeled as x=0, 0.05, 0.1, 0.15, 0.2, and 0.25, corresponding to the Gd substitution percentage as 0, 5%, 10%, 15%, 20% and 25%, respectively.

The O 1*s* XPS spectra

The XPS spectrum of O 1*s* for 3C Fe_7S_8 in figure 2.21a reveals four types of oxygen[46]— OI (~530 eV), OII (~531 eV), OIII (~533 eV), and OIV (~535 eV). These four types of oxygen correspond to lattice oxygen at the surface of the compound, —OH group, S—O group, and physi-/chemisorbed water on surfaces as a result of air exposure, respectively. It is evident that the compound readily undergoes surface oxidation when exposed to air while preparing the sample for the measurement. For all the samples (figure 2.21b-f), O 1*s* core level spectra are nearly identical.

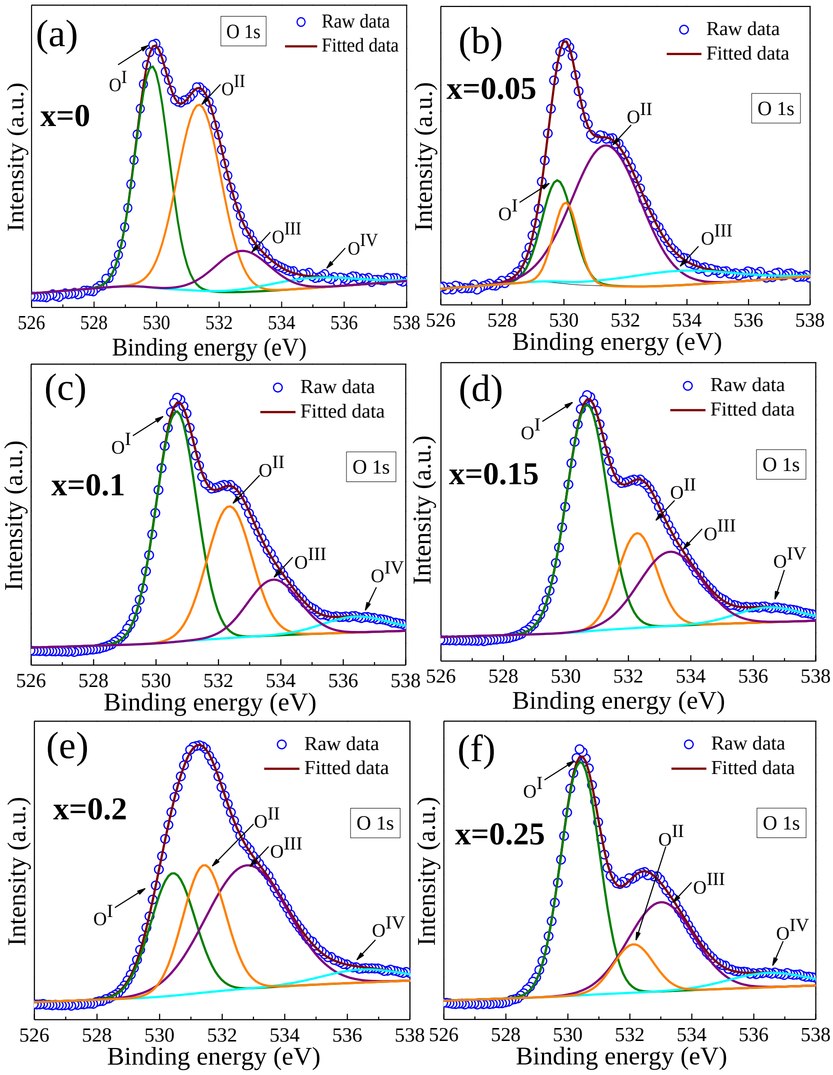

Figure 2.21: High-resolution spectra of O 1*s* (a) for 3C Fe_7S_8 and (b-f) for Gd-substituted iron sulphide samples as x = 0, 0.05, 0.1, 0.15, 0.2, and 0.25. The samples are labeled as x=0, 0.05, 0.1, 0.15, 0.2, and 0.25, corresponding to the Gd substitution percentage as 0, 5%, 10%, 15%, 20% and 25%, respectively.

2.3.4. Raman spectroscopy

Lattice strain and bond disorder may both be studied very effectively using Raman scattering. Raman spectroscopy at laboratory temperature (23 °C ± 2 °C) was recorded in the frequency range from 100 to 1500 cm^{-1} to under the laser of 632 nm wavelength (figure 2.22). The Raman spectra of all the samples were found to be similar, with a small variation in peak position and full-width at half-maximum (FWHM). Due to the lack of prior studies on the Raman spectra of 3C Fe_7S_8, which led us to conclude that this is the first study of its kind, we compared our results to those of 3C Fe_7Se_8, which crystallizes in the same $P3_121$ space group symmetry and 4C pyrrhotite. The Raman spectra of trigonal Fe_7S_8 revealed the strongest phonon bands ~218, 280 cm^{-1}, which are also characteristic peaks of pyrrhotite[48]. The data shows two A_{1g} (~218, 488 cm^{-1}) and three E_g (~280, 403, 602 cm^{-1}) Raman active modes. The small peak at ~ 602 cm^{-1} corresponds to the Fe-O bond[49]. The distinct peak at ~1300 cm^{-1} can be attributed to C=C from the oleylamine[41]. The peak ~1080 cm^{-1} may arise due to the asymmetric stretching of the S-O bond[49]. We found that both Raman peaks shift towards the higher wavelength with a dip at x=0.15, and then shift back to lower wavelength as the Gd concentration increases. This result leads to the conclusion that the lattice strain increases for Gd-substitution up to x= 0.15 and reduces for higher Gd concentrations. As with peak and higher doping concentration samples, the FWHM likewise exhibits the same substitution concentration (x=0.15) (figure 2.23).

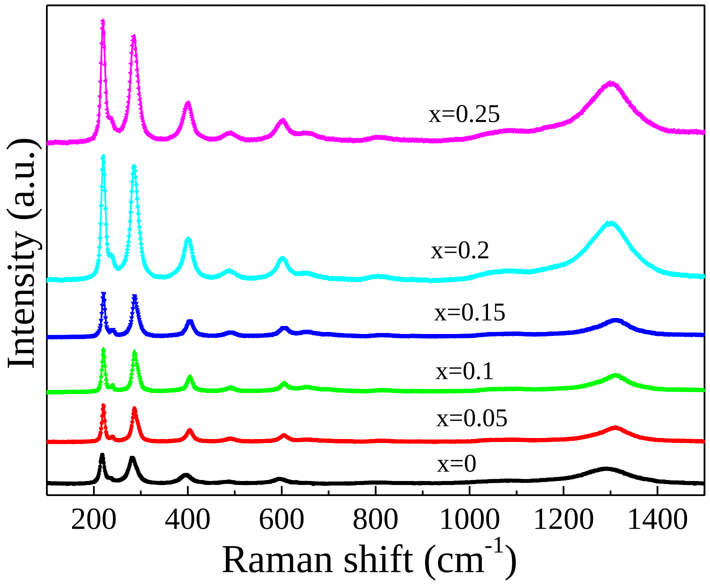

Figure 2.22: Raman shift of 3C Fe_7S_8 and for Gd-substituted iron sulphide samples plotted from 100-1500 cm^{-1} as x = 0, 0.05, 0.1, 0.15, 0.2, and 0.25. The samples are labeled as x=0, 0.05, 0.1, 0.15, 0.2, and 0.25, corresponding to the Gd substitution percentage as 0, 5%, 10%, 15%, 20% and 25%, respectively.

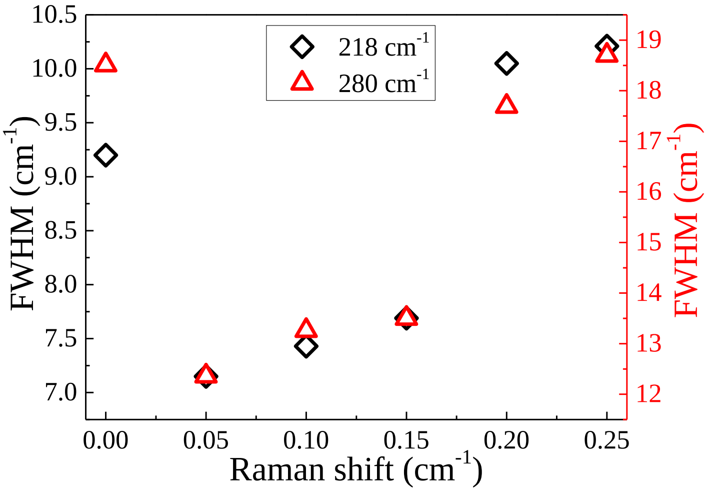

Figure 2.23: Variation of the FWHM of Raman modes of 218 cm-1 and 280 cm-1 in the Raman spectra for 3C Fe_7S_8 and Gd-substituted iron sulphide samples as x = 0, 0.05, 0.1, 0.15, 0.2, and 0.25. The samples are labeled as x=0, 0.05, 0.1, 0.15, 0.2, and 0.25, corresponding to the Gd substitution percentage as 0, 5%, 10%, 15%, 20% and 25%, respectively.

2.4. Conclusions

The trigonal 3C Fe_7S_8 were synthesized using the thermal decomposition method at the nanoscale. The trigonal phase was obtained after quenching the sample from a high temperature to the wet ice. The Gd-substituted samples, substituted in 5%, 10%, 15%, 20% and 20% concentration in the trigonal 3C Fe_7S_8 lattice are represented as x=0.05, 0.1, 0.15, 0.2, 0.20. All the Gd-substituted samples were synthesized using the similar pathway, used for the synthesis of 3C Fe_7S_8 nanoparticles.

The phase purity and crystallinity of all the samples were confirmed using PXRD. The reflection peaks match well with those of the JCPDS card number 710591. The crystallite size, estimated using the Scherrer's formula for all the samples, increase as the concentration of Gd is increased in the trigonal 3C Fe_7S_8 lattice. A shift towards the lower angle has been observed as the concentration of Gd-substitution in the lattice is increased, indicating the lattice expansion. Rietveld refinement was performed on all the as-synthesized samples. The lower values of χ^2 for all the samples indicate good fit. The lattice parameters, obtained after the refinement, increase with the increase in the concentration of Gd-substitution in the lattice.

The as-synthesized samples exhibit distorted hexagonal shaped morphology of variable size. However, the average particle size of the nanoparticles increases with the increase in the concentration Gd in the lattice. The presence of Fe^{2+}, Fe^{3+} and Gd^{3+} ions in all the as-synthesized samples were confirmed by the means of XPS analysis. Raman spectra indicate towards the lattice strain in the samples. The precise control over the tuning of morphology and the substitution of a foreign element to is subject to more vigorous research in this area.

References

1 B. D. Cullity, *Elements of X-ray diffraction, 2nd edition*, 1978.

2 F. Hamzaoui, M. Drissi, A. Chouaih, P. Lagant and G. Vergoten, *Int. J. Mol. Sci.*,

2007, 8, 103–115.

3 É. M. Moroz, X-ray diffraction method of the radial electron density distribution. Structure of nanophase supports and supported catalysts, *J. Struct. Chem.*, 2012, **53**, 63–85.

4 M. Drissi, A. Chouaih, Y. Megrouss and F. Hamzaoui, Electron Charge Density Distribution from X-Ray Diffraction Study of the 4-Methoxybenzenecarbothioamide Compound, *J. Crystallogr.*, 2013, **2013**, 326457.

5 Y. Tsubomoto, S. Hayashi, W. Nakanishi, L. K. Mapp and S. J. Coles, High-resolution X-ray diffraction determination of the electron density of 1-(8-PhSC(10)H(6))SS(C(10)H(6)SPh-8')-1' with the QTAIM approach: evidence for S(4) σ(4c-6e) at the naphthalene peri-positions., *RSC Adv.*, 2018, **8**, 9651–9660.

6 G. Artioli, ed. A. S. Gilbert, Springer Netherlands, Dordrecht, 2017, pp. 1019–1025.

7 F. Izumi, in *Applications of Synchrotron Radiation to Materials Analysis*, eds. H. Saisho and Y. B. T.-A. S. L. Gohshi, Elsevier, 1996, vol. 7, pp. 405–452.

8 T. Runčevski and C. M. Brown, The Rietveld Refinement Method: Half of a Century Anniversary, *Cryst. Growth Des.*, 2021, **21**, 4821–4822.

9 H. M. Rietveld, A profile refinement method for nuclear and magnetic structures, *J. Appl. Crystallogr.*, 1969, **2**, 65–71.

10 N. Sahu and S. Panigrahi, Mathematical aspects of Rietveld refinement and crystal structure studies on PbTiO3 ceramics, *Bull. Mater. Sci.*, 2011, **34**, 1495–1500.

11 L. B. McCusker, R. B. Von Dreele, D. E. Cox, D. Louër and P. Scardi, Rietveld refinement guidelines, *J. Appl. Crystallogr.*, 1999, **32**, 36–50.

12 M. R. Daymond, M. A. M. Bourke and R. B. Von Dreele, Use of Rietveld refinement to fit a hexagonal crystal structure in the presence of elastic and plastic anisotropy, *J. Appl. Phys.*, 1998, **85**, 739–747.

13 M. E. Fleet, The crystal structure of a pyrrhotite (Fe7S8), *Acta Crystallogr. Sect. B Struct. Crystallogr. Cryst. Chem.*, 1971, **27**, 1864–1867.

14 M Nishiguchi, Osaka University, 1977.

15 A. Nakano, M. Tokonami and N. Morimoto, Refinement of 3C Pyrrhotite, Fe7S8, *Acta Cryst.*, 1979, **35**, 724–725.

16 M. Kawaminami and A. Okazaki, Neutron Diffraction Study of Fe7Se8. II, *J. Phys. Soc. Japan*, 1970, **29**, 649–655.

17 A. Okazaki and K. Hirakawa, Structural Study of Iron Selenides FeSex. I Ordered Arrangement of Defects of Fe Atoms, *J. Phys. Soc. Japan*, 1956, **11**, 930–936.

18 E. F. Bertaut, Contribution à l’étude des structures lacunaires: la pyrrhotine, *Acta Crystallogr.*, 1953, **6**, 557–561.

19 H. Nakazawa and N. Morimoto, Phase relations and superstructures of pyrrhotite, Fe1−xS, *Mat. Res. Bull*, 1971, **6**, 345–358.

20 D. Koulialias, B. Lesniak, M. Schwotzer, P. G. Weidler, J. F. Löffler and A. U. Gehring, The Besnus Transition in Single-Domain 4C Pyrrhotite, *Geochemistry, Geophys. Geosystems*, 2019, **20**, 5216–5224.

21 D. Koulialias, R. Schäublin, G. Kurtuldu, P. G. Weidler, J. F. Löffler and A. U. Gehring, On the Magnetism Behind the Besnus Transition in Monoclinic Pyrrhotite, *J. Geophys. Res. Solid Earth*, 2018, **123**, 6236–6246.

22 C. S. Horng and A. P. Roberts, The Low-Temperature Besnus Magnetic Transition: Signals Due to Monoclinic and Hexagonal Pyrrhotite, *Geochemistry, Geophys. Geosystems*, 2018, **19**, 3364–3375.

23 Y. A. Koksharov, in *Magnetic Nanoparticles*, 2009, pp. 197–254.

24 P. Kattan, Ratio of Surface Area to Volume in Nanotechnology and Nanoscience.

25 I. Khan, K. Saeed and I. Khan, Nanoparticles: Properties, applications and toxicities,

Arab. J. Chem., 2019, **12**, 908–931.

26 A. T. Odularu, Metal Nanoparticles: Thermal Decomposition, Biomedicinal Applications to Cancer Treatment, and Future Perspectives., *Bioinorg. Chem. Appl.*, 2018, **2018**, 9354708.

27 G. Cotin, C. Kiefer, F. Perton, D. Ihiawakrim, C. Blanco-Andujar, S. Moldovan, C. Lefevre, O. Ersen, B. Pichon, D. Mertz and S. Bégin-Colin, Unravelling the Thermal Decomposition Parameters for The Synthesis of Anisotropic Iron Oxide Nanoparticles., *Nanomater. (Basel, Switzerland)*, , DOI:10.3390/nano8110881.

28 M. Unni, A. M. Uhl, S. Savliwala, B. H. Savitzky, R. Dhavalikar, N. Garraud, D. P. Arnold, L. F. Kourkoutis, J. S. Andrew and C. Rinaldi, Thermal Decomposition Synthesis of Iron Oxide Nanoparticles with Diminished Magnetic Dead Layer by Controlled Addition of Oxygen., *ACS Nano*, 2017, **11**, 2284–2303.

29 S. Daengsakul, C. Mongkolkachit, C. Thomas, S. Siri, I. Thomas, V. Amornkitbamrung and S. Maensiri, A simple thermal decomposition synthesis, magnetic properties, and cytotoxicity of La0.7Sr0.3MnO3 nanoparticles, *Appl. Phys. A*, 2009, **96**, 691–699.

30 S. Prasad, A. Vijayalakshmi and N. S. Gajbhiye, Synthesis of Ultrafine Cobalt Ferrite by Thermal Decomposition of Citrate Precursor, *J. Therm. Anal. Calorim.*, 1998, **52**, 595–607.

31 U. Holzwarth and N. Gibson, The Scherrer equation versus the ‘Debye-Scherrer equation’, *Nat. Nanotechnol.*, 2011, **6**, 534.

32 C. R. Lin, S. Z. lu, I. S. Lyubutin, yu V. Korzhetskiy, S. C. Wang and I. P. Suzdalev, Synthesis and magnetic properties of iron sulfide nanosheets with a NiAs-like structure, *J. Appl. Phys.*, 2010, **107**, 547.

33 F. Keller-Besrest, G. Collin and R. Comès, Structure and planar faults in the defective

NiAs-type compound 3c Fe7S8, *Acta Crystallogr. Sect. B*, 1983, **39**, 296–303.

34 P. Jiang, J. C. Neuefeind, M. Avdeev, Q. Huang, M. Yue, X. Yang, R. Cong and T. Yang, Unprecedented lattice volume expansion on doping stereochemically active Pb2+ into uniaxially strained structure of CaBa1−xPbxZn2Ga2O7, *Nat. Commun.*, 2020, **11**, 1303.

35 M. Coduri, S. Checchia, M. Longhi, D. Ceresoli and M. Scavini, *Front. Chem.* , 2018, 6.

36 B. H. Toby, R factors in Rietveld analysis: How good is good enough?, *Powder Diffr.*, 2006, **21**, 67–70.

37 M. K. Anupama and B. Rudraswamy, Effect of Gd3+- Cr3+ ion substitution on the structural, electrical and magnetic properties of Ni - Zn ferrite nanoparticles, *IOP Conf. Ser. Mater. Sci. Eng.*, 2016, **149**, 12194.

38 R. H. Kadam, R. B. Borade, M. L. Mane, D. R. Mane, K. M. Batoo and S. E. Shirsath, Structural, mechanical, dielectric properties and magnetic interactions in Dy3+-substituted Co–Cu–Zn nanoferrites, *RSC Adv.*, 2020, **10**, 27911–27922.

39 M. Sen Bishwas, R. Das and P. Poddar, Large Increase in the Energy Product of Fe 3 Se 4 by Fe-Site Doping.

40 M. Malik, P. Padhye and P. Poddar, Graphene Quantum Dots-Driven Multiform Morphologies of β-NaYF4:Gd3+/Tb3+ Phosphors: The Underlying Mechanism and Their Optical Properties, *ACS Omega*, 2018, **3**, 1834–1849.

41 S. Mourdikoudis and L. M. Liz-Marzán, Oleylamine in Nanoparticle Synthesis, *Chem. Mater.*, 2013, **25**, 1465–1476.

42 T. Tadros, ed. T. Tadros, Springer Berlin Heidelberg, Berlin, Heidelberg, 2013, p. 820.

43 A. Fujimoto, Y. Yamada, M. Koinuma and S. Sato, Origins of sp3C peaks in C1s X-ray Photoelectron Spectra of Carbon Materials, *Anal. Chem.*, 2016, **88**, 6110–6114.

44 J. Y. Y. Loh and N. P. Kherani, X-ray photospectroscopy and electronic studies of reactor parameters on photocatalytic hydrogenation of carbon dioxide by defect-laden indium oxide hydroxide nanorods, *Molecules*, 2019, **24**, 1–11.

45 M. G. and P. Poddar, Remarkable Effect of Fe and Se Composition on Magnetic Properties─Comparative Study of the Fe–Se System at the Nanoscale, *J. Phys. Chem. C*, 2022, **9**, 4655–4663.

46 R. A. Berner, Global biogeochemical cycles of carbon and sulfur and atmospheric O2 over phanerozoic time, *Chem. Geol.*, 1990, **84**, 159.

47 D. Briggs, Handbook of X-ray Photoelectron Spectroscopy C. D. Wanger, W. M. Riggs, L. E. Davis, J. F. Moulder and G. E.Muilenberg Perkin-Elmer Corp., Physical Electronics Division, Eden Prairie, Minnesota, USA, 1979. 190 pp., *Surf. Interface Anal.*, 1981, **3**, v–v.

48 Q. He, K. Rui, J. Yang and Z. Wen, Fe7S8 Nanoparticles Anchored on Nitrogen-Doped Graphene Nanosheets as Anode Materials for High-Performance Sodium-Ion Batteries, *ACS Appl. Mater. Interfaces*, 2018, **10**, 29476–29485.

49 N. Buzgar, A. Buzatu and I. V. Sanislav, The Raman study on certain sulfates, *Analele Stiint. ale Univ. ‘ Al. I. Cuza’ din Iasi , Geol.*, 2009, **55**, 5–23.

Chapter 3

Study of magnetism in 3C Fe_7S_8 and Gd-substituted 3C Fe_7S_8 nanoparticles

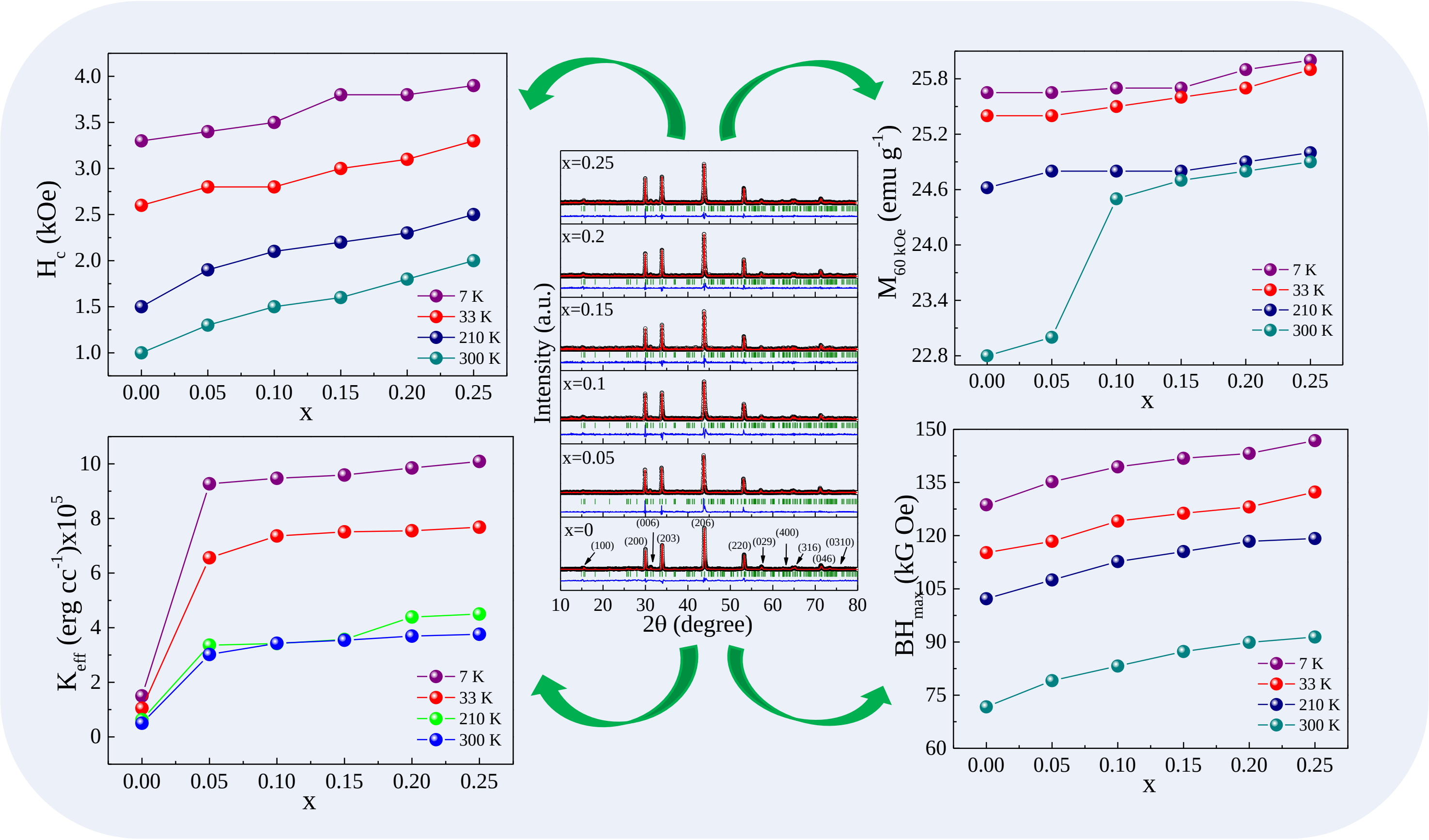

Highlights

Below are some of the findings that we would like to highlight.

- The ZFC and FC magnetization data, recorded at 100 Oe and 1000 Oe, reveal magnetic ordering with high T_C (above 300 K) in all the samples.
- The hysteresis curves measured at different temperatures (7 K, 33 K, 210 K, and 300 K) show the ferrimagnetic behavior of 3C Fe_7S_8 nanoparticles and Gd-substituted 3C iron sulphide nanoparticles.
- The magnetic parameters— coercivity (H_C), magnetization ($M_{60\ kOe}$), the effective anisotropy constant (K_{eff}), and the maximum energy product (BH_{max}) appear to increase as the measuring temperature is lowered down. With the increase in the concentration of Gd, these values of H_C and K_{eff} increase as the measurement temperature is lowered down.
- The highest value of BH_{max} is possessed by unsubstituted 3C Fe_7S_8 nanoparticles at 7 K. The high value of BH_{max} at a lower temperature signifies that the compound may be considered for low-temperature industrial applications.

Keywords: Iron sulphide, ferrimagnetism, energy product, magnetocrystalline anisotropy

3.1. Introduction

Due to the fascinating and peculiar thermal, electrical, optical, and magnetic properties, iron sulphides (Fe-S) have attracted a lot of attention lately[1–5]. The Fe-S system exhibits a number of stable polymorphs under ambient conditions, including FeS, FeS_2, 4C Fe_7S_8 (monoclinic NiAs-type), 3C Fe_7S_8 (hexagonal NiAs-type), and others[6–14]. These compounds could be metal, semiconductors, or superconductors depending on the composition of Fe:S, and their magnetic characteristics can range greatly from antiferromagnetic to ferro- to ferrimagnetic[15–18]. Recent research has revealed that the bulk form of 3C Fe_7S_8, which is naturally occurring metastable phase of 4C Fe_7S_8, exhibits ferromagnetic ordering[19,20]. There is, however, scant information in the literature about the magnetic characteristics of the compound in different phases. The physical and chemical properties of materials can be further tuned in their nanoscopic forms.

Based on a deep literature survey, we believe that the 3C Fe_7S_8 pyrrhotite has not been studied intensively as its single crystal and the bulk phase and the magnetic ordering of the compound is still not fully understood. There is no report on the synthesis of the compound in the nano phase. However, an equivalent phase, 3C Fe_7Se_8, as reported by Okazaki & Hirakawa (1956), has the $P3_121$ symmetry[21,22] as well. The magnetic moments[14] of the Fe ions in 3C Fe_7Se_8 are parallel to one another (ferromagnetic ordering of moments), while the magnetic moments in the adjacent *c*-plane are antiparallel (antiferromagnetic ordering of moments). As a result, 3C Fe_7Se_8 exhibits ferrimagnetic ordering[23] due to a net spontaneous moment below the ordering temperature brought on by a deficiency of Fe ions[14,24] in alternating layers. At room temperature (RT), where the Curie temperature (T_C) is ~453 K, 3C Fe_7Se_8 exhibits ferrimagnetic nature in both its bulk and nanostructured forms[21]. Based on the structural similarity[14,20,22] between 3C Fe_7Se_8 and 3C Fe_7S_8, the 3C pyrrhotites are known to exhibit ferrimagnetism[22].

Permanent magnets are widely used in devices including loudspeakers, rotors, printers, phones, televisions, cars, and more[25–28]. The Fe-Nd-B[29] class of permanent magnets, with energy-product values ranging from 20 MGOe to more than 50 MGO, is the most effective class of magnets currently known. Ordinary rare-earth hard magnets have been used extensively worldwide up until this point. There has been substantial rare-earth mining because of the increase in demand for Fe-Nd-B magnets, which are utilised in permanent magnets. Due to the radioactive compounds[30,31], they contain, these minerals can be relatively expensive to mine and can be hazardous. It is well known that $Nd_2Fe_{14}B$ is the perfect hard magnetic material[32,33]. The scope of replacing it with a rare-earth-free material and keeping the same energy-product is currently thin. However, rare-earth free permanent magnetic materials, which are reasonably cost-effective and non-toxic to produce, may be able to replace rare-earth magnets for a number of applications. However, there is very little probability of obtaining a high energy-product without employing a rare earth ion. The room-temperature ferromagnetic phase of MnBi is recognized to be a viable candidate among the rare-earth free magnetic materials[34], with a high anisotropy constant. The low melting point of Bi and high vapour pressure[35] of Mn, however, make its processing difficult. FePt exhibits a high energy product and large uniaxial magnetocrystalline anisotropy[36], however, owing to the presence of platinum makes it expensive for its mass production. Among chalcogenides, Fe_3Se_4 has been studied for the application for rare-earth free magnetic material[37], however, the low saturation magnetization of this compound causes its energy-product to be low.

The maximum energy-product, (BH_{max}), is the most imperative figure of merit for the hard-magnets[38]. The maximum area of the rectangle under the B-H curve in the second quadrant of the B-H hysteresis loop is used to determine the maximum energy-product (BH_{max}), which is a measure of the magnetic energy stored in the material. The maximum energy product is defined as follows:

$$BH_{max} = \frac{1}{4}\mu_0 M_S^2 \tag{3.1}$$

where M_S is the saturation magnetization, and μ_0 is the magnetic permeability of free space. According to the aforementioned equation, M_S plays a crucial role in determining the energy product of the material.

Substitution is well known to be one of the effective routes to modulate various physical properties of nanoparticles, such as— optical, electrical, magnetic properties. It is well known that the transition metals such as— Co, Ni, Mn, and Pt are efficient dopants[39–42] of magnetic nanoparticles with the potential to enhance their magnetic characteristics. However, a rare-earth element has a far greater potential for displaying strong magnetic characteristics[43,44] than a transition metal because of the substantial unquenched orbital angular momentum attributed to the *f*-electrons[45] that exhibit higher spin-orbit coupling. The orbital component of the magnetic moment is significantly larger for the rare-earth ions than the transition metal ions, as the crystal-field effects are less and spin-orbit coupling is stronger for *f*-electrons of transition metal ions than for *d*-electrons. Additionally, materials manufactured from these elements have the potential to display useful magnetic properties due to the unique *f*-electronic structure of metals in the rare-earth series. Rare earth elements comprise of 15 kinds of lanthanide elements ranging from lanthanum to lutetium in the periodic table. In recent decades, the development of lanthanides-based nanomaterials[46–48] with novel optical, electrical and magnetic properties has been an emerging research field. Due to their partially occupied 4*f* electronic state, the substitution of rare-earth ions in the fundamental structure offers distinctive optical, electrical, and magnetic properties, thereby modulating the structural disorder and lattice strain in the structure. The large magnetic moment of the Gd ion, which results from the partially occupied 4*f* electronic state (figure 3.1), as well as its outstanding magnetic characteristics, make it particularly intriguing.

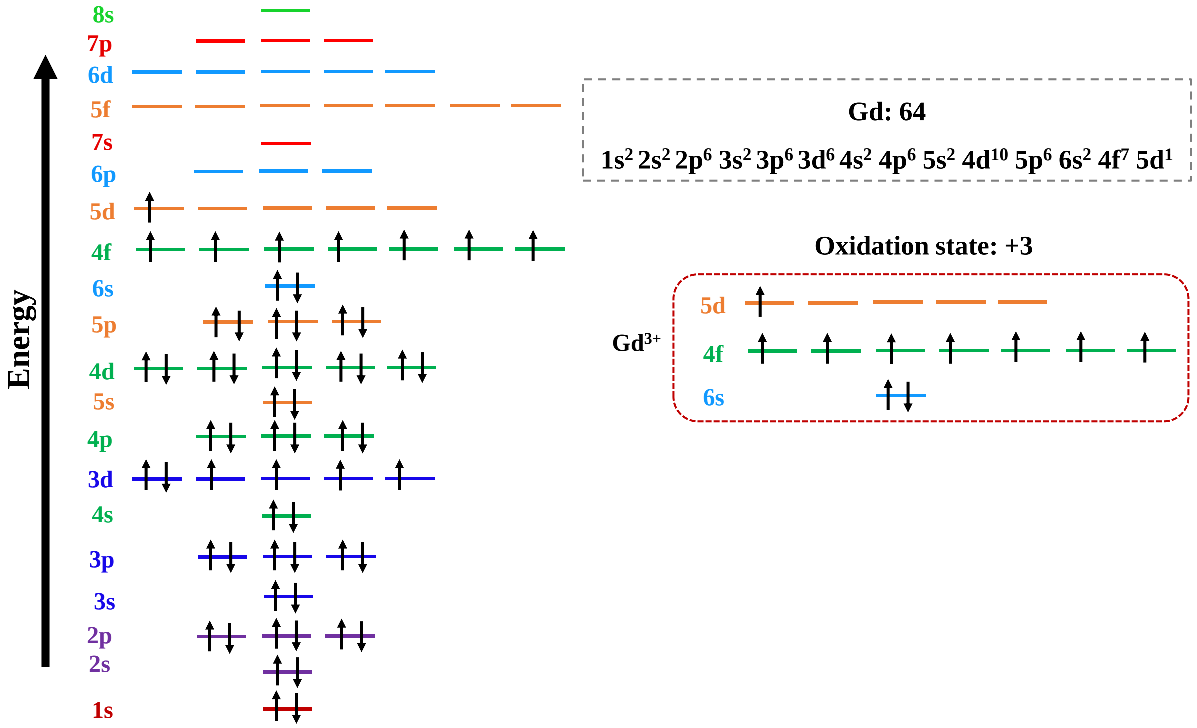

Figure 3.1: Schematic illustration of the electronic configuration of gadolinium with +3 oxidation state.

Unfortunately, there has been no information in the literature on the modification of trigonal iron sulphide in bulk or nano phases upon the addition of a transition metal or a rare-earth ion. Therefore, it will be intriguing and interesting to study the modification in the magnetic properties of 3C Fe_7S_8 nanoparticles and the Gd-substituted 3C Fe_7S_8, owing to the ferrimagnetic ordering in the compound and high value of magnetic moment of Gd ion. We have introduced Gd ions using the thermal decomposition method to synthesize Gd-substituted trigonal phase of iron sulphide nanoparticles. The substitution was made in 5%, 10%, 15%, 20% and 25% concentration of Gd ions in the parent compound, represented in the thesis throughout as x= 0.05, 0.1, 0.15, 0.2, and 0.25, respectively. The single phase 3C Fe_7S_8 is represented as x= 0. By contrasting the various magnetic properties of all the as-synthesized samples, this chapter discusses the fundamental ideas of magnetic ordering in the compound and its attributes. The net ferrimagnetic moment of the system was shown to be favorably influenced by the substitution with Gd ions. By substituting Gd ions, we found that the magnetization of 3C Fe_7S_8 nanostructures, measured at 60 kOe, increased significantly.

3.2. Characterization techniques

The magnetic measurements were performed using the Physical Property Measurement System (PPMS) manufactured by Quantum Design Inc., San Diego, California, equipped with a vibrating sample magnetometer (VSM) and superconducting magnet. The powder samples were precisely weighed and packed inside a plastic sample holder, which fits into a brass sample holder provided by Quantum Design Inc. with a negligible contribution to an overall magnetic signal. The magnetization versus temperature (M−T) measurements in zero-field- cooled (ZFC) and field-cooled (FC) modes was performed at a temperature sweep from 7 K to 300 K in a field of 100 Oe and 1000 Oe using the VSM attachment. The magnetization versus field (M–H) loops were collected at a rate of 50 Oe s-1 in a field sweep from ±60 kOe at the vibrating frequency of 40 Hz.

3.3. Results and discussion

In Chapter 2, the 3C Fe_7S_8 and Gd-substituted 3C Fe_7S_8 compounds were synthesized *via* thermal decomposition method. The discussion in Chapter 2 demonstrates that the as-synthesized phases are single phase and devoid of any secondary phases within the detection limit of laboratory XRD. The morphology of phase appears to be distorted hexagonal for all samples. All the Gd-substituted samples were found to have +3 oxidation state of Gd according to XPS measurements.

A schematic representation of an electronic configuration of iron is shown in figure 3.2. Iron is most likely to be in the +2 and +3 oxidation states. Figure 3.2 depicts the outermost shell electronic configuration of Fe^{2+} and Fe^{3+}. In Fe^{2+} there are four and in Fe^{3+} there are five unpaired electrons.

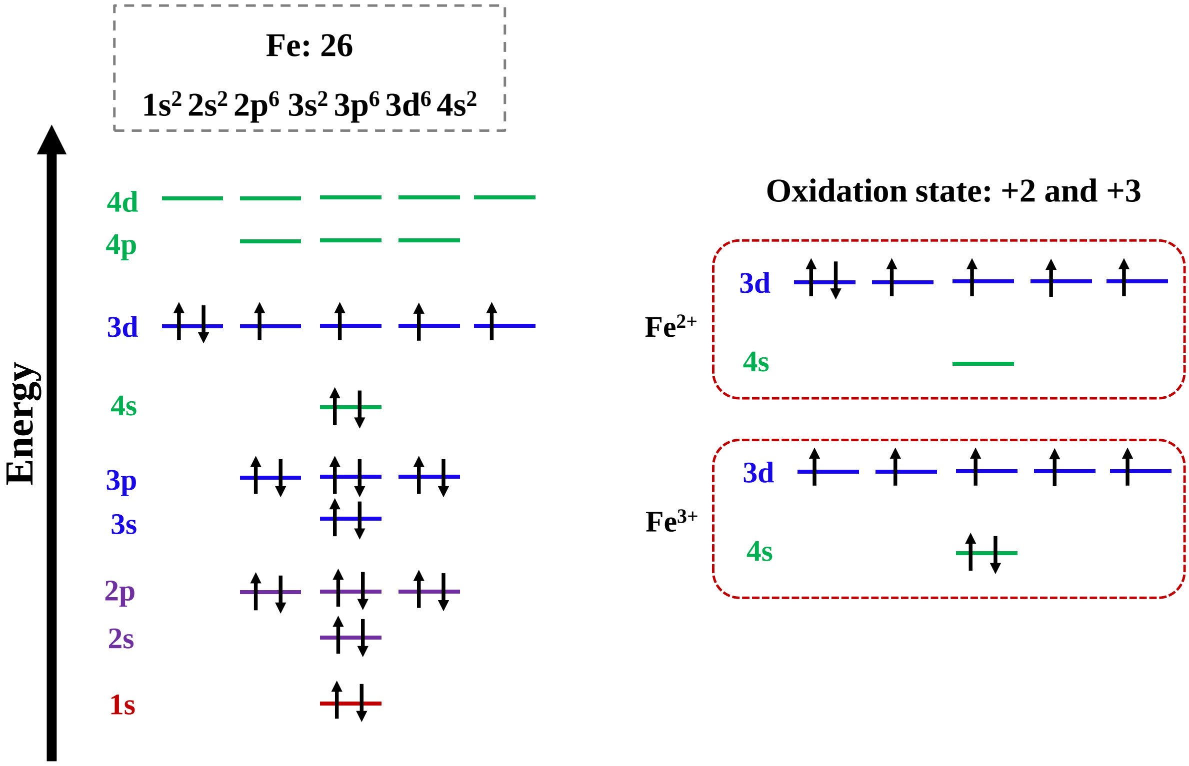

Figure 3.2: Schematic illustration of the electronic configuration of iron with two oxidation states, Fe^{2+} and Fe^{3+}.

3.3.1. Magnetic properties of 3C Fe_7S_8 nanoparticles

In the NiAs-type crystal structures of 3C Fe_7S_8, the cations are octahedrally coordinated by six anions (FeS6 octahedra), and the coordination polyhedron of the anions is a trigonal prism produced by six cations (SFe6 prisms)[49]. Two different forms of Fe ionic states, Fe^{2+} and Fe^{3+}, as well as ordered Fe vacancies[14,49], can be found in $Fe_{1-x}S$ compounds. The magnetic behaviour of the compounds is produced by these configurations[21,24]. The compound exhibits overall ferrimagnetic behavior because each layer is of the ferromagnetic order in the opposite direction from the adjacent layer. In the $Fe_{1-x}S$ system, figure 3.3(a,b) depicts the crystal field splitting (CFS) of the *d*-orbitals into the 3-fold t_{2g} and 2-fold e_g states of 3*d* Fe cations (Fe^{2+}/Fe^{3+}). The octahedrally coordinated Fe^{2+} and Fe^{3+} ions have 4 and 5 unpaired electrons, respectively. Figure 3.3c depicts the CFS of the *d*-orbitals at the tetrahedral site into 3*d* Fe cations (Fe^{3+}) in the $Fe_{1-x}S$ system in 2-fold e_g and 3-fold t_{2g} states.

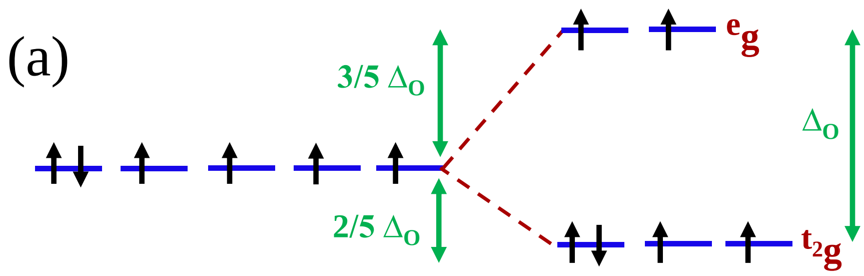

Fe^{2+} in octahedral coordination

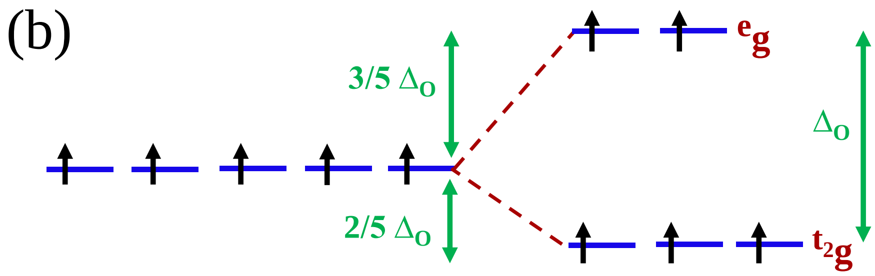

Fe^{3+} in octahedral coordination

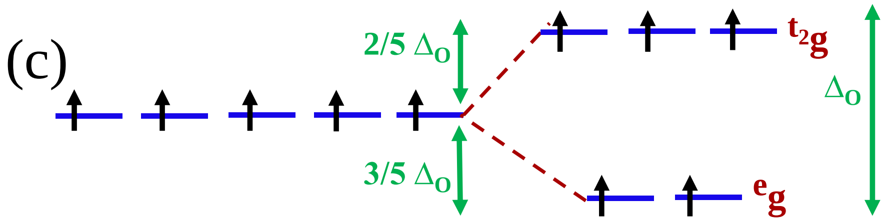

Fe^{3+} in tetrahedral coordination

Figure 3.3: (a) and (b) Crystal field splitting (CSF) of the 3*d*-orbitals of Fe cations (Fe^{2+}/Fe^{3+}) at the octahedral site into 3-fold t_{2g} and 2-fold e_g states, (c) at the tetrahedral site (Fe^{3+}) into 2-fold e_g and 3-fold t_{2g} states in the $Fe_{1-x}S$ system.

The Fe ions are coupled together. Their shared S ion facilitates the localised electronic orbital overlap on the Fe ion sites. Therefore, exchange interactions are present in these molecules *via* their common S ion. Figure 3.4 illustrates the superexchange interaction in Fe^{3+}

octahedron-octahedron in the $Fe_{1-x}S$ compounds.

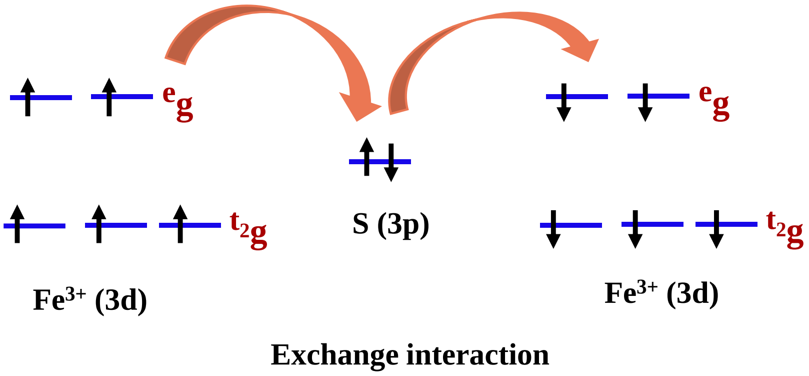

Figure 3.4: $Fe_{1-x}S$ exhibits the exchange interactions: the overlap of localized electronic orbitals on Fe ion sites is mediated through their common S ion.

The basic building block of $Fe_{1-x}S$ superstructures with cation vacancies is the NiAs-type crystal structure. The crystal structure of the 3C Fe_7S_8 ($Fe_5^{2+}Fe_2^{3+}S_8^{2-}$) is hexagonal NiAs-type. The compound displays the $P3_121$ space group, with lattice parameters a = 6.8652±0.0006 Å, c = 17.047±0.002 Å.

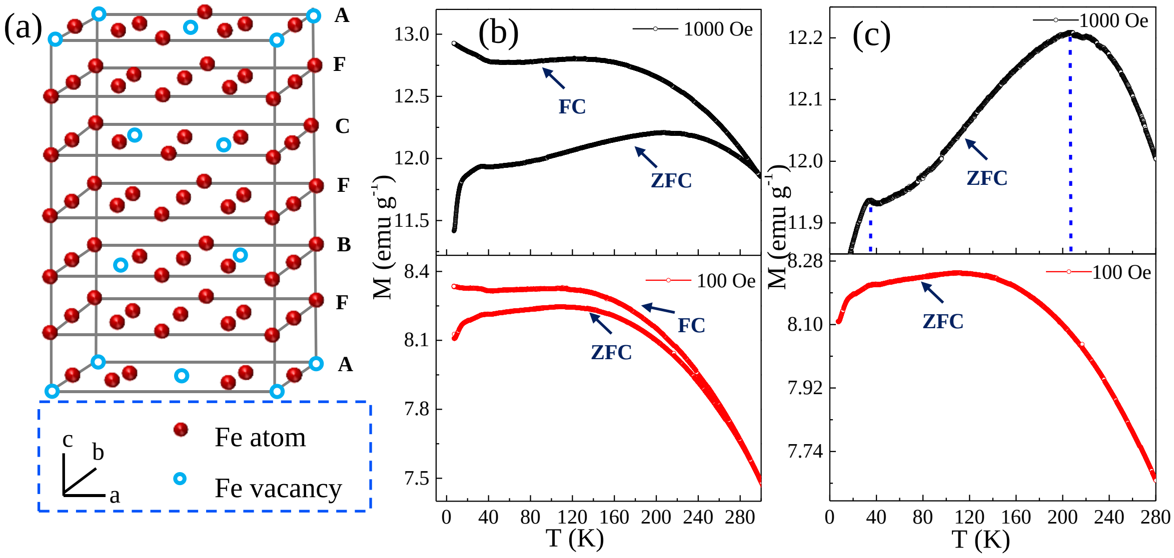

Figure 3.5: (a) Schematic of the unit cell of 3C Fe_7S_8, solid red spheres represent the Fe cations, the open blue circles represent Fe cation vacancies, S sites are omitted for the clarity, (b) Zero-field-cooled (ZFC) and field-cooled (FC) magnetization *vs.* temperature (M-T)

curves for the sample 3C Fe_7S_8 nanoparticles at 1000 Oe (black curve) and 100 Oe (red curve), (b) ZFC M-T curves for the sample 3C Fe_7S_8 at applied external fields of 1000 Oe and 100 Oe in the temperature range of 7-300 K.

As already mentioned, the magnetic properties of the 3C Fe_7S_8 compound are not clearly discussed in the earlier reports. Hence, to investigate the magnetic properties of the as-synthesized 3C Fe_7S_8 nanoparticles, the ZFC-FC M-T measurements have been recorded using SQUID-VSM. Figure 3.5a shows the ZFC-FC M-T curves obtained for as-synthesized 3C Fe_7S_8 nanoparticles at the applied magnetic field of 100 Oe and 1000 Oe, respectively. The ZFC and FC *M-T* curves are split in the temperature range from 7 to 300 K. Without using an external magnetic field, the sample is first cooled to 7 K in the ZFC procedure. After applying the magnetic field (100 Oe or 1000 Oe), the magnetization is measured for increasing temperature till 300 K. In the same magnetic field, in the FC process, the magnetization is recorded for decreasing temperature till 7 K. The M-T curves show that the ZFC and FC curves do not follow the same path. Hence, in each case (100 and 1000 Oe), the M-T curves show an irreversible behavior. The emergence of an ordered magnetic state with a high T_C of the sample above 300 K is shown by the divergence of the ZFC-FC M-T curves of 3C Fe_7S_8 over the entire range of temperature up to 300 K. The magnetization and shapes of ZFC and FC curves at a specific field strength are strongly influenced by the magnetic anisotropy[50]. The spins are aligned in a preferred direction by magnetic anisotropy. The spins are locked in random directions throughout the ZFC process as the sample is cooled down without a magnetic field being applied. The resultant magnetization depends on the anisotropy of the system when an external field is applied[50] at the lowest temperature (7 K). To rotate the spins in the direction of the applied magnetic field in a highly anisotropic system, a large anisotropic field is necessary, leading to a small magnetization. Because the spins are locked in a specific direction, dependent on the magnetic field strength during the

FC process, the magnetization increases as the temperature decreases[50].

The interparticle interaction, particle size, anisotropy energy, and measurement time scale influence the blocking temperature[51] (T_B). The spins freeze and orient randomly above T_B because the thermal activation energy is now greater than the effective anisotropy energy. Spins, however, freez in the direction of their easy axis below T_B.

The sample exhibits coercivity below T_B and becomes zero above T_B. As shown in the TEM images, the as-synthesized nanoparticles are agglomerated as many nanocrystallites; hence the average blocking temperature (T_B) is considered as the peak of the ZFC curve[50,51]. Polydispersity in the sample may cause the blocking phenomena for each particle on each side of the ZFC peak, resulting in the bifurcation of the ZFC-FC curve above T_B. Figure 3.5b shows the T_B for the sample as 210 K at 1000 Oe applied magnetic field. However, there is no noticeable peak in the ZFC curve at 100 Oe. Hence, now the question is to consider how the energy barrier (the temperature where the ZFC curve exhibits a maximum) disappears as the external magnetic field is decreased to 100 Oe. The applied magnetic field, interparticle interaction, magnetic anisotropy energy, and thermal activation energy impact the blocking phenomena of the spins. Magnetic moment of each particle is parallel to the easy axis and separated from its antiparallel direction by an energy barrier[38,52], K_uV. The easy axes of the particles are randomly oriented when there is no applied magnetic field, and the system has no net magnetization. The energy barrier shifts[51] from K_uV to $K_uV[1 \pm (H/H_o)]^2$ when an external magnetic field (H) lower than the anisotropic field (Ha) is applied, where K_u and V are the uniaxial anisotropy constant and the particle volume, respectively. The formula for H_o is $H_o=2H_a=2K_u/M_S$. A moment flip from parallel to antiparallel is represented by the (+) sign, and a moment flip from antiparallel to parallel by the (-) sign. The ZFC curves of the specimen at 100 and 1000 Oe magnetic fields are shown in figure 3.5b. A peak appears at ~210 K at a higher applied magnetic field (1000 Oe) and diminishes as the magnetic field is reduced to 100 Oe. The argument discussed above is also supported by the fact that T_B depends directly on anisotropy energy. With the decrease in the anisotropy energy, a decrease in T_B will also be observed. This again explains the shape of ZFC-FC curves obtained at 1000 Oe and 100 Oe. Another low-temperature magnetic transition is observed at ~33 K. The structure of 3C pyrrhotite with space group $P3_121$ resembles that of the 4C structure[14,22,24] in the sense that vacancies are confined to alternate layers of iron. Powder samples of 4C pyrrhotite show an anomaly at low-temperature ~30-34 K (known as Besnus transition[19,20,53,54]). This low-temperature magnetic transition stems from the spin rotation[19,20], which can be related to the structural changes at an atomic level caused by the highly ordered vacancies in 4C pyrrhotite, which in turn affect the spin-orbit coupling with no crystallography change of the structure. Assuming the similar spin arrangements in 3C and 4C pyrrhotites, the low-temperature magnetic transition observed at ~33 K at 1000 Oe applied magnetic field (Figure 3.5b) for as-synthesized 3C pyrrhotite may be assigned as the Besnus transition.

To acquire further insights into the magnetic properties of the 3C Fe_7S_8 nanoparticles, the M-H curves were measured using a SQUID-VSM. Figure 3.6(a-d) shows M-H hysteresis curves taken at 7, 33, 210 K, and 300 K in the magnetic field range of ±60 kOe because of the anomalies observed at these temperature values in M-T graphs (figure 3.5b).

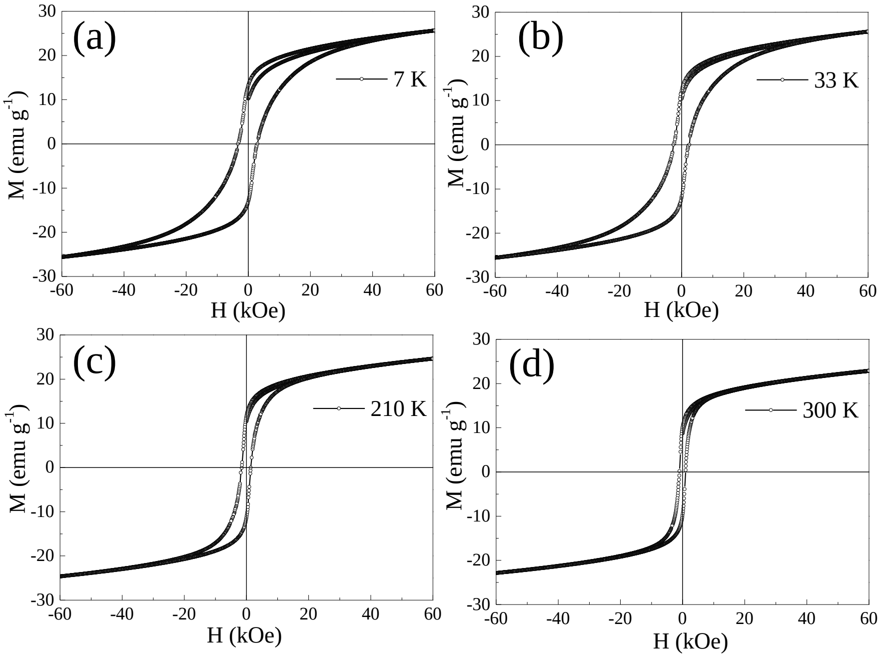

Figure 3.6: (a-d) Magnetization vs. external magnetic field (M-H) hysteresis loops of the sample 3C Fe_7S_8 nanoparticles at 7 K, 33 K, 210 K and 300 K. The M-H hysteresis loops illustrate the increase in $M_{60\ kOe}$, H_C, and M_R values of the sample with decrease in temperature.

As shown in Figure 3.6(a-d), the sample demonstrates ferrimagnetic-like behavior at all measurement temperatures. However, at the maximum applied magnetic field of 60 kOe, the magnetization did not exhibit saturation. Such behavior indicates that the spins of the system require a high anisotropic field to align in a particular direction. We observed an initial remanence in the sample at all measurement temperatures. Remanence comes from the vacancies in the specimen. The presence of initial remanence in the M-H hysteresis loop may be attributed to the induced magnetization due to the Fe vacancies in a powdered polycrystalline sample. The hysteresis curves illustrate that H_C, $M_{60\text{ kOe}}$, and M_R values of the sample increase with a decrease in temperature. Among all four measurement temperature values, the 3C Fe_7S_8 NPs appear to exhibit hysteresis with H_C ~1.0 kOe, $M_{60\text{ kOe}}$, ~23 emu g^{-1}, and M_R ~10 emu g^{-1} at 300 K, which increases to H_C ~3.0 kOe, $M_{60\text{ kOe}}$, ~26 emu g^{-1},and M_R

~13 kOe at 7 K (table 3.1).

Table 3.1: Summary of the magnetic parameters calculated for the sample 3C Fe_7S_8 nanoparticles at different measurement temperatures.

Measurement temperature (K)	**H_C (kOe)**	**M_R (emu g^{-1})**	**$M_{60\ kOe}$ (emu g^{-1})**	**M_R/M_S**	**H_a (kOe)**	**K_{eff} (erg cc^{-1}) $\times 10^5$**	**BH_{max} (kG Oe)**
7	3.3	13.1	25.65	0.510	11.7	1.50	128.7
33	2.6	12.3	25.60	0.480	8.2	1.05	115.2
210	1.5	11.5	24.62	0.467	5.1	0.63	102.2
300	1.0	10.0	22.80	0.439	4.4	0.50	71.7

The decrease in thermal activation energy and the rise in total effective magnetic anisotropy, which creates more spins available to align in the direction of the applied magnetic field, may have contributed to the increase in these values at the lower temperature[51,55]. Fe^{2+} and Fe^{3+} ionic states, as well as ordered Fe vacancies, are present in the $Fe_{1-x}S$ compounds in addition to alternate levels of the lattice. The magnetic moments of Fe in the compound are ferromagnetically arranged inside each layer but are coupled antiferromagnetically to each other between adjacent layers. The vacancies in every second layer contribute to the spin orientation. The presence of ionic states of iron and the vacancies in the lattice lead to uncompensated magnetic moments, giving rise to the ferrimagnetic ordering in the compound. The neutron diffraction of the compound is still awaited. However, in the equivalent phase[22], 3C Fe_7Se_8, the moments of Fe ions are in *c*-plane are parallel to one another (ferromagnetic ordering of moments), whereas the moments of Fe ions in the adjacent *c*-plane are antiparallel (antiferromagnetic ordering of moments). Thus, owing to a net spontaneous moment caused by the uncompensated moments below the ordering temperature, 3C Fe_7Se_8 possesses ferrimagnetic ordering, which further suggests the 3C pyrrhotite exhibits ferrimagnetic ordering.

For a polycrystalline powdered sample, calculation of the magnetic anisotropy constant (K) is not simple as it is composed of several agglomerated nanocrystallites (shown in the TEM image in chapter 2). Therefore, the orientation of the powdered sample along one easy axis and subsequently the hard axis is not as straightforward as it may be for a single crystal in VSM. The magnetic anisotropy of any materials is its intrinsic property. Therefore, calculation of K from the measured hysteresis loop of the particles in the specimen of the sample will give the effective magnetic anisotropy (K_{eff}) of all the particles oriented in random directions. The ordered Fe vacancies in 3C Fe_7S_8 structure brings about a highly anisotropic crystal field and spin-orbit coupling, which in turn greatly increases the magnetocrystalline anisotropy[51] of the system. The field necessary to saturate the magnetization in the hard direction is known as the anisotropy field (H_a). The value of K_{eff} at all temperatures is calculated from Ms and Ha using the following equation.

$$K_{eff} = \frac{1}{2} M_S H_a \tag{3.2}$$

The value of K_{eff} is 0.5×10^5 erg cc^{-1} at 300 K, which increases to 1.5×10^5 erg cc^{-1} at 7 K (table 3.1). To determine the type of magnetocrystalline anisotropy, ln (K_{eff}) is plotted against ln ($M_{60\ kOe}$), as shown in figure 3.7. For a system with uniaxial magnetocrystalline anisotropy[38], K_{eff} should be proportional to $M_{60\ k\ Oe}{}^{3}$, whereas for a cubic magnetocrystalline anisotropy, K_{eff} should be proportional to $M_{60\ kOe}{}^{10}$. The linear fit of the plot gives a slope of 7.2, indicating that the sample predominantly exhibits uniaxial anisotropy.

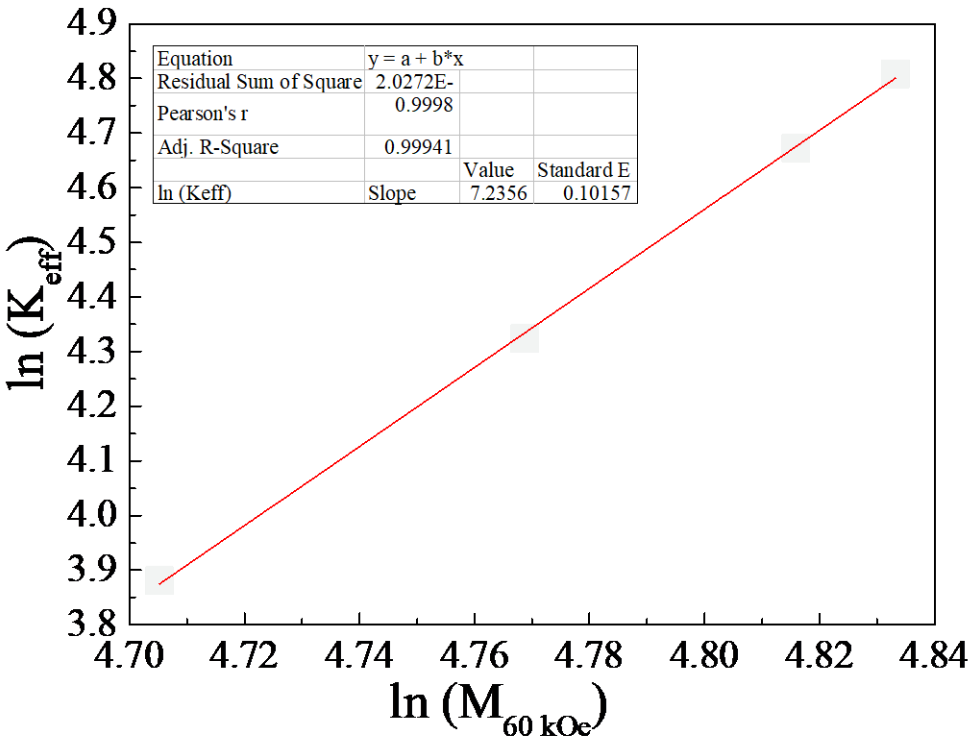

Figure 3.7: Linear relationship between K_{eff} and $M_{60\ kOe}$ in the logarithmic scale, with a slope of 7.2, indicating that the sample predominantly exhibits uniaxial anisotropy.

The maximum area of the rectangle under the B-H curve in the second quadrant of the B-H hysteresis loop is used to determine the maximum energy-product (BH_{max}), which is a measure of the magnetic energy stored in the material[38] (figure 3.8(a-h)). The BH_{max} for all the samples is estimated using the equation 3.1. The 2nd quadrant of the B-H loop for 3C Fe_7S_8 nanostructure at all temperatures is shown in the inset of the figure. The area under the gray shaded portion represents the BH_{max} of the sample. For the given set of measurement temperature values (7 K, 33 K, 210 K, and 300 K), the value of BH_{max} at 300 K is 71.7 kG Oe, which becomes 128 kG Oe at 7 K (table 3.1), making the compound valuable for various applications at low-temperature.

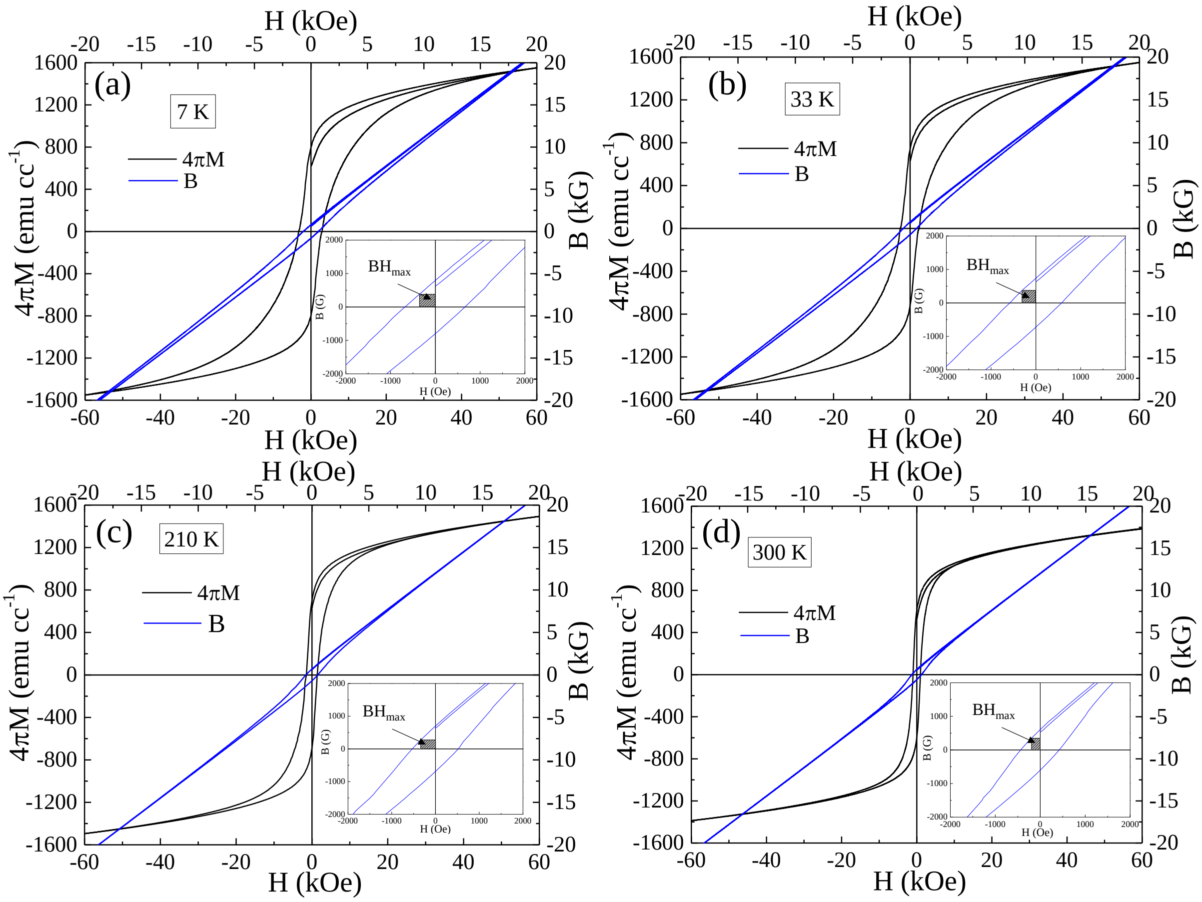

Figure 3.8: (a-h) M-H plot and B-H plot for the sample 3C Fe_7S_8 nanoparticles. The inset in each figure shows the calculation of the maximum energy product from B-H hysteresis loop at 7, 33, 210 and 300 K.

3.3.2. Magnetic properties of the Gd-substituted trigonal Fe_7S_8 nanoparticles

(i) x=0.05

To investigate the magnetic properties of the 5 at% Gd-substituted 3C Fe_7S_8 nanoparticles, the ZFC-FC M-T measurements have been recorded using SQUID-VSM. Figure 3.9a shows the ZFC-FC M-T curves obtained for as-synthesized 5 at% Gd-substituted 3C Fe_7S_8 nanoparticles at the applied magnetic field of 1000 Oe. The ZFC and FC *M-T* curves are split in the temperature range from 7 to 300 K. The M-T curves show that the ZFC and FC curves do not follow the same path. Hence, the M-T curves show an irreversible behavior. The emergence of an ordered magnetic state with a high T_C of the sample above 300 K is shown by the divergence of the ZFC-FC M-T curves of 5 at% Gd-substituted 3C Fe_7S_8 over the entire range of temperature up to 300 K. As shown in the TEM images, the as-synthesized nanoparticles are agglomerated as many nanocrystallites; hence peak of the ZFC curve is regarded as the average blocking temperature (T_B). Polydispersity in the sample may cause the blocking phenomena for each particle on each side of the ZFC peak[51], resulting in the bifurcation of the ZFC-FC curve above T_B. Figure 3.9b shows the T_B for the sample at ~210 K at 1000 Oe applied magnetic field. Another low-temperature magnetic transition is observed at ~33 K. The structure of 3C pyrrhotite with space group $P3_121$ resembles that of the 4C structure[14,22,24] in the sense that vacancies are confined to alternate layers of iron. Powder samples of 4C pyrrhotite show an anomaly at low-temperature ~30-34 K (known as Besnus transition[19,20]). This low-temperature magnetic transition stems from the spin rotation, which can be related to the structural changes at an atomic level caused by the highly ordered vacancies in 4C pyrrhotite, which in turn affect the spin-orbit coupling with no crystallography change of the structure. Assuming the similar spin arrangements in 3C and 4C pyrrhotites, the low-temperature magnetic transition observed at ~33 K at 1000 Oe applied magnetic field (Figure 3.9b) for as-synthesized sample may be assigned as the Besnus transition.

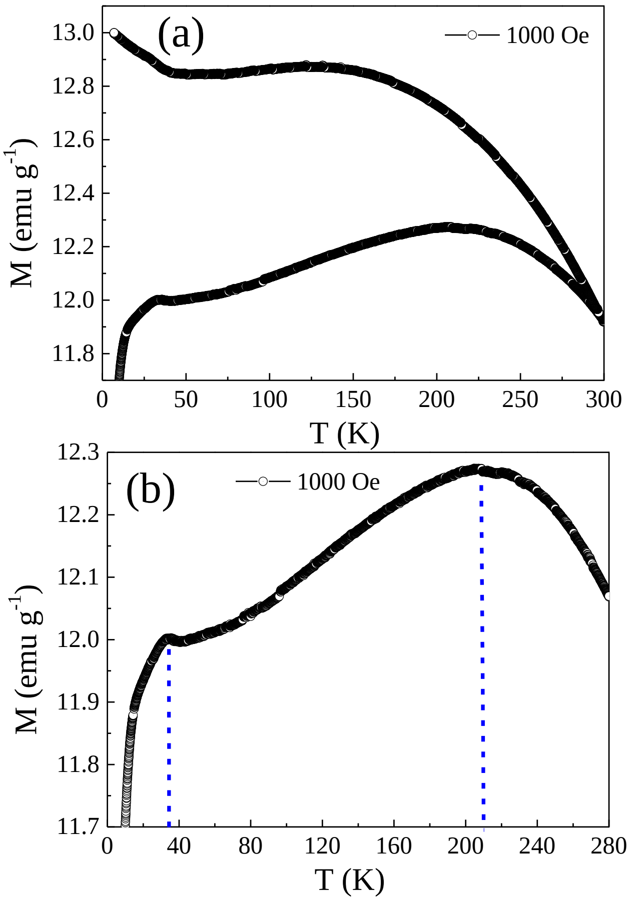

Figure 3.9: (a) Zero-field-cooled (ZFC) and field-cooled (FC) magnetization *vs*. temperature (M-T) curves for the sample 5 at% Gd-substituted 3C Fe_7S_8 nanoparticles at 1000 Oe, (b) ZFC M-T curves for the sample 5 at% Gd-substituted 3C Fe_7S_8 at applied external fields of 1000 Oe in the temperature range of 7-300 K.

To acquire further insights into the magnetic properties of the 5 at% Gd-substituted 3C Fe_7S_8 nanoparticles, the M-H curves were measured using a SQUID-VSM. Figure 3.10(a-d) shows M-H hysteresis curves taken at 7, 33, 210 K, and 300 K in the magnetic field range of ±60 kOe because of the anomalies observed at these temperature values in M-T graphs (figure 3.9b). As shown in Figure 3.10(a-d), the sample demonstrates ferrimagnetic-like behavior at all measurement temperatures. However, at the maximum applied magnetic field of 60 kOe, the magnetization does not exhibit saturation. Such behavior indicates that the spins of the system require a high anisotropic field to align in a particular direction. We observed an initial remanence in the sample at all measurement temperatures. Remanence comes from the vacancies in the specimen. The presence of initial remanence in the M-H hysteresis loop may be attributed to the induced magnetization due to the Fe vacancies in a powdered polycrystalline sample. The hysteresis curves illustrate that H_C, $M_{60\ kOe}$, and M_R values of the sample increase with a decrease in temperature.

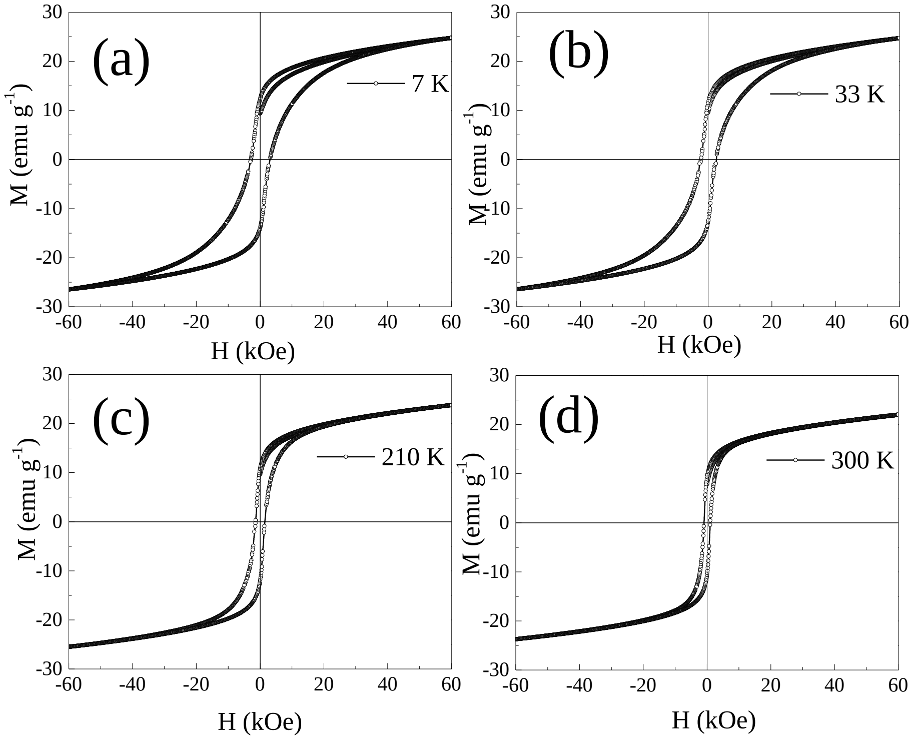

Figure 3.10: (a-d) Magnetization vs. external magnetic field (M-H) hysteresis loops of the sample 5 at% Gd-substituted 3C Fe_7S_8 nanoparticles at 7 K, 33 K, 210 K and 300 K. The M-H hysteresis loops illustrate the increase in $M_{60\ kOe}$, H_C, and M_R values of the sample with decrease in temperature.

Among all four measurement temperature values, the 5 at% Gd-substituted 3C Fe_7S_8 NPs appear to exhibit hysteresis with H_C ~1.0 kOe, $M_{60\ kOe}$, ~23 emu g^{-1}, and M_R ~10 emu g^{-1} at 300 K, which increases to H_C ~3.0 kOe, $M_{60\ kOe}$, ~26 emu g^{-1},and M_R ~13 kOe at 7 K (table 3.2).

Table 3.2: Summary of the magnetic parameters calculated for the sample 5 at% Gd-substituted 3C Fe_7S_8 nanoparticles at different measurement temperatures.

Measurement temperature (K)	H_C (kOe)	M_R (emu g^{-1})	$M_{60\ kOe}$ (emu g^{-1})	M_R/M_S	H_a (kOe)	K_{eff} (erg cc^{-1}) $\times10^5$	BH_{max} (kG Oe)
7	3.4	13.2	25.6	0.516	12.3	9.27	135.2
33	2.8	12.4	25.2	0.492	8.9	6.56	118.4
210	1.9	11.6	24.8	0.468	5.3	3.36	107.5
300	1.3	10.1	23	0.439	4.7	3.01	79.1

The decrease in thermal activation energy and the rise in total effective magnetic anisotropy, which creates more spins available to align in the direction of the applied magnetic field, may have contributed to the increase in these values at the lower temperature[51,55]. Fe^{2+} and Fe^{3+} ionic states, as well as ordered Fe vacancies, are present in the $Fe_{1-x}S$ compounds in addition to alternate levels of the lattice. The magnetic moments of Fe in the compound are ferromagnetically arranged inside each layer, however, are coupled antiferromagnetically to each other between adjacent layers. The vacancies in every second layer contribute to the spin orientation. The presence of ionic states of iron and the vacancies in the lattice lead to uncompensated magnetic moments, giving rise to the ferrimagnetic ordering in the compound.

The value of K_{eff} is 3.0×10^5 erg cc^{-1} at 300 K, which increases to 9.3×10^5 erg cc^{-1} at 7 K (table 3.2). To determine the type of magnetocrystalline anisotropy, ln (K_{eff}) is plotted against ln ($M_{60\ kOe}$), as shown in figure 3.11.

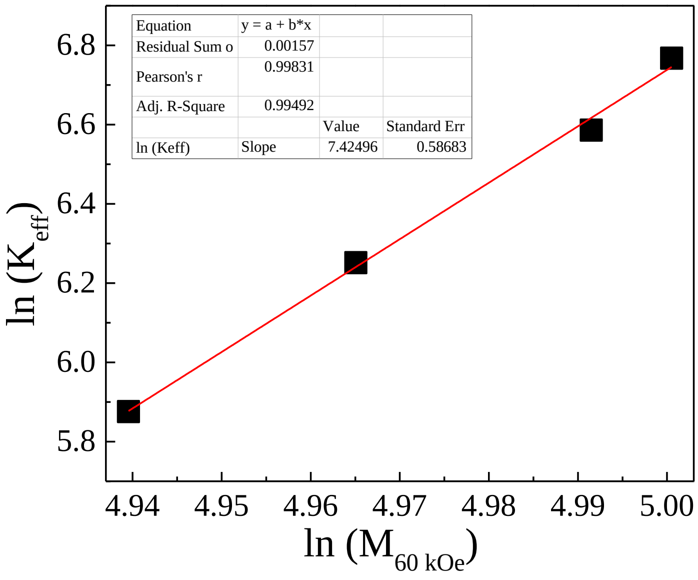

Figure 3.11: Linear relationship between K_{eff} and $M_{60\ kOe}$ in the logarithmic scale for the sample with 5 at% Gd-substituted 3C Fe_7S_8 nanoparticles, with a slope of 7.4, indicating that the sample predominantly exhibits uniaxial anisotropy.

For a system with uniaxial magnetocrystalline anisotropy[38], K_{eff} should be proportional to $M_{60\ kOe}^{3}$, whereas for a cubic magnetocrystalline anisotropy, K_{eff} should be proportional to $M_{60\ kOe}^{10}$. The linear fit of the plot gives a slope of 7.4, indicating that the sample predominantly exhibits uniaxial anisotropy.

The BH_{max} for all the samples is estimated using the equation 3.1. The 2nd quadrant of the B-H loop for 3C Fe_7S_8 nanostructure at all temperatures is shown in the inset of the figure 3.12. The area under the gray shaded portion represents the BH_{max} of the sample[38]. For the given set of measurement temperature values (7 K, 33 K, 210 K, and 300 K), the value of BH_{max} at 300 K is 79.1 kG Oe, which becomes 135.2 kG Oe at 7 K (table 3.2), making the compound valuable for various applications at low-temperature.

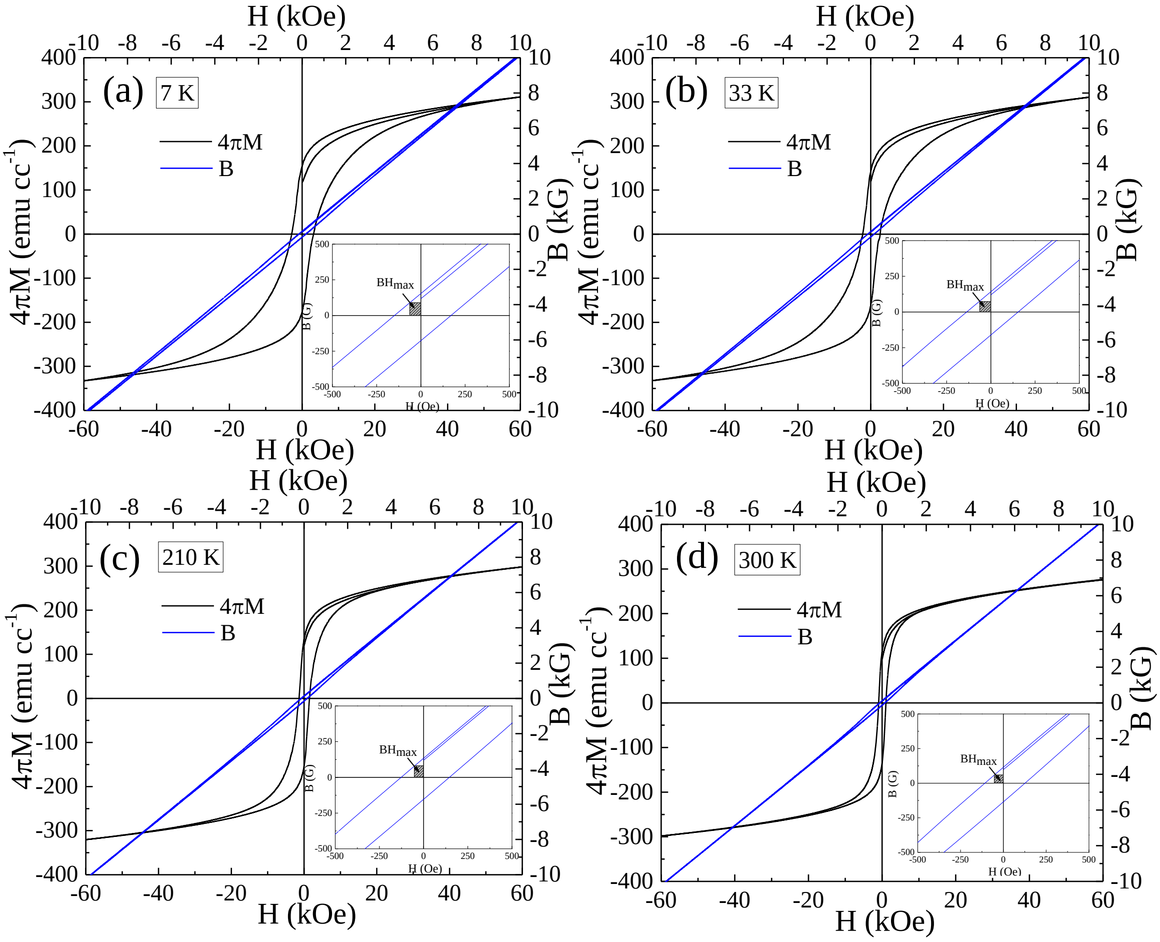

Figure 3.12: (a-h) M-H plot and B-H plot for the sample 5 at% Gd-substituted 3C Fe_7S_8 nanoparticles. The inset in each figure shows the calculation of the maximum energy product from B-H hysteresis loop at 7, 33, 210 and 300 K.

(ii) x=0.1

To investigate the magnetic properties of the 10 at% Gd-substituted 3C Fe_7S_8 nanoparticles, the ZFC-FC M-T measurements have been recorded using SQUID-VSM. Figure 3.13a shows the ZFC-FC M-T curves obtained for as-synthesized 10 at% Gd-substituted 3C Fe_7S_8 nanoparticles at the applied magnetic field of 1000 Oe, respectively. The ZFC and FC *M-T* curves are split in the temperature range from 7 to 300 K. The M-T curves show that the ZFC and FC curves do not follow the same path. Hence, the M-T curves show an irreversible behavior. The emergence of an ordered magnetic state with a high T_C of the sample above

300 K is shown by the divergence of the ZFC-FC M-T curves of 10 at% Gd-substituted 3C Fe_7S_8 over the entire range of temperature up to 300 K. As shown in the TEM images, the as-synthesized nanoparticles are agglomerated as many nanocrystallites; hence the peak of ZFC curve is regarded as the average blocking temperature (T_B). Polydispersity in the sample may cause the blocking phenomena for each particle on each side of the ZFC peak[51], resulting in the bifurcation of the ZFC-FC curve above T_B. Figure 3.13b shows the T_B for the sample at ~210 K at 1000 Oe applied magnetic field. Another low-temperature magnetic transition[20] is observed at ~33 K. The structure of 3C pyrrhotite with space group $P3_121$ resembles that of the 4C structure in the sense that vacancies are confined to alternate layers of iron. Powder samples of 4C pyrrhotite show an anomaly at low-temperature ~30-34 K (known as Besnus transition[19,20]). This low-temperature magnetic transition stems from the spin rotation, which can be related to the structural changes at an atomic level caused by the highly ordered vacancies in 4C pyrrhotite, which in turn affect the spin-orbit coupling with no crystallography change of the structure. Assuming the similar spin arrangements in 3C and 4C pyrrhotites, the low-temperature magnetic transition observed at ~33 K at 1000 Oe applied magnetic field (Figure 3.13b) for as-synthesized 3C pyrrhotite may be assigned as the Besnus transition.

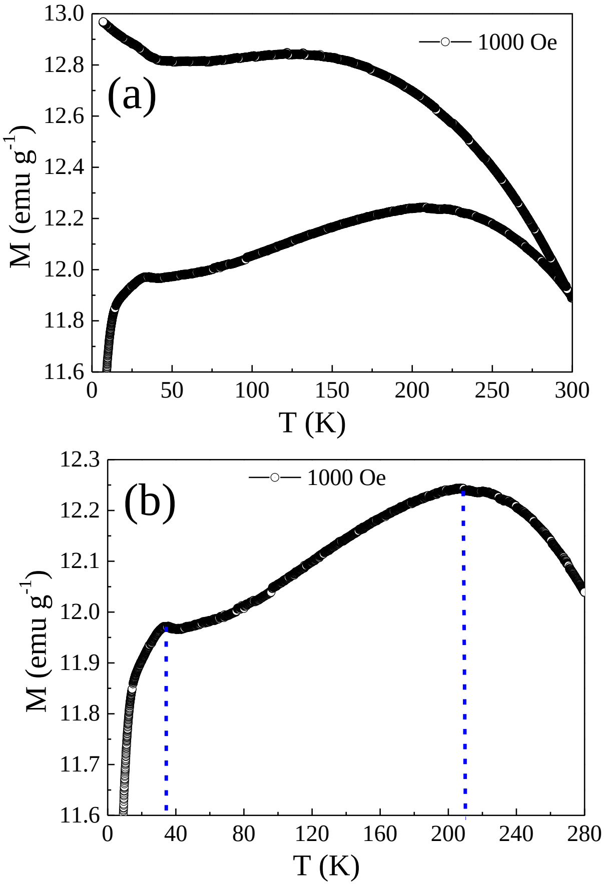

Figure 3.13: (a) Zero-field-cooled (ZFC) and field-cooled (FC) magnetization *vs.* temperature (M-T) curves for the sample 10 at% Gd-substituted 3C Fe_7S_8 nanoparticles at 1000 Oe, (b) ZFC M-T curves for the sample 10 at% Gd-substituted 3C Fe_7S_8 at applied external fields of 1000 Oe in the temperature range of 7-300 K.

To acquire further insights into the magnetic properties of the 10 at% Gd-substituted 3C Fe_7S_8 nanoparticles, the M-H curves were measured using a SQUID-VSM. Figure 3.14(a-d) shows M-H hysteresis curves taken at 7, 33, 210 K, and 300 K in the magnetic field range of ±60 kOe because of the anomalies observed at these temperature values in M-T graphs (figure 3.13b). As shown in Figure 3.14(a-d), the sample demonstrates ferrimagnetic-like behavior at all measurement temperatures. However, at the maximum applied magnetic field of 60 kOe, the magnetization does not exhibit saturation at the highest applied magnetic field of 60 kOe. Such behavior indicates that the spins of the system require a high anisotropic field to align in a particular direction. We observed an initial remanence in the sample at all measurement temperatures. Remanence comes from the vacancies in the specimen. The presence of initial remanence in the M-H hysteresis loop may be attributed to the induced magnetization due to the Fe vacancies in a powdered polycrystalline sample. The hysteresis curves illustrate that H_C, $M_{60\ kOe}$, and M_R values of the sample increase with a decrease in temperature.

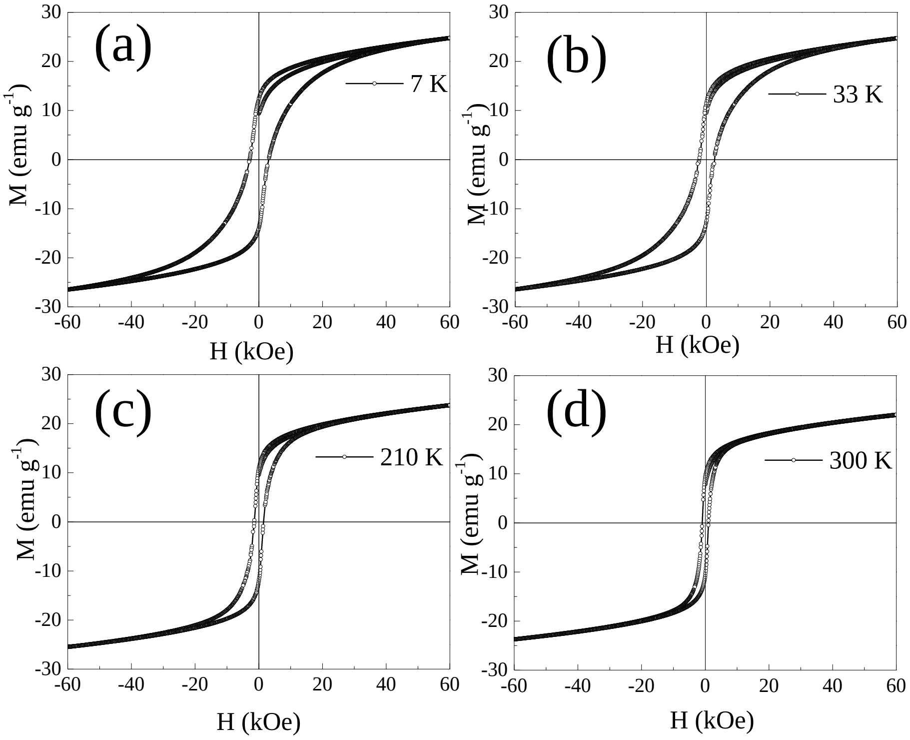

Figure 3.14: (a-d) Magnetization vs. external magnetic field (M-H) hysteresis loops of the sample 10 at% Gd-substituted 3C Fe_7S_8 nanoparticles at 7 K, 33 K, 210 K and 300 K. The M-H hysteresis loops illustrate the increase in $M_{60\ kOe}$, H_C, and M_R values of the sample with decrease in temperature.

Among all four measurement temperature values, the 10 at% Gd-substituted 3C Fe_7S_8 NPs appear to exhibit hysteresis with H_C ~2.0 kOe, $M_{60\ kOe}$, ~25 emu g^{-1}, and M_R ~10 emu g^{-1} at 300 K, which increases to H_C ~4.0 kOe, $M_{60\ kOe}$, ~26 emu g^{-1},and M_R ~13 kOe at 7 K (table 3.3).

Table 3.3: Summary of the magnetic parameters calculated for the sample 10 at% Gd-substituted 3C Fe_7S_8 nanoparticles at different measurement temperatures.

Measurement temperature (K)	H_C (kOe)	M_R (emu g^{-1})	$M_{60\ kOe}$ (emu g^{-1})	M_R/M_S	H_a (kOe)	K_{eff} (erg cc^{-1}) $\times 10^5$	BH_{max} (kG Oe)
7	3.5	13.4	25.7	0.521	12.3	9.47	139.4
33	2.8	12.6	25.3	0.498	8.9	7.36	124.1
210	2.1	11.7	24.7	0.474	5.3	3.42	112.7
300	1.5	10.2	24.5	0.416	4.7	3.43	83.2

The decrease in thermal activation energy and the rise in total effective magnetic anisotropy, which creates more spins available to align in the direction of the applied magnetic field, may have contributed to the increase in these values at the lower temperature[51,55]. Fe^{2+} and Fe^{3+} ionic states, as well as ordered Fe vacancies, are present in the $Fe_{1-x}S$ compounds in addition to alternate levels of the lattice. The magnetic moments of Fe in the compound are ferromagnetically arranged inside each layer, however, are coupled antiferromagnetically to each other between adjacent layers. The vacancies in every second layer contribute to the spin orientation. The presence of ionic states of iron and the vacancies in the lattice lead to uncompensated magnetic moments, giving rise to the ferrimagnetic ordering in the compound.

The value of K_{eff} is 3.4×10^5 erg cc^{-1} at 300 K, which increases to 9.5×10^5 erg cc^{-1} at 7 K (table 3.3). To determine the type of magnetocrystalline anisotropy, ln (K_{eff}) is plotted against ln ($M_{60\ kOe}$), as shown in figure 3.15.

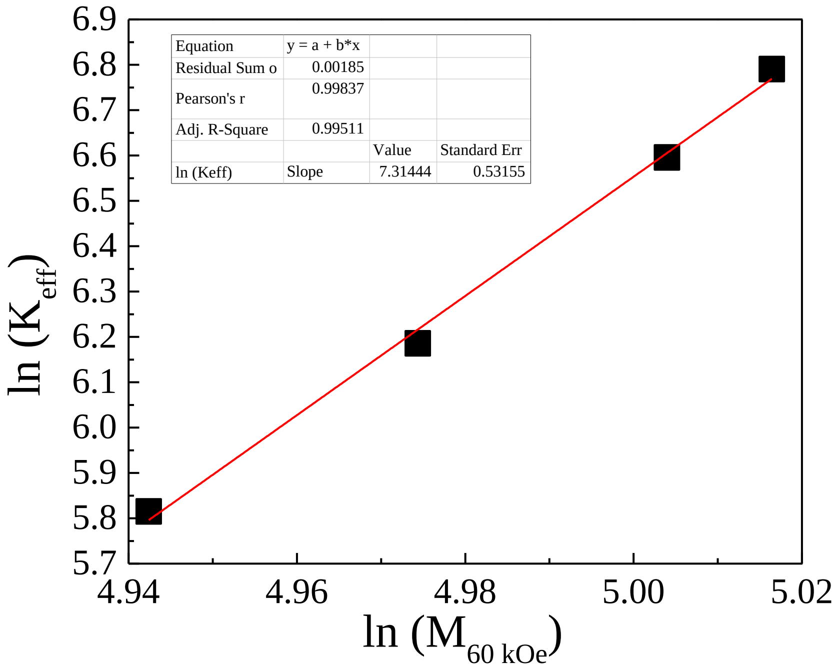

Figure 3.15: Linear relationship between K_{eff} and $M_{60\ kOe}$ in the logarithmic scale for the sample with 10 at% Gd-substituted 3C Fe_7S_8 nanoparticles, with a slope of 7.3, indicating that the sample predominantly exhibits uniaxial anisotropy.

For a system with uniaxial magnetocrystalline anisotropy[38], K_{eff} should be proportional to $M_{60\ k\ Oe}^{3}$, whereas for a cubic magnetocrystalline anisotropy, K_{eff} should be proportional to $M_{60\ kOe}^{10}$. The linear fit of the plot gives a slope of 7.3, indicating that the sample predominantly exhibits uniaxial anisotropy.

The BH_{max} for all the samples is estimated using the equation 3.1. The 2nd quadrant of the *B-H* loop for 3C Fe_7S_8 nanostructure at all temperatures is shown in the inset of the figure 3.16. The area under the gray shaded portion represents the BH_{max} of the sample[38]. For the given set of measurement temperature values (7 K, 33 K, 210 K, and 300 K), the value of BH_{max} at 300 K is 83.2 kG Oe, which becomes 139.4 kG Oe at 7 K (table 3.3), making the compound valuable for various applications at low-temperature.

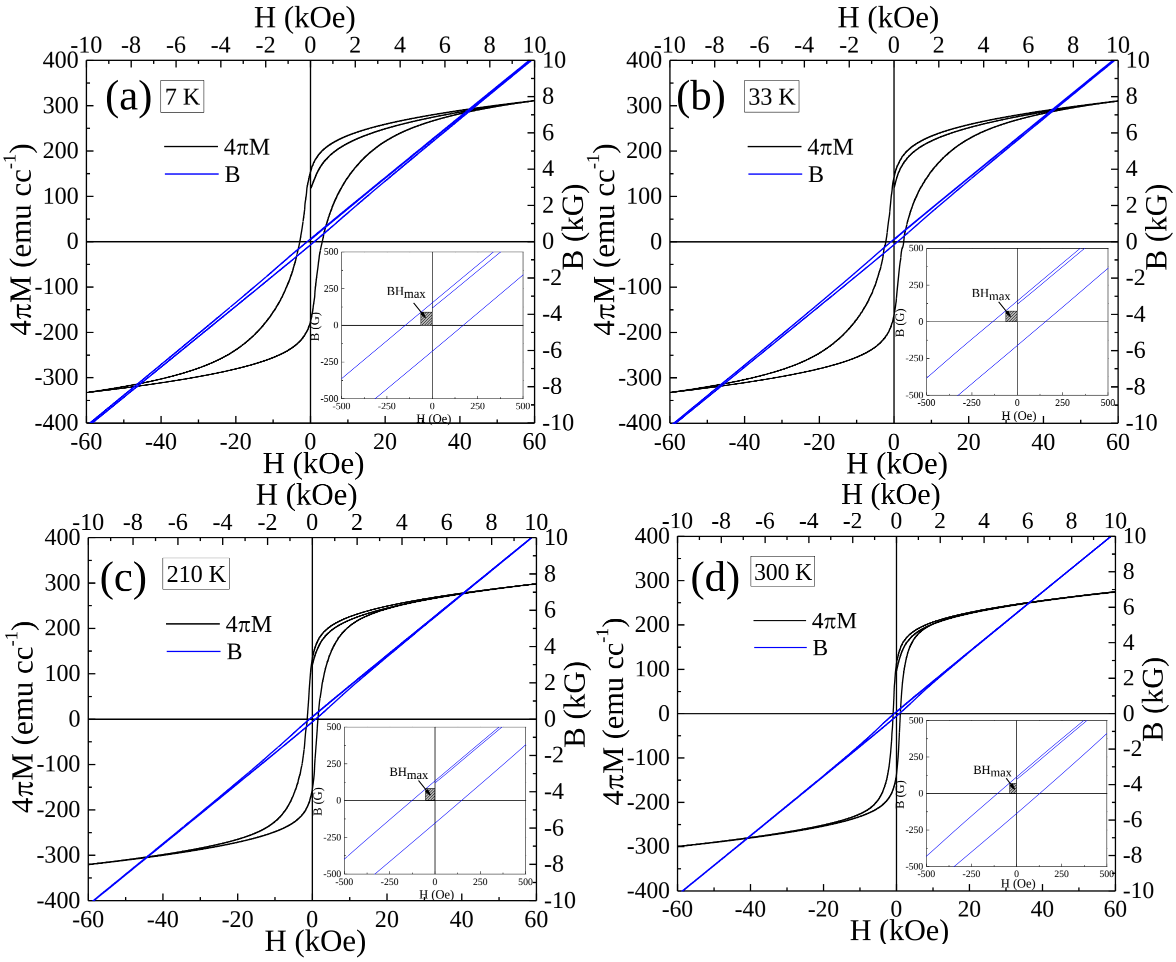

Figure 3.16: (a-h) M-H plot and B-H plot for the sample 10 at% Gd-substituted 3C Fe_7S_8 nanoparticles. The inset in each figure shows the calculation of the maximum energy product from B-H hysteresis loop at 7, 33, 210 and 300 K.

(iii) x=0.15

To investigate the magnetic properties of the 15 at% Gd-substituted 3C Fe_7S_8 nanoparticles, the ZFC-FC M-T measurements have been recorded using SQUID-VSM. Figure 3.17a shows the ZFC-FC M-T curves obtained for as-synthesized 15 at% Gd-substituted 3C Fe_7S_8 nanoparticles at the applied magnetic field of 1000 Oe, respectively. The ZFC and FC *M-T* curves are split in the temperature range from 7 to 300 K. The M-T curves show that the ZFC and FC curves do not follow the same path. Hence, the M-T curves show an irreversible behavior. The emergence of an ordered magnetic state with a high T_C of the sample above

300 K is shown by the divergence of the ZFC-FC M-T curves of 15 at% Gd-substituted 3C Fe_7S_8 over the entire range of temperature up to 300 K. As shown in the TEM images, the as-synthesized nanoparticles are agglomerated as many nanocrystallites; hence the peak of the ZFC curve is regarded as the average blocking temperature (T_B). Polydispersity in the sample may cause the blocking phenomena for each particle on each side of the ZFC peak[51], resulting in the bifurcation of the ZFC-FC curve above T_B. Figure 3.17b shows the T_B for the sample at ~210 K at 1000 Oe applied magnetic field. Another low-temperature magnetic transition is observed at ~33 K[20]. The structure of 3C pyrrhotite with space group $P3_121$ resembles that of the 4C structure in the sense that vacancies are confined to alternate layers of iron. Powder samples of 4C pyrrhotite show an anomaly at low-temperature ~30-34 K (known as Besnus transition[19,20]). This low-temperature magnetic transition stems from the spin rotation, which can be related to the structural changes at an atomic level caused by the highly ordered vacancies in 4C pyrrhotite, which in turn affect the spin-orbit coupling with no crystallography change of the structure. Assuming the similar spin arrangements in 3C and 4C pyrrhotites, the low-temperature magnetic transition observed at ~33 K at 1000 Oe applied magnetic field (Figure 3.17b) for as-synthesized 3C pyrrhotite may be assigned as the Besnus transition.

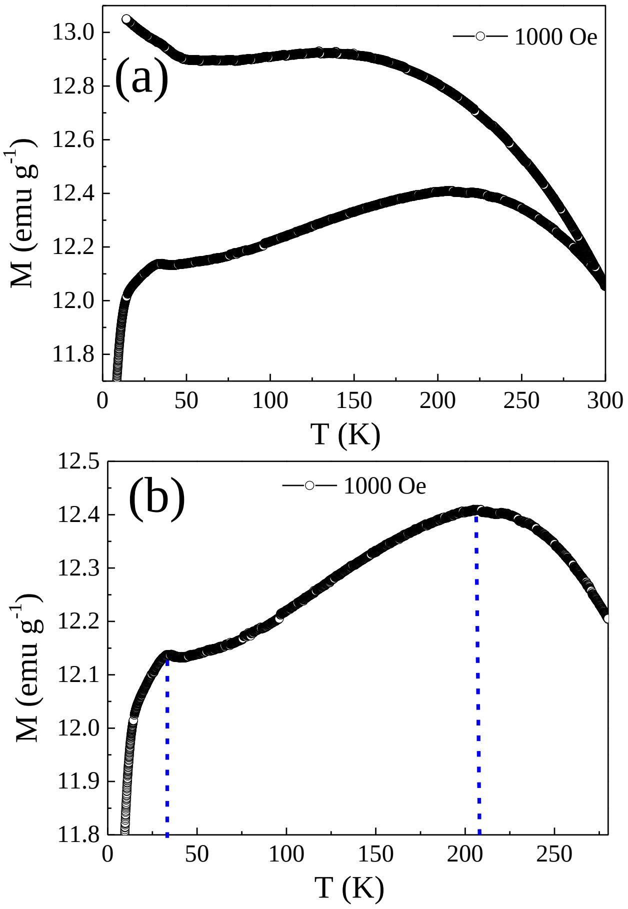

Figure 3.17: (a) Zero-field-cooled (ZFC) and field-cooled (FC) magnetization *vs.* temperature (M-T) curves for the sample 15 at% Gd-substituted 3C Fe_7S_8 nanoparticles at 1000 Oe, (b) ZFC M-T curves for the sample 15 at% Gd-substituted 3C Fe_7S_8 at applied external fields of 1000 Oe in the temperature range of 7-300 K.

To acquire further insights into the magnetic properties of the 15 at% Gd-substituted 3C Fe_7S_8 nanoparticles, the M-H curves were measured using a SQUID-VSM. Figure 3.18(a-d) shows M-H hysteresis curves taken at 7, 33, 210 K, and 300 K in the magnetic field range of ±60 kOe because of the anomalies observed at these temperature values in M-T graphs (figure 3.17b). As shown in Figure 3.18(a-d), the sample demonstrates ferrimagnetic-like behavior at all measurement temperatures. However, at the maximum applied magnetic field of 60 kOe, the magnetization does not exhibit saturation. Such behavior indicates that the spins of the system require a high anisotropic field to align in a particular direction. We observed an initial remanence in the sample at all measurement temperatures. Remanence comes from the vacancies in the specimen. The presence of initial remanence in the M-H hysteresis loop may be attributed to the induced magnetization due to the Fe vacancies in a powdered polycrystalline sample. The hysteresis curves illustrate that H_C, $M_{60\ kOe}$, and M_R values of the sample increase with a decrease in temperature.

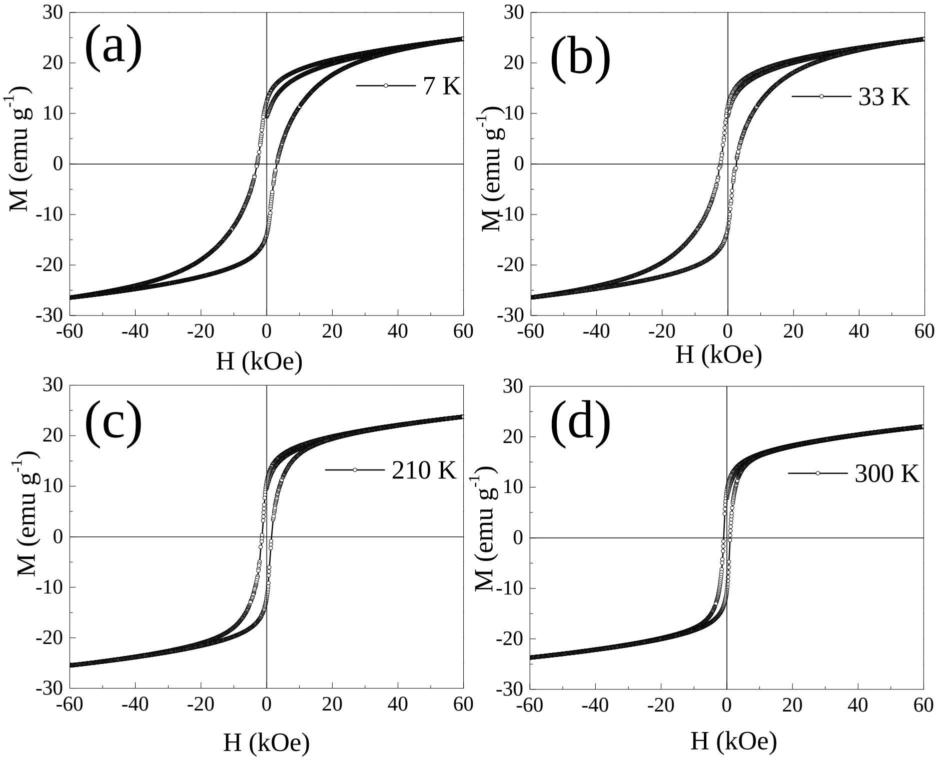

Figure 3.18: (a-d) Magnetization vs. external magnetic field (M-H) hysteresis loops of the sample 15 at% Gd-substituted 3C Fe_7S_8 nanoparticles at 7 K, 33 K, 210 K and 300 K. The M-H hysteresis loops illustrate the increase in $M_{60\ kOe}$, H_C, and M_R values of the sample with decrease in temperature.

Among all four measurement temperature values, the 15 at% Gd-substituted 3C Fe_7S_8 NPs appear to exhibit hysteresis with H_C ~2.0 kOe, $M_{60\ kOe}$, ~25 emu g^{-1}, and M_R ~10 emu g^{-1} at 300 K, which increases to H_C ~4.0 kOe, $M_{60\ kOe}$, ~26 emu g^{-1},and M_R ~14 kOe at 7 K (table 3.4).

Table 3.4: Summary of the magnetic parameters calculated for the sample 15 at% Gd-substituted 3C Fe_7S_8 nanoparticles at different measurement temperatures.

Measurement temperature (K)	**H_C (kOe)**	**M_R (emu g^{-1})**	**$M_{60\ kOe}$ (emu g^{-1})**	**M_R/M_S**	**H_a (kOe)**	**K_{eff} (erg cc^{-1}) ×10^5**	**BH_{max} (kG Oe)**
7	3.8	13.5	25.7	0.525	12.3	9.59	141.8
33	3	12.7	25.4	0.5	8.9	7.51	126.3
210	2.2	11.9	24.8	0.479	5.3	3.57	115.5
300	1.6	10.4	24.7	0.421	4.7	3.54	87.3

The decrease in thermal activation energy and the rise in total effective magnetic anisotropy, which creates more spins available to align in the direction of the applied magnetic field[51,55], may have contributed to the increase in these values at the lower temperature. Fe^{2+} and Fe^{3+} ionic states, as well as ordered Fe vacancies, are present in the $Fe_{1-x}S$ compounds in addition to alternate levels of the lattice. The magnetic moments of Fe in the compound are ferromagnetically arranged inside each layer, however, are coupled antiferromagnetically to each other between adjacent layers. The vacancies in every second layer contribute to the spin orientation. The presence of ionic states of iron and the vacancies in the lattice lead to uncompensated magnetic moments, giving rise to the ferrimagnetic ordering in the compound.

The value of K_{eff} is 3.54×10^5 erg cc^{-1} at 300 K, which increases to 9.59×10^5 erg cc^{-1} at 7 K (table 3.4). To determine the type of magnetocrystalline anisotropy, ln (K_{eff}) is plotted against ln ($M_{60\ kOe}$), as shown in figure 3.19.

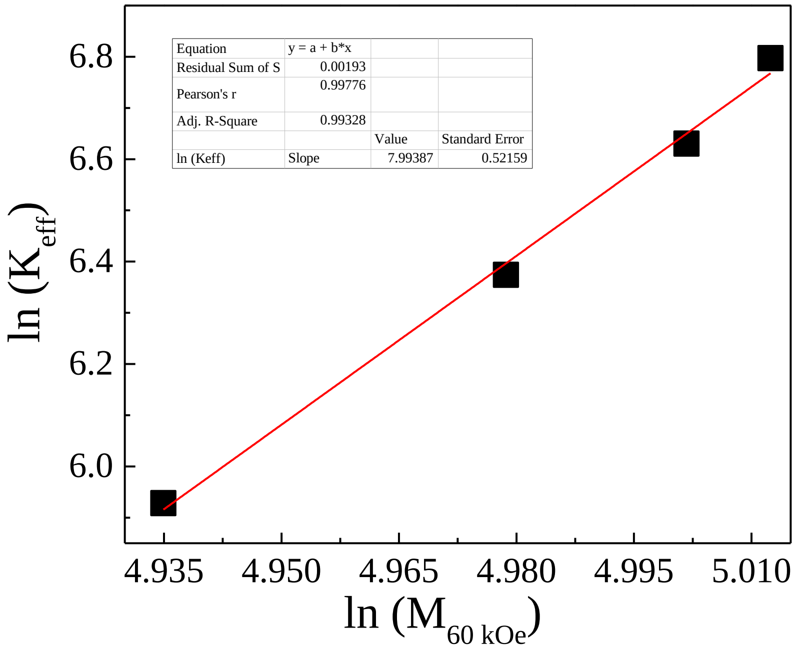

Equation	y = a + b*x		
Residual Sum of S	0.00193		
Pearson's r	0.99776		
Adj. R-Square	0.99328		
		Value	Standard Error
ln (Keff)	Slope	7.99387	0.52159

Figure 3.19: Linear relationship between K_{eff} and $M_{60\ kOe}$ in the logarithmic scale for the sample with 15 at% Gd-substituted 3C Fe_7S_8 nanoparticles, with a slope of 7.9, indicating that the sample predominantly exhibits uniaxial anisotropy.

For a system with uniaxial magnetocrystalline anisotropy[38], K_{eff} should be proportional to $M_{60\ kOe}^{3}$, whereas for a cubic magnetocrystalline anisotropy, K_{eff} should be proportional to $M_{60\ kOe}^{10}$. The linear fit of the plot gives a slope of 7.9, indicating that the sample predominantly exhibits uniaxial anisotropy.

The BH_{max} for all the samples is estimated using the equation 3.1. The 2nd quadrant of the *B*-*H* loop for 3C Fe_7S_8 nanostructure at all temperatures is shown in the inset of the figure 3.20. The area under the gray shaded portion represents the BH_{max} of the sample[38]. For the given set of measurement temperature values (7 K, 33 K, 210 K, and 300 K), the value of BH_{max} at 300 K is 87.3 kG Oe, which becomes 141.8 kG Oe at 7 K (table 3.1), making the compound valuable for various applications at low-temperature.

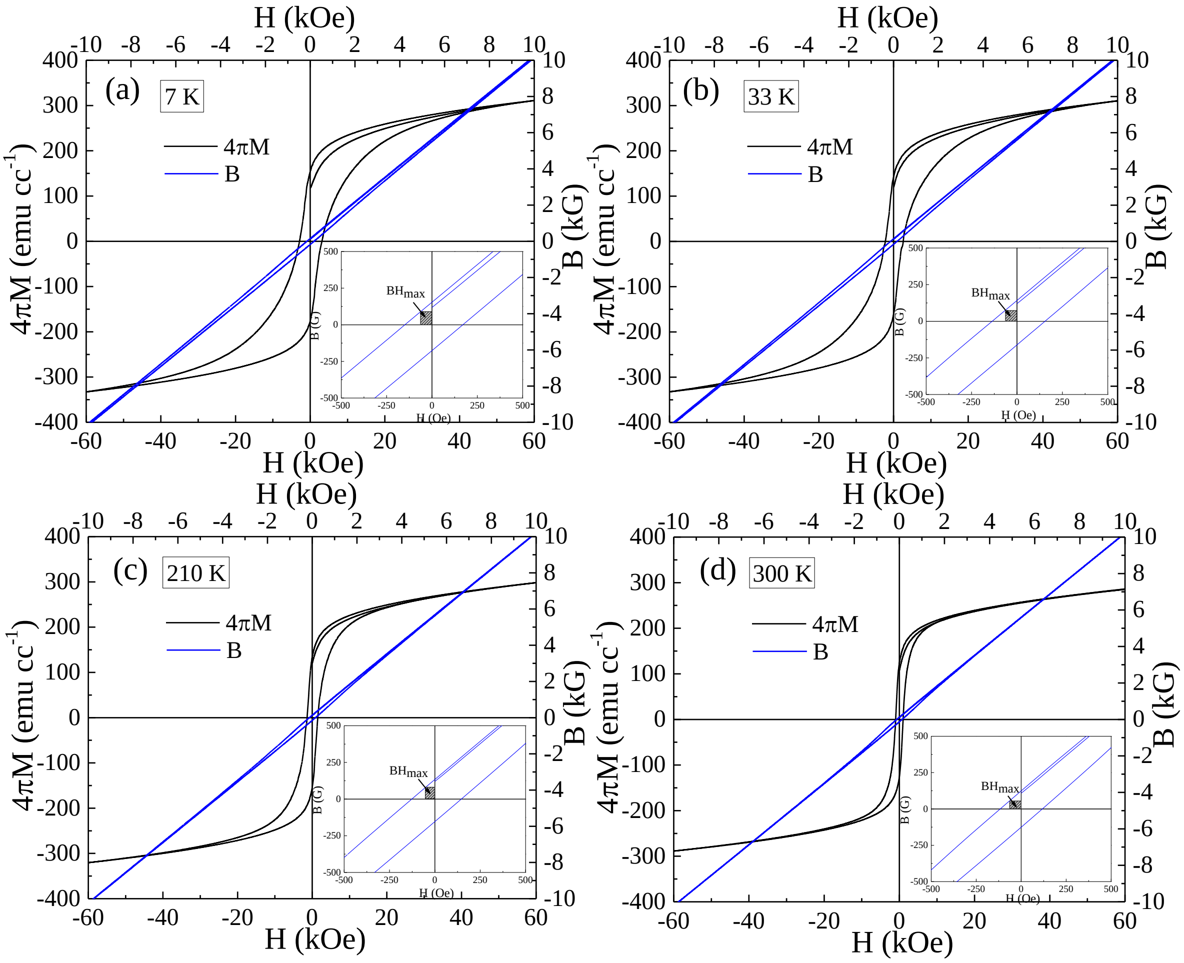

Figure 3.20: (a-h) M-H plot and B-H plot for the sample 15 at% Gd-substituted 3C Fe_7S_8 nanoparticles. The inset in each figure shows the calculation of the maximum energy product from B-H hysteresis loop at 7, 33, 210 and 300 K.

(iv) <u>x=0.2</u>

To investigate the magnetic properties of the 20 at% Gd-substituted 3C Fe_7S_8 nanoparticles, the ZFC-FC M-T measurements have been recorded using SQUID-VSM. Figure 3.21a shows the ZFC-FC M-T curves obtained for as-synthesized 20 at% Gd-substituted 3C Fe_7S_8 nanoparticles at the applied magnetic field of 1000 Oe, respectively. The ZFC and FC *M-T* curves are split in the temperature range from 7 to 300 K. The M-T curves show that the ZFC and FC curves do not follow the same path. Hence, the M-T curves show an irreversible behavior. The emergence of an ordered magnetic state with a high T_C of the sample above

300 K is shown by the divergence of the ZFC-FC M-T curves of 20 at% Gd-substituted 3C Fe_7S_8 over the entire range of temperature up to 300 K. As shown in the TEM images, the as-synthesized nanoparticles are agglomerated as many nanocrystallites; hence the ZFC peak is regarded as the average blocking temperature (T_B). Polydispersity in the sample may cause the blocking phenomena for each particle on each side of the ZFC peak[51], resulting in the bifurcation of the ZFC-FC curve above T_B. Figure 3.21b shows the T_B for the sample at ~210 K at 1000 Oe applied magnetic field. Another low-temperature magnetic transition is observed at ~33 K[20]. The structure of 3C pyrrhotite with space group $P3_121$ resembles that of the 4C structure in the sense that vacancies are confined to alternate layers of iron. Powder samples of 4C pyrrhotite show an anomaly at low-temperature ~30-34 K (known as Besnus transition[19,20]). This low-temperature magnetic transition stems from the spin rotation, which can be related to the structural changes at an atomic level caused by the highly ordered vacancies in 4C pyrrhotite, which in turn affect the spin-orbit coupling with no crystallography change of the structure. Assuming the similar spin arrangements in 3C and 4C pyrrhotites, the low-temperature magnetic transition observed at ~33 K at 1000 Oe applied magnetic field (Figure 3.21b) for as-synthesized 3C pyrrhotite may be assigned as the Besnus transition.

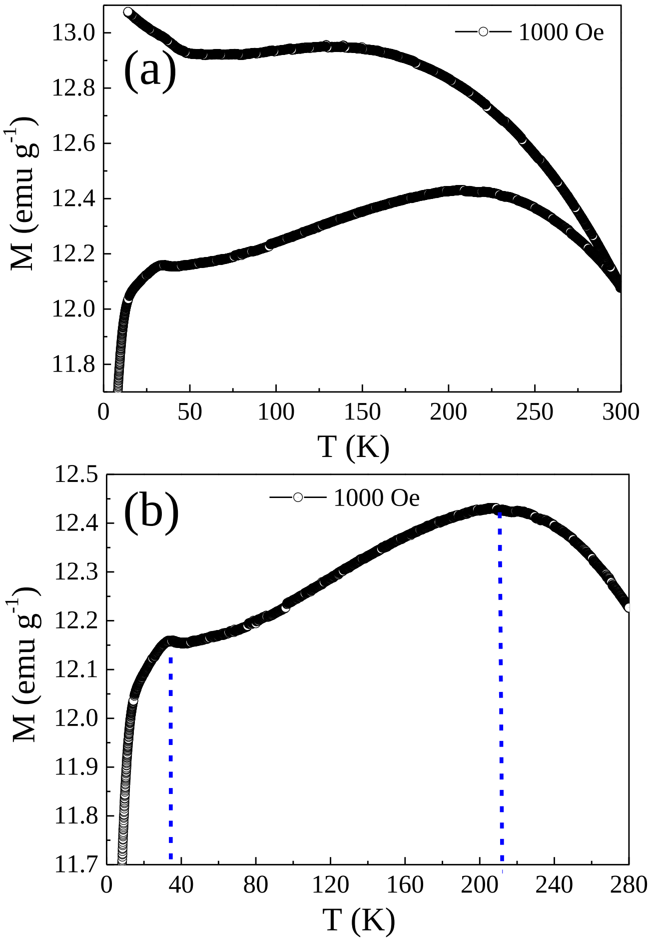

Figure 3.21: (a) Zero-field-cooled (ZFC) and field-cooled (FC) magnetization *vs.* temperature (M-T) curves for the sample 20 at% Gd-substituted 3C Fe_7S_8 nanoparticles at 1000 Oe, (b) ZFC M-T curves for the sample 20 at% Gd-substituted 3C Fe_7S_8 at applied external fields of 1000 Oe in the temperature range of 7-300 K.

To acquire further insights into the magnetic properties of the 20 at% Gd-substituted 3C Fe_7S_8 nanoparticles, the M-H curves were measured using a SQUID-VSM. Figure 3.12(a-d) shows M-H hysteresis curves taken at 7, 33, 210 K, and 300 K in the magnetic field range of ±60 kOe because of the anomalies observed at these temperature values in M-T graphs (figure 3.21b). As shown in Figure 3.22(a-d), the sample demonstrates ferrimagnetic-like behavior at all measurement temperatures. However, at the maximum applied magnetic field of 60 kOe, the magnetization does not exhibit saturation. Such behavior indicates that the spins of the system require a high anisotropic field to align in a particular direction. We observed an initial remanence in the sample at all measurement temperatures. Remanence comes from the vacancies in the specimen. The presence of initial remanence in the M-H hysteresis loop may be attributed to the induced magnetization due to the Fe vacancies in a powdered polycrystalline sample. The hysteresis curves illustrate that H_C, $M_{60\ kOe}$, and M_R values of the sample increase with a decrease in temperature.

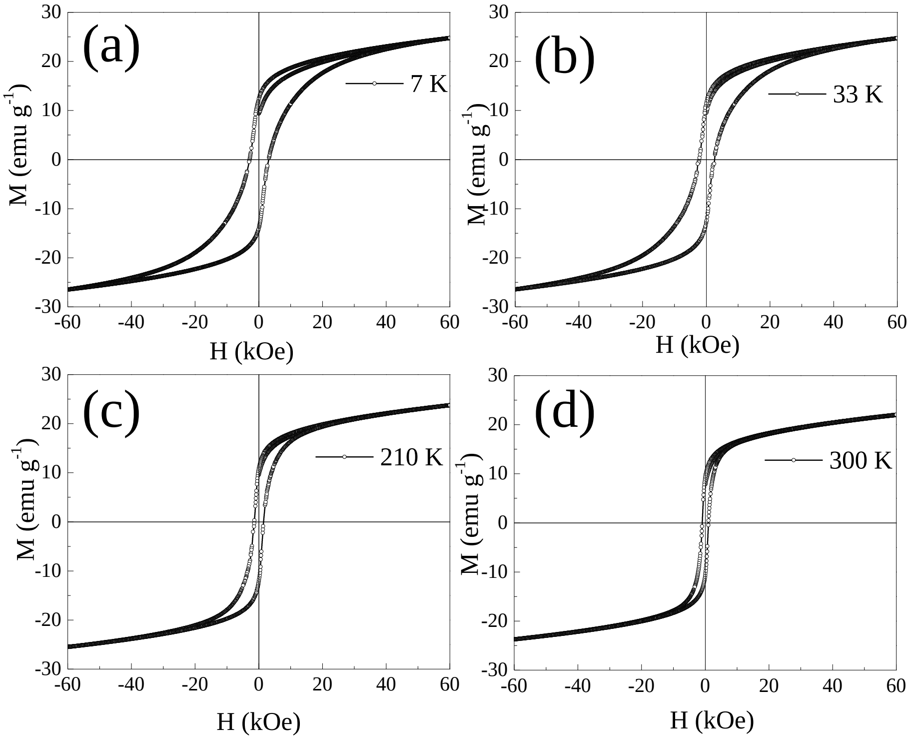

Figure 3.22: (a-d) Magnetization vs. external magnetic field (M-H) hysteresis loops of the sample 20 at% Gd-substituted 3C Fe_7S_8 nanoparticles at 7 K, 33 K, 210 K and 300 K. The M-H hysteresis loops illustrate the increase in $M_{60\ kOe}$, H_C, and M_R values of the sample with decrease in temperature.

Among all four measurement temperature values, the 20 at% Gd-substituted 3C Fe_7S_8 NPs appear to exhibit hysteresis with H_C ~2.0 kOe, $M_{60\ kOe}$, ~25 emu g^{-1}, and M_R ~11 emu g^{-1} at 300 K, which increases to H_C ~4.0 kOe, $M_{60\ kOe}$, ~26 emu g^{-1},and M_R ~14 kOe at 7 K (table 3.5).

Table 3.5: Summary of the magnetic parameters calculated for the sample 20 at% Gd-substituted 3C Fe_7S_8 nanoparticles at different measurement temperatures.

Measurement temperature (K)	H_C (kOe)	M_R (emu g^{-1})	$M_{60\ kOe}$ (emu g^{-1})	M_R/M_S	H (kOe)	K_{eff} (erg cc^{-1}) $\times 10^5$	BH_{max} (kG Oe)
7	3.8	13.6	25.9	0.525	12.3	9.85	143.2
33	3.1	12.9	25.5	0.506	8.9	7.55	128.1
210	2.3	12.1	24.9	0.486	5.3	4.39	118.4
300	1.8	10.5	24.8	0.423	4.7	3.69	89.9

The decrease in thermal activation energy and the rise in total effective magnetic anisotropy, which creates more spins available to align in the direction of the applied magnetic field, may have contributed to the increase in these values at the lower temperature[51,55]. Fe^{2+} and Fe^{3+} ionic states, as well as ordered Fe vacancies, are present in the $Fe_{1-x}S$ compounds in addition to alternate levels of the lattice. The magnetic moments of Fe in the compound are ferromagnetically arranged inside each layer, however, are coupled antiferromagnetically to each other between adjacent layers. The vacancies in every second layer contribute to the spin orientation. The presence of ionic states of iron and the vacancies in the lattice lead to uncompensated magnetic moments, giving rise to the ferrimagnetic ordering in the compound.

The value of K_{eff} is 3.69×10^5 erg cc^{-1} at 300 K, which increases to 9.85×10^5 erg cc^{-1} at 7 K (table 3.5). To determine the type of magnetocrystalline anisotropy, ln (K_{eff}) is plotted against ln ($M_{60\ kOe}$), as shown in figure 3.23.

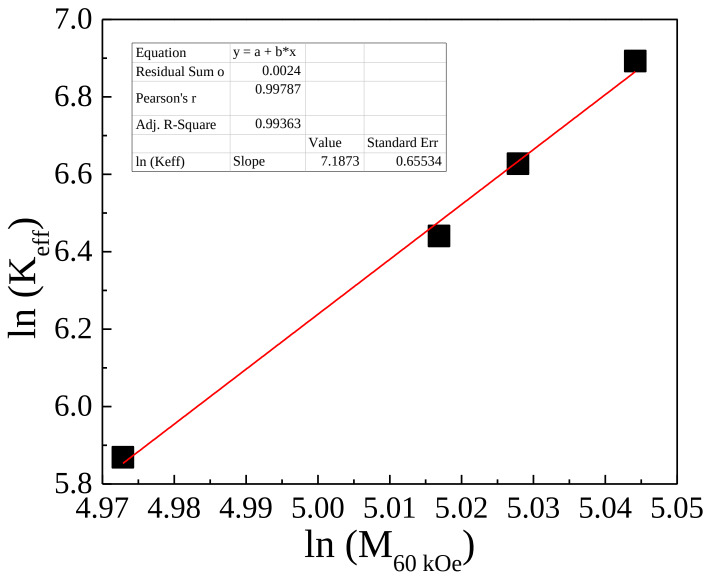

Figure 3.23: Linear relationship between K_{eff} and $M_{60\ kOe}$ in the logarithmic scale for the sample with 20 at% Gd-substituted 3C Fe_7S_8 nanoparticles, with a slope of 7.2, indicating that the sample predominantly exhibits uniaxial anisotropy.

For a system with uniaxial magnetocrystalline anisotropy[38], K_{eff} should be proportional to $M_{60\ k\ Oe}^{3}$, whereas for a cubic magnetocrystalline anisotropy, K_{eff} should be proportional to $M_{60\ kOe}^{10}$. The linear fit of the plot gives a slope of 7.2, indicating that the sample predominantly exhibits uniaxial anisotropy.

The BH_{max} for all the samples is estimated using the equation 3.1. The 2nd quadrant of the *B-H* loop for 3C Fe_7S_8 nanostructure at all temperatures is shown in the inset of the figure 3.24. The area under the gray shaded portion represents the BH_{max} of the sample[38]. For the given set of measurement temperature values (7 K, 33 K, 210 K, and 300 K), the value of BH_{max} at 300 K is 89.9 kG Oe, at 300 K, which becomes 143.2 kG Oe at 7 K (table 3.1), making the compound valuable for various applications at low-temperature.

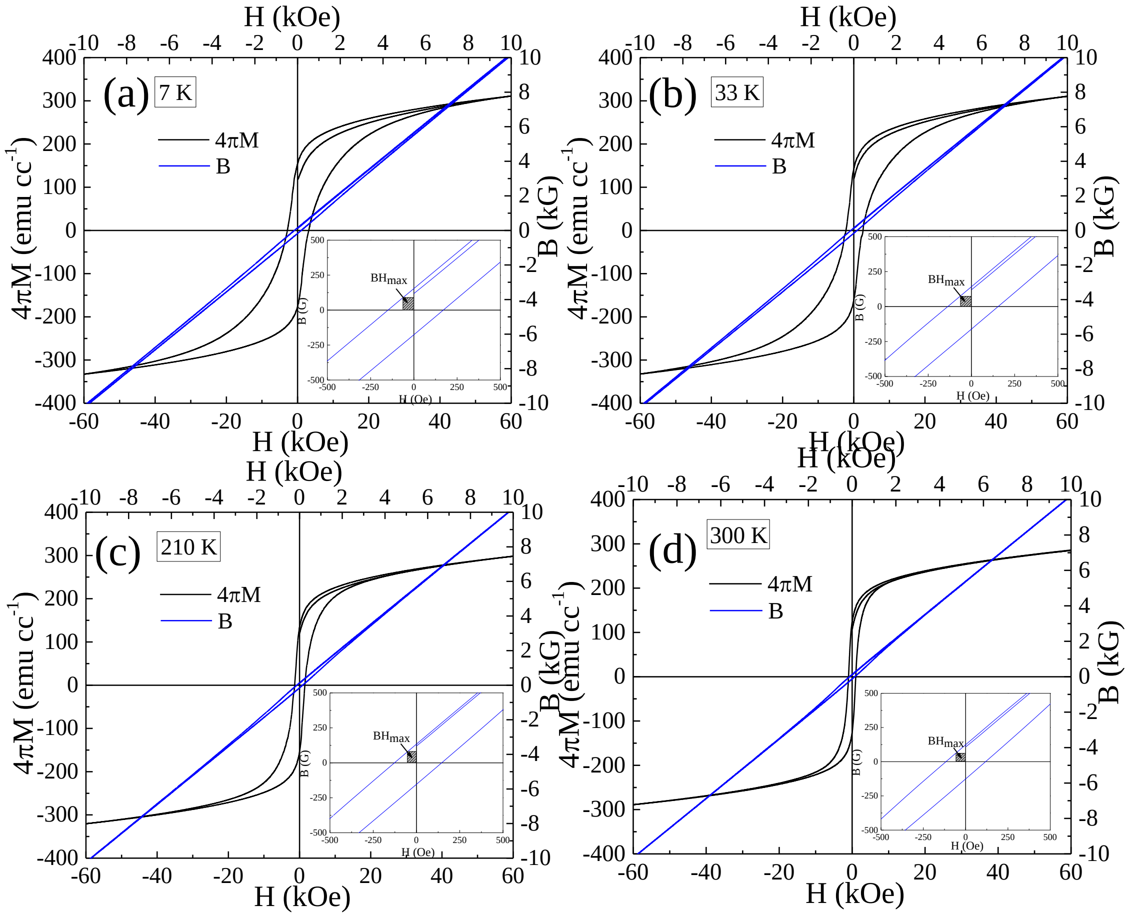

Figure 3.24: (a-h) M-H plot and B-H plot for the sample 20 at% Gd-substituted 3C Fe_7S_8 nanoparticles. The inset in each figure shows the calculation of the maximum energy product from B-H hysteresis loop at 7, 33, 210 and 300 K.

(iv) x=0.25

To investigate the magnetic properties of the 25 at% Gd-substituted 3C Fe_7S_8 nanoparticles, the ZFC-FC M-T measurements have been recorded using SQUID-VSM. Figure 3.25a shows the ZFC-FC M-T curves obtained for as-synthesized 25 at% Gd-substituted 3C Fe_7S_8 nanoparticles at the applied magnetic field of 1000 Oe, respectively. The ZFC and FC *M-T* curves are split in the temperature range from 7 to 300 K. The M-T curves show that the ZFC and FC curves do not follow the same path. Hence, the M-T curves show an irreversible behavior. The emergence of an ordered magnetic state with a high T_C of the sample above 300 K is shown by the divergence of the ZFC-FC M-T curves of 25 at% Gd-substituted 3C

Fe_7S_8 over the entire range of temperature up to 300 K. As shown in the TEM images, the as-synthesized nanoparticles are agglomerated as many nanocrystallites; hence the ZFC peak is regarded as the average blocking temperature (T_B). Polydispersity in the sample may cause the blocking phenomena for each particle on each side of the ZFC peak[51], resulting in the bifurcation of the ZFC-FC curve above T_B. Figure 3.25b shows the T_B for the sample at ~210 K at 1000 Oe applied magnetic field. Another low-temperature magnetic transition is observed at ~33 K[20]. The structure of 3C pyrrhotite with space group $P3_121$ resembles that of the 4C structure in the sense that vacancies are confined to alternate layers of iron. Powder samples of 4C pyrrhotite show an anomaly at low-temperature ~30-34 K (known as Besnus transition[19,20]). This low-temperature magnetic transition stems from the spin rotation, which can be related to the structural changes at an atomic level caused by the highly ordered vacancies in 4C pyrrhotite, which in turn affect the spin-orbit coupling with no crystallography change of the structure. Assuming the similar spin arrangements in 3C and 4C pyrrhotites, the low-temperature magnetic transition observed at ~33 K at 1000 Oe applied magnetic field (Figure 3.25b) for as-synthesized 3C pyrrhotite may be assigned as the Besnus transition.

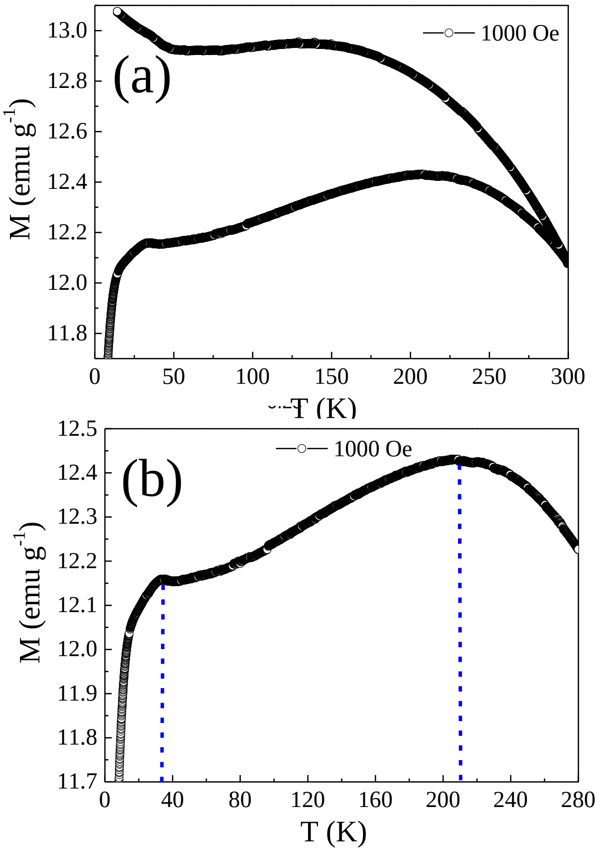

Figure 3.25: (a) Zero-field-cooled (ZFC) and field-cooled (FC) magnetization *vs.* temperature (M-T) curves for the sample 25 at% Gd-substituted 3C Fe_7S_8 nanoparticles at 1000 Oe, (b) ZFC M-T curves for the sample 25 at% Gd-substituted 3C Fe_7S_8 at applied external fields of 1000 Oe in the temperature range of 7-300 K.

To acquire further insights into the magnetic properties of the 25 at% Gd-substituted 3C Fe_7S_8 nanoparticles, the M-H curves were measured using a SQUID-VSM. Figure 3.10(a-d) shows M-H hysteresis curves taken at 7, 33, 210 K, and 300 K in the magnetic field range of ±60 kOe because of the anomalies observed at these temperature values in M-T graphs (figure 3.25b). As shown in Figure 3.26(a-d), the sample demonstrates ferrimagnetic-like behavior at all measurement temperatures. However, at the maximum applied magnetic field of 60 kOe, the magnetization does not exhibit saturation. Such behavior indicates that the spins of the system require a high anisotropic field to align in a particular direction. We observed an initial remanence in the sample at all measurement temperatures. Remanence comes from the vacancies in the specimen. The presence of initial remanence in the M-H hysteresis loop may be attributed to the induced magnetization due to the Fe vacancies in a powdered polycrystalline sample. The hysteresis curves illustrate that H_C, $M_{60\ kOe}$, and M_R values of the sample increase with a decrease in temperature.

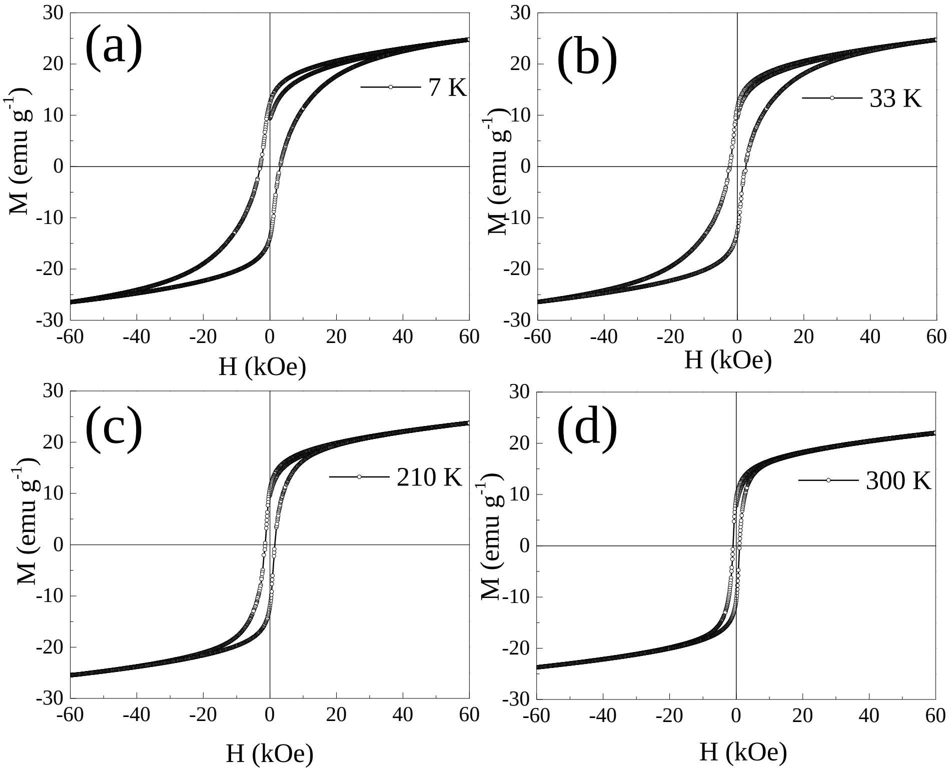

Figure 3.26: (a-d) Magnetization vs. external magnetic field (M-H) hysteresis loops of the sample 25 at% Gd-substituted 3C Fe_7S_8 nanoparticles at 7 K, 33 K, 210 K and 300 K. The M-H hysteresis loops illustrate the increase in $M_{60\ kOe}$, H_C, and M_R values of the sample with decrease in temperature.

Among all four measurement temperature values, the 25 at% Gd-substituted 3C Fe_7S_8 NPs appear to exhibit hysteresis with H_C ~2.0 kOe, $M_{60\ kOe}$, ~25 emu g^{-1}, and M_R ~13 emu g^{-1} at 300 K, which increases to H_C ~4.0 kOe, $M_{60\ kOe}$, ~26 emu g^{-1},and M_R ~14 kOe at 7 K (table 3.6).

Table 3.6: Summary of the magnetic parameters calculated for the sample 25 at% Gd-substituted 3C Fe_7S_8 nanoparticles at different measurement temperatures.

Measurement temperature (K)	H_C (kOe)	M_R (emu g^{-1})	$M_{60\ kOe}$ (emu g^{-1})	M_R/M_S	H_a (kOe)	K_{eff} (erg cc^{-1}) ×10^5	BH_{max} (kG Oe)
7	3.9	13.7	26	0.527	12.3	10.09	146.8
33	3.3	13.1	25.7	0.509	8.9	7.68	132.3
210	2.5	12.3	25	0.492	5.3	4.5	119.2
300	2	10.9	24.9	0.438	4.7	3.76	91.4

The decrease in thermal activation energy and the rise in total effective magnetic anisotropy, which creates more spins available to align in the direction of the applied magnetic field, may have contributed to the increase in these values at the lower temperature[51,55]. Fe^{2+} and Fe^{3+} ionic states, as well as ordered Fe vacancies, are present in the $Fe_{1-x}S$ compounds in addition to alternate levels of the lattice. The magnetic moments of Fe in the compound are ferromagnetically arranged inside each layer, however, are coupled antiferromagnetically to each other between adjacent layers. The vacancies in every second layer contribute to the spin orientation. The presence of ionic states of iron and the vacancies in the lattice lead to uncompensated magnetic moments, giving rise to the ferrimagnetic ordering in the compound.

The value of K_{eff} is 3.76×10^5 erg cc^{-1} at 300 K, which increases to 10.09×10^5 erg cc^{-1} at 7 K (table 3.6). To determine the type of magnetocrystalline anisotropy, ln (K_{eff}) is plotted against ln ($M_{60\ kOe}$), as shown in figure 3.27.

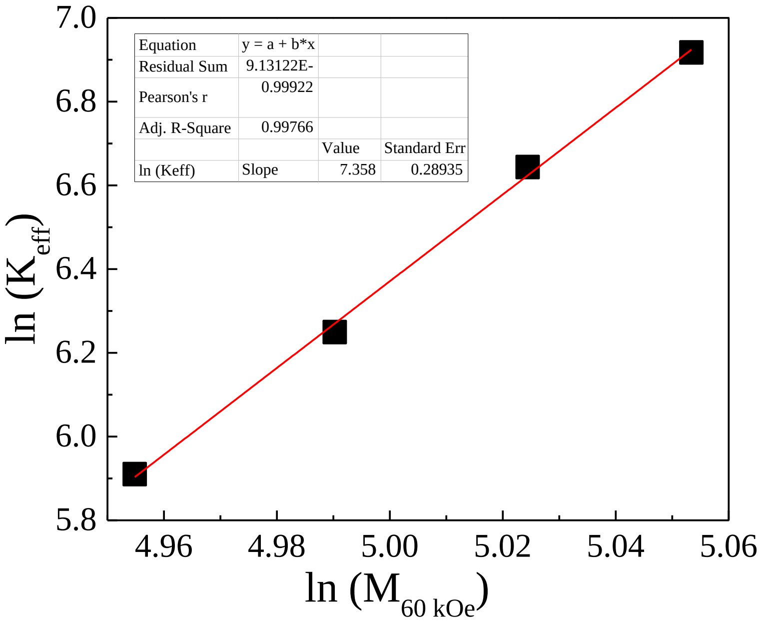

Figure 3.27: Linear relationship between K_{eff} and $M_{60\ kOe}$ in the logarithmic scale for the sample with 25 at% Gd-substituted 3C Fe_7S_8 nanoparticles, with a slope of 7.4, indicating that the sample predominantly exhibits uniaxial anisotropy.

For a system with uniaxial magnetocrystalline anisotropy[38], K_{eff} should be proportional to $M_{60\ k\ Oe}{}^{3}$, whereas for a cubic magnetocrystalline anisotropy, K_{eff} should be proportional to $M_{60\ kOe}{}^{10}$. The linear fit of the plot gives a slope of 7.4, indicating that the sample predominantly exhibits uniaxial anisotropy.

The BH_{max} for all the samples is estimated using the equation 3.1. The 2nd quadrant of the B-H loop for 3C Fe_7S_8 nanostructure at all temperatures is shown in the inset of the figure 3.28. The area under the gray shaded portion represents the BH_{max} of the sample[38]. For the given set of measurement temperature values (7 K, 33 K, 210 K, and 300 K), the value of BH_{max} at 300 K is 91.4 kG Oe, which becomes 146.8 kG Oe at 7 K (table 3.1), making the compound valuable for various applications at low-temperature.

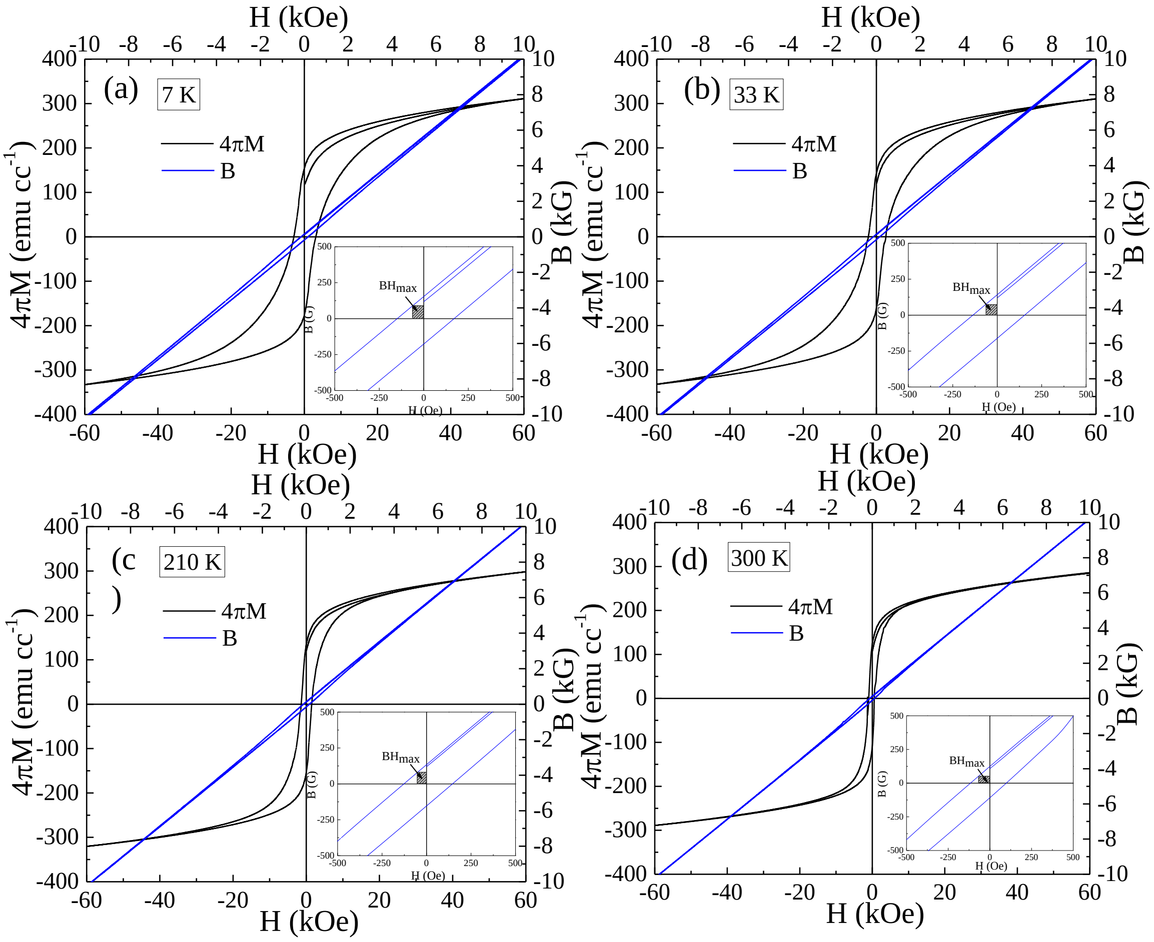

Figure 3.28: (a-h) M-H plot and B-H plot for the sample 25 at% Gd-substituted 3C Fe_7S_8 nanoparticles. The inset in each figure shows the calculation of the maximum energy product from B-H hysteresis loop at 7, 33, 210 and 300 K.

3.3.3 Effect of Gd-substitution in 3C Fe_7S_8 lattice

From the results shown above, we have observed the increase in the values H_C, K_{eff}, $M_{60\ kOe}$ and BH_{max} as the concentration of Gd is increased in the sample 3C Fe_7S_8 at different measurement temperatures. The magnetic moment of Gd^{3+} ions (7.94 μB) is higher as compared to the Fe^{3+} ions (5 μB). The magnetic moment of Gd^{3+} ion comes from the $4f_{7}$ shell electrons. The dipole moments in Gd^{3+} are randomly oriented at the room temperature, owing to which their impact to magnetic moment contribution is very slight. As the temperature is decreased the moments of Gd^{3+} get aligned in the direction of applied magnetic field, owing to the lesser thermal activation energy. Hence, the magnetization (at 60 k Oe) increases with the decrease in temperature. The energy product depends directly on the saturation magnetization, resulting in the decrease in the value of BH_{max} as $M_{60\ kOe}$ decreases. The H_C values overall increases with Gd^{3+} substitution in the parent lattice. The huge enhancement in the values of H_C could be due to the gain in the effective anisotropy constant (K). Figure 3.29(a-d) shows the variation of different magnetic parameters with the change in Gd concentration in the parent lattice.

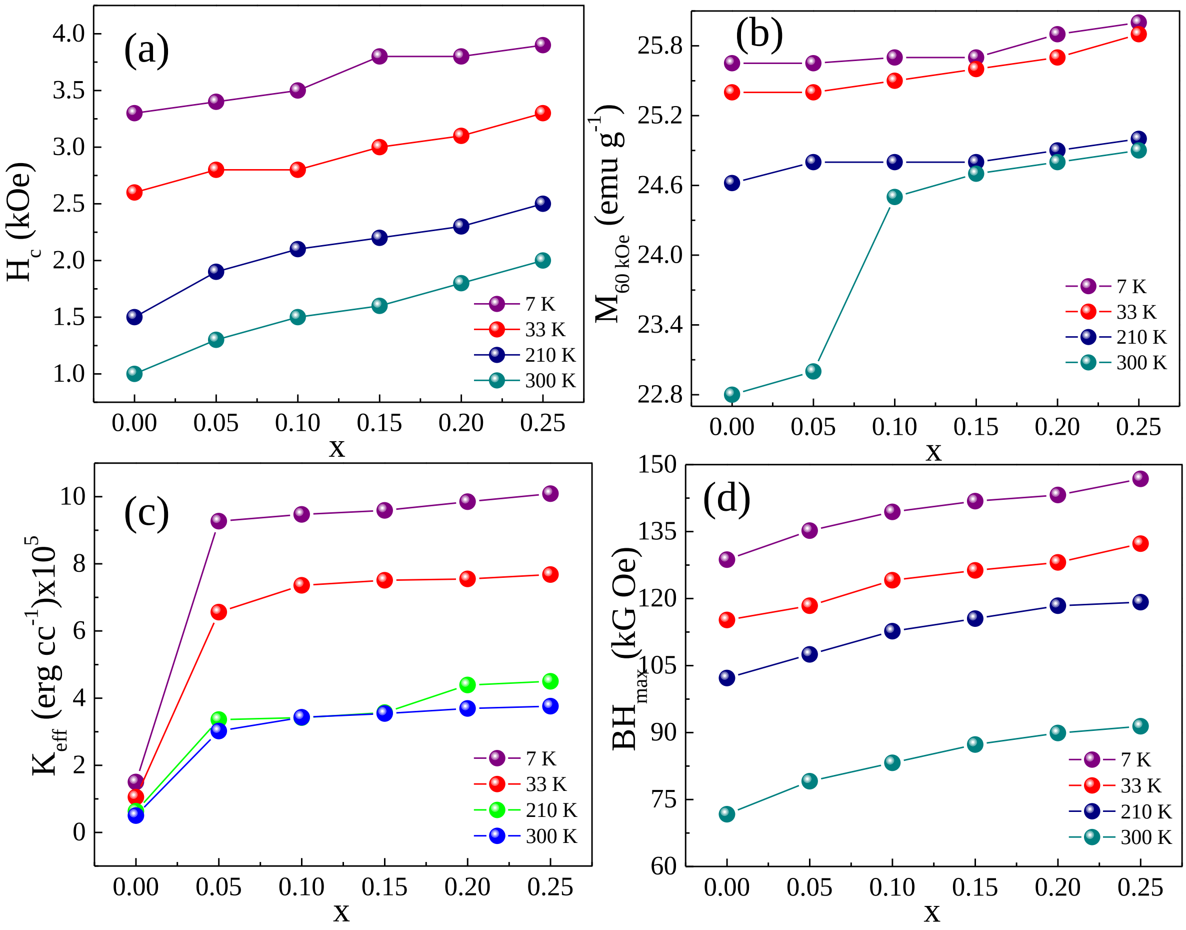

Figure 3.29: Variation of (a) H_C, (b) $M_{60\ kOe}$, (c) K_{eff}, and (d) BH_{max} at different measurement temperature as a function of change in the concentration of Gd^{3+} ions in the lattice.

3.4. Conclusions

The impact of Gd-substitution on the magnetic properties of 3C Fe_7S_8 nanoparticles has been studied. The results show that the blocking temperature of all the samples remain nearly constant at all concentration of Gd in the lattice. The magnetization value measured at highest applied field (60 kOe) increased with the increase in the concentration of Gd. The value of coercivity increased as the concentration of Gd was increased, which resulted from the increase in the effective anisotropy constant. The increase in the $M_{60\ kOe}$ resulted in the increased value of energy product. The pure phase of 3C Fe_7S_8 nanoparticles exhibited a high value of BH_{max} (~129 kG Oe) at 7 K. These values increased with increased Gd concentration in the lattice. The high value of energy product without the presence of rare earth indicate towards its low-temperature applications. The findings in this work open doors for vivid scope research in this area.

References

1 Y. Yuan, L. Wang and L. Gao, *Front. Chem.* , 2020, 8.

2 Y. Shan, W. Lu, J. Xi and Y. Qian, *Front. Chem.* , 2022, 10.

3 W. Davison, The solubility of iron sulphides in synthetic and natural waters at ambient temperature, *Aquat. Sci.*, 1991, **53**, 309–329.

4 L. Sagnotti, eds. D. Gubbins and E. Herrero-Bervera, Springer Netherlands, Dordrecht, 2007, pp. 454–459.

5 P. S. Minyuk, E. E. Tyukova, T. V Subbotnikova, A. Y. Kazansky and A. P. Fedotov, Thermal magnetic susceptibility data on natural iron sulfides of northeastern Russia, *Russ. Geol. Geophys.*, 2013, **54**, 464–474.

6 A. Matamoros-Veloza, O. Cespedes, B. R. G. Johnson, T. M. Stawski, U. Terranova, N. H. de Leeuw and L. G. Benning, A highly reactive precursor in the iron sulfide system., *Nat. Commun.*, 2018, **9**, 3125.

7 M. Saeed Akhtar, A. Alenad and M. Azad Malik, Synthesis of mackinawite FeS thin films from acidic chemical baths, *Mater. Sci. Semicond. Process.*, 2015, **32**, 1–5.

8 R. A. Berner, Sedimentary pyrite formation: An update, *Geochim. Cosmochim. Acta*, 1984, **48**, 605–615.

9 G. W. Luther, Pyrite synthesis via polysulfide compounds, *Geochim. Cosmochim. Acta*, 1991, **55**, 2839–2849.

10 J. R. Craig, F. M. Vokes and T. N. Solberg, Pyrite: physical and chemical textures, *Miner. Depos.*, 1998, **34**, 82–101.

11 M. Tokonami, K. Nishiguchi and N. Morimoto, Crystal Structure of a Monoclinic Pyrrhotite (Fe7S8), *Am. Mineral.*, 1972, **57**, 1066–1080.

12 J. R. Gosselin, M. G. Townsend, R. J. Tremblay and A. H. Webster, Mössbauer investigation of synthetic single crystal monoclinic Fe7S8, *Mater. Res. Bull.*, 1975, **10**, 41–49.

13 W. Han and M. Gao, Investigations on Iron Sulfide Nanosheets Prepared via a Single-Source Precursor Approach, *Cryst. Growth Des.*, 2008, **8**, 1023–1030.

14 A. Nakano, M. Tokonami and N. Morimoto, Refinement of 3C Pyrrhotite, Fe7S8, *Acta Cryst.*, 1979, **35**, 724–725.

15 A. H. CLARK, Iron-deficient Low-temperature Pyrrhotite, *Nature*, 1965, **205**, 792–793.

16 A. D. Elliot, Structure of pyrrhotite 5C (Fe9S10), *Acta Crystallogr. Sect. B*, 2010, **66**, 271–279.

17 S. Hunger and L. G. Benning, Greigite: A true intermediate on the polysulfide pathway to pyrite, *Geochem. Trans.*, , DOI:10.1186/1467-4866-8-1.

18 E.J. SCHWARZ and D.J. VAUGHAN, Magnetic Phase Relations of Pyrrhotite, *J. Geomag. Geoelectr*, 1972, **139**, 66–89.

19 D. Koulialias, B. Lesniak, M. Schwotzer, P. G. Weidler, J. F. Löffler and A. U. Gehring, The Besnus Transition in Single-Domain 4C Pyrrhotite, *Geochemistry, Geophys. Geosystems*, 2019, **20**, 5216–5224.

20 C. R. S. Haines, C. J. Howard, R. J. Harrison and M. A. Carpenter, Group-theoretical analysis of structural instability, vacancy ordering and magnetic transitions in the system troilite (FeS){--}pyrrhotite (Fe${\sb 1{$-$}{\it x}}$S), *Acta Crystallogr. Sect. B*, 2019, **75**, 1208–1224.

21 M. Kawaminami and A. Okazaki, Neutron Diffraction Study of Fe7Se8. II, *J. Phys. Soc. Japan*, 1970, **29**, 649–655.

22 A. Okazaki and K. Hirakawa, Structural Study of Iron Selenides FeSex. I Ordered Arrangement of Defects of Fe Atoms, *J. Phys. Soc. Japan*, 1956, **11**, 930–936.

23 L. Néel, Some New Results on Antiferromagnetism and Ferromagnetism, *Rev. Mod. Phys.*, 1953, **25**, 58–63.

24 E. F. Bertaut, Contribution à l'étude des structures lacunaires: la pyrrhotine, *Acta Crystallogr.*, 1953, **6**, 557–561.

25 S. Parker, *Opposites Attract: Magnetism*, Heinemann-Raintree Library, 2004.

26 C. C. Pavel, A. Marmier, P. Alves Dias, D. Blagoeva, E. Tzimas, D. Schüler, T. Schleicher, W. Jenseit, S. Degreif and M. Buchert, Substitution of critical raw materials in low-carbon technologies: lighting, wind turbines and electric vehicles, *Luxemb. Eur. Comm. Oko-Institut eV*.

27 V. Chaudhary, S. A. Mantri, R. V Ramanujan and R. Banerjee, Additive manufacturing of magnetic materials, *Prog. Mater. Sci.*, 2020, **114**, 100688.

28 M. Grönefeld, I. Teliban and J. Krzywinski, 9.7 Permanent magnets, *From Magn. to Bioact. Mater.*, 2022, 114.

29 J. D. Livingston, The history of permanent-magnet materials, *Jom*, 1990, **42**, 30–34.

30 Z. Zhu, Y. Pranolo and C. Y. Cheng, Separation of uranium and thorium from rare earths for rare earth production–A review, *Miner. Eng.*, 2015, **77**, 185–196.

31 Y. Kanazawa and M. Kamitani, Rare earth minerals and resources in the world, *J. Alloys Compd.*, 2006, **408**, 1339–1343.

32 M. Honshima and K. Ohashi, High-energy NdFeB magnets and their applications, *J. Mater. Eng. Perform.*, 1994, **3**, 218–222.

33 S. C. Westmoreland, C. Skelland, T. Shoji, M. Yano, A. Kato, M. Ito, G. Hrkac, T. Schrefl, R. F. L. Evans and R. W. Chantrell, Atomistic simulations of α-Fe/Nd2Fe14B magnetic core/shell nanocomposites with enhanced energy product for high temperature permanent magnet applications, *J. Appl. Phys.*, 2020, **127**, 133901.

34 V. Ly, X. Wu, L. Smillie, T. Shoji, A. Kato, A. Manabe and K. Suzuki, Low-temperature phase MnBi compound: A potential candidate for rare-earth free permanent magnets, *J. Alloys Compd.*, 2014, **615**, S285–S290.

35 V. Van Nguyen and T. X. Nguyen, Effects of microstructures on the performance of rare-earth-free MnBi magnetic materials and magnets, *Phys. B Condens. Matter*, 2018, **532**, 103–107.

36 X. Rui, J. E. Shield, Z. Sun, L. Yue, Y. Xu, D. J. Sellmyer, Z. Liu and D. J. Miller, High-energy product exchange-spring FePt/Fe cluster nanocomposite permanent magnets, *J. Magn. Magn. Mater.*, 2006, **305**, 76–82.

37 M. Sen Bishwas, R. Das and P. Poddar, Large Increase in the Energy Product of Fe 3 Se 4 by Fe-Site Doping.

38 B. D. Cullity, *Introduction to Magnetic Materials*, Addision Wesley Publicating Company, Reading, MA, 1972.

39 S. Amiri and H. Shokrollahi, The role of cobalt ferrite magnetic nanoparticles in medical science, *Mater. Sci. Eng. C*, 2013, **33**, 1–8.

40 S. Sivakumar, D. Anusuya, C. P. Khatiwada, J. Sivasubramanian, A. Venkatesan and P. Soundhirarajan, Characterizations of diverse mole of pure and Ni-doped α-Fe2O3 synthesized nanoparticles through chemical precipitation route, *Spectrochim. Acta Part A Mol. Biomol. Spectrosc.*, 2014, **128**, 69–75.

41 S. Del Sol-Fernández, Y. Portilla-Tundidor, L. Gutiérrez, O. F. Odio, E. Reguera, D. F. Barber and M. P. Morales, Flower-like Mn-Doped Magnetic Nanoparticles Functionalized with α v β3-Integrin-Ligand to Efficiently Induce Intracellular Heat after Alternating Magnetic Field Exposition, Triggering Glioma Cell Death, *ACS Appl. Mater. Interfaces*, 2019, **11**, 26648–26663.

42 Y.-H. Chen, M. Franzreb, R.-H. Lin, L.-L. Chen, C.-Y. Chang, Y.-H. Yu and P.-C. Chiang, Platinum-doped TiO2/magnetic poly (methyl methacrylate) microspheres as a novel photocatalyst, *Ind. Eng. Chem. Res.*, 2009, **48**, 7616–7623.

43 A. Petran, T. Radu, G. Borodi, A. Nan, M. Suciu and R. Turcu, Effects of rare earth doping on multi-core iron oxide nanoparticles properties, *Appl. Surf. Sci.*, 2018, **428**, 492–499.

44 K. P. Rice, S. E. Russek, R. H. Geiss, J. M. Shaw, R. J. Usselman, E. R. Evarts, T. J. Silva, H. T. Nembach, E. Arenholz and Y. U. Idzerda, Temperature-dependent structure of Tb-doped magnetite nanoparticles, *Appl. Phys. Lett.*, 2015, **106**, 62409.

45 A. R. Jha, *Rare Earth Materials: Properties and Applications*, CRC Press, Boca Raton, 2016.

46 M. Bottrill, L. Kwok and N. J. Long, Lanthanides in magnetic resonance imaging, *Chem. Soc. Rev.*, 2006, **35**, 557–571.

47 A. Rękorajska, G. Cichowicz, M. K. Cyranski, M. Pękała and P. Krysinski, Synthesis and characterization of Gd3+-and Tb3+-doped iron oxide nanoparticles for possible endoradiotherapy and hyperthermia, *J. Magn. Magn. Mater.*, 2019, **479**, 50–58.

48 R. M. Pallares and R. J. Abergel, Transforming lanthanide and actinide chemistry with nanoparticles, *Nanoscale*, 2020, **12**, 1339–1348.

49 M. E. Fleet, The crystal structure of a pyrrhotite (Fe7S8), *Acta Crystallogr. Sect. B Struct. Crystallogr. Cryst. Chem.*, 1971, **27**, 1864–1867.

50 P. A. Joy, P. S. Anil Kumar and S. K. Date, The relationship between field-cooled and zero-field-cooled susceptibilities of some ordered magnetic systems, *J. Phys. Condens. Matter*, 1998, **10**, 11049–11054.

51 G. Long, H. Zhang, D. Li, R. Sabirianov, Z. Zhang and H. Zeng, Magnetic anisotropy and coercivity of Fe3Se4 nanostructures, *Appl. Phys. Lett.*, 2011, **99**, 4–7.

52 J. M. D. Coey, *Magnetism and Magnetic Materials*, Cambridge University Press, Cambridge, UK, 2010.

53 D. Koulialias, R. Schäublin, G. Kurtuldu, P. G. Weidler, J. F. Löffler and A. U. Gehring, On the Magnetism Behind the Besnus Transition in Monoclinic Pyrrhotite, *J. Geophys. Res. Solid Earth*, 2018, **123**, 6236–6246.

54 C. S. Horng and A. P. Roberts, The Low-Temperature Besnus Magnetic Transition: Signals Due to Monoclinic and Hexagonal Pyrrhotite, *Geochemistry, Geophys. Geosystems*, 2018, **19**, 3364–3375.

55 M. G. and P. Poddar, Remarkable Effect of Fe and Se Composition on Magnetic Properties─Comparative Study of the Fe–Se System at the Nanoscale, *J. Phys. Chem. C*, 2022, **9**, 4655–4663.

Chapter 4

Dielectric properties of 3C Fe_7S_8 and Gd-substituted 3C Fe_7S_8 nanoparticles

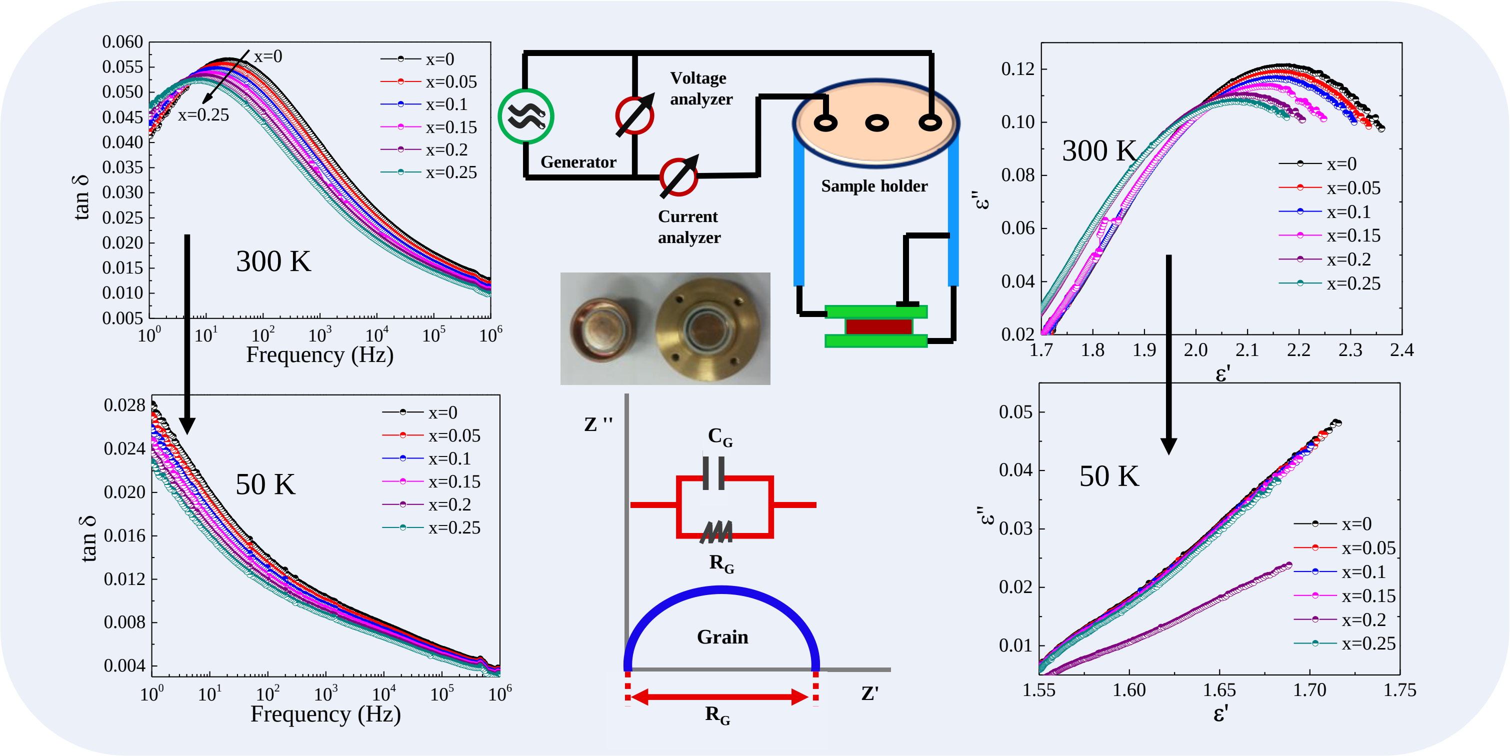

Highlights

Below are some of the findings that we would like to highlight.

- Both the real and out of phase parts of the complex dielectric permittivity (ε′ and ε′’, respectively) along with absolute permittivity (|ε|) and dielectric loss factor (tan δ) as a function of frequency for unsubstituted and Gd-substituted samples at different measurement temperatures (50, 100, 150, 200, 250 and 300 K) are measured.
- The effect of the Gd substitution has been observed as the decrease in the values of ε′ and tan δ.
- The material exhibits a negative temperature coefficient of resistance-type behavior-type behavior.
- The Cole-Cole plot highlights the decrease in resistivity from the grain with an increasing temperature and concentration of Gd, indicating the non-Debye kind of relaxation process.

Keywords: Impedance spectroscopy, dielectric constant, dielectric loss, Cole-Cole plot

4.1. Introduction

Impedance spectroscopy is a technique that can be used to study all of the fundamental immittance levels[1,2]. The method that comprises the measurement of a material's small-signal linear electrical response that follows to offer essential details regarding a system's electrical characteristics[3–5], not only limited to data interpretation and measurement at the impedance level, given that impedance spectroscopy deals with complex quantities directly[6,7]. Although measurements are occasionally taken in the time domain and then Fourier converted to the frequency domain, analysis is often done in the frequency domain[8–10]. Given that impedance spectroscopy deals with complex quantities directly, the field of electrical engineering actually began in the 1880s with Oliver Heaviside's development of impedance[11,12]. Additionally, A.E. Kennelly and C.P. Steinmetz added complex representation and vector diagrams[13] to their technique. It took very little time for field to start immittance responses in the complex plane with frequency and using the Argand diagram of mathematics[14,15]. Examples from the field of electrical engineering include P. H. Smith's Smith-Chart impedance diagram and C. W. Carter's circle diagram[16]. After the Cole-Cole plot, which is a plot of ε' on the x (or real) axis vs. ε'' on the y (or imaginary) axis, was introduced[17–19] in 1941, the aforementioned methods were quickly adopted in the dielectric response area. These complex plane plots are now frequently used to depict the responses of all immittance kinds in two dimensions.

Impedance spectroscopy can be divided into two basic categories: electrochemical impedance spectroscopy[20] and everything else. In electrochemical impedance spectroscopy, materials with a strong ionic conduction bias are measured and examined. Ionically conducting glasses, solid and liquid electrolytes, fused salts, and polymers are a few examples of such materials, in which motion of ions in the interstitial space and vacancies can contribute to conduction. The other class of impedance spectroscopy involves dielectric materials[1], such as solid or liquid nonconductors with dipolar rotational electrical properties, and materials with a predominance of electronic conduction. Examples include glasses, amorphous semiconductors, single-crystal as well as polymers.

Debye response[1,21], which only involves a single time constant, is a crucial component of impedance spectroscopy. Figure 4.1 depicts the response as a Cole-Cole plot. The direction of increasing frequency is shown by the arrow. Complex representation of the Debye response is presented as $\varepsilon=\varepsilon_\infty+[\varepsilon_o-\varepsilon_\infty]/[1+(i\omega\tau)]$. The formula, $\tau=RC$, yields the time constant or relaxation time.

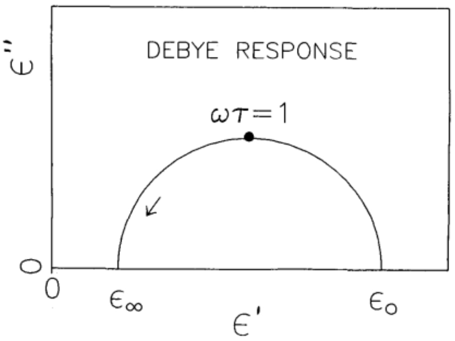

Figure 4.1: Complex-plane plot of the complex dielectric constant for Debye frequency response.

Binary metal chalcogenide, 3C Fe_7S_8, which was covered in earlier chapters, has not received much attention to date. However, the studies in chapter 3 show that even without Gd, it has a high uniaxial magnetic anisotropy constant, resulting in extremely high coercivity at room temperature. With a high Curie temperature (over 300 K) and a trigonal structure with the space group $P3_121$, 3C Fe_7S_8 is ferrimagnetic at room temperature. However, owing to the excellent magnetic properties, the electrical properties of the trigonal iron sulphide is yet to be explored. The electrical structure variations with particle size and the high surface to volume ratio of nanocrystalline materials may have a significant impact on the magnetic and dielectric properties of nanomaterials.

In this chapter, we investigate a novel and unexpected perspective of 3C Fe_7S_8 in unsubstituted form using impedance spectroscopy. The Gd-substitution trigonal 3C Fe_7S_8 nanoparticles have been synthesized to further tailor the dielectric properties of the material. We found that the Gd^{3+} content significantly influences both the dielectric constant and dielectric loss. The use of Gd^{3+} is intended to lower its dielectric loss.

4.2. Characterization techniques

The frequency-dependent dielectric measurements were performed using Novocontrol Beta NB Impedance Analyzer, capable of measuring impedance response of sample from few µHz to MHz. The analyzer was connected with home-built sample holder to couple with a helium closed cycle refrigerator (Janis Inc.) for temperature control of the sample space. The powdered sample was compressed in a hydraulic press in the form of circular pellet of diameter 13 mm and a custom designed sample holder was used to form parallel plate capacitor geometry. The principle of dielectric spectroscopy is illustrated schematically in figure 4.2.

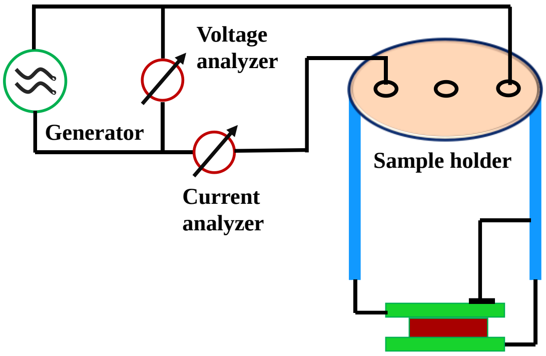

Figure 4.2: Principle of a dielectric/impedance measurement with a parallel plate geometry.

4.3. Results and discussions

Both the real and out of phase parts of the complex dielectric permittivity (ε′ and ε′′, respectively) along with absolute permittivity (|ε|) and dielectric loss factor (tan δ) as a function of frequency for unsubstituted and Gd-substituted samples at different measurement temperatures (50, 100, 150, 200, 250 and 300 K) are shown in Figure 4.3 - 4.8, respectively. The curves illustrate that ε′, ε′′, |ε| and tan δ decrease with the increase of frequency.

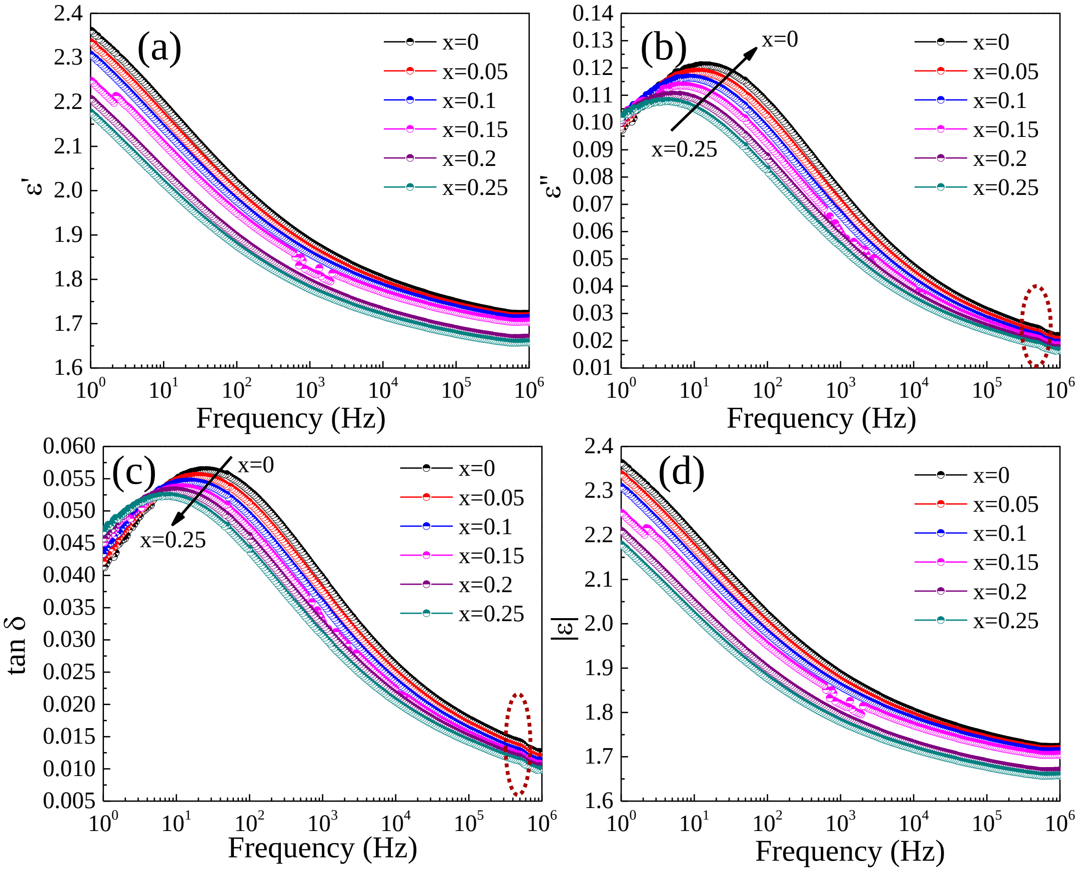

Figure 4.3: Frequency dependence of (a) real part of permittivity (b) out of phase part of permittivity (c) loss factor (d) absolute permittivity measured for 3C Fe_7S_8 and Gd-substituted 3C Fe_7S_8 samples with ac 1 V rms value at 300 K.

The Maxwell-Wagner theory[22] can be used to describe the contributions from the dipolar, interfacial, atomic, ionic, and electronic polarisation to the permittivity values at low frequencies. Values of ε are larger because heavier dipoles can follow the external field at low frequencies. The dipoles fall behind the field as the frequency increases, and the value of ε decreases. Due to ionic impurities in the sample, significantly higher values of permittivity are observed in several compounds.

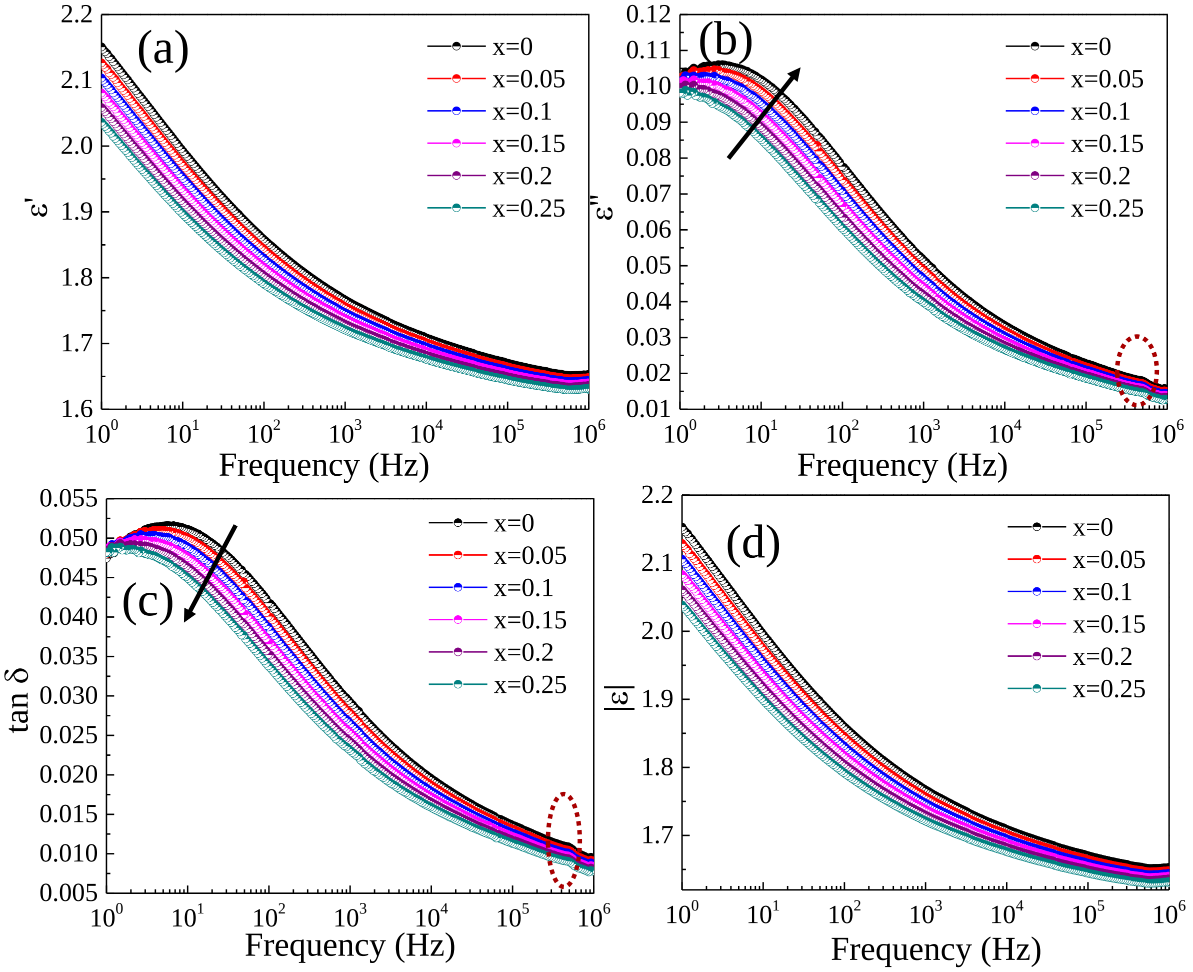

Figure 4.4: Frequency dependence of (a) real part of permittivity (b) out of phase part of permittivity (c) loss factor (d) absolute permittivity measured for 3C Fe_7S_8 and Gd-substituted 3C Fe_7S_8 samples with ac 1 V rms value at 250 K.

As clearly seen in the graphs the both ε′ and tan δ are higher in pure 3C Fe_7S_8 sample than Gd-substituted samples at all measurement temperatures. With the presence of Gd ions, a decrease in the values of ε′ and tan δ is observed with the increasing Gd content and is found to be minimum for x=0.25. A small polarizability of Gd^{3+} ion in comparison with Fe^{3+} and Fe^{3+} ions may be the reason for the small value of ε′. At higher frequencies, however, electronic polarization takes over, and the contribution of dipolar polarization diminishes. The phenomena of dipole relaxation could be used to explain the decrease in dielectric constant as the frequency increases. As lowest dielectric loss is very desirable in nonvolatile FeRAM applications, materials like ours have potential to used in such applications.

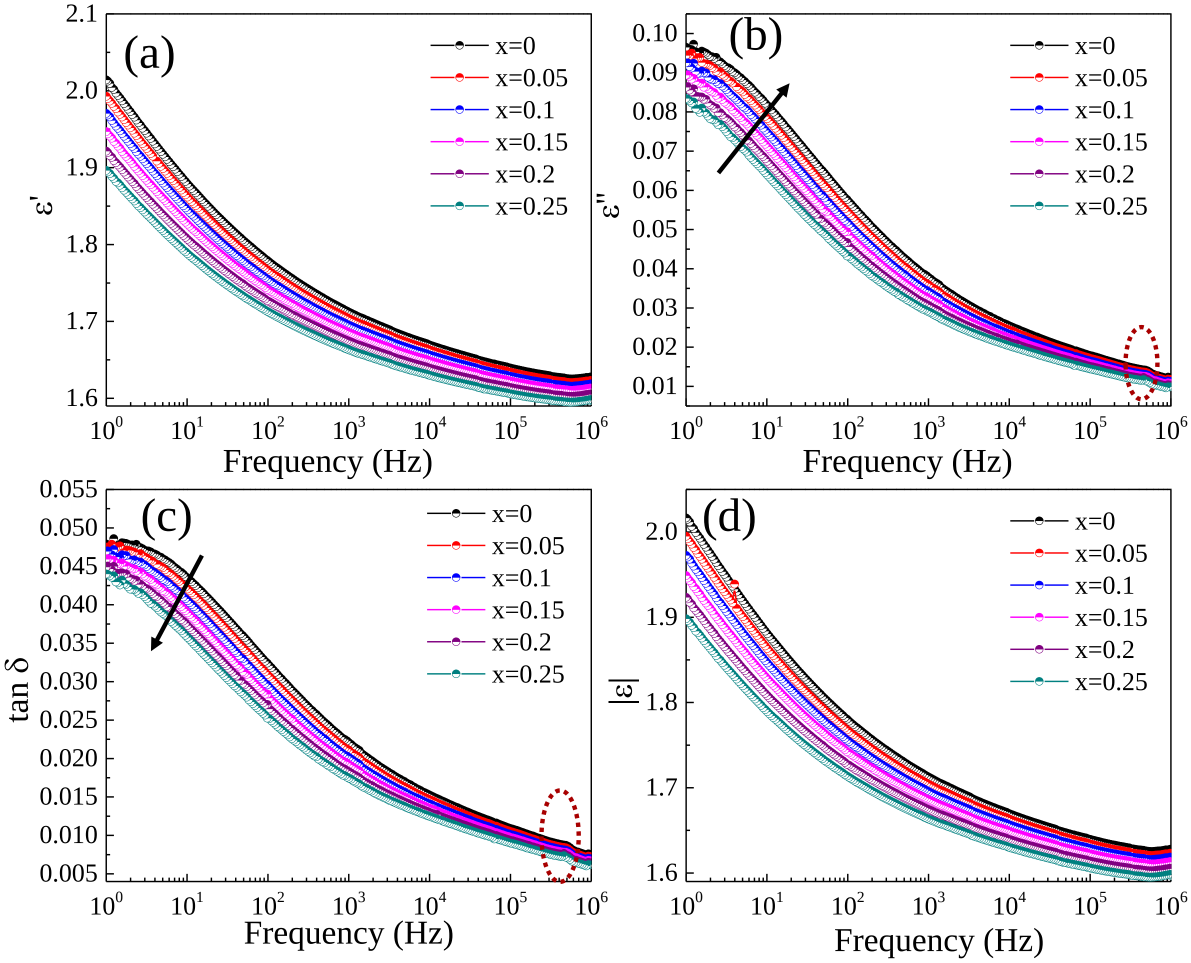

Figure 4.5: Frequency dependence of (a) real part of permittivity (b) out of phase part of permittivity (c) loss factor (d) absolute permittivity measured for 3C Fe_7S_8 and Gd-substituted 3C Fe_7S_8 samples with ac 1 V rms value at 200 K.

At lower frequency, a broad peak is observed for ε″ and tan δ all the samples at 300 K (figure 4.3). These peaks gradually start to disappear at 250 K (figure 4.4) and vanish completely beyond 150 K (figure 4.5-4.8). The sample behaves in a low-frequency domain with a negative temperature coefficient of resistance, as evidenced by the decreasing trend in the dielectric parameters seen together with the rise in measurement temperature in the low-frequency region. This implies that if the barrier qualities of the samples are reduced, it's feasible that the space charge will be released.

The decreasing trend in the dielectric parameters observed along with the increase in measuring temperature in the low-frequency area shows that the sample behaves in a low-frequency domain with a negative temperature coefficient of resistance. This implies that if the material's barrier qualities are reduced, it's feasible that the space charge will be released.

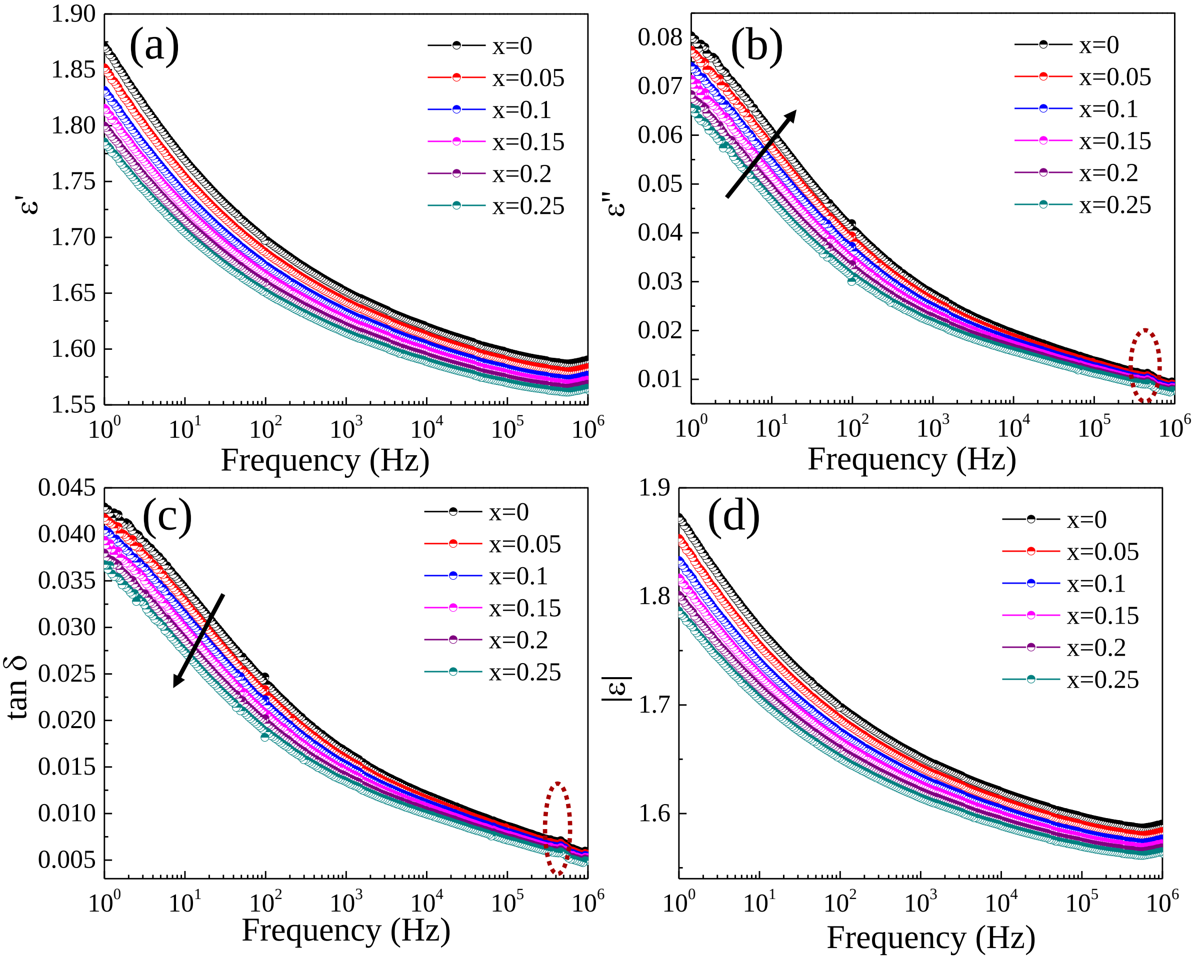

Figure 4.6: Frequency dependence of (a) real part of permittivity (b) out of phase part of permittivity (c) loss factor (d) absolute permittivity measured for 3C Fe_7S_8 and Gd-substituted 3C Fe_7S_8 samples with ac 1 V rms value at 150 K.

The value of the dielectric parameters shows a declining trend as frequency and temperature increase, indicating a potential increase in conductivity as these two variables increase. This suggests that, as temperature rises, electrical conduction will increase, with the process requiring the release of space charge.

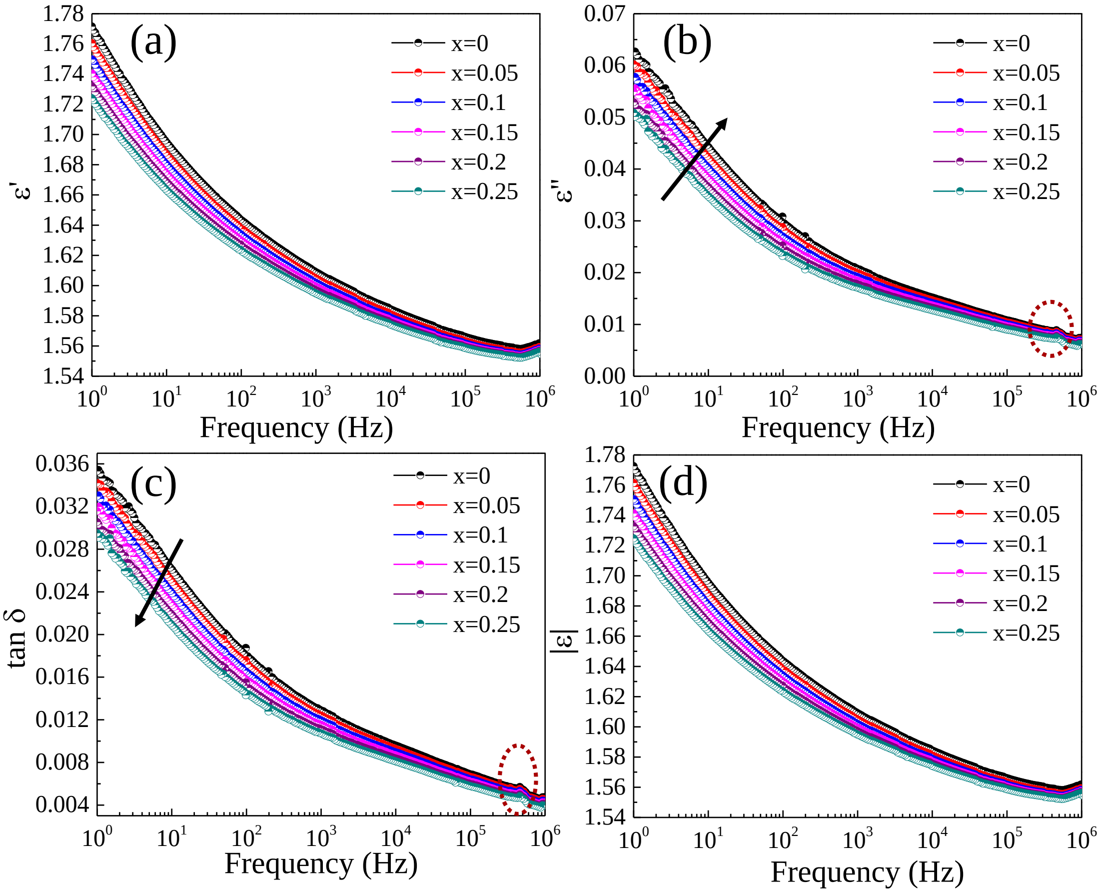

Figure 4.7: Frequency dependence of (a) real part of permittivity (b) out of phase part of permittivity (c) loss factor (d) absolute permittivity measured for 3C Fe_7S_8 and Gd-substituted 3C Fe_7S_8 samples with ac 1 V rms value at 100 K.

The important elements of the fluctuation of ε″ are (a) the relaxation frequency, or the emergence of the peak at a specific frequency, (b) a reduction in the amplitude of ε″ and an apparent shift in the peak frequency toward the high-frequency area, and (c) the broadening nature of the peak as the temperature rises. Peak asymmetry and broadening as well as peak shifting towards low frequency are two characteristics that make the effects of Gd substitution on the compound's electrical processes abundantly obvious. Immobile charge carriers or electrons may be the cause of relaxation at low and high temperatures, which may be a result of defects or vacancies in the samples. At 300 K, a dispersion in the medium frequency range (96 to 105 Hz) has been seen at a given temperature, followed by a gradual drop in the value of ε' in the low frequency region (100 Hz). The dispersion is observed to shift towards lower frequency as temperature increases and vanish below 150 K. The merging of ε' at higher frequencies is related to the non-alignment of dipoles with the electric field, or, more specifically, their failure to follow it. As a result, the polarization contribution is minimal, resulting in a static value for ε'. In general, the relaxation peak of the frequency versus frequency plot is influenced by the dispersion behaviour in ε'. The Gd^{3+} alteration may also be a likely cause of the dispersion characteristic in the samples.

A small kink was observed around temperature 4.8×10^5 Hz in ε" verses frequency curves for all the samples at all measurement temperatures. The kink is encircled in all the graphs. Although the feature is quite weak in nature, the kink observed in this combination may indicate the presence of some coupling in the complex.

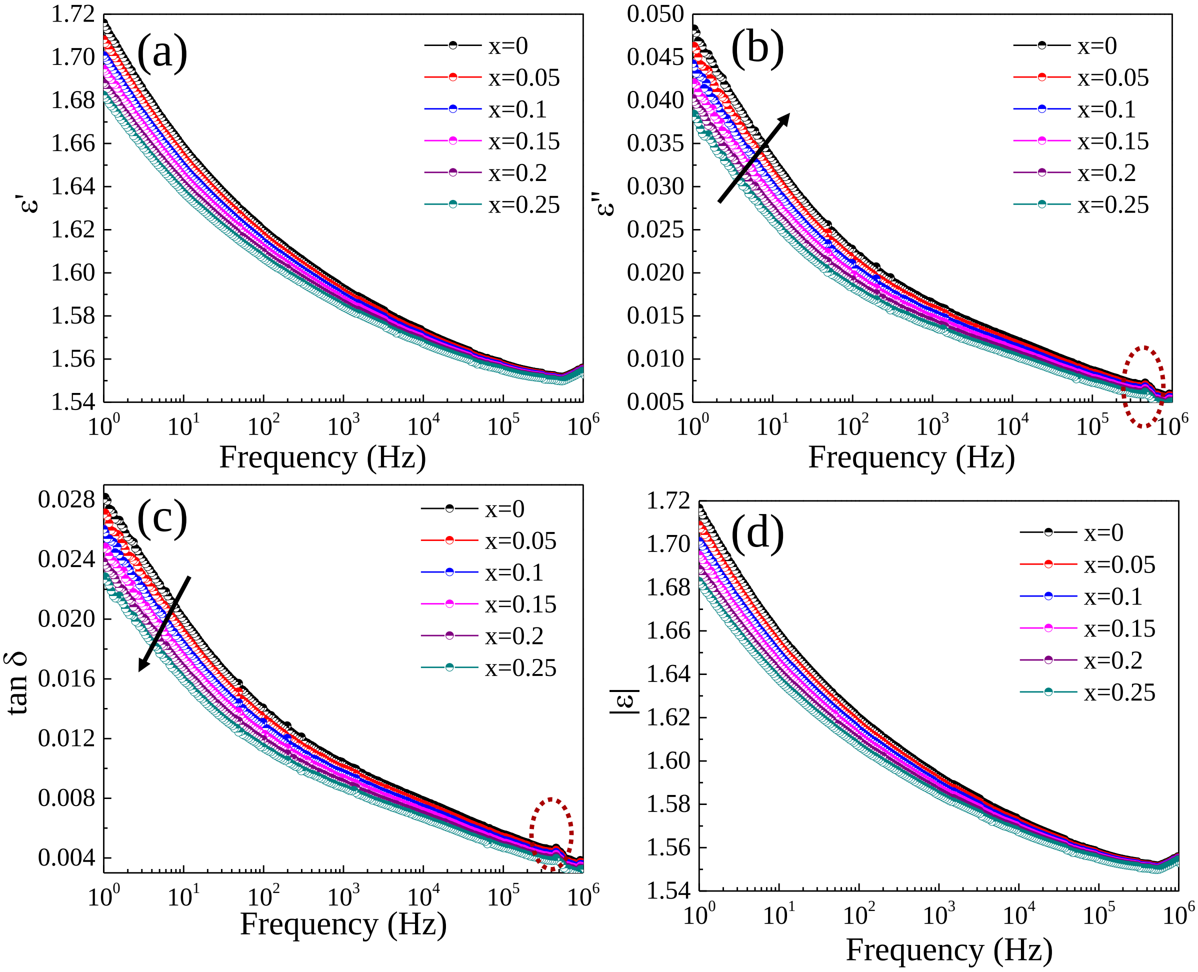

Figure 4.8: Frequency dependence of (a) real part of permittivity (b) out of phase part of permittivity (c) loss factor (d) absolute permittivity measured for 3C Fe_7S_8 and Gd-substituted 3C Fe_7S_8 samples with ac 1 V rms value at 50 K.

Complex Argand plane plots, also known as Cole-Cole plots, were explored to better understand the nature of dielectric relaxation in the samples under investigation. Figure 4.9 displays the graphs for all the samples between the real (ε') and out of phase (ε'') parts of the impedance at various temperatures. As seen in the figure, only one semi-circular-like arc is visible at high temperatures (plots at 300 K and 250 K), which may be due to the contribution from grains. The semi-circular-like arc shrinks in size as the temperature increases. This indicates that the intercept points on the x-axis are pushed toward the origin, further demonstrating that the samples' grain/bulk resistance decreases with increasing temperature. Possible causes of the high-temperature electrical processes may include intra-grain phenomena.

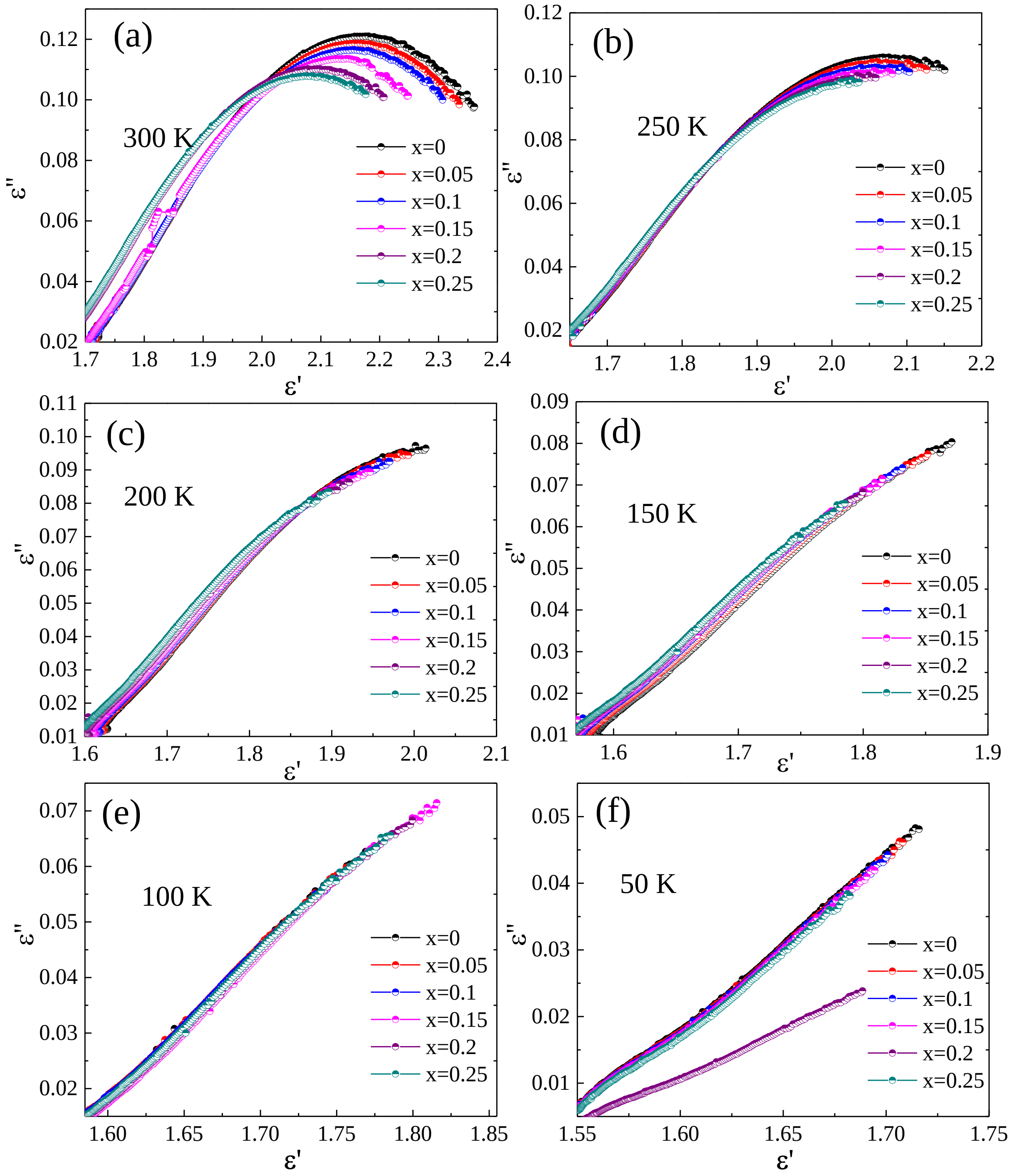

Figure 4.9: (a-f) Cole-Cole plot of as-synthesized unsubstituted and Gd-substituted 3C iron sulphide nanoparticles (ε'' versus ε') measured by impedance spectroscopy at temperatures 50, 100, 150, 200, 250 and 300 K, respectively.

Conclusions

In this chapter, observation of the dielectric behaviour of 3C Fe_7S_8 and Gd-substituted Fe_7S_8 at different measurement temperatures is discussed. Both the real and out of phase parts of the complex dielectric permittivity (ε′ and ε′’, respectively) along with absolute permittivity (|ε|) and dielectric loss factor (tan δ) as a function of frequency for unsubstituted and Gd-substituted samples at different measurement temperatures (50, 100, 150, 200, 250 and 300 K) are measured. The A weak anomaly is observed in dielectric permittivity towards higher frequency range, of which the microscopic origin is not clearly understood. The effect of the Gd substitution has been observed as the decrease in the values of ε′ and tan δ. The origin of such behavior may be attributed to the random distribution of gadolinium in the lattice. From the analysis, it is concluded that the material exhibits a negative temperature coefficient of resistance-type behavior-type behavior. The Cole-Cole plot highlights the decrease in resistivity from the grain with an increasing temperature and concentration of Gd, indicating the non-Debye kind of relaxation process. These results suggest that the Gd-substituted samples could be suitable for FeRAM applications.

References

1 J. R. Macdonald, Impedance spectroscopy, *Ann. Biomed. Eng.*, 1992, **20**, 289–305.

2 J. R. Macdonald and W. B. Johnson, Fundamentals of impedance spectroscopy, *Impedance Spectrosc. theory, Exp. Appl.*, 2018, 1–20.

3 J. R. Macdonald, Impedance spectroscopy and its use in analyzing the steady-state AC response of solid and liquid electrolytes, *J. Electroanal. Chem. interfacial Electrochem.*, 1987, **223**, 25–50.

4 J. Thorson, Small-signal analysis of a visual reflex in the locust, *Kybernetik*, 1966, **3**, 53–66.

5 J. R. Macdonald and D. R. Franceschetti, Theory of small-signal ac response of solids

and liquids with recombining mobile charge, *J. Chem. Phys.*, 1978, **68**, 1614–1637.

6 J. R. Macdonald, Impedance spectroscopy: old problems and new developments, *Electrochim. Acta*, 1990, **35**, 1483–1492.

7 R. L. Hurt and J. R. Macdonald, Distributed circuit elements in impedance spectroscopy: A unified treatment of conductive and dielectric systems, *Solid State Ionics*, 1986, **20**, 111–124.

8 T. A. Polom, M. Andresen, M. Liserre and R. D. Lorenz, Frequency-domain electrothermal impedance spectroscopy of an actively switching power semiconductor converter, *IEEE Trans. Ind. Appl.*, 2019, **55**, 6161–6172.

9 J. E. Garland, C. M. Pettit and D. Roy, Analysis of experimental constraints and variables for time resolved detection of Fourier transform electrochemical impedance spectra, *Electrochim. Acta*, 2004, **49**, 2623–2635.

10 B. A. Boukamp, Impedance spectroscopy, strength and limitations (Impedanzspektroskopie, Stärken und Grenzen), *tm-Technisches Mess.*, 2004, **71**, 454–459.

11 O. Heaviside, On the electro-static capacity of suspended wires, *J. Soc. Telegr. Eng.*, 1880, **9**, 115–120.

12 O. Heaviside, On the resistance of galyanometers, *J. Soc. Telegr. Eng.*, 1880, **9**, 202–206.

13 G. Windred, LXXXI. Early developments in AC circuit theory. Some notes on the application of complex methods to the solution of AC circuit problems, *London, Edinburgh, Dublin Philos. Mag. J. Sci.*, 1930, **10**, 905–916.

14 M. A. Alim, S. Khanam and M. A. Seitz, Immittance spectroscopy of smart components and novel devices, *Act. Passiv. Electron. components*, 1994, **16**, 153–170.

15 E. T. McAdams and J. Jossinet, Problems in equivalent circuit modelling of the

electrical properties of biological tissues, *Bioelectrochemistry Bioenerg.*, 1996, **40**, 147–152.

16 M. Dogotari, 2017.

17 E. McCafferty, On the determination of distributed double-layer capacitances from Cole-Cole plots, *Corros. Sci.*, 1997, **39**, 243–254.

18 J. G. Powles, Cole-Cole plots as they should be, *J. Mol. Liq.*, 1993, **56**, 35–47.

19 D. B. Stroud, B. H. Cornish, B. J. Thomas and L. C. Ward, The use of Cole-Cole plots to compare two multi-frequencybioimpedance instruments, *Clin. Nutr.*, 1995, **14**, 307–311.

20 Y. Barsukov and J. R. Macdonald, Electrochemical impedance spectroscopy, *Charact. Mater.*, 2012, **2**, 898–913.

21 J. R. Macdonald, Impedance spectroscopy: Models, data fitting, and analysis, *Solid state ionics*, 2005, **176**, 1961–1969.

22 A. Mansoorifar, A. Ghosh, A. C. Sabuncu and A. Beskok, Accuracy of the Maxwell–Wagner and the Bruggeman–Hanai mixture models for single cell dielectric spectroscopy, *IET Nanobiotechnology*, 2017, **11**, 874–882.

Chapter 5

Summary and future outlook

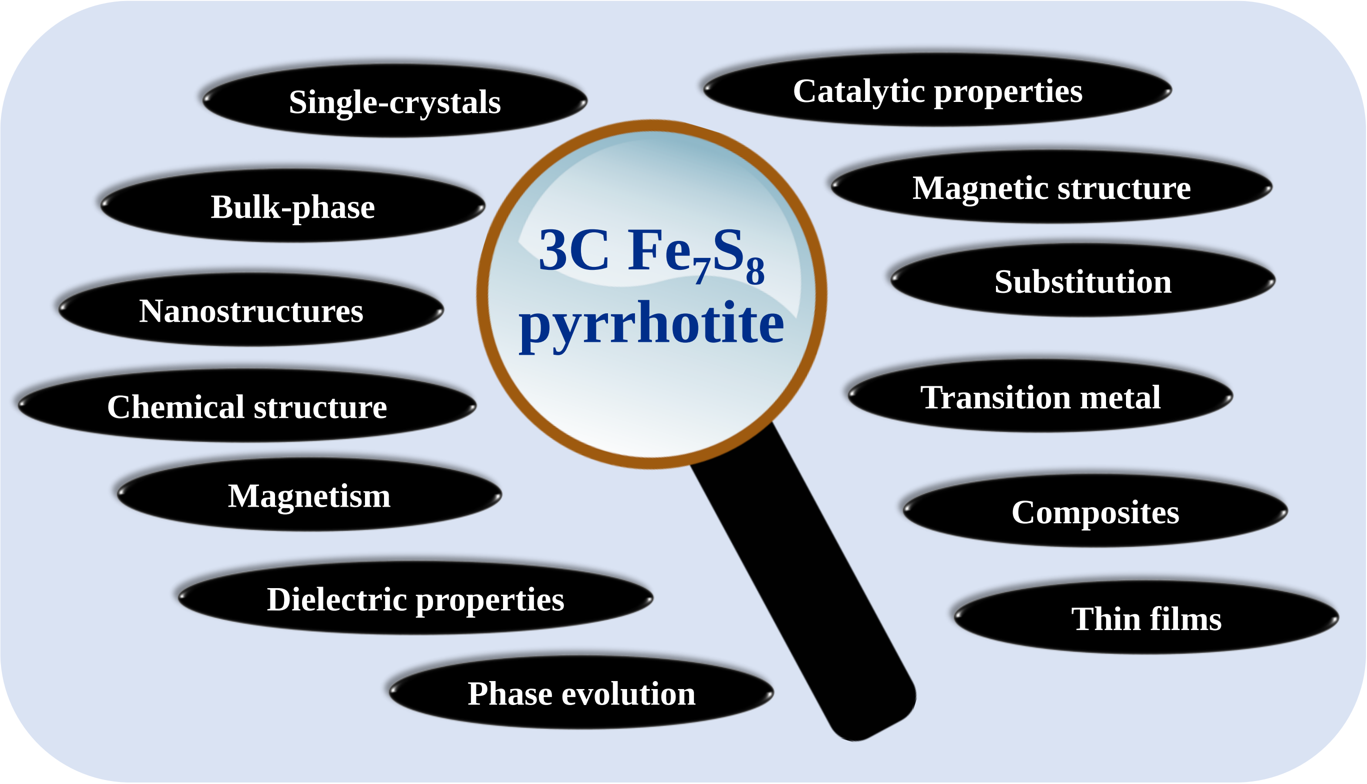

Highlights

This chapter summarized the work presented in the thesis and highlights the potential direction for future work.

Keywords: Summary, future scope

5.1. Summary of the thesis

The compounds in Fe-S system are of great importance because of their exciting and unique optical, thermal, electrical, and magnetic properties that are firmly related to the Fe−S elemental ratio as well as their crystalline structure. The family of iron sulphides has many compositions including FeS, FeS_2, 4C Fe_7S_8, 3C Fe_7S_8, and so forth. Depending upon the composition of Fe:S, these compounds could be metal, or semiconductors, and their magnetic properties also vary a lot from antiferro- to ferro- to ferrimagnetic. Among the different phases in Fe-S system, 3C Fe_7S_8 seems intriguing because of its chemical structure, which may give rise to many interesting physical properties. Unfortunately, the compound has been less studied because of the fact that the compound exists as the metastable state of 4C Fe_7S_8 in natural marine sediments around the world. The natural existence of the compound is recent. Prior to that, the compound was known to be obtained only by synthesis in the laboratories. However, we have little information about the compound in the literature. The compound was synthesized in the single crystal form using the solid-state routes in order to understand the crystal structure of the compound. Much later in 2017, the existence of the compound in the natural submarine sediments came int o the knowledge. The researchers extracted the bulk sample in the powder form to study its magnetic characteristics. The compound exhibits the ferrimagnetic ordering with a high T_C of ~423 K. However, the neutron diffraction of the compound is still awaited. To the best of our knowledge, the compound has not been synthesized in the nano phase and its properties have not been investigated. A material can exhibit intriguing properties when the size of the particles is brought down to the nano scale. This thesis describes the efforts made to understand some of the physical properties of 3C Fe_7S_8 nanoparticles— the structural, magnetic and dielectric properties. We further made a conscious effort to understand the physical behaviour of the compound when modified with substitution of a rare-earth ion. The 3C Fe_7S_8 and Gd-substituted 3C Fe_7S_8 nanoparticles have been fabricated using the wet-chemical method—thermal decomposition method. An easy-to- control synthetic procedure was developed by introducing quenching at the end of the procedure.

As evident from the results of the previous chapters, 3C Fe_7S_8 holds tremendous potential for both fundamental studies and technical applications. It is observed that the crystallite size and the lattice parameters increase with the increase in Gd concentration in 3C Fe_7S_8. The crystallite along the highest intensity peak, the (206) plane is in the range of about 33 nm-42 nm with increasing Gd concentration. The morphology of all the samples is observed to in the form of distorted hexagon. The presence of two oxidation states of Fe— +2 and +3 in all the samples is confirmed using XPS. The presence of Gd^{3+} is evident in all the Gd-substituted sample. Further, the magnetic properties of these as-synthesized nanoparticles were studied. The correlation between the concentration of Gd^{3+} ions and the magnetic properties has been presented. The distinct arrangement of Fe and S atoms results in drastically varying magnetic properties with the change in Gd concentration due to the change in crystal field environment around Fe-ions, magnetocrystalline anisotropy, Fe-vacancies, and so forth. The crystal structure of 3C Fe_7S_8 is based on NiAs phase. The M-H hysteresis loops for each sample shows ferrimagnetic-like ordering, with a high value of Curie transition temperature (above 300 K), as evident from the M-T curves. All the samples exhibit a low temperature transition at ~33 K (Besnus transition), which may occur because of the change in spin orientation of Fe^{2+} ions around that temperature. We have observed a high value of energy product in the samples, especially at the lower measurement temperatures, which makes the compounds a potential candidate in low-temperature applications. The magnetic parameters such as M_S, H_C, K_{eff}, BH_{max}, and T_B exhibited a strong dependence on size, shape and the concentration of Gd in the parent compound. For 3C Fe_7S_8 nanoparticles, the $M_{60\ kOe}$ increases by lowering the temperature to 7 K to a maximum observed value of ~25 emu/g. The H_C and M_R values increase with the decrease in the measurement temperature, to a maximum upto 3.3 kOe and 31.1 emu/g, respectively, at 7 K. The BHmax increases linearly with the decrease in the measurement temperature up to a maximum value of ~128 kG Oe at 7 K. The intrinsic and extrinsic properties of the samples enhanced with the increased Gd concentration and decreased measurement temperature. However, the magnetic and dielectric properties can be tuned and optimised by modifying the parent compound 3C Fe_7S_8. Futher, in dielectric easurements, both the real and out of phase parts of the complex dielectric permittivity (ε' and ε'', respectively) along with absolute permittivity ($|\varepsilon|$) and dielectric loss factor ($\tan \delta$) as a function of frequency for unsubstituted and Gd-substituted samples at different measurement temperatures (50, 100, 150, 200, 250 and 300 K) are measured. The A weak anomaly is observed in dielectric permittivity towards higher frequency range, of which the microscopic origin is not clearly understood. The effect of the Gd substitution has been observed as the decrease in the values of ε' and $\tan \delta$. The origin of such behavior may be attributed to the random distribution of gadolinium in the lattice. From the analysis, it is concluded that the material exhibits a negative temperature coefficient of resistance-type behavior-type behavior. The Cole-Cole plot highlights the decrease in resistivity from the grain with an increasing temperature and concentration of Gd, indicating the non-Debye kind of relaxation process. These results suggest that the Gd-substituted samples could be suitable for FeRAM applications.

In conclusion, the work provides an insight into the formation of 3C Fe_7S_8 nanoparticles, reported for the first time by introducing quenching in the thermal decomposition method. The three physical properties of the compound have been investigated— the structural, magnetic and the dielectric properties. These properties were further modified by the substitution of Gd ions.

However, there is huge scope that open up with the work done in this thesis. These scopes are discussed below.

5.2. Directions for future work

We believe that this thesis provides a deep understanding of the structural, magnetic and dielectric properties that 3C Fe_7S_8 exhibits at the nano scale.

The simple thermal decomposition route has been proven to be a brilliant method to synthesize the phase by introducing quenching process in the method for the first time. However, there is a further need to understand and develop the formation mechanism of the phase using the wet chemical method. The magnetic and the dielectric properties of the compound have been examined for the first time. However, there is a need of deep understanding of the magnetic structure of the compound by employing neutron diffraction on the bulk sample or the single crystal. The findings in the presented work show that considerable attention should be given to tuning the size and morphology of the compound, which may have potential industrial and technical applications. These properties need to be compared to the bulk counterpart of the compound. These properties are yet to investigated for the bulk 3C Fe_7S_8. The other physical characteristics, which have not been covered in the thesis, such as— ferroelectric, magnetoelectric, catalytic characteristics, and so forth, need to be addressed in the future work. Future studies on this topic will look at the effects of stoichiometry, size and morphology on the above-mentioned characteristics of the compound both in bulk as well as in the nano phases.

It will be interesting to explore a new area of the Fe-S system, which has received a narrow attention till date. Further, it will be interesting to modify the properties of the compound by incorporating the transition metal into the parent compound, and consciously forming the composites. Owing to the dangling bonds at the surface of the compound, it will be intriguing to investigate the surface effect of the compound by forming the thin film, followed by studying its properties.

Thus, the thesis opens a new door to for formation of trigonal phase of iron sulphide nanoparticles, which may be extended to understand its formation mechanism using the thermal decomposition method in the thesis. With appropriate modifications in the synthesis method, the properties of the compound can be modified for its industrial applications. Further, the properties can be investigated for the bulk counterpart of the compound.

ABSTRACT

Name of the Student: Shubhra Jyotsna**Registration No.:** 10PP15J26031

Faculty of Study: Physical Sciences **Year of Submission:** 2023

CSIR Lab: NCL, Pune **Name of the Supervisor:** Dr. Pankaj Poddar

Title of the Thesis: Influence of rare-earth element substitution on the structural and physical properties of trigonal iron sulphide at the nano scale

---

This thesis aims to create an understanding of the structural and physical properties of single-phase 3C Fe_7S_8 and Gd-substituted 3C Fe_7S_8 at the nanoscale. In the first chapter, the transition metal chalcogenides are introduced and their applications in various fields are discussed. A review about Fe-S system is presented, which was narrowed down to the pyrrhotites. It is highlighted in the chapter as why the trigonal Fe_7S_8 is of fundamental and technological importance. Brief literature review of the trigonal Fe_7S_8 is given, highlighting the structural and magnetic characteristics of the compound. In the end, objective of the thesis is discussed. The second chapter discusses the structural aspects of trigonal phase of Fe_7S_8 at nanoscale. In order to modify the characteristics, the compound was substituted with a rare-earth element— Gd. The chapter further discusses and compares the different structural parameters of all the samples. The third chapter discusses the magnetic characteristic of trigonal phase of Fe_7S_8 at nanoscale with the aim of understanding the magnetism in the compound and finally to calculate the energy product. The magnetic characteristics of the compound were modified by the substitution of Gd of varying at%. The chapter further discusses and compares the different magnetic parameters of all the samples. The fourth chapter discusses the dielectric properties of trigonal phase of Fe_7S_8 at nanoscale The dielectric characteristics of the compound were modified by the substitution of Gd of varying at%. The chapter further discusses and compares the different dielectric parameters of all the samples. The conclusion of this thesis and scope of future works are discussed in fifth chapter.

List of Publication(s) in SCI Journal(s) Emanating from the Thesis Work

1. **Shubhra Jyotsna**, Pankaj Poddar. Investigation of the ferrimagnetic behaviour of 3C Fe_7S_8 nanoparticles. (Under revision)

List of Papers with Abstract Presented (Oral or Poster) at National or International Conferences /Seminars

1. *Electron microscopy society of India, EMSI*, IIT-Bombay, 2015 (Presented poster titled "Effect of surface chemistry on structural and magnetic properties of DCO nanoparticles")
2. *International Conference on Technologically Advanced Materials and Asian Meeting on Ferroelectricity, ICTAM-AMF10*, University of Delhi, 2016 (Presented poster titled " Gold island decorated bismuth selenide nanosheets and its application in CO oxidation")
3. *Science Day Celebration*

- CSIR-NCL, 2017 (Presented poster titled "Luminescence turn-off detection of metal ions and explosives using graphene quantum dots")
- CSIR-NCL, 2019 (Presented poster titled "Gold island decorated bismuth selenide nanosheets and its application in CO oxidation")

Bull. Mater. Sci. (2023)46:108
https://doi.org/10.1007/s12034-023-02943-1

Investigating the ferrimagnetic behaviour of trigonal 3C Fe_7S_8 nanoparticles

SHUBHRA JYOTSNA[1,2] **and PANKAJ PODDAR**[1,2,*]
[1] Physical and Materials Chemistry Division, CSIR-National Chemical Laboratory, Dr. Homi Bhabha Road, Pune 411008, India
[2] Academy of Scientific and Innovative Research (AcSIR), Sector 19, Ghaziabad 201002, India
*Author for correspondence (p.poddar@ncl.res.in)

MS received 21 November 2022; accepted 23 January 2023

Abstract. The magnetic properties of trigonal 3C Fe_7S_8 nanoparticles, synthesized *via* the thermal decomposition method, are investigated using temperature-dependent zero-field cooled (ZFC) and field-cooled (FC) magnetization (M–T) curves. The M–T data, recorded at 100 and 1000 Oe, reveal magnetic ordering with high Curie transition temperature ($T_C > 300$ K) in the specimen. The magnetization *vs.* applied magnetic field (M–H) data measured in the temperature range from 7 to 300 K show that the compound exhibits ferrimagnetic ordering. The values of coercivity (H_C), saturation magnetization ($M_{60\ \mathrm{kOe}}$) and remanent magnetization (M_R) appear to increase at lower measuring temperatures. As the result of increasing $M_{60\ \mathrm{kOe}}$ at lower measuring temperatures, within the temperature range of 7 to 300 K, the maximum energy product (BH_{max}) has the highest value of 128 kG Oe at 7 K.

Keywords. Pyrrhotites; Fe_7S_8; trigonal phase; ferrimagnetism; anisotropy; energy product.

1. Introduction

Iron sulphide (Fe-S) minerals are studied intensively to understand the evolution of Earth [1,2]. These biogeochemical minerals are categorized into various groups based on their compositions, crystal structures and phase relations [3–6]. In the Fe-S system, 1C FeS, 2C FeS, 3C Fe_7S_8 and 4C Fe_7S_8, where C denotes the *c*-axis of the NiAs unit cell, are some of the known compounds that exhibit the magnetic ordering in both bulk phase [3–6] and at the nanoscale (except 3C Fe_7S_8) [7,8]. They also have applications in catalysis [9], fuel cells, gas sensing [9], and so on. However, there is hardly any study on the properties of the 3C Fe_7S_8 compound. Hence, it becomes essential to investigate the compound and explore its possible applications.

In the Fe-S system, the $Fe_{1-x}S$ ($0 \leq x \leq 0.125$) group is collectively called the pyrrhotite minerals [10]. These pyrrhotites have crystal structures identical to NiAs structure (scheme 1a) [11,12]. In the NiAs structure, nickel atoms are in octahedral coordination, and arsenic atoms are in trigonal prismatic coordination. Similarly, in pyrrhotites, Fe atoms are positioned on octahedral sites (scheme 1b and c), and S atoms occupy the trigonal prismatic position (not shown in the figure for clarity) of the hexagonal lattice. Further, pyrrhotites form a lattice by extending the dimensions of the unit cell of NiAs along the *a*-axis and *c*-axis and are known as superstructures. Wuensch Bernhardt [13] introduced a nomenclature system that describes these pyrrhotite superstructures. Accordingly, the dimensions of the superlattice are decided depending upon the repetition of the NiAs unit cell either along the *a*-axis or *c*-axis [13]. For example, pyrrhotite with the structure and cell dimensions of NiAs is referred to as a 1C pyrrhotite. Similarly, pyrrhotites that have unit cell parameters of *c* equal to two times, three times, and four times the dimension of *c* in the NiAs unit cell are known as 2C (troilite), 3C (trigonal pyrrhotite) and 4C (monoclinic pyrrhotite), respectively and so forth.

The pyrrhotite superstructures are non-stoichiometric with varying crystal systems and composition, stability and various physical properties, such as electronic, optical, magnetic and so forth. The presence of metal cation vacancies gives rise to such variations in the pyrrhotite structure. The Fe_7S_8 composition exists in two structural types—trigonal (3C type) and monoclinic (4C type) pyrrhotites, which also depends on the stacking sequence, direction and repetition of the vacancy layers within the superlattice. According to Nakazawa and Morimoto [3], the 4C and 3C structures of Fe_7S_8 differ in the arrangement of vacancies and the type of Fe-clustering in the alternate layers of Fe and S in the lattice [3]. The monoclinic 4C Fe_7S_8 structure was first proposed by Bertaut [11] with unit cell parameters of $a = 2\sqrt{3}A$, $b = 2A$, $c = 4C$ [11], where A and C represent the NiAs subcell dimensions. The superstructures are characterized by the distinct ordering of vacancy layers oriented along the *c*-axis. The Fe layers with and without vacancy are alternately sequenced as

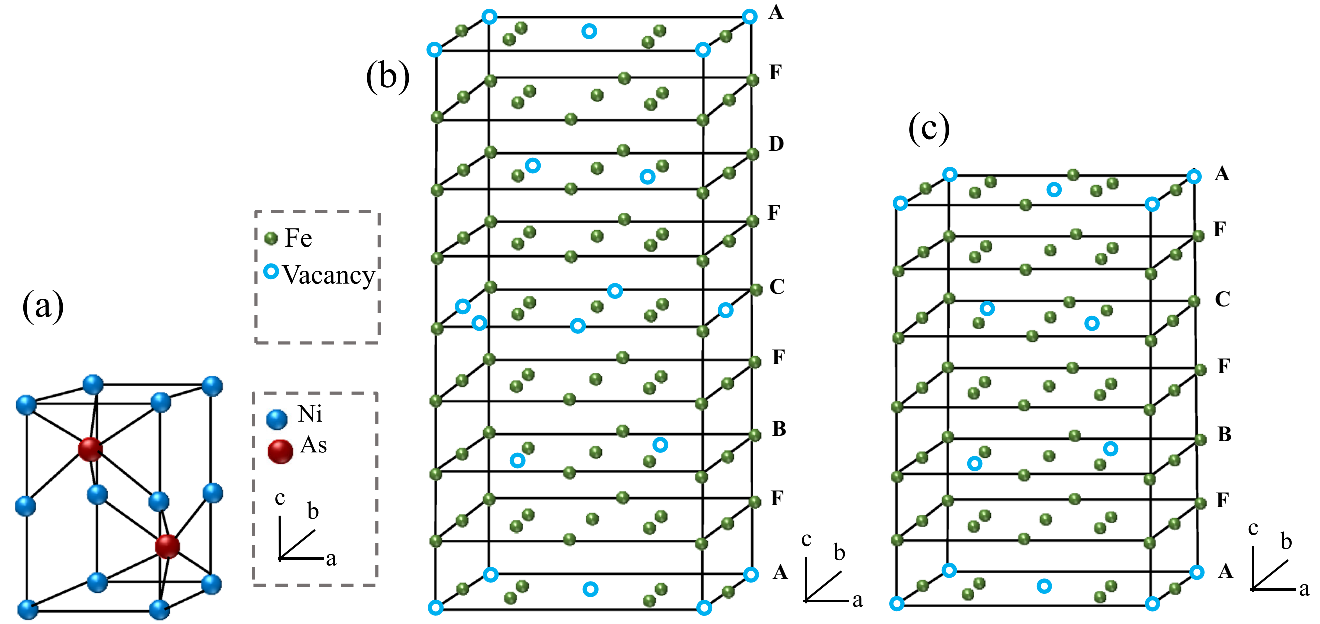

Scheme 1. Schematic representation of (**a**) the NiAs unit cell. The pyrrhotite group is derived from the structure of hexagonal NiAs subcell, (**b**) illustration of the vacancy structure in 4C Fe_7S_8 in the sequence AFBFCFDFA and based on the space group *F*2/d, (**c**) illustration of the vacancy structure in 3C Fe_7S_8 in the sequence AFBFCFA and based on the space group $P3_121$. Sulphur sites are omitted for clarity.

AFBFCFDF, where A, B, C and D denote layers containing Fe vacancies (marked by blue circles), and F is an iron layer without vacancy, as shown in scheme 1b. As a quarter of iron atoms are absent within this structure, it has been proposed by Bertuat [11] that charge balance is maintained by the presence of ferric iron in the pyrrhotite structure and the hence to account for the non-stoichiometry in the pyrrhotite structure, Fe_7S_8 can be represented as $Fe_2^{3+}Fe_5^{2+}S_8$.

Soon after the determination of the crystal structure of monoclinic 4C Fe_7S_8, Fleet [12] was able to identify and determine the crystal structure of the naturally occurring 3C Fe_7S_8 with space group $P3_1$, considering the contribution of the crystal twinning. Based on the $P3_1$ space group, a similar structural study was made by Nishiguchi [14] in 1977 on a synthesized single crystal of 3C Fe_7S_8. However, Fleet and Nishiguchi did not examine the possibility of a $P3_121$ space group in the structure. Later in 1979, the structure of 3C Fe_7S_8 was refined by Nakano *et al* [6] with space group $P3_121$ based on Fe vacancies and unit cell parameters $a = 6.8652 \pm 0.0006$ Å, $c = 17.047 \pm 0.002$ Å, confirming the trigonal symmetry. The structure is essentially the same as that of 3C Fe_7Se_8, as reported by Okazaki Hirakawa [15], which has the $P3_121$ symmetry. Scheme 1c exhibits a layered 3C Fe_7S_8 structure with vacant and filled iron layers stacked normal to the *c*-axis in a sequence described as AFBFCF, where A, B and C denote the layers containing Fe vacancies, and F represents the layer without Fe vacancy.

There has been a little information about 3C Fe_7S_8 pyrrhotites in the literature. Due to the poor understanding about the material, it was known that the compound exists merely in the extra-terrestrial region. However, as the field evolved, many researchers studied the crystal structure of naturally obtained and synthetic sample by the means of X-ray diffraction [6,12]. The compound started to gain attention only after researchers found the sample of 3C Fe_7S_8 pyrrhotite in selected submarine sediments around the world as a metastable phase of 4C Fe_7S_8 pyrrhotite, formed as a consequence of shock or quenching [16]. Soon after the discovery of the trigonal phase of pyrrhotite, researchers extracted the powder sample from the rock obtained from the submarine sediments and studied its structure and magnetic properties. Although the neutron diffraction of the compound is still awaited, it was proposed that the compound exhibits ferrimagnetic ordering [17]. However, based on the limited studies available about 3C pyrrhotite, there is a need to understand the material in detail. Any material when reduced to nano-dimensions, may exhibit interesting magnetic properties. To the best of our knowledge, we have not found any report suggesting the synthesis of the compound in the nanoscale regime and the changes in their properties at the nanoscale. In the present investigation, the trigonal 3C Fe_7S_8 pyrrhotite nanoparticles were synthesized by adding a quenching process in the existing thermal decomposition method, reported by Lin *et al* [18] for the synthesis of hexagonal $Fe_{1-x}S$ pyrrhotite. The quenching process introduced at a specific temperature led to the formation of 3C trigonal Fe_7S_8 pyrrhotite nanoparticles. This study is devoted to understand the magnetic properties of the compound.

2. Experimental

2.1 *Materials*

Thiourea (NH_2CSNH_2, 99.9%), iron (II) chloride ($FeCl_2 \cdot 4H_2O$, 99.9%) and olaylamine (OLA, 99.9%) were purchased from Sigma-Aldrich chemicals. All chemicals were used without any further purification.

2.2 *Characterization techniques*

The phase purity and crystallinity of the as-synthesized samples were characterized by powder X-ray diffraction (PXRD) using a PANalytical X'PERT PRO instrument, and the iron-filtered Cu-Kα radiation (λ = 1.54 Å) in the 2θ range of $10°-80°$ covered in a step size of 0.08° with a count time of 2 s. The operating voltage and current for the PXRD instrument were kept at 30 kV and 40 mA, respectively. A highly sensitive surface technique—X-ray Photoelectron Spectroscopy—data were recorded for Fe and S on Thermo Fisher Scientific X-ray Photoelectron Spectrometer (XPS) K-Alpha+. The monochromatic Al Kα (h_v = 1486.6 eV) as the X-ray source was operated with a beam current of 6 mA and voltage of 12 kV coupled with a Physical Electronics 04–548 dual Mg/Al anode and in an ultra-high vacuum system with a base pressure of $\leq 5\times10^{-9}$ Torr. The spot size of 400 μm was used during the XPS measurement. The recorded XPS data were deconvoluted using XPS PEAK 41. All measurements mentioned above were performed at a laboratory temperature (23 ± 2 °C). Raman spectroscopy measurements were recorded at laboratory temperature (23 ± 2 °C) on an HR 800 Raman spectrophotometer (Jobin Yvon, HORIBA, France) equipped with an achromatic Czerny−Turner type monochromator (800 mm focal-length) with silver-treated mirrors. Monochromatic radiation emitted by a 632 nm laser, operating at 20 mW, was used. The specific structural details and morphology were obtained using an FEI Tecnai T20 transmission electron microscope (TEM) equipped with a super-twin (s-twin) lens operated at 200 keV accelerating voltage. The powders obtained were dispersed in *n*-hexane and then drop-casted on a carbon-coated copper TEM grid with 200 mesh and loaded in a single-tilt sample holder. The magnetic measurements were carried out using a superconducting quantum interference device-based S4 vibrating sample magnetometer (SQUID-VSM) manufactured by Quantum Design, Inc., San Diego, USA. The powder samples were precisely weighed and packed inside a plastic sample holder, which fits into a brass specimen holder provided by Quantum Design Inc. with a negligible contribution to the overall magnetic signal. The M–H loops are collected at a rate of 50 Oe s^{-1} in a field sweep from ± 60 kOe at the vibrating frequency of 40 Hz. The magnetization *vs.* temperature ($M-T$) measurements were performed at a temperature sweep from 7 to 300 K in a field of 100 and 1000 Oe following standard zero-field cooled (ZFC) and field-cooled (FC) sequences.

2.3 *Synthesis pathway of 3C Fe_7S_8 nanoparticles*

Polycrystalline 3C Fe_7S_8 was synthesized by a thermal decomposition method, according to the steps reported by Lin *et al* [18] for the synthesis of hexagonal $Fe_{1-x}S$ pyrrhotite. A mixture of iron–oleylamine (Fe–OLA) and sulphur–oleylamine (S–OLA) complexes were prepared separately in a three-neck flask equipped with an inlet of nitrogen gas, condenser, magnetic stirrer, thermocouple and heating mantle. The S–OLA complex was obtained from the reaction of NH_2CSNH_2 (4 mmol) dissolved in OLA (10 ml) at 180°C under nitrogen gas and then cooled down to laboratory temperature (27 ± 3°C). The Fe–OLA complex was prepared separately by dissolving $FeCl_2 \cdot 4H_2O$ (2 mmol) at 150°C in OLA. Further, the S–OLA complex was injected into the Fe–OLA complex. The mixture was initially heated at 180°C for 2 h, followed by reflux (260°C) for another 2 h, and was quenched in wet ice (0 ± 3°C) from a relatively high temperature (260°C). As the temperature of the suspension reached the laboratory temperature (27 ± 3°C), *n*-hexane was added to it. Black precipitates were obtained, further separated *via* centrifugation, and then vacuum-dried to obtain the 3C Fe_7S_8 nanoparticles. The schematic for the synthesis of trigonal 3C Fe_7S_8 nanoparticles is shown in scheme 2.

3. Results and discussions

3.1 *Powder X-ray diffraction*

The composition, crystallinity and phase purity of 3C Fe_7S_8 nanoparticles are confirmed by PXRD, as shown in figure 1a. The experimentally obtained sample diffraction peaks (relative intensities containing the c-axis and peak positions (table 1)) are in good agreement with standard JCPDS data (JCPDS no. 710591) [6], ensuring the hexagonal phase with the trigonal crystal structure ($P3_121$ space group) of the as-synthesized product with no additional peak within the detection limit of the instrument. The most intense diffraction peak centred at $2\theta \sim 44°$ corresponds to the plane (206). The peaks around 10°, 30°, 32°, 34°, 53°, 57°, 63°, 72°, and 73° correspond to planes (100), (200), (006), (203), (220), (029), (400), (316), (046) and (0310), respectively. Following the method given by Paul Scherrer [19] in 1918, the crystallite size of as-synthesized 3C Fe_7S_8 is calculated considering the effect of limited particle size on XRD patterns. Paul Scherrer approximated an expression to relate peak-broadening and crystallite size. The formula to estimate the crystallite size along the *hkl* plane from the

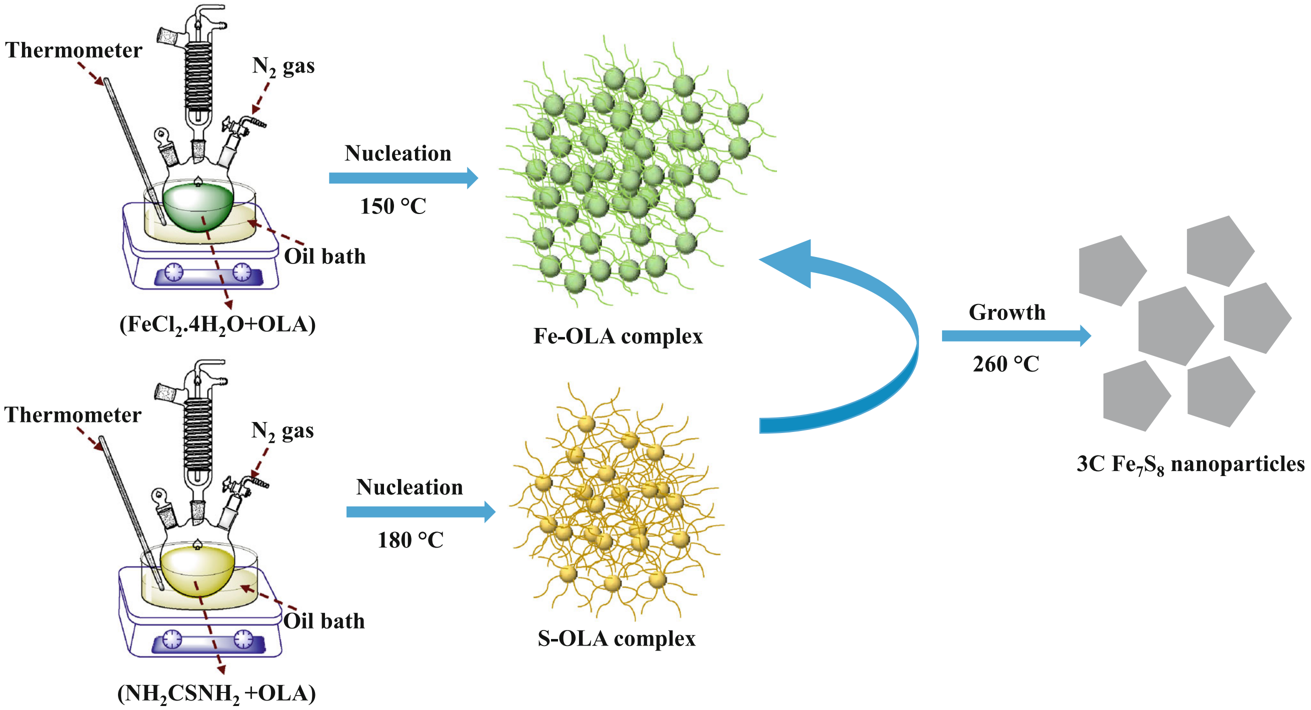

Scheme 2. Schematic of the synthesis pathway of trigonal 3C Fe_7S_8 nanoparticles by thermal decomposition method in triple-neck flask under nitrogen atmosphere followed by centrifugation and vacuum drying to obtain the final product.

measured width of their diffraction curves is given as equation (1) [19]:

$$D = \frac{K\lambda}{\beta\cos\theta} \tag{1}$$

here, the width β of the diffraction curve at an intensity equal to half the maximum intensity, known as the full-width at half-maxima (FWHM), is usually measured in radians. The wavelength, λ of the incident X-rays for Cu K_α is $\lambda \sim 0.154$ nm, θ is the Bragg angle, corresponding to the hkl plane (hkl are the Miller indices of the planes being analysed), and K is the numerical constant typically referred to as the crystallite-shape factor, however, in the absence of details of shape information, $K = 0.94$ is a good approximation. Instead of directly considering the β values from peak broadening, it is corrected from standard data using equation (2).

$$\beta = \beta_M^2 - \beta_S^2 \tag{2}$$

where β_M and β_S are the measured widths of the diffraction peaks of Fe_7S_8 and the standard sample. This results in subtracting the instrumental errors from the peak broadening. The crystallite size corresponding to the highest intensity peak along the (206) plane is $\sim$27 nm.

The comprehensive analysis of crystal structure was carried out using the Rietveld refinement technique in the trigonal phase with space group $P3_121$ using the FullProf Suite program to determine structural parameters like the fractional lattice parameters, atomic coordinates, lattice parameters and occupancy. The refinement is performed with the Fe_7S_8 model (ICSD collection code no. 2106932) [20], and the corresponding profile is shown in figure 1b. The twelve-coefficient polynomial has been used to model the background intensity. The Pseudo-Voigt profile functions were applied to refine the shape and FWHM parameters of the XRD peak profiles. The refinement shows that the diffraction peaks corresponding to this sample can be indexed in the hexagonal system with the $P3_121$ space group. The quality of the refinement was evaluated through the goodness of fit parameter (χ^2). Phase identification by XRD for some systems, especially nanoscale materials, can be particularly challenging because of nearly indistinguishable diffraction patterns [21]. Nanomaterial samples that include multiple distinct subpopulations of different sizes and/or shapes can produce more complex XRD patterns [22]. In our experiment, the value is relatively higher due to the fact that the model adopted for the refinement is based on the bulk sample. However, when the dimension of the particles reduces, the appropriate fitting of the model is not simple as it is in the case of a bulk sample [21,22]. Moreover, due to a shorter scan time (15 min), fitting the model in the refinement method will give a relatively larger value of χ^2 (= 3.6). The experimental diffraction pattern in figure 1b is displayed as black circles, and the calculated diffraction pattern is shown as a red line. The blue lines indicate the Bragg-allowed peak positions. The bottom green curve indicates the difference profile between the calculated and observed XRD pattern. The values of

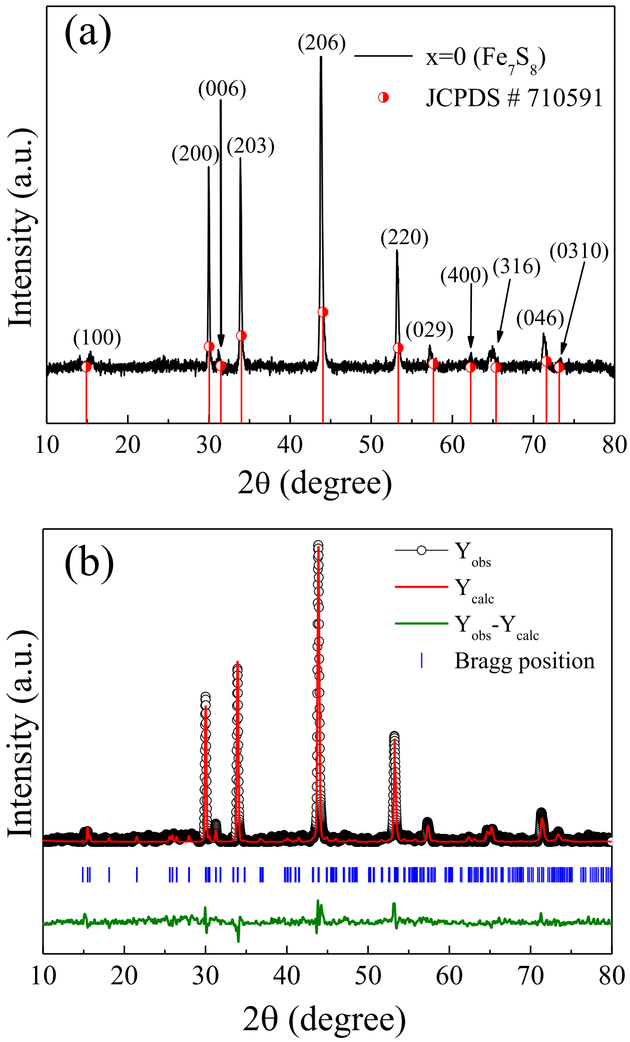

Figure 1. (**a**) XRD pattern of as-prepared 3C Fe_7S_8 nanoparticles. The data have been compared with standard data of trigonal Fe_7S_8, JCPDS# 710591 as the reference. (**b**) Rietveld refined XRD pattern of as-synthesized 3C Fe_7S_8 nanoparticles, obtained using Fullprof Suite program.

R-factors—profile factor (R_p), weighted profile factor (wR_p) along with χ^2, and the lattice parameters for the as-synthesized sample are summarized in table 2. The low values of various *R*-factors and χ^2, obtained after the refinement, justify that the experimental data and the model used to refine the XRD data match well. The electron density mapping is obtained using the GFourier program to understand the electron density and recognize the atomic positions of the elements within the unit cell. The scattering density, also known as electron density, $\rho(x,y,z)$, is calculated from equation (3) [23]:

$$\rho(x,y,z) = \frac{1}{V}\sum |F_{hkl}| e^{-\{2\pi i(hx+ky+lz-\alpha_{hkl})\}} \qquad (3)$$

where V is the unit cell volume, F_{hkl} is the structure factor amplitude, and α_{hkl} is the phase angle of each Bragg reflection (h,k,l). Electron density maps can be displayed as two-dimensional (2D) or three-dimensional (3D) Fourier maps. In 2D Fourier maps, the denser electron density contours indicate the position of a relatively heavier element in the unit cell. On the contrary, the 3D Fourier maps employ a chicken-wire style network, indicating a single electron density level. The 2D map for the as-synthesized sample is shown in figure 2a. The low charge density region is represented by dark blue colour and the high charge density region by red. The coloured region violet to red indicates increasing levels of electron density around the Fe cation. The unit cell of 3C Fe_7S_8, generated by the VESTA program using a CIF file obtained through FullProf Suite structural refinement of experimental data, is illustrated in figure 2b to demonstrate a clear picture of the sites occupied by the sulphur (S) and iron (Fe) ions. In the system under investigation, S1, S2, S3, S4, Fe1 and Fe2 ions occupy the 6c sites, cations Fe3 and Fe4 occupy 3b sites, while 3a sites are occupied by Fe5 and Fe6 cations. The difference in the scattering density between the sulphur anion and Fe cations and their bond lengths are marked

Table 1. Comparison of the relative intensities reported in JCPDS no: 710591 with that of the obtained experimental PXRD data for 3C Fe_7S_8.

JCPDS # 710591		Experimental PXRD data	
2θ (°) Containing *c*-axis	Relative intensity	*2θ* (°) Containing *c*-axis	Relative intensity
31.463	0.03303	31.373	0.0341
34.008	0.57558	34.0653	0.58614
44.053	1	44.0073	1
57.662	0.07508	57.4387	0.07608
65.382	0.003	65.0043	0.00349
71.588	0.11912	71.186	0.10671
73.174	0.00501	73.1113	0.00525

The relative intensities are compared only for the planes containing *c*-axis.

Table 2. Structural parameters obtained after Rietveld refinement of XRD data of as-synthesized 3C Fe_7S_8 nanoparticles, using the Fullprof Suite program.

χ^2	3.6
wR_p (%)	6.2
R_p (%)	5.1
Space group	$P3_121$
$a = b$ (Å)	6.8
c (Å)	17.2
γ (°)	118

	x	*y*	*z*	Occupancy
S3	0.60383	0.34262	0.07661	1.09124
Fe1	0.50389	0.50479	0.16125	1.04526
S2	0.31630	0.14991	0.25052	1.04983
Fe4	0.50633	0.00000	0.83333	0.53566
Fe2	0.52585	0.51569	0.33672	0.92194
S4	0.17068	0.84899	0.10169	0.82666
Fe3	0.00658	0.00000	0.83333	0.50000
Fe6	6.03173	0.00000	0.33333	0.09350
Fe5	− 0.01151	0.00000	0.33333	0.41500
S1	0.18997	0.36539	0.07716	1.09545

The values χ^2 and wR_P (%) represent the χ^2 and weighted profile *R*-value, respectively. Unit cell parameters are denoted by *a*, *b*, *c* and γ.

in figure 2a. Figure 3a demonstrates a 3D Fourier map of individual atoms in the unit cell for the 3C Fe_7S_8 sample, with strong peaks corresponding to the 6c sites of Fe cations. The Fe atoms have a greater number of electrons than S. Hence, Fe is expected to scatter the X-rays strongly in comparison to S. Thus, the peaks corresponding to Fe are more intense than that of S. Figure 3b shows the polyhedron representation of 3C Fe_7S_8 generated by the VESTA program using CIF file obtained through FullProf Suite structural refinement of experimental data.

3.2 *Transmission electron microscopy*

The bright-field TEM images (figure 4a–d) show the morphology of the 3C Fe_7S_8 nanoparticles. The nanoparticles are oriented in different directions with respect to electron beams. This interaction between the particles and the electron beam changes the elastic scattering diffraction, which appears as different contrast in the TEM image. The nanoparticles were grown in hexagonal-shaped particles. However, some nanoparticles were observed to be disordered in shape, which can be related [24] to the preferential growth of the low-interfacial energy surface planes. The hexagonal morphology observed in TEM can be related to the diffracted planes, which confirms that the dominant growth of direction is ⟨0001⟩. This means that the growth happens along the normal direction (*c*-axis) of a low-energy facet. The growth of the hexagonal-shaped nanoparticles is assumed to be favoured by the HCP packaging and the tendency of the nanoparticles to have energy stability by energy minimization. The region (marked as the black circle) in the HRTEM image in figure 4d gives the interplanar spacing of ∼0.59 nm (shown in the inset of figure 4d), which corresponds to the (100) plane of the 3C Fe_7S_8 lattice. In the selected area electron diffraction pattern

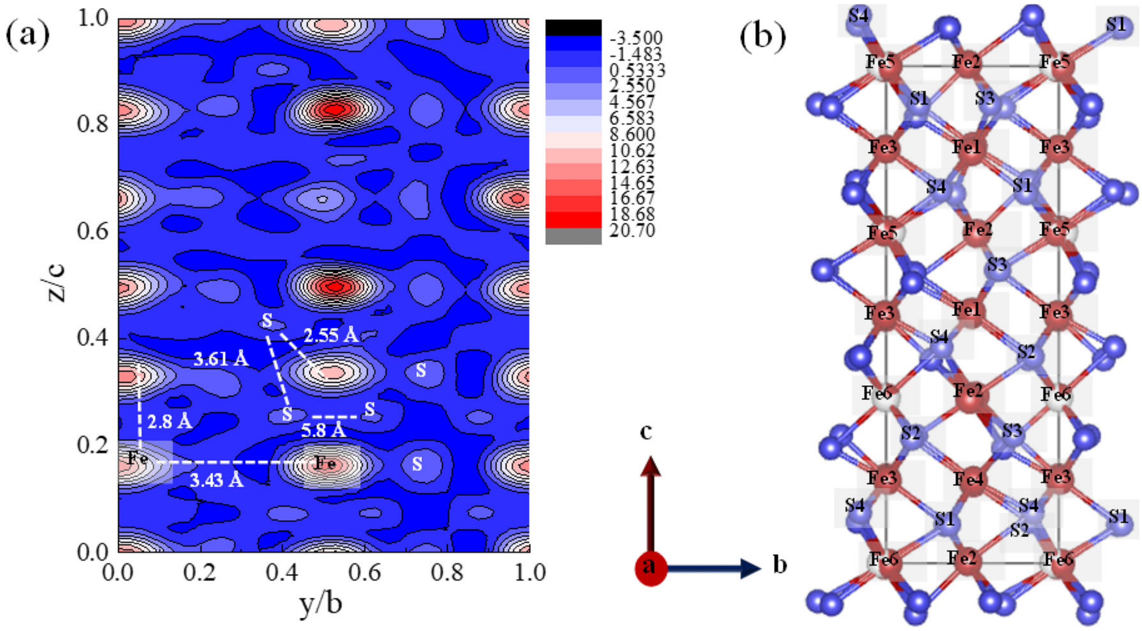

Figure 2. (**a**) Two-dimensional (2D) electron density (e/Å^3) map in the unit cell of 3C Fe_7S_8 determined from GFourier program, (**b**) unit cell of 3C Fe_7S_8 in (011) orientation, generated in VESTA program from CIF file obtained after the Rietveld refinement of PXRD data of the sample in Fullprof Suite program.

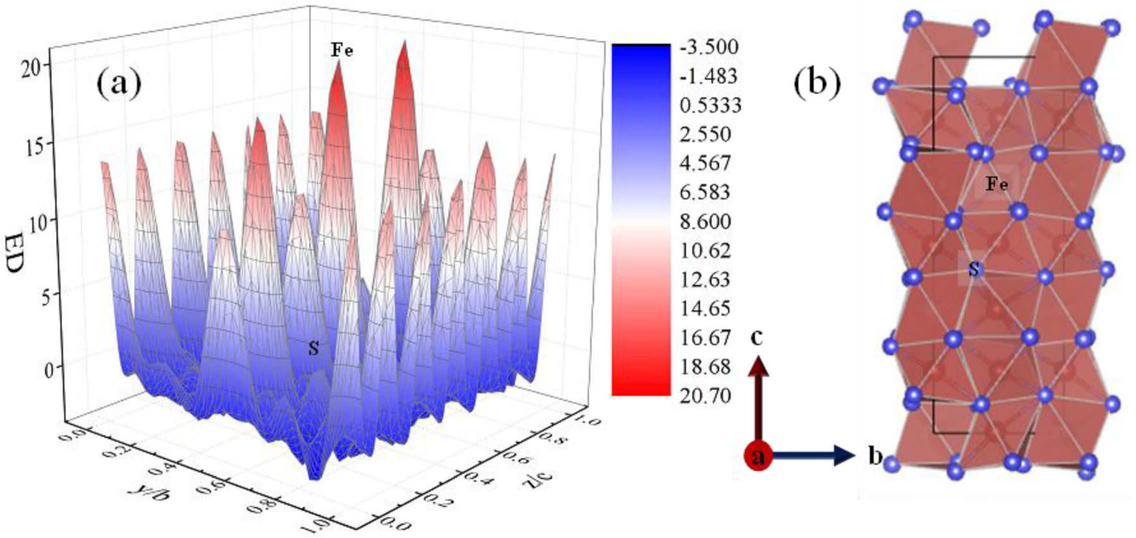

Figure 3. (**a**) Three-dimensional (3D) electron density (e/Å^3) map in the unit cell of 3C Fe_7S_8 determined from GFourier program. (**b**) Polyhedron representation of 3C Fe_7S_8, generated in VESTA program from CIF file obtained after the Rietveld refinement of PXRD data of the sample Fullprof Suite program.

(figure 4e), the reflection planes (200), (203), (006) and (206) are indexed, revealing the crystalline nature of 3C Fe_7S_8 nanoparticles. The analysis is consistent with the findings of XRD data. The prepared nanoparticles are composed of many nanocrystals. The growth direction of these nanocrystallites, along $\langle 0001 \rangle$ direction, reveals the most stable (minimum energy) facet. This particular growth of the nanoparticles may strongly be favoured by OLA used as the surfactant in the synthesis. This also opens the doors to study the growth mechanism of these nanoparticles under variable conditions. Figure 4f represents the particle size distribution of the as-synthesized sample with an average particle size of ~150 nm, which may be related to the Oswald ripening process, in which the synthesis temperature significantly affects the growth rate of nanoparticles [25]. When the reaction temperature is high, the dissolution rate of small nanoparticles in a supersaturated solution increase, resulting in the formation of large nanoparticles.

3.3 *X-ray photoelectron spectrometer*

The surface composition and the oxidation state in 3C Fe_7S_8 of the Fe and Se spectrum were investigated by the XPS technique. Figure 5a shows the survey spectrum of the as-synthesized compound, confirming the presence of Fe and S along with the other elements. The presence of C 1*s* and N 1*s* in the spectrum was due to the capping of oleylamine on the surface of the synthesized nanoparticles. The survey spectrum shows the presence of O 1*s* due to the surface oxidation of the compound by the ambiance. The core-level binding energy (BE) was aligned with the carbon BE of ~284 eV (figure 5b). Figure 5c shows the XPS spectra of Fe 2*p* core level BE of Fe_7S_8 containing two characteristic peaks at ~711 and ~724 eV corresponding to Fe $2p_{3/2}$ and Fe $2p_{1/2}$, respectively, with the spin-orbit splitting energy of 13 eV. The peak Fe $2p_{1/2}$ (~724 eV) further divides into two peaks at ~723 and 725 eV. In the Fe 2*p* core-level spectrum, the peaks ~707 and 720 eV imply the existence of the Fe^{2+} state in the compound [26]. The other two peaks at ~711 and 724 eV imply the existence of a higher oxidation state (Fe^{3+}) of the iron species in corresponding Fe−S nanoparticles. This analysis is favourable with the expectation that Fe_7S_8 should have both Fe^{2+} and Fe^{3+} for electron neutrality [26]. The deconvoluted peaks at BE ~711 and 724 eV are due to the Fe–S bond [26]. The peak at ~725 eV is due to $2p_{1/2}$ of Fe^{2+} in the compound, attributed to the Fe–O bond may be due to the surface oxidation [26]. Hence, Fe exists in two oxidation states—Fe^{2+} and Fe^{3+}, to account for the electron neutrality in the compound. Figure 5d shows the XPS spectrum of S 2*p* in 3C Fe_7S_8, with the characteristic peaks at ~161 and ~164 eV, corresponding to S $2p_{3/2}$ and S $2p_{1/2}$, respectively. After deconvolution, two sub-peaks were obtained for a distinct peak at ~162 eV, whose binding energies are nearly the same, signifying the presence of C–S–C and C=S bonds, respectively [26]. In addition, the deconvolution also depicts the presence of S–O peaks (~165 and 168 eV) in the core S 2*p* spectrum (figure 5d) of the compound, indicating surface oxidation. Further, the XPS spectrum of O 1*s* (figure 5e) shows four types of oxygen—O^{I} (~530 eV), O^{II} (~531 eV), O^{III} (~533 eV) and O^{IV} (~535 eV) correspond to lattice oxygen at the surface of the compound, –OH group, S–O group, and physi-/chemisorbed water on the surfaces due to the air exposure, respectively [27]. Thus, the formation of 3C Fe_7S_8 is confirmed by XPS analysis. Still, it is also

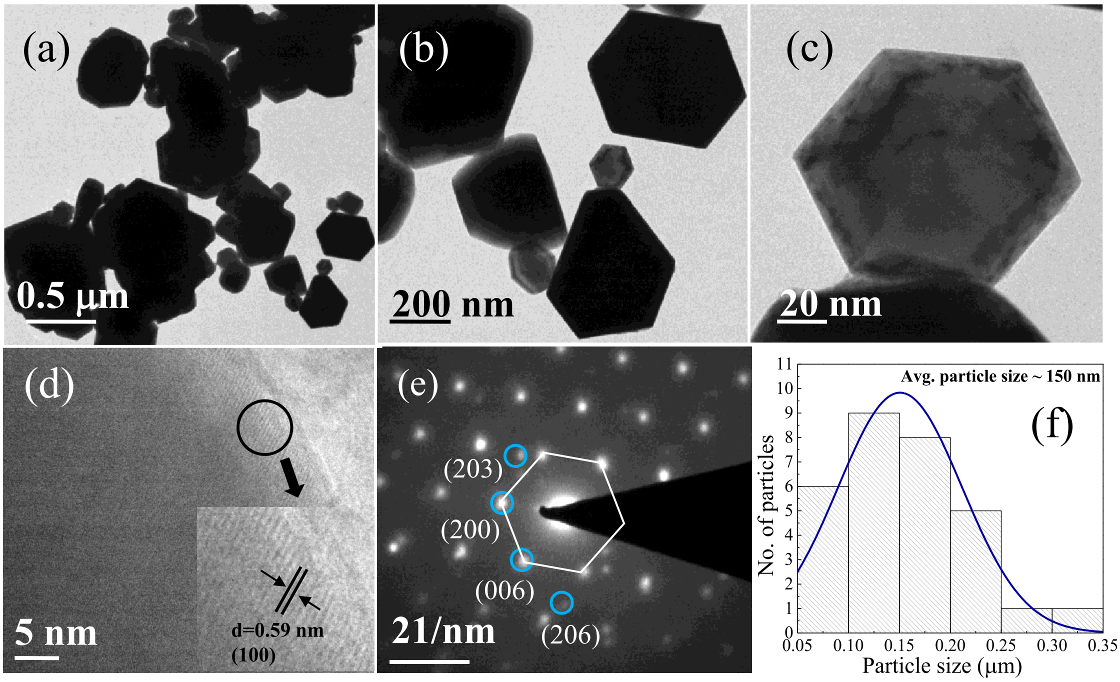

Figure 4. (**a**–**c**) The bright-field TEM images of as-prepared 3C Fe_7S_8 nanoparticles at different scales. (**d**) HRTEM; inset depicts the zoomed-in view of the lattice fringes spaced at ~0.59 nm, representing the (100) plane of 3C Fe_7S_8. (**e**) The selected area electron diffraction pattern reveal the presence of most intense peak (206) obtained from XRD data. (**f**) Particle size distribution of the sample 3C Fe_7S_8 nanoparticles.

evident that the compound readily undergoes surface oxidation when exposed to air [28] while preparing the sample for the measurement.

3.4 *Raman spectroscopy*

To explore the local structure of 3C Fe_7S_8 nanoparticles, Raman spectroscopy at laboratory temperature (23 ± 2°C) was recorded in the frequency range from 100 to 1500 cm^{-1} to under the laser of 632 nm wavelength (figure 5f). The Raman spectra of trigonal Fe_7S_8 revealed the strongest phonon bands ~218, 280 cm^{-1}, which are also characteristic peaks of pyrrhotites [26]. The data shows two A_{1g} (~218, 488 cm^{-1}) [29] and three E_g (~280, 403, 602 cm^{-1}) [29] Raman active modes. The small peak at ~602 cm^{-1} corresponds to the Fe–O bond [27]. The distinct peak at ~1300 cm^{-1} can be attributed to C=C from the oleylamine [27]. The peak ~1080 cm^{-1} may arise due to the asymmetric stretching of the S–O bond [29]. Based on the earlier reported data, the frequency positions of the Raman peak for the as-synthesized sample support the formation of the trigonal structure of the synthesized sample.

3.5 *Magnetic properties of 3C Fe_7S_8 nanoparticles*

As already mentioned, the magnetic properties of the 3C Fe_7S_8 compound are not clearly discussed in the earlier reports. Hence, to investigate the magnetic properties of the as-synthesized 3C Fe_7S_8 nanoparticles, the ZFC-FC M-T measurements have been recorded using SQUID-VSM. Figure 6a shows the ZFC-FC M-T curves obtained for as-synthesized 3C Fe_7S_8 nanoparticles at the applied magnetic field of 100 and 1000 Oe, respectively. The ZFC and FC *M*–*T* curves are split in the temperature range from 7 to 300 K. In the ZFC process the sample is first cooled down to 7 K without applying an external magnetic field. After applying the magnetic field (100 or 1000 Oe), the magnetization is measured for increasing temperature till 300 K. In the same magnetic field, in the FC process, the magnetization is recorded for decreasing temperature till 7 K. The *M*–*T* curves show that the ZFC and FC curves do not follow the same path. Hence, in each case (100 and 1000 Oe), the *M*–*T* curves show an irreversible behaviour. Thus, the divergence of ZFC-FC M-T curves of 3C Fe_7S_8 over the whole range of temperature up to 300 K signifies the formation of an ordered magnetic state with a high T_C of the sample above 300 K. The magnetic anisotropy plays a crucial role in determining the magnetization and shapes of ZFC and FC curves at a given field strength. It aligns the spins in a preferred direction. As the sample is cooled without an applied magnetic field during the ZFC process, the spins are locked in random directions. When an external field is applied at the lowest temperature (7 K), the resultant magnetization will depend on the anisotropy of the system. A highly anisotropic system requires a high anisotropic field to rotate the spins in the direction of the applied magnetic

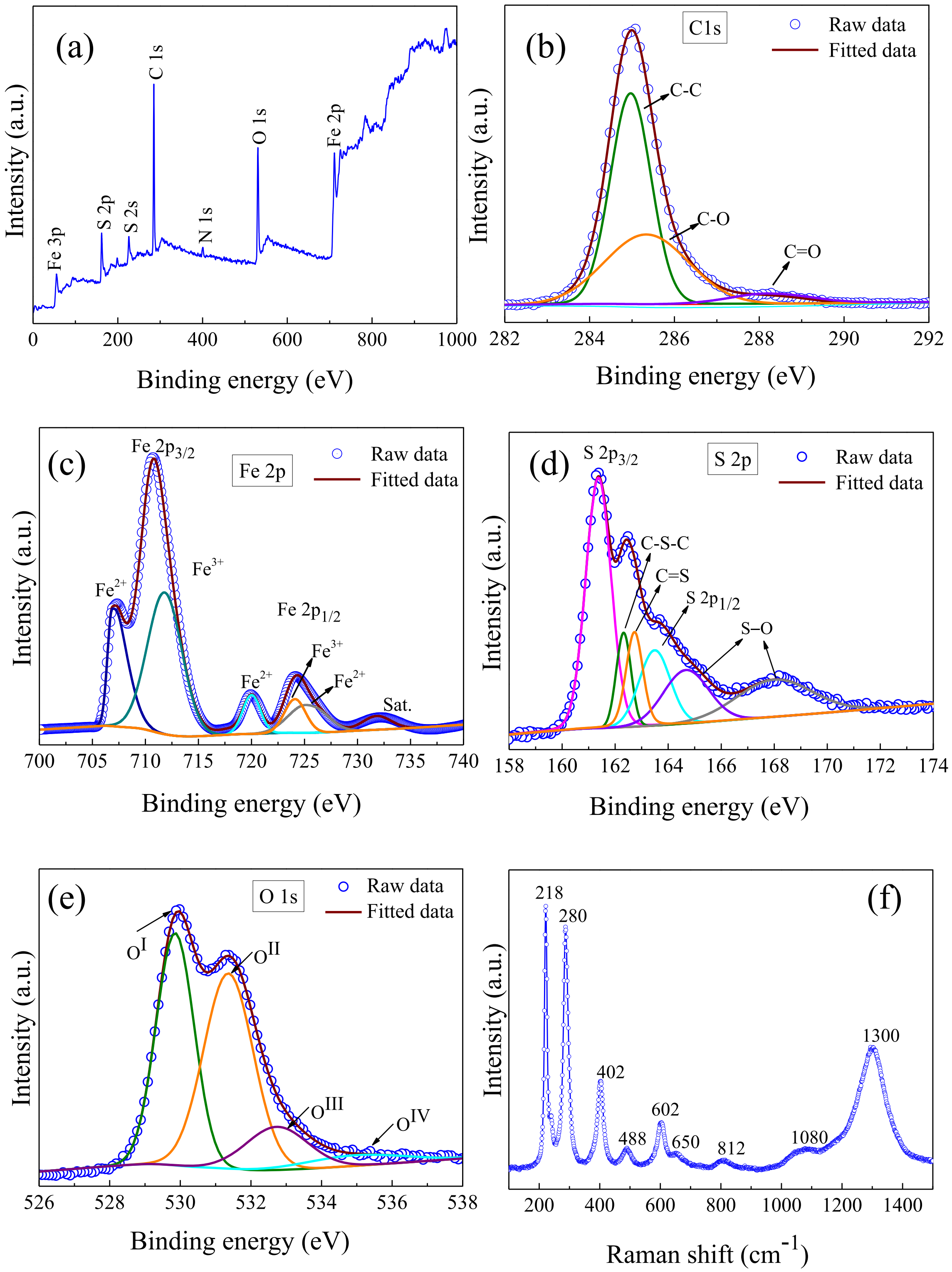

Figure 5. (**a**) XPS survey spectrum of as-synthesized 3C Fe_7S_8 nanoparticles, and high-resolution spectra of (**b**) C 1*s*, (**c**) Fe 2*p*, (**d**) S 2*p*, (**e**) O 1*s* are showing the binding energy of the core levels. (**f**) The Raman spectrum of as-synthesized 3C Fe_7S_8 nanoparticles from 100 to 1500 cm^{-1} excited under wavelength of 632 nm. The prominent peaks ∼218 and 280 cm^{-1} are the characteristic peaks of the pyrrhotites.

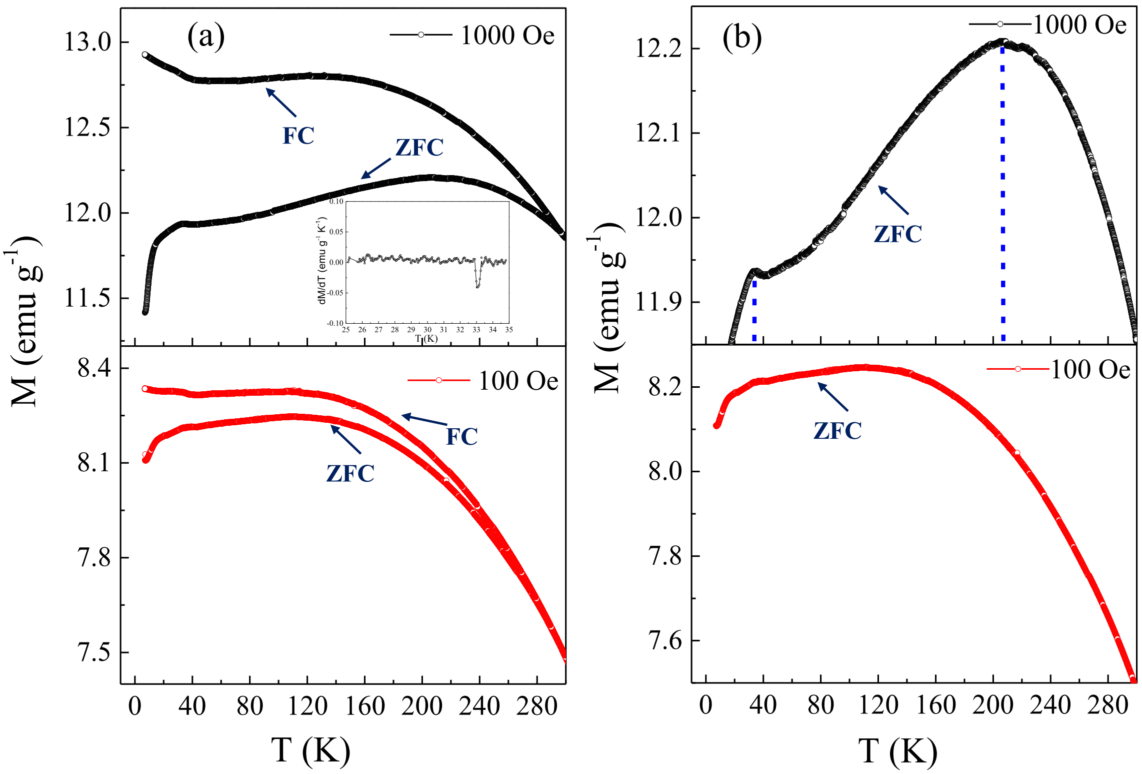

Figure 6. (**a**) Zero-field-cooled (ZFC) and field-cooled (FC) magnetization *vs*. temperature (*M–T*) curves for the sample 3C Fe_7S_8 nanoparticles at 1000 Oe (black curve) and 100 Oe (red curve). The inset shows d*M*/d*T* for the moment calculated from the ZFC data has a peak ∼33 K. (**b**) ZFC *M–T* curves for the sample 3C Fe_7S_8 at applied external fields of 1000 and 100 Oe in the temperature range of 7–300 K.

field [30], resulting in small magnetization. During the FC process, the magnetization will increase with a decrease in temperature, as the spins will be locked in a particular direction depending on the magnetic field strength. The blocking temperature (T_B) is a function of the interparticle interaction, the particle size, the anisotropy energy and the measurement timescale. Above T_B, the thermal activation energy becomes higher than the effective anisotropy energy, making the spins freeze and orient in random directions. However, below T_B, spins freeze in the direction of their easy axis. The sample exhibits coercivity below T_B and becomes zero above T_B [31,32]. As shown in the TEM images, the as-synthesized nanoparticles are agglomerated as many nanocrystallites; hence the average blocking temperature (T_B) is considered as the peak of the ZFC curve. Polydispersity in the sample may cause the blocking phenomena for each particle on each side of the ZFC peak, resulting in the bifurcation of the ZFC–FC curve above T_B. Figure 6b shows the T_B for the sample as 210 K at 1000 Oe applied magnetic field. However, there is no noticeable peak in the ZFC curve at 100 Oe. Hence, now the question is to consider how the energy barrier (the temperature where the ZFC curve exhibits a maximum) disappears as the external magnetic field is decreased to 100 Oe. The applied magnetic field, interparticle interaction, magnetic anisotropy energy and thermal activation energy impact the blocking phenomena of the spins. The magnetic moment of each particle is oriented along the easy axis, and the parallel and antiparallel directions of these moments are separated by an energy barrier K_uV. When the applied magnetic field is zero, the easy axes of the particles are randomly oriented, and the net magnetization of the system is zero. Upon applying an external applied magnetic field (*H*) smaller than the anisotropic field (H_a), the energy barrier changes [32] from K_uV to $K_uV\ [1 \pm (H/H_o)]^2$, where K_u and *V* are uniaxial anisotropy constant, and the volume of the particle. H_o is presented as $H_o = 2H_a = 2K_u/M_S$. The sign (+) represents the moment flip from parallel to antiparallel, and the sign (–) represents the moment flip from antiparallel to parallel direction. The ZFC curves of the specimen at 100 and 1000 Oe magnetic fields are shown in figure 6b. A peak appears at ∼210 K at a higher applied magnetic field (1000 Oe) and diminishes as the magnetic field is reduced to 100 Oe. The argument discussed above is also supported by the fact that T_B depends directly on anisotropy energy [31]. With the decrease in the anisotropy energy, a decrease in T_B will also be observed. This again explains the shape of ZFC–FC curves obtained at 1000 and 100 Oe. Another low-temperature magnetic transition is observed at ∼33 K. The structure of 3C pyrrhotite with space group $P3_121$ resembles that of the 4C structure in the sense that vacancies are confined to alternate layers of iron. Powder samples of 4C

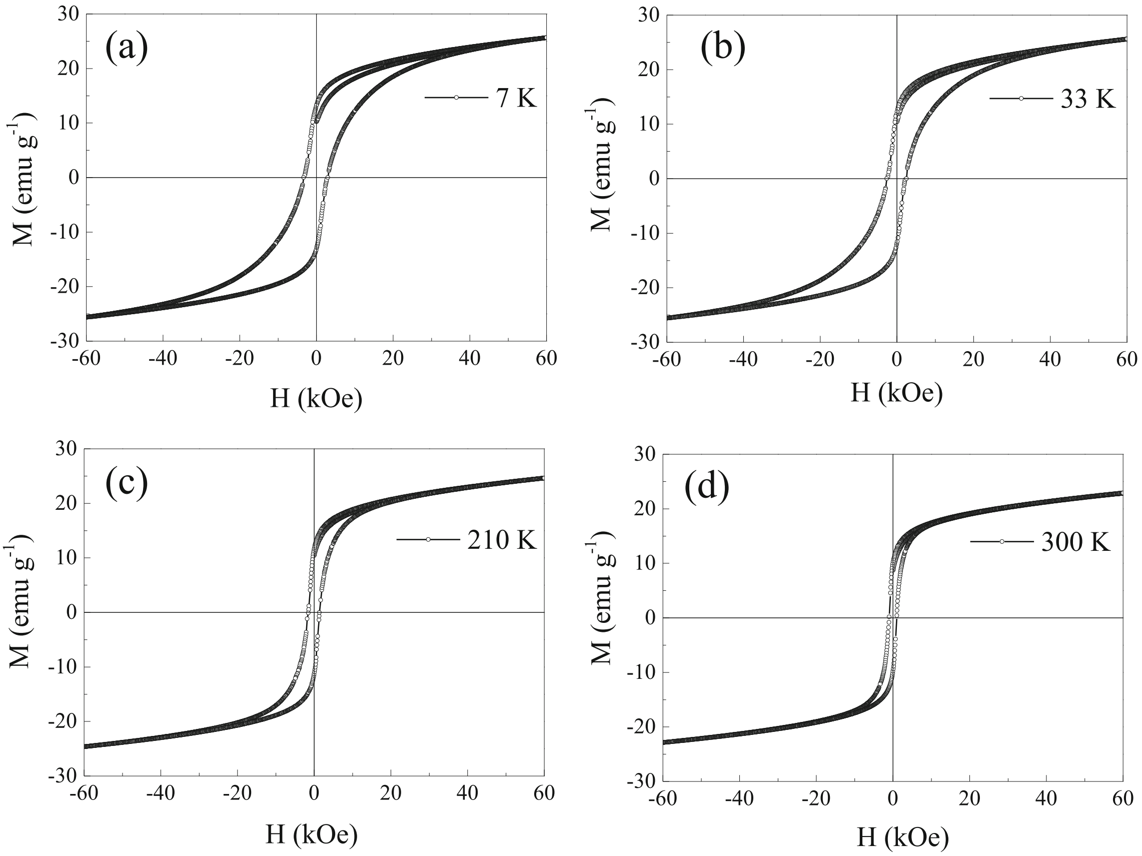

Figure 7. (**a–d**) Magnetization *vs.* external magnetic field (*M–H*) hysteresis loops of the sample 3C Fe_7S_8 nanoparticles at 7, 33, 210 and 300 K. The *M–H* hysteresis loops illustrate the increase in $M_{60\ \mathrm{kOe}}$, H_C and M_R values of the sample with decrease in temperature.

pyrrhotite show an anomaly at low temperature ~30–34 K (known as Besnus transition) [16,17]. This low-temperature magnetic transition stems from the spin rotation, which can be related to the structural changes at an atomic level caused by the highly ordered vacancies in 4C pyrrhotite, which in turn affect the spin-orbit coupling with no crystallography change of the structure [33,34]. Assuming the similar spin arrangements in 3C and 4C pyrrhotites, the low-temperature magnetic transition observed at ~33 K at 1000 Oe applied magnetic field (figure 6b) for as-synthesized 3C pyrrhotite may be assigned as the Besnus transition. The inset shows d*M*/d*T* for the moment calculated from the ZFC data has a peak ~33 K. The shoulder around the Besnus transition implies a rotation of magnetic moments out of the *a–c* planes of the structure, however it appears that the transition temperature might vary locally [35]. Further, a clear low-temperature sharp fall is observed in the ZFC curve of the sample. This may be due to several reasons like formation of canted ferromagnetic domains or anti-parallel spins, or presence of diamagnetic S^{2-} ions [35].

To acquire further insights into the magnetic properties of the 3C Fe_7S_8 nanoparticles, the *M–H* curves were measured using a SQUID-VSM. Figure 7a–d shows *M–H* hysteresis curves taken at 7, 33, 210 and 300 K in the magnetic field range of ±60 kOe, because of the anomalies observed at these temperature values in *M–T* graphs (figure 6b). As shown in figure 7a–d, the sample demonstrates ferrimagnetic-like behaviour at all measurement temperatures. However, the magnetization does not show saturation at the highest applied magnetic field of 60 kOe. Such behaviour indicates that the spins of the system require a high anisotropic field to align in a particular direction. We observed an initial remanence in the sample at all measurement temperatures. Remanence comes from the vacancies in the specimen. The presence of initial remanence in the *M–H* hysteresis loop may be attributed to the induced magnetization due to the Fe vacancies in a powdered polycrystalline sample. The hysteresis curves illustrate that H_C, $M_{60\ \mathrm{kOe}}$ and M_R values of the sample increase with a decrease in temperature. Among all four measurement temperature values, the 3C Fe_7S_8 NPs appear to exhibit hysteresis with H_C, $M_{60\ \mathrm{kOe}}$ and M_R of ~1.5 kOe, ~22 emu g^{-1} and ~11 emu g^{-1}, respectively, at 300 K, which increases to ~3.3 kOe, ~25 emu g^{-1} and ~13 emu g^{-1}, respectively at 7 K (table 3). The increase in these values at the lower temperature may have contributions from the reduction in thermal activation energy and the increase in overall

Table 3. Summary of the magnetic parameters calculated for the sample 3C Fe_7S_8 nanoparticles at different measurement temperatures.

Measurement temperature (K)	H_C (kOe)	M_R (emu g^{-1})	$M_{60\ kOe}$ (emu g^{-1})	M_R/M_S	H_a (kOe)	K_{eff} (erg cc^{-1}) × 10^5	BH_{max} (kG Oe)
7	3.3	13.1	25.65	0.510	11.7	1.50	128.7
33	2.6	12.3	25.60	0.480	8.2	1.05	115.2
210	1.5	11.5	24.62	0.467	5.1	0.63	102.2
300	1.0	10.0	22.80	0.439	4.4	0.50	71.7

effective magnetic anisotropy, making more spins available to align in the direction of the applied magnetic field. In the $Fe_{1-x}S$ compounds, there are two types of Fe ionic states—Fe^{2+} and Fe^{3+} along with ordered Fe vacancies in alternate layers of the lattice [11]. The magnetic moments of Fe in the compound are ferromagnetically arranged inside each layer but are coupled antiferromagnetically to each other between adjacent layers [36]. The vacancies in every second layer contribute to the spin orientation. The presence of ionic states of iron and the vacancies in the lattice lead to uncompensated magnetic moments, giving rise to the ferrimagnetic ordering in the compound [37]. The neutron diffraction of the compound is still awaited. However, in the equivalent phase, 3C Fe_7Se_8, the moments of Fe ions in *c*-plane are parallel to one another (ferromagnetic ordering of moments), whereas the moments of Fe ions in the adjacent *c*-plane are antiparallel (antiferromagnetic ordering of moments) [38]. Thus, owing to a net spontaneous moment caused by the uncompensated moments below the ordering temperature, 3C Fe_7Se_8 possesses ferrimagnetic ordering, which further suggests that the 3C pyrrhotite exhibits ferrimagnetic ordering.

For a polycrystalline powdered sample, calculation of the magnetic anisotropy constant (K) is not simple as it is composed of several agglomerated nanocrystallites (shown in the TEM image). Therefore, the orientation of the powdered sample along one easy axis and then the hard axis is not as simple as it may be for a single crystal in VSM. The magnetic anisotropy of any material is its intrinsic property. Therefore, calculation of K from the measured hysteresis loop of the sample will give the effective magnetic anisotropy (K_{eff}) of all the particles oriented in random directions. The presence of ordered Fe vacancies in the 3C Fe_7S_8 structure gives rise to a highly anisotropic crystal field and the spin–orbit coupling, which in-turn creates a large magnetocrystalline anisotropy in the system [39]. The anisotropy field (H_a) is defined as the field required to saturate the magnetization in the hard direction. The M–H curve in both the easy and hard axes is extrapolated to calculate H_a. The value of K_{eff} at all temperatures is calculated from M_s and H_a using the following equation [39,40].

$$K_{eff} = \frac{1}{2} M_S H_a \tag{4}$$

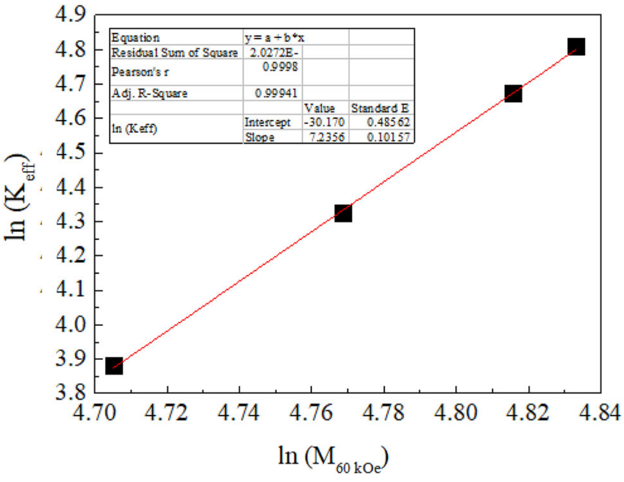

Figure 8. Linear relationship between K_{eff} and $M_{60\ kOe}$ in the logarithmic scale, with a slope of 7.2, indicating that the sample predominantly exhibits uniaxial anisotropy.

The value of K_{eff} is 0.5×10^5 erg cc^{-1} at 300 K, which increases to 1.5×10^5 erg cc^{-1} at 7 K (table 3). To determine the type of magnetocrystalline anisotropy, ln(K_{eff}) is plotted against ln($M_{60\ kOe}$), as shown in figure 8. For a system with uniaxial magnetocrystalline anisotropy, K_{eff} should be proportional to ${M_{60\ kOe}}^3$, whereas for a cubic magnetocrystalline anisotropy, K_{eff} should be proportional to ${M_{60\ kOe}}^{10}$ [41]. The linear fit of the plot gives a slope of 7.2, indicating that the sample predominantly exhibits uniaxial anisotropy [41].

The maximum energy product (BH_{max}) is the measure of the magnetic energy stored in the material, which is estimated by the maximum area of the rectangle under the B–H curve in the second quadrant of the B–H hysteresis loop (figure 9a–d) [40]. Theoretically, the maximum energy product is defined as:

$$BH_{max} = \frac{1}{4} \mu_0 M_S^2 \tag{5}$$

where μ_0 defines the magnetic permeability of free space, and M_S is the saturation magnetization. The given equation describes an important role played by M_S in determining the energy product of the material. The 2nd quadrant of the B–H loop for 3C Fe_7S_8 nanostructure at all temperatures is shown in the inset of figure. The area under the grey shaded

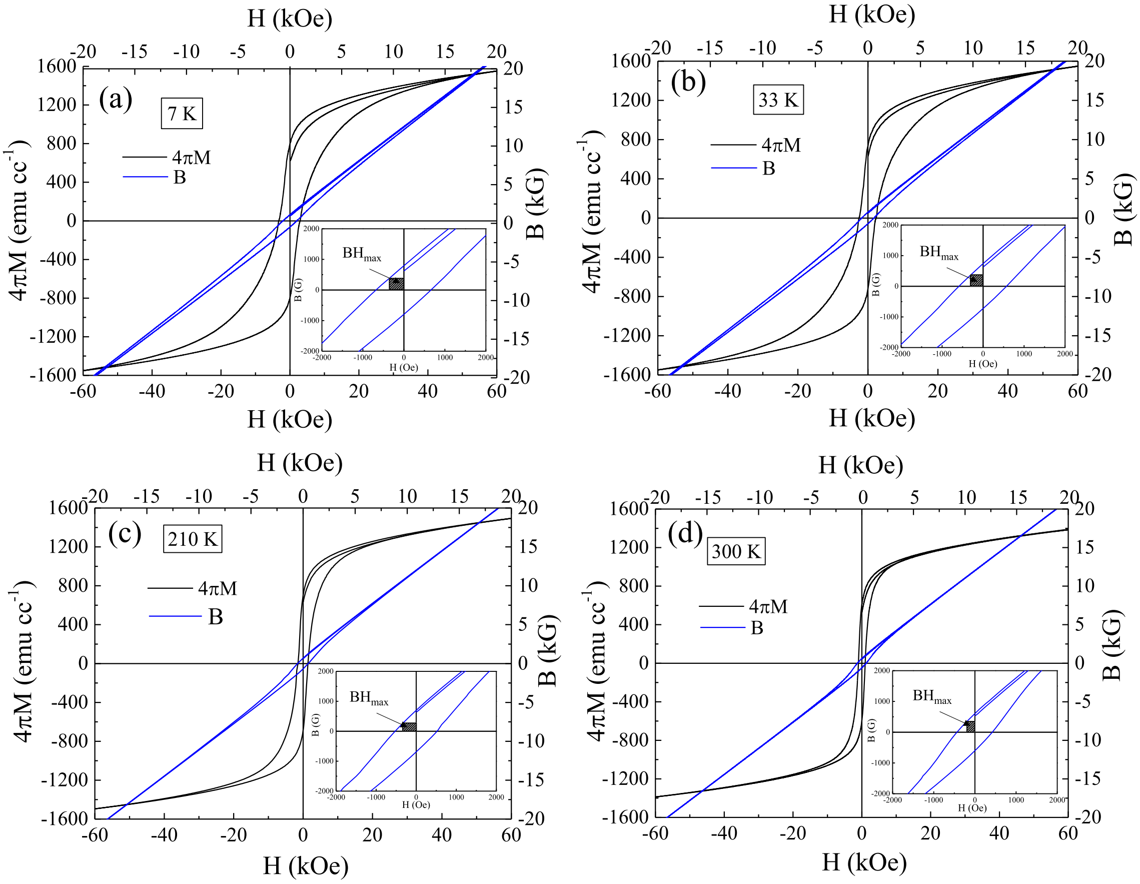

Figure 9. (**a**–**d**) *M*–*H* and *B*–*H* plots for the sample 3C Fe_7S_8 nanoparticles. The inset in each figure shows the calculation of the maximum energy product from *B*–*H* hysteresis loop at 7, 33, 210 and 300 K.

portion represents the BH_{max} of the sample. For the given set of measurement temperature values (7, 33, 210 and 300 K), the value of BH_{max} is 71.7 kG Oe, at 300 K and becomes 128 kG Oe at 7 K (table 3), making the compound valuable for various applications at low temperature.

4. Conclusions

The trigonal 3C Fe_7S_8 nanoparticles are prepared using the thermal decomposition method. The crystallite size of the nanoparticles along the (206) plane is $\sim$27 nm, as estimated from the XRD pattern. The ZFC and FC magnetization data, recorded at 100 and 1000 Oe, reveal magnetic ordering with high T_C (above 300 K). The hysteresis curves measured at different temperatures (7, 33, 210 and 300 K) show the ferrimagnetic behaviour of 3C Fe_7S_8 nanoparticles. The magnetic parameters—coercivity (H_C), saturation magnetization ($M_{60\ kOe}$), the effective anisotropy constant (K_{eff}) and the maximum energy product (BH_{max}) appear to increase as the measuring temperature is lowered down. Among the set of measurement temperatures, the H_C, $M_{60\ kOe}$ and M_R show the highest value of $\sim$3.3 kOe, 25.6 emu g^{-1} and 13 emu g^{-1}, respectively, at 7 K. As a result of increasing $M_{60\ kOe}$ at lower measurement temperatures, the BH_{max} value increases with decreasing temperature. It becomes $\sim$128 kG Oe at 7 K, the highest value obtained for the given set of measurement temperatures in this study. The high value of BH_{max} of $\sim$128 kG Oe at 7 K signifies that the compound may be considered for low-temperature industrial applications. To the best of our knowledge, these findings for 3C Fe_7S_8 nanoparticles have been done for the first time.

Acknowledgement

SJ acknowledges the financial support from the Department of Science and Technology, New Delhi, India, as a Senior Research Fellow (SRF) through the INSPIRE, and the useful scientific discussions with Dr Bhavana Joshi.

References

[1] Rickard D and Luther G W 2006 *Rev. Mineral. Geochem.* **61** 421
[2] Berner R A 1990 *Chem. Geol.* **84** 159
[3] Nakazawa H and Morimoto N 1971 *Mater. Res. Bull.* **6** 345

[4] Fleet M E 2006 *Rev. Mineral. Geochem.* **61** 365

[5] Morimoto N, Nakazawa H, Nishigumi K and Tokonami M 1970 *Science* **168** 964

[6] Nakano A, Tokonami M and Morimoto N 1979 *Acta Cryst.* **35** 724

[7] Rao C N R 2005 *Int. J. Nanosci.* **4** 811

[8] Kong X, Lou T and Li Y 2005 *J. Alloys Compd.* **390** 236

[9] Mlowe S, Osman N S E, Moyo T, Mwakikunga B and Revaprasadu N 2017 *Mater. Chem. Phys.* **198** 167

[10] Andresen Arne F and Torbo Per 1967 *Acta Chem. Scand.* **21** 2841

[11] Bertaut E F 1953 *Acta Crystallogr.* **6** 557

[12] Fleet M E 1971 *Acta Crystallogr.* **27** 1864

[13] Wuensch Bernhardt J 1963 *Mineral. Soc. Am.* **1** 157

[14] Nishiguchi M 1977 MS Thesis (Osaka University)

[15] Okazaki A and Hirakawa K 1956 *J. Phys. Soc. Jpn.* **11** 930

[16] Horng C S and Roberts A P 2018 *Geochem. Geophys.* **19** 3364

[17] Koulialias D, Lesniak B, Schwotzer M, Weidler P G, Löffler J F and Gehring A U 2019 *Geochem. Geophys.* **20** 5216

[18] Lin C R, Lu S Z, Lyubutin I S, Korzhetskiyyu V, Wang S C and Suzdalev I P 2010 *J. Appl. Phys.* **107** 547

[19] Cullity B D 1978 *Elements of X-ray diffraction* (Phillippines: Addison-Wesley Publishing Company Inc.)

[20] Keller-Besrest F, Collin G and Comès R 1983 *Acta Crystallogr.* **39** 296

[21] Holder C F and Schaak R E 2019 *ACS Nano* **13** 7359

[22] Uvarov V 2019 *J. Appl. Crystallogr.* **52** 252

[23] Velders G J M and Feil D 1989 *Acta Crystallogr.* **45** 359

[24] Argueta-Figueroa L, Torres-Gómez N, García-Contreras R, Vilchis-Nestor A R, Martínez-Alvarez O and Acosta-Torres L S 2018 *Prog. Nat. Sci. Mater.* **28** 447

[25] Mc Cabe W L, Smith J C and Harriot Peter 2018 Unit operations of chemical engineering. McGraw-Hill, Inc., New York

[26] Lara R H, Monroy M G, Mallet M, Dossot M, González M A and Cruz R 2015 Environ. *Earth Sci.* **73** 1849

[27] Loh J Y Y and Kherani N P 2019 *Molecules* **24** 1

[28] Ghalawat M and Poddar P 2022 *J. Phys. Chem. C* **9** 4655

[29] Buzgar N, Buzatu A and Sanislav I V 2009 *Geol.* **55** 5

[30] Joy P A, Anil Kumar P S and Date S K 1998 *J. Phys. Condens. Matter* **10** 11049

[31] Coey J M D 2010 Magnetism and magnetic materials. Cambridge University Press

[32] Zhang Y D, Budnick J I, Hines W A, Chien C L, Xiao J Q and Zhang Y D 1998 *Appl. Phys. Lett.* **72** 2053

[33] Fillion G and Rochette P 1998 *J. Phys. Colloq.* **49** 907

[34] Dekkers M J, Mattéi J L, Fillion G and Rochette P 1989 *Geophys. Res. Lett.* **16** 855

[35] Haines C R S, Dutton S E, Volk M W R and Carpenter M A 2020 *J. Phys. Condens. Matter* **32** 405401

[36] Živković A, King H E, Wolthers M and De Leeuw N H 2021 *J. Phys. Condens. Matter* **33** 465801

[37] Issa B, Obaidat I M, Albiss B A and Haik Y 2013 *Int. J. Mol. Sci.* **14** 21266

[38] Kawaminami M and Okazaki A 1970 *J. Phys. Soc. Jpn.* **29** 649

[39] Long G, Zhang H, Li D, Sabirianov R, Zhang Z and Zeng H 2011 *Appl. Phys. Lett.* **99** 4

[40] Sen Bishwas M, Das R and Poddar P 2014 *J. Phys. Chem. C* **118** 8

[41] Cullity B D and Graham C D 2008 *Introduction to magnetic materials* (Willey-IEEE Press)